Morphodynamic Modelling of Sediment Control Groynes in a Meandering River entering a Reservoir

2017

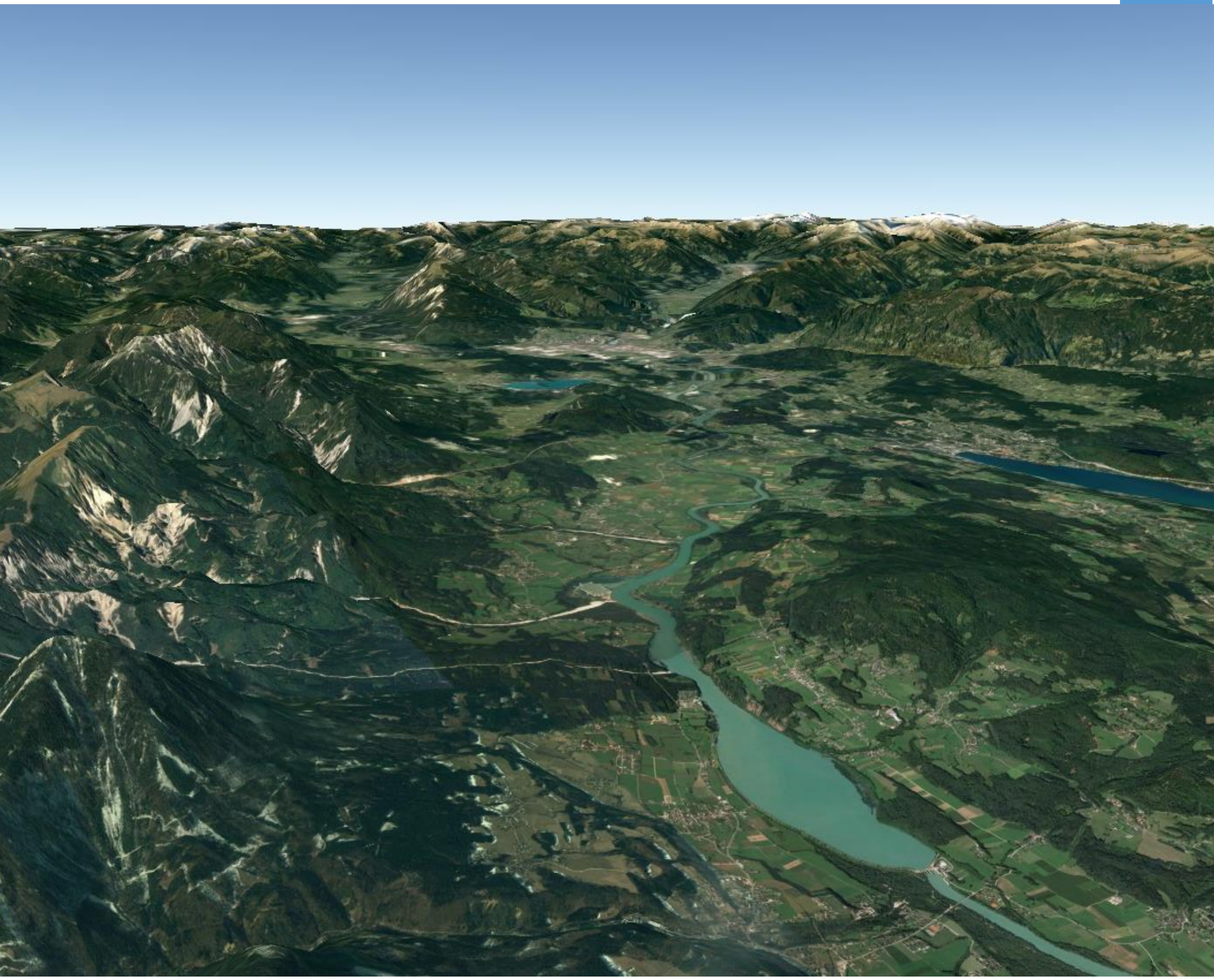

MASc. Thesis

Zhina Mohammed

uOttawa

Morphodynamic modelling of sediment control groynes in a meandering river entering a reservoir

Zhina Mohammed

Submitted in fulfilment of the
Requirements of the degree of

Master of Applied Science

in

Civil Engineering

University of Ottawa

January 2017, Ottawa, Canada

Graduation Committee:

Professor Rennie Colin (Supervisor)
Professor Mohammadian Abdolmajid (Evaluation committee)
Professor Seidou Ousmane (Evaluation committee)

Acknowledgments:

I would like to express my gratitude and thanks to the many people who made this study possible

First, I would like to give my sincere appreciation and thanks to my supervisor, Professor Colin Rennie, for his support, patience, guidance, motivation, and the weekly meeting time that he invested in me. I benefited a lot from his enormous knowledge, and it was a privilege to work under his supervision.

The second person who made a huge contribution to this study is my co-supervisor, Clemens Dorfmann, from the Graz University of Technology, Austria. I would like to offer him special thanks and gratitude for allowing me to work on this project and providing me with all his support and knowledge.

In addition, I would like to thank Verbund VHP for providing me with some of the data.

During these two years, I have benefited from the feedback and knowledge of many colleagues from back home and all those I got to know at the University of Ottawa. Many thanks go to them.

During these two years, this path of my life would not have been as easy without my lovely family, who stand by my side and always encourage me to do better. Thank you, Dad and Mom, for all your support and love. Words cannot express my gratitude for everything you have done for me. I have been fortunate also to have siblings who are always there for me. Thanks for cheering me up in my hardest times.

I dedicate this study to my parents

“Never regard study as a duty, but as the enviable opportunity to learn to know the liberating influence of beauty in the realm of the spirit for your own personal joy and to the profit of the community to which your later work belongs”

Albert Einstein

Abstract:

Sedimentation is one of the consequences of hydropower plant construction. Such structures not only have an influence on reservoir morphology, but also have great impact on both upstream and downstream river morphology.

This study focuses on fluvial morphological changes in between two hydropower plants on the Drava River, Austria. The influence of both reservoir management methods (flushing) and human intervention (groynes) have been investigated. The first stage started with validating an unsteady Delft3D morphodynamic model of the meandering reach. This validation shows the importance of spatial grain size distribution in predicting bed load transport. Analysis of the flushing method includes investigation of the duration of gate-opening before and after peak flood. The results show that the duration of lowering the water level at the hydropower plant (by opening the gate) before starting the peak flood will not have a big influence on the river morphology upstream of the reservoir. However, the duration of maintaining the low water level after the peak flood has a large influence on both the river morphology in the upstream portion of the reservoir and on the sediment transport toward the reservoir

In the second part of this study, hydraulic structural groynes were applied in the river reach. The objective was to design a groyne field that will minimize sediment transport to the reservoir. Both emerged and submerged groynes were investigated. In addition, the influences of both groyne head shape and the distribution of sediment grain size in the groyne zone were examined. This study shows that under an unsteady simulation, when the groynes are submerged by 1m at normal flow, the sediment supply to the groyne zone decreases compared to the emerged case. However, if the groynes are submerged by 0.5m, the sediment supply to the groyne zone will be greater than the emerged case for an aspect ratio in between (0.5-2). Finally, applying L-head groynes produces less erosion in the main stream and a higher sediment supply compared to straight groynes.

Contents:

List of Figures:

List of Tables

List of Charts

List of Symbols:

α_2: Correction factor for sediment concentration

α_1: Correction factor to represent concentration at bottom of kmx layer

βc: 2D secondary flow model –constant in the range[0-1]

C_a: Mass concentration at reference height (kg/m^3)

C_{kmx}: Average concentration of the kmx cell of sediment fraction

C_{Soil}: Reference sediment density

C_m^{tot} Summation of all fraction concentration

C': Chezy's coefficient related to grains

Ds: Representative diameter of suspended sediment (m)

D_*: Dimensionless particle size

D_{50}: Median particle diameter (m)

d: Depth below some horizontal plane of reference (datum)

D_H^{back}: Background horizontal eddy diffusivity (m^2/s)

D_V^{back}: Background vertical eddy diffusivity for transport equation

g: Gravity(m/s^2)

h: Water depth

H: Total water depth (H = d + ζ; d positive downward)

I: Spiral motion intensity (secondary flow)

K: turbulent kinetic energy in 3D turbulence closure model

k_1: Correction factor for the groynes head type

k_2: Correction factor for the alignment of groynes system

k_3: correction factor for the function of groynes

κ : Von Karman constant (0.41)

L: Mixing length in 3D turbulence closure model (m)

Morfac: User-defined morphological acceleration factor

P: porosity (0.4)

ρ_s: Sediment density (kg/m^3)

ρ : Fluid density (kg/m^3)

Q_{in}: Local source per unit volume

Q_{out}: Local sink per unit volume

R_b: Hydraulic radius related to the bed according to sidewall correction method of Vanoni-Brooks

Rs: Radius of curvature of a streamline in the secondary flow model (m)

Re^*: Reynold number

s: Relative density

S: Salinity (ppt)

S: Source sink term in advection diffusion equation

Smax: Maximum salinity for flocculation calculations (ppt)

$S_{b,\,n}$: Additional bedload transport vector. The direction of this vector is normal to the unadjusted bedload transport vector, in the down slope direction

$|S_b'|$: Magnitude of the unadjusted bedload transport vector (adjusted for longitudinal bed slope only)

$|S_b''|$: Magnitude of the bedload transport vector (kg/ms)

$S_{b,uu}^{(m,n)}$: Computed bedload-sediment transport vector in u-direction, held at the u-point of the computational cell at location (m, n), (kg/ms)
T: Non-dimensional bed-shear stress
U: Velocity in stream wise (m/s)
u^*: Shear velocity (m/s)
ū : Mean flow velocity related to grains
u'_*: Bed shear velocity related to grains
V: Velocity in transverse directions (m/s)
W: Velocity in vertical direction (m/s)
z: Vertical coordinate in physical space
Z': Modified suspension number and is equal to summation of (suspension number and overall correction factor representing all additional effects
ζ: Free surface elevation above the reference plane (at z = 0)
η: Relative availability of the sediment fraction in the mixing layer
μ: Efficiency factor current
$\Delta_{SED}^{(m.n)}$ Change in quantity of bottom sediment at location (m; n), (kg/m^2)
Δ_z: Difference in elevation between the centre of the kmx cell and Van Rijn's reference level
λ_d: First order decay coefficient
ν : Kinematic viscosity
v_{mol}: Kinematic viscosity (molecular) coefficient (m^2/s)
v_H^{back}: Background horizontal eddy viscosity)(m^2/s)
v_V^{back}: Background vertical eddy viscosity for momentum equations (m^2/s)
v_V: Vertical eddy viscosity (m^2/s)
v_{2D}: Part of eddy viscosity due to horizontal turbulence model (m^2/s)
v_{3D}: Part of eddy viscosity due to turbulence model in vertical direction (m^2/s)
τ_b: Bed shear stress (N/m^2)
$\tau_{b,cr}$: Critical bed shear stress (N/m^2)
ε_s: Sediment diffusion coefficient computed at bottom of kmx layer.
θ: Shield mobility number
θ_{cr}: Critical Shield mobility number
$\omega_{s,max}$: Settling velocity of sediment fraction at maximum salinity concentration.
$\omega_{s,f}$: Fresh water settling velocity of fraction

1. Introduction:

1.1 Problem Definition

In 1968, a hydropower plant was constructed in a segment of the Drava River in the western part of Austria's Carinthia province. Like other power plants, construction of such a structure has severe impacts on sediment transport, and produces large sedimentation in both the reservoir and the upstream river reach. Such sedimentation was evident in a Drava River bathymetric survey conducted in 2012 by researchers at the Graz University of Technology on behalf of Verbund (AHP), the Austrian hydroelectric utility. However, sedimentation in this study area was not only due to the downstream reservoir but also due to a series of hydropower plants upstream of this reach. These reservoirs release large quantities of suspended sediment to the current reach. This suspended sediment also influences the operation of the downstream hydropower plant.

To manage such a complex area more effectively in order to meet all the demands, a powerful numerical modeling tool is required to understand the interaction between sediment transport, morphology development, and flowing water. Therefore, a model was set up for the river reach upstream of the hydropower plant. In this model, the influence of both the reservoir management method (flushing) and human intervention (groynes) in this reach are investigated.

1.2 Objective and Research Questions

The objective of this study is divided into two major parts.

The first part is aimed at understanding and investigating several physical theories of sediment transport on predicting morphology change in a meandering reach. This examination aimed to answer the following questions:

- Is the secondary flow model available in Delft3D capable of predicting secondary circulation in a meandering river?
- Is it possible to predict bed load transport or entrainment using a constant grain size distribution over the entire reach?

Regarding managing sediment transport:

- What is the sediment load entering this reach per year, and how much of it will remain in the reach and how much will be transported toward the reservoir?
- What is the influence of flushing operations on this river reach? Does the timing of opening the gate have an influence on the river morphology?

The second part of this study is aimed at answering the following questions regarding human intervention (i.e., groynes construction) in this river reach and understanding the sediment dynamic in both emerged and submerged groynes.

- What impact does constructing groynes produce on river morphology and on sediment transport toward the reservoir?
- What is the influence of groynes submergence on sediment supply to the groynes zone?
- What is the influence of cohesive versus non-cohesive sediment distribution in the groyne zone?

1.3 Research Novelty

Some parts of this study will be added to the worldwide research for this field.

To the best of the author's knowledge, this is the first study to apply Delft3D to investigate sediment dynamics with multiple grain sizes (cohesive and non-cohesive) in the groyne zone of a river reach. Previously, two other studies applied Delft3D, but one of them investigated sediment dynamics in a coastal area (Stive, 2010). In Stive's (2010) thesis, the model were able to produce the sediment exchange in the groyne zone by applying thin dams. In addition, Yossef's (2005) thesis used Delft3D to predict sediment transport in the emerged groyne zone of a river reach, but in that case the model was not capable of predicting morphology changes in the groynes zone accurately due to only having only one non-cohesive fraction in the model. Yossef (2005) concluded this result go back to underestimation of sediment transport formula of non-cohesive sediment, in addition to underestimation of turbulence in the mixing layer. Furthermore, in Yossef's (2005) model, the groynes were defined in the bathymetry.

1.4 Research Outline:

2-Literature Review - Theoretical Background

- River morphology
- Sediment
- Sediment Management
- Groynes

3-Model Description (Delft3D)

- Grid
- Hydrodynamic and Morphodynamic
- Groynes Structures

4-Study Area

- Study Area Description
- Field Data

5-Model Setup (Meandering)

- Grid, Boundary Condition, Initial Condition, Physical Parameters

6-Model Assessment

- Hydrodynamic Calibration
- Morphodynamic Calibration

7-Sediment Transport Estimation-1year

- Bed load, Suspended load, and Total transport

8-Flushing Analysis

- Analysis of River morphology and Sediment Transport

9-Groynes&River Morphology

- 2D weir validation by modeling flume
- Applying groynes to the river

10-Conclusions& Recommendations

-

2. Literature Review- Theoretical background:

2.1. River Morphology

Change in river form has correlation with many inter-related elements such as channel geometry, bed forms, forcing flow distribution, sediment characteristics, bed composition, bank material, and vegetation. Because of the complexity of the interactions between these elements, until now no complete physical and mathematical equation for determining morphological change is available. Therefore, researchers have relied on either empirical studies (e.g., field studies, laboratory experiments) or theoretical studies based on Navier Stokes equations with varying degrees of simplification (Przedwojski, 1995). Generally, a river planform can be categorized as either straight, meandering, or braided. Meandering rivers are also divided into various types depending on channel pattern and channel bars (Przedwojski, 1995). One of the main physical process distinctions between straight and meandering rivers is the formation of helical flows in a meandering river. The lateral component of a helical flow is known as "secondary current", as shown in Figure (2.1), which has a huge influence on flow patterns and morphology changes. Such a phenomenon occurs as a result of a combination of degree of curvature and Coriolis acceleration (Hey and Throne, 1975; Kalkwijk and Booij, 1986). Because of its three-dimensional complexity and small values compared to main flow velocity, sometimes secondary circulation cannot be predicted easily by a 2D depth-averaged model. In 1986, Kalkwijk and Booij developed a model to account for the secondary flow in the momentum equation by taking in to account the curvature and Coriolis effect. In this model, additional terms (shear stress) were added to the momentum equation; however, the model had restrictions on the width and curvature of the channel. Song et al. (2011) solved the depth-averaged velocity with dispersion stresses by the SU/PG (Steam line Upwind/Petrov-Galerkin) scheme of the FEM. The dispersion term included deformation of the vertical profile of the stream-wise velocity, the roughness coefficient, and the curvature ratio. On the other hand, in the case of applying a 3D model, secondary flow can be estimated accurately without applying any empirical formula (e.g., Rüther, 2006), but it is time-consuming. Numerous studies have shown the reliability of 3D models in predicting secondary flow as compared to 2D models (e.g., Lane et al., 1999; Kasvi et. al., 2015).

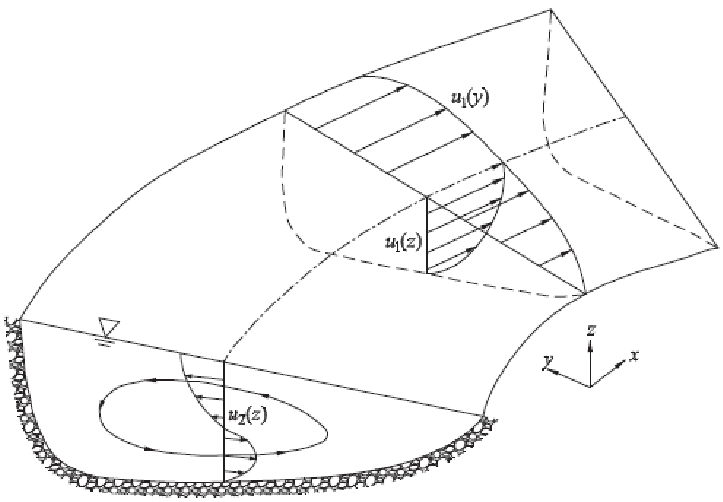

Figure (2.1) Secondary flow pattern in a meandering channel (from Song et. al., 2011)

2.2. Sediment

Sediment transport commences when the mobilizing forces acting on the particles are greater than the resisting forces holding the sediment. This resistance varies depending on bed particle size. When the bed consists of coarse particles like sand and gravel, the resistance force depends on particle weight, friction force and degree of exposure. However, in the case of the presence of cohesive sediment like clay and silt, the cohesive force will also be included (Van Rijn, 2013). In 1936, in a classic study, Shields examined the initiation of particle movement. His experimental curve (Figure 2.2) showed that particle movement depends mainly on the particles, Reynolds number and the non-dimensional bed shear stress (known as the Shields parameter). The curve defines the critical Shields parameter. When the Shields parameter is greater than the critical Shields parameter, the particles start moving. The Shields parameter depends on shear velocity, relative density, median particle diameter and gravity. Van Rijn (2016) defined the Shields particle movement as "conditions with frequent particle movement at all locations". Because of the complexity of sediment transport, scientists divide the sediment movement into three categories: bed load, suspended load and wash load.

$$\boldsymbol{D_* = D_{50}(\frac{(s-1)g}{\nu^2})^{1/3}} \quad (2.1) \qquad , \boldsymbol{\theta = \frac{\tau_b}{(\rho_s-\rho)gD_{50}}} \quad (2.2)$$

$$\boldsymbol{\theta_{cr} = \frac{\tau_{bcr}}{(\rho_s-\rho)gD_{50}}} \quad (2.3) \qquad , \boldsymbol{Re^* = \frac{u^* D_{50}}{\nu}} \quad (2.4)$$

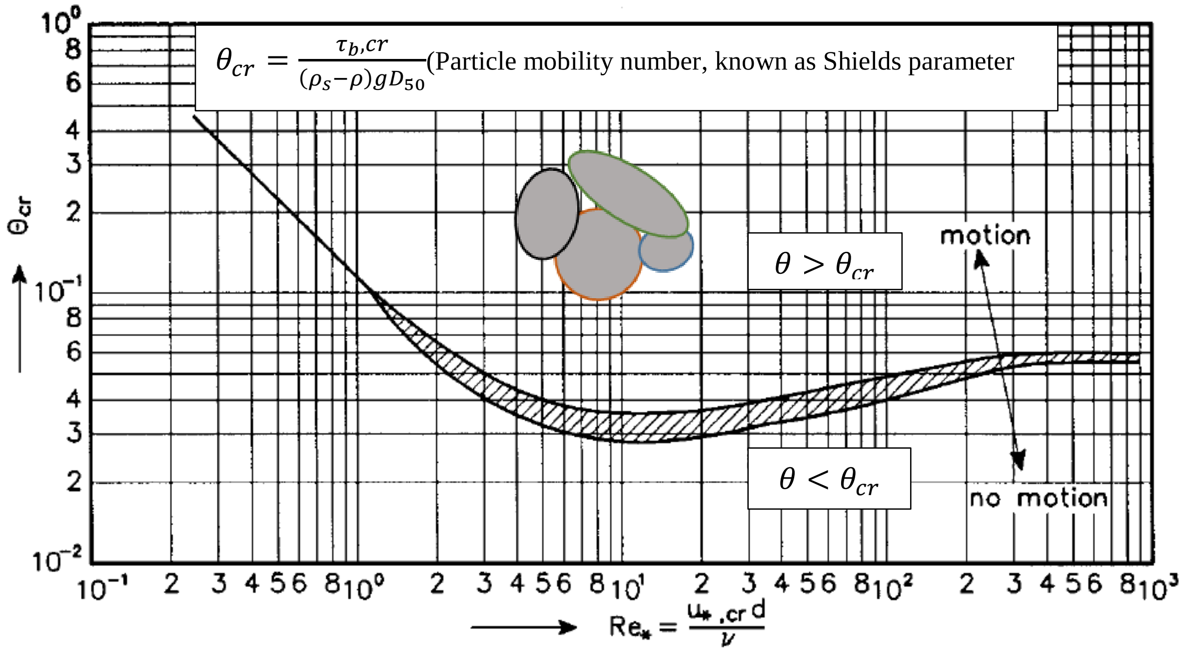

Figure (2.2) Shields curve for initiating particle movement (From Van Rijn, 2016)

D_*: Dimensionless particle size
D_{50}: Median particle diameter
θ: Shield mobility number θ_{cr}: Critical Shields mobility number
τ_b: Bed shear stress $\tau_{b,cr}$: Critical bed shear stress
ρ_s: Sediment density; ρ : Fluid density; s: Relative density
Re^*: Reynolds number
u^*: Shear velocity, : Kinematic viscosity; g: gravity;

2.2.1 Bed Load Transport

Bed load is defined as the sediment that is transported immediately above the bed. This movement occurs in numerous forms such as sliding, rolling, or saltation. When the bed shear stress is small, the movement form is sliding and rolling; however, in the case of larger bed shear stress compared with the critical value of initiation of motion, the particles start to jump short distances on the bed, which is known as saltation (Dey, 2014).

Many theories are available to describe bed load transport. Einstein (1950) stated that the layer thickness of sliding and rolling is equal to two times the particle size, whereas the saltation (jump) mode thickness is more than two diameter thickness from the bed. In addition, Bagnold (1956) illustrated that bed movement results from both gravity and bed shear stress (as cited in Dey, 2014).

Based on various concepts like bed shear stress, discharge, velocity, stream power, bed form, probabilistic, deterministic, and equal mobility, many approaches have been developed to estimate bed load transport (Dey, 2014).

2.2.2. Suspended Load Transport

Suspended load is defined as the sediment that is transported in suspension between the water surface and above the bed layer under the mechanisms of advection and diffusion. Sediment becomes suspended when the bed shear velocity is greater than the settling velocity. Then, both turbulence (diffusion) and flow velocity (advection) have an influence on the sediment transport (Van Rijn, 1984b). Wash load is a particular type of suspended load in which sediment particles are sufficiently fine that they do not settle to the bed.

Suspended sediment has been analysed based on multiple theories like energy, diffusion, and stochastic concepts. For example, Van Rijn's (1984b) formula depends on the diffusion concept in determining the suspended load transport.

2.2.3. Non-Cohesive Sediment Transport Formula

Van Rijn Formula:

Van Rijn's sediment transport concept is based on the equations of motion. Van Rijn (1984a) determined the bedload transport rate as a function of particle velocity, saltation height, and bed load concentration. Based on bedload measurements in many flume experiments, the sediment concentration of solitary particles in the 200-2000μm range was determined as a function of excess non-dimensional bed shear stress and dimensionless particle size. In this study, the interaction between sediment particles was not taken into account (Van Rijn, 1983). Subsequently, suspended load transport rate was determined as a function of reference concentration, flow velocity and diffusion, as shown in Diagram (2.1) (Van Rijn, 1984b).

In 1993, Van Rijn conducted an experiment to estimate the sediment transport rate for particle sizes 100μm and 200μm under the effects of both current and waves. This study showed the influence of bed roughness height, waves, and current strength on concentration and sediment transport rate prediction. The accuracy of the measured and computed sediment transport rates was higher for particle size 100μm than for 200μm. In addition, the concentration prediction accuracy was higher near the bed than at the surface when higher waves were imposed. Here, only the equation for sediment transport rate due to current will be shown in more detail (Van Rijn, 1993)

The diagram of the concept of Van Rijn 1984 formula:

Dimensional

Flow depth-(d)

Water density (ρ)

Dynamic viscosity

Channel slop (S)

Acceleration gravity (g)

Particle size (D)

Dimension less

Particle mobility parameter= $\frac{u_*^2}{(s-1)gd}$

Reynold number= $\frac{u_* D}{v}$

Depth particle size ratio= $\frac{d}{D}$

Reference density parameter= $\frac{\rho_s}{\rho}$

$$u_*' = \left(\frac{g^{0.5}}{C'}\right)\bar{u}$$

$$C' = 18log\left(\frac{12R_b}{3D_{90}}\right)$$

Particle parameter (D_*)

$$= D_{50}\left(\frac{(s-1)g}{v^2}\right)^{1/3}$$

Transport stage parameter (T)

$$= \frac{(u_*')^2 - (u_{*,cr})^2}{(u_{*,cr})^2}$$

F=

$$\frac{\left[\frac{a}{d}\right]^{z'} - \left[\frac{a}{d}\right]^{1.2}}{\left[1-\frac{a}{d}\right]^{z'}[1.2 - Z']}$$

Reference concentration (Ca):

$$= 0.015\frac{D_{50}}{a}\frac{T^{1.5}}{D_*^{0.3}}$$

Bed load:

$$q_b = 0.053\frac{[(s-1)g]^{0.5}D_{50}^{1.5}T^{2.1}}{D_*^{0.3}}$$

Suspend load:

$$q_s = F\bar{u}dc_a$$

Chart (2.1) Diagram of developing Van Rijn

*For grain size 200-2000µm with a score of 77% percent accuracy compared to measured data

2.2.4. Cohesive Sediment Transport Formula

The transport of cohesive sediment is controlled by critical shear stress of erosion (critical bed shear stress). Due to the absence of field measurements in the study area, a literature review of this parameter is essential.

Research by Van Rijn in 2016 showed the critical bed shear stress for fine particles excluding cohesion, as shown in Figure 2.3. According to this curve, the critical bed shear stress for particles smaller than 10µm is estimated to be less than 0.05N/m^2.

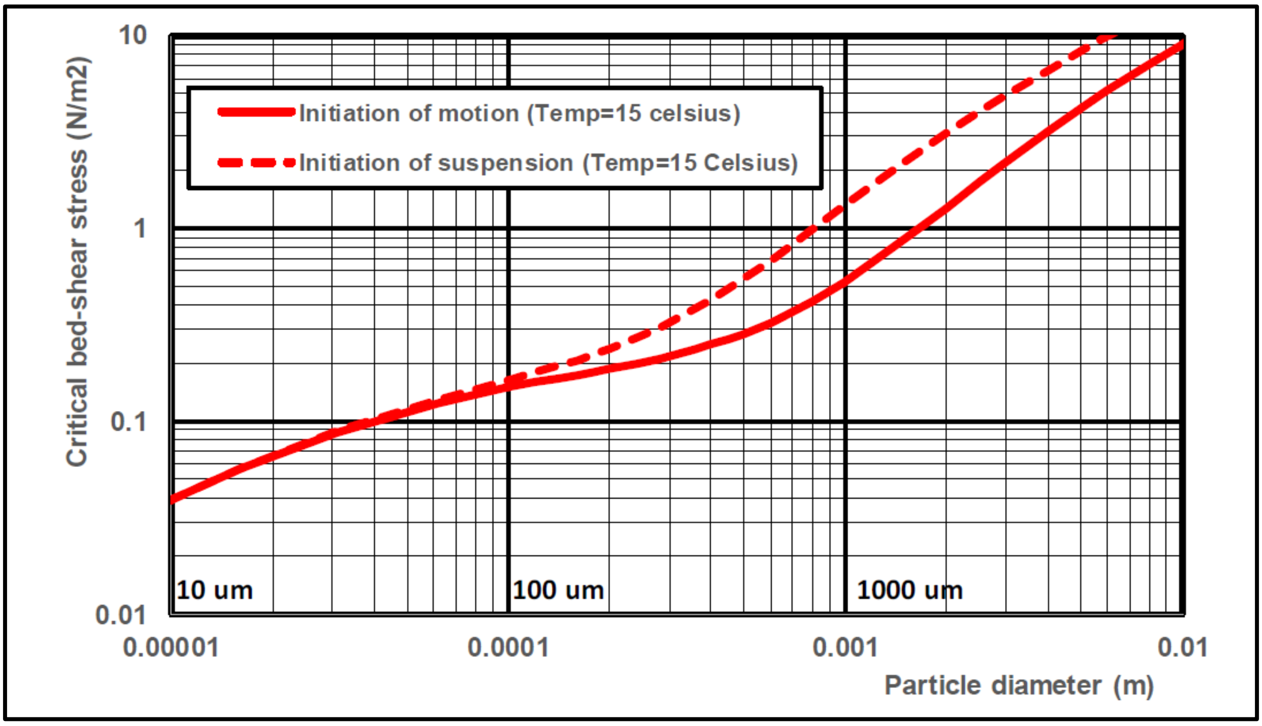

Figure (2.3) Critical bed shear stress excluding cohesion estimation, by Van Rijn (2016)

However, in cases including cohesion as well as mud-sand interaction, other research studies are available. According to Winterwerp et al. (2012), the bed can be divided into three categories. First, there is the Fulful thin surface layer, which is produced mostly in the presence of tide. The second is the permeable layer, and the third is the relatively impermeable consolidated layer comprising the mobilized multiple bed layer. In the second and the third layers, the erosion is defined as surface erosion and mass erosion respectively (Van Rijn, 2016).

Table (2.1) Critical bed-shear stress for erosion; pure mud beds ($d_{50} < 32$ µm), from Van Rijn (2016)

Mud beds	Test Method	Dry bulk density (kg/m^3)	Critical bed shear stress of surface erosion(N/m^2)	Critical bed shear stress of mass erosion(N/m^2)
Kaolinite (distilled water) (Van Rijn, 1993)	Lab flume	1000-2000	0.05-0.2	-
Dutch lake muds (fresh water) (Van Rijn, 1993)	Lab flume	100-200	0.1-0.5	0.6-0.7
River mud (submerged) (Mostafa, 2008)	Lab flume	>1000	0.05-0.3	0.3-1.5
China muds (Dou, 2000)	Lab flume	200-400	0.05-0.2	-
Hong Kong mud (Mitchener-Torfs, 1996)	Lab flume	<400	0.1-0.15	-

According to Van Rijn (2016), the critical bed shear stress of pure mud beds is generally less than 1N/m^2 (Table 2.1). However, when sand and mud coexist, bed critical shear stress increases depending on the percentage of both (Table 2.2). When 50% sand is added to a mud bed or 30% mud is added to a sandy bed, the critical shear stress of erosion increases by factors of 2 and 10 respectively (Van Rijn, 2016).

Table (2.2) Critical bed-shear stress of mud-sand mixtures (laboratory and field), from Van Rijn (2016)

Type of bed	Percentage sand (150-250µm)	Wet and dry bulk density (kg/m^3)	Critical bed shear stress (N/m^2)	
			Natural bed of UK site (intertidal and subtidal)	Artificial beds (homogenously mixed)
Pure mud	0%	1200-1300 (350-450)	0.05-0.25	0.1-0.15 (HK-mud)
Light sandy mud	20%	1300-1400 (450-650)	0.15-0.25	0.15-0.2 (HK-mud)
Sandy mud	40%	1400-1600 (650-950)	0.2-1	0.2-0.4 (HK-mud)
Muddy sand	60%	1600-1700	0.4-1.5	0.4-0.8 (K,M,S-muds)
Muddy sand	80%	1700-1800	0.6-1.8	1-3 (K,M,S-muds)
Light muddy sand	90%	1800-1900		0.5-1.5 (K,M,S-muds)
Pure sand	100%	1900-2000	0.15-0.2	0.15-0.2 (K, M,S-muds)

HK=Hong Kong, S=Kaolinite, M=Montmorillonite

On the other hand, in 2005, Le Heir conducted a study on core samples from Mont St-Michel Bay in France. The samples consisted of sand particles less than 148µm, kaolinite, and illite clay-mineral with very small percentages of organic material. As can be seen from Table 2.3, for these consolidated bed materials, the critical shear stress for erosion increased with the percentage of fine particles. When the mud percentage was larger than 90%, the surface erosion was predicted to be 2±3.05N/m^2 (Van Rijn, 2016).

Table (2.3) Critical bed shear stress of surface erosion of consolidated mud-sand mixture in laboratory flume (Van Rijn, 2016)

Percentage mud<63µm (%)	**Critical bed shear stress of surface erosion (N/m^2)**
20	0.25±20%
30	0.4±20%
40	0.6±20%
60	1.1±25%
70	1.5±25%
90	2.0±305%

All of the studies described in this section were conducted on surface or subsurface bed mixtures. In other words, the critical shear of erosion was not determined for individual particle sizes, as required in the Delft3D numerical model. Therefore, in this study the Van Rijn curve in Figure 2.3 will be applied.

2.3. Sediment Management in a Reservoir

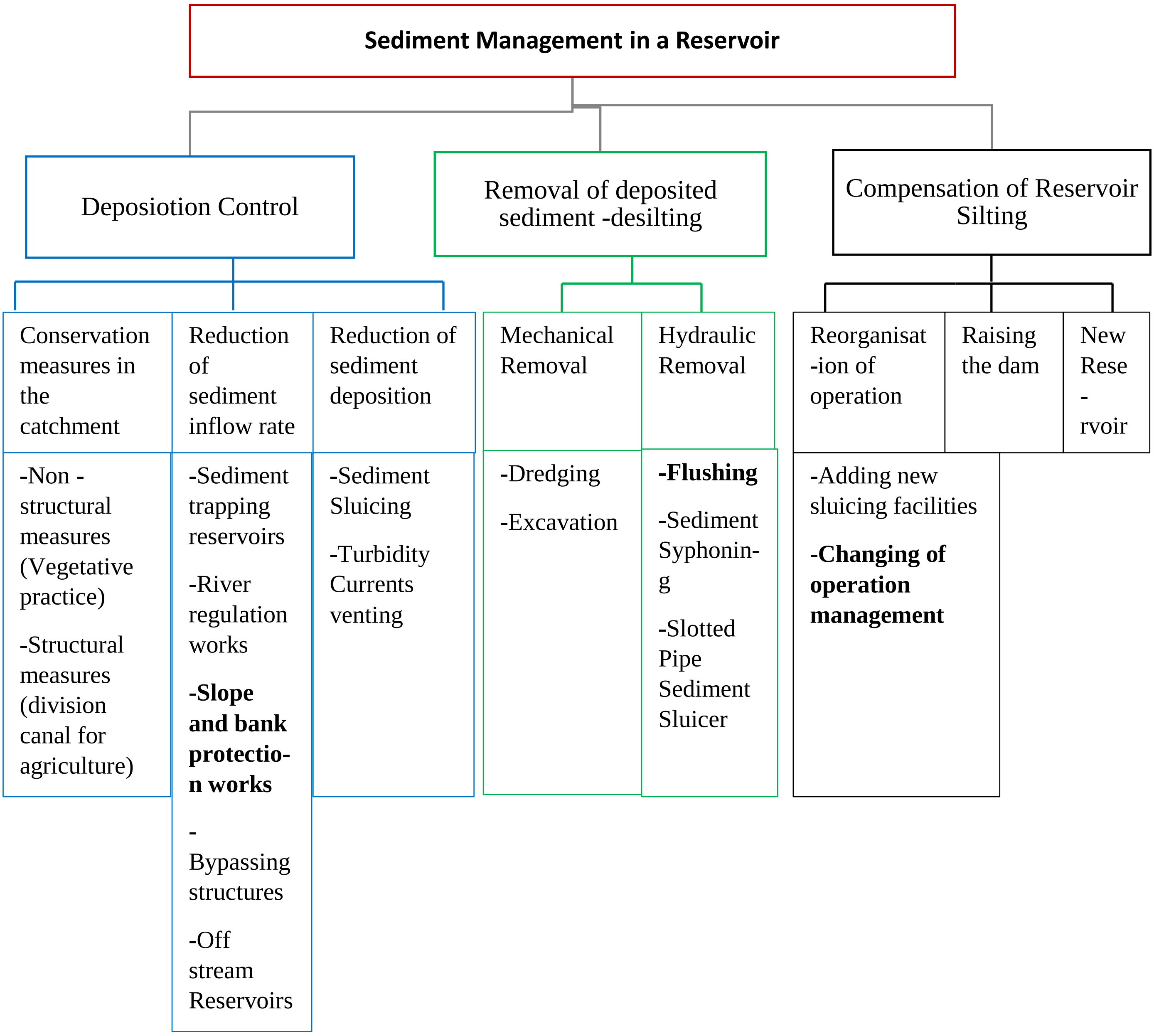

Chart (2.2) Sediment management in a reservoir, from Batuca and Jordan, (2000)

Many techniques are available in the literature to manage sediment in reservoirs. Most of them are shown in Chart (2.2). In this study, the influence of slope and bank protection works, flushing, and changing of operation management will be studied.

In this review only a brief description will be given about flushing, changing of operation management, and slope and bank protection, since this study was conducted only on the river reach at the upstream end of a reservoir.

Sediment flushing can be divided into three types.

1. Sediment routing during floods (flood flushing)

In this method, the reservoir water level remains low during most seasons. Then, during flooding, most of the sediment will be removed through the large bottom gate. In most cases, 80-90 percent of the deposited sediment will be removed from the reservoir. In addition, sediment will not build up in the downstream end of the reservoir. However, implementing such a technique is rare or difficult, especially in rainy seasons (Fan and Morris, 1992).

2. Drawdown flushing

In this technique, the water level will be lowered prior to flooding. The turbulent flood flow may flush out some of the deposited (consolidated) sediment, depending on flood capacity and the water level in the reservoir. The period of reservoir lowering prior to flooding varies because it is controlled by many factors; for example, the volume of the reservoir that needs to be regained, the estimated capacity of the flood, which type of sediment is deposited in the reservoir, and other factors (Fan and Morris, 1992).

3. Emptying and flushing

Unlike the previous schemes, in this method the reservoir must be emptied prior to flooding. This may regain the entire capacity of the reservoir. However, this method may only be applied in small reservoirs because the application of this method means losing all the stored water, which is not practical in a large reservoir. This means it also cannot be implemented in regions with low precipitation (Fan and Morris, 1992).

2.4. Groynes

According to Przedwojski et al. (1995), groynes design is a function of multiple factors, such as flow pattern (flood depth, suspended and bed load amount), channel parameters (channel size, slope, velocity, bed material), and miscellaneous factors (debris, ice).

The designing of groynes is classified based on:

- Method and material of construction (permeable, impermeable)
- Condition (submerged, non-submerged)
- Their action on stream flow (attracting, deflecting, or repelling)
- Their appearance (Straight, T-head, and L-head.)

- **Method and material of construction (permeable, impermeable):**

Permeable groynes, which in most cases are made from timber, piles, or bamboo, are characterized by the fact that they transmit some flow through the groynes. On the other hand, impermeable groynes are made of rock, gravel, or gabions, which deflect all of the flow. Permeable groynes are mostly applied in alluvial rivers with a considerable bed load and high sediment concentration, which leads to rapid deposition around the groynes. In comparison, impermeable groynes are implemented when bank protection is desirable, since they push the flow away from the bank. In addition, impermeable groynes are applied in order to obtain navigation depth in a channel because of the scour that is produced at the head of the groynes.

- **Condition (submerged, non-submerged):**

Groynes can be either fully emergent from the flow, or submerged such that flow is conveyed both over and around the groynes. Traditionally, submerged groynes are made permeable, because submerged-impermeable groynes can cause erosion near the bank. However, recent research has demonstrated that submerged impermeable groynes can be designed carefully to minimize bank erosion (Jamieson et al., 2013). Non-submerged groynes may be permeable or impermeable depending on the purpose of the design.

- **Action on stream flow (attracting, deflecting, or repelling):**

Attracting groynes point downstream and attract flow. For this reason, attracting groynes are not applied on a concave bank. Deflecting groynes only change the direction of the flow without repelling it. Repelling groynes are pointed upstream, and direct flow away from the bank (Figure 2.4).

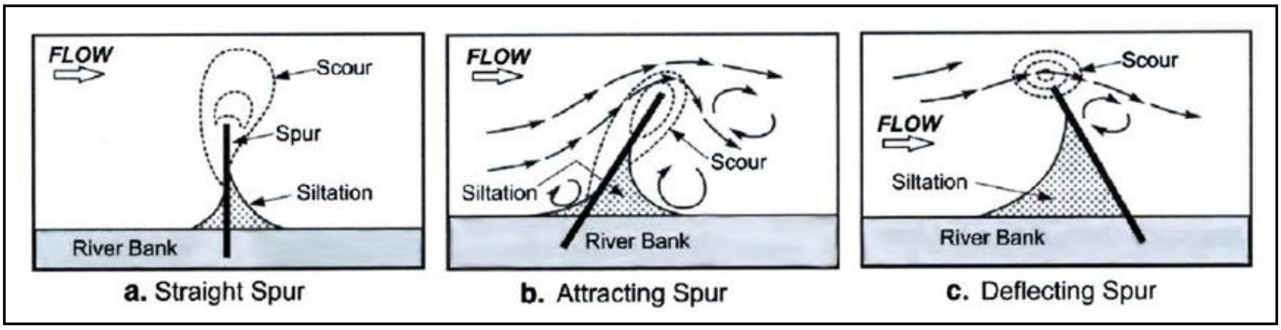

Figure (2.4) Design of groyne based on action on stream flow (from Kashyap, 2010)

- **Appearance (Straight, T-head, L-head):**

In most applications of straight groynes, some protection will be applied at the head of each groyne to reduce the scour at the head zone. T-head and L-head groynes are set at right angles to the bank (Figure 2.5). In most applications of L-head groynes, the rate of sedimentation is higher at the bank and the scour rate at the head is lower compared to other types. This means that this type is more practical for bank protection, especially if the length of the wings is close to 45-65 percent of the gap between the groynes.

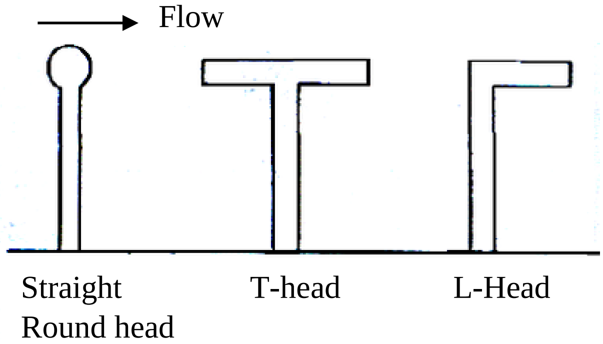

Figure (2.5) Designs of groyne heads

2.4.1 Groynes Dimensional Design

Groyne spacing:

Although spacing between the groynes is a function of river width, groyne length, velocity of flow, bank curvature, angle (α), and purpose, in most designs more weight will be given to the relationship between the spacing and length of the groynes (Figure 2.6). Depending on United Nation guides in 1953, the spacing between permeable groynes is larger compared to the spacing between impermeable groynes (Przedwojski, 1995). The US Department of Agriculture has specified a spacing algorithm for submerged groynes in a channel bend (USDA 2005). In addition, Moselmann (2000) developed an equation for determining spacing as a function of groyne head type, groyne orientation, and purpose of groyne application, as follows.

$$S=2.5\, k_1\, k_2\, k_3\, B_{mc} \qquad (2.7)$$

k_1= correction factor for the groyne head type: k_1 js equal to one for ordinary groynes, and is greater than one for T-head groynes.

k_2= correction factor for the alignment of a groyne system: for straight alignment it is equal to one, for convex alignment it is greater than one, and for a concave bank it is less than one.

k_3= correction factor for the function of groynes: for bank protection it is equal to one, and for navigation it is equal to 0.5.

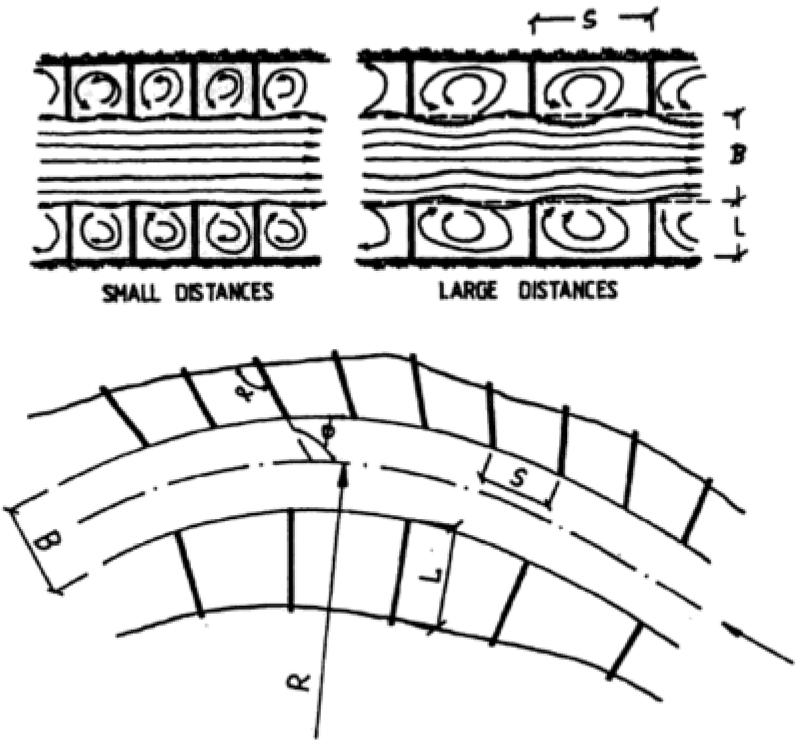

Figure (2.6) Appearance of groynes (from Przedwojski, 1995)

Groyne length:

Groyne length is divided into two parts; the anchor length is embedded in the bank, while the working length protrudes into the flow (Figure 2.7). As mentioned by Yossef (2005), in most cases the anchoring length is about a quarter of the free surface width in order to prevent flow redirection to the opposite bank. In addition, groyne length may also be restricted for economic considerations.

Author	Recommended spacing ratio		Type of bank	Remarks
	S/L	S/B		
United Nations (1953)	1		Concave	General practice
	$2 \div 2.5$		Convex	General practice
Ahmad (1951)	4.29		Straight	
	$\simeq 5$		Curves	
Joglekar (1971)	$2 \sim 2.5$			Upstream groynes
US Army (1984a)	2			Mississippi River
Mathes (1956)	1.5			
Strom (1962)	$3 \div 5$			
Acheson (1968)	$3 \div 4$			Varies depending on curvature and stream slope
Altunin (1962)	4		Straight	$\alpha > 75°$
	3			For $0.005 \leqslant I \leqslant 0.01$
	2			For $I \geqslant 0.01$
Richardson et al. (1975)	$2 \div 6$			For bank protection
	$3 \div 4$			T-head groynes for navigation channels
	$1.5 \div 2$			Deep channel for navigation
Mamak (1956)	$2 \div 3$	1		
Macura (1966)		0.5	Concave	
		5/4	Convex	
		$3/4 \div 1$	Straight	
Jansen et al. (1979)		$1 \div 2$		In constricted rivers
		$0.5 \div 1$		
Blench et al. (1976)	3.5			
Copeland (1983)	> 3		Concave	
Akantisz et al. (1983, 1986, 1989)		$0.9 \div 1$		For $\phi = 45° \div 50°$ $R/B = 8 \div 13.5$
		1.1		For $\phi = 55°$ $R/B = 8$
		$1.1 \div 0.9$		For $\phi = 55°$ $R/B = 13.5$
Kovacs et al. (1983)	$1 \div 2$			Danube River
Mohan and Agraval (1979)	5			Submerged groynes of height one-third the depth
Maza Alvarez (1989)	$5.1 \div 6.3$		Straight	sloping-crested groynes for bank protection
	$2.5 \div 4$		Curves	

Figure (2.7) Groyne spacing ratios (from Przedwojski, 1995)

Regarding slope and crest height, in the case of presence of ice it has been recommended to make the crest of the groyne near the bank higher in order to prevent ice coverage. In addition, sloping of groynes is recommended when the main concern is solving navigation (Przedwojski, 1995).

3. Model Description (Delft3D)

In this study, Delft3D, 4.00.02 (Open Source Hydro-Morphodynamic, Online) was applied in the hydrodynamic simulation, and Delft3D 4.01.01.rc.03 was applied for the morphodynamic simulation. The following descriptions have been taken from the Delft3D Flow Manual.

3.1. Grid

Horizontally, two types of grid are available: rectangular grid and curvilinear grid. In the case of a complex boundary, it is advised to apply a curvilinear grid because of its capability to make a fitted boundary. This type of grid is known as a structured grid. Recently an unstructured grid (Flexible mesh) has also been developed. Vertically, two different grid systems are available, which are the б co-ordinate system and the Cartesian Z co-ordinate system. Note that if a single vertical layer is used, then a 2D depth-averaged computation is performed.

б co-ordinate system- б grid:

Philips (1957) originally developed this grid type. The number of layers is constant along the model domain, but the layer thicknesses are non-uniform, as shown in Figure (3.1-a). This characteristic is important when variable vertical resolution is desired. For example, in sediment transport modelling, it can give higher resolution near the bed layer (Stelling and van Kester, 1994). The σ coordinates are defined as:

$$\boldsymbol{\sigma = \frac{z - \zeta}{d + \zeta} = \frac{z - \zeta}{H}} \qquad (3.1)$$

where z is the vertical coordinate in physical space, ζ is the free surface elevation above the reference plane (at z = 0), and d is the depth below a horizontal plane of reference (datum). H is the total water depth (H = d + ζ; d positive downward).

Z co-ordinate system:

In the case of a stratified flow and steep slope, this grid is recommended because it can give high resolution at the pycnocline. The difference between this coordinate system grid with the previous grid is that the boundary of this grid has a staircase (zigzag) shape. This property allows the grid to have a variable number of cells in the vertical direction, which is especially appropriate for coastal area estuaries.

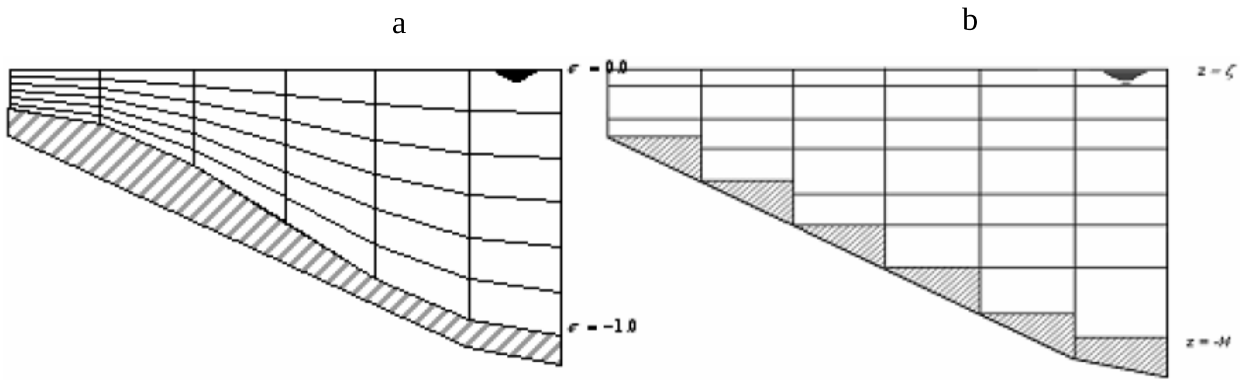

Figure (3.1) a-б grid, b-Z grid (from Delft3D Flow-Manual)

3.2. Hydrodynamic

In this description, only those equations that have an influence on model validation will be described. More details about other equations can be found in the Delft3D-Flow manual.

Velocity in the stream-wise (U) and transverse (V) directions are determined from momentum equations (3.2 and 3.3) respectively, whereas vertical velocity (W) is calculated from continuity equation (3.4). This means that vertical acceleration is neglected in determining vertical velocity, and instead the hydrostatic pressure equation is implemented. This assumption is necessarily applied in the б grid which has been used in this study. Delft3D in this formulation is thus considered a shallow water model.

- **Horizontal Momentum Equation:**

$$\frac{\partial U}{\partial t} + U\frac{\partial U}{\partial x} + V\frac{\partial U}{\partial y} + \frac{\omega}{h}\frac{\partial U}{\partial \sigma} - fv = -\frac{1}{\rho_0}P_x + F_x + F_{sx} + M_x + \frac{1}{h^2}\frac{\partial}{\partial \sigma}\left(v_v\frac{\partial u}{\partial \sigma}\right) \quad (3.2)$$

$$\frac{\partial V}{\partial t} + U\frac{\partial V}{\partial x} + V\frac{\partial V}{\partial y} + \frac{\omega}{h}\frac{\partial V}{\partial \sigma} - fU = -\frac{1}{\rho_0}P_y + F_y + F_{sy} + M_y + \frac{1}{h^2}\frac{\partial}{\partial \sigma}\left(v_v\frac{\partial v}{\partial \sigma}\right) \quad (3.3)$$

- **Continuity Equation:**

$$\frac{\partial \rho}{\partial t} + \frac{\partial \rho U}{\partial x} + \frac{\partial \rho U}{\partial y} + \frac{\partial \rho \omega}{\partial z} = H(q_{in} - q_{out}) \quad (3.4)$$

where fv is the Coriolis coefficient, $P_{x,\,y}$ is the pressure, $F_{sx,sy}$ is the effect of secondary flow on depth-averaged velocity. F_x and F_y represent the Reynolds stresses modeled by the eddy viscosity concept. The eddy viscosity varies depending on the grid size and horizontal and vertical turbulence in 2D and 3D simulations. Specifically, the turbulent forces that cannot be predicted by the Reynolds averaged shallow water equations are parameterized by horizontal eddy viscosity.

$$\upsilon_H = \nu_{SGS} + \nu_V + \nu_H^{back} \quad (3.5)$$

where υ_H is the horizontal eddy viscosity, ν_{SGS} is the sub-grid scale horizontal eddy viscosity, ν_H^{back} is the background horizontal eddy viscosity, and ν_V is used to represent three-dimensional turbulence.

In 2D depth-averaged momentum and transport computations, the redistribution of momentum is included as dispersion. This dispersion can be calculated from the Elder formula, which represents the relationship between gradient velocity and the ν_{SGS} horizontal eddy viscosity coefficient. This formula can be applied only if the Horizontal Large Eddy Simulation (HLES) is evoked by the user. This value will represent the 2D turbulence and dispersion coefficient in the case that the HLES is not included, and it will represent the 3D turbulence and dispersion coefficient when the HLES is enclosed in the simulation. ν_V will only be computed in the 3D simulation which represents three-dimensional turbulence.

This method was developed by Uittenbogaard (1998) and Uittenbogaard and Van Vossen (2003), and was summarised by Van Vossen (2000). More can be found about this method in the Delft3-Flow manual.

Finally, ν_V is computed only in the 3D simulation to represent three-dimensional turbulence.

$$\boldsymbol{\nu_V = \nu_{mol} + max\left(\nu_{3D} + \nu_V^{back}\right)} \qquad (3.6)$$

where ν_{3D} is determined from a 3D turbulence closure model such as: constant coefficient, Algebraic Eddy viscosity closure Model (AEM), k-L turbulence closure model, or k-ε turbulence closure model. The parameter ν_V^{back} is the background vertical eddy viscosity, which is required because the turbulent closure model accounts only for mixing due to shear. The background eddy viscosity will account for other mixing in the model. Finally,ν_{mol}, is the kinematic viscosity of water.

Secondary Flow:

It is crucial to take into account in the equations the transfer of momentum due to secondary flow, especially in meandering rivers. In a 2D simulation, to account for secondary flow correction, F_{sx} and F_{sy} must be added to the momentum equations. This will correct the spiral motion. However, in a 3D simulation, the secondary flow will be resolved in the vertical grid.

F_{sx} and F_{sy} represent the horizontal effective shear stresses that are produced by secondary flow. This is added to the momentum equation:

$$\boldsymbol{F_{sx} = \frac{2\beta}{\partial x}\{(U^2 - V^2) - \partial(UV)\} + \frac{\beta}{\partial y}\{\partial(U^2 - V^2) + (2UV)\}} \qquad (3.7)$$

$$\boldsymbol{F_{sy} = \frac{\beta}{\partial x}\{\partial(U^2 - V^2) + 2(U^2 - V^2)\} + \frac{2\beta}{\partial y}\{\partial(UV) + (2UV)\}} \qquad (3.8)$$

where:

$\beta = \beta^* \frac{d+\zeta}{R_{s*}}$, $\beta = \beta c\,(5\alpha - 15.6\,\alpha^2 + 37.5\,\alpha^3)$,

$$\alpha = \frac{\sqrt{g}}{\kappa C_{2D}} < \frac{1}{2}$$

Rs* is the effective radius of curvature in 2D obtained from spiral motion intensity. κ : Von Karman constant (0.41). βc is specified by the user in a 2D model only which is in the range [0-1]. When βc is equal to zero, it means that the secondary flow correction is excluded.

Spiral motion intensity (I) changes with time and space, and is determined from the advection diffusion equation. In this equation, it has been accounted for both centrifugal force and calories force.

$$\frac{\partial(d+\zeta)I}{\partial t}+\left\{\frac{\partial(d+\zeta)UI}{\partial x}+\frac{\partial(d+\zeta)VI}{\partial y}\right\} = (d+\zeta)\left\{\frac{\partial}{\partial x}\left[D_H\frac{\partial I}{\partial x}\right]+\frac{\partial}{\partial y}\left[D_H\frac{\partial I}{\partial y}\right]\right\}+(d+\zeta)S \qquad (3.9)$$

D_H : Horizontal diffusion coefficient, $R_{s*} = \frac{(d+\zeta)|U|}{I}$

3D turbulence closure model:

There are three main turbulence models to determine vertical eddy viscosity and diffusivity. The main dissimilarities between the following turbulence closure models are in estimating the turbulent kinetic energy (k), the dissipation rate of turbulent kinetic energy (ε), and the mixing length (L):

- Constant coefficient
- Algebraic Eddy viscosity closure Model (AEM)
- k-L turbulence closure model
- k-ε turbulence closure model

The first method is a constant value for horizontal eddy viscosity, which produces a parabolic vertical velocity profile. The other methods are based on eddy viscosity concept that depend on length and velocity scale are developed by of Kolmogorov (1942) and Prandtl (1945).

$$v_{3D} = c'_\mu L\sqrt{k} \qquad (3.10)$$

where c'_μ is a constant that is calculated from calibration and (c_μ) in the k-ε model: $c'_\mu = c_\mu{}^{1/4}$ c_μ= 0:09. L is the mixing length, and k is the turbulent kinetic energy.

The AEM model is a zero-order closure scheme (i.e., it excludes the transport equation for turbulent kinetic energy). Instead, k and L depend on algebraic equations; k is determined from the gradient velocity and L from Bakhmetev's (1932) formula (3.11). In the case of a stratified flow, this formula will be corrected by adding a damping function (F_L (R_i)) (Simonin et al., 1989).

$$L = \kappa(z+d)\sqrt{1-\frac{z+d}{H}} \qquad (3.11)$$

Similar to AEM, the k-L model implements the same formula in determining L. However, k is determined from a transport equation (first-order turbulence closure scheme).

Unlike the previous models, in the k-ε model, L will be determined from both k and ε, which are obtained from transport equations (second-order turbulence closure model). Therefore, it is not essential to apply any damping effect in the case of a stratified flow.

3.3. Morphodynamic

3.3.1. Suspended Load Transport

For estimating suspended sediment transport, the advection-diffusion equation is implemented:

$$\boldsymbol{\frac{\partial C}{\partial t}+\frac{\partial uC}{\partial x}+\frac{\partial vC}{\partial y}+\frac{\partial(\omega-\omega_s)C}{\partial z}}$$

$$\boldsymbol{=\frac{\partial}{\partial x}\left(D_H\frac{\partial C}{\partial x}\right)+\frac{\partial}{\partial y}\left(D_H\frac{\partial C}{\partial y}\right)+\frac{\partial}{\partial z}\left(D_V\frac{\partial C}{\partial z}\right)+\lambda_d C+S} \qquad \mathbf{(3.12)}$$

Depth average suspended load transport:

$$\frac{\partial \mathrm{C}}{\partial \mathrm{t}}+\frac{\partial \bar{\mathrm{u}}\bar{\mathrm{C}}}{\partial \mathrm{x}}+\frac{\partial \bar{\mathrm{v}}\bar{\mathrm{C}}}{\partial \mathrm{y}}=\frac{\partial}{\partial \mathrm{x}}\left(\mathrm{D_H}\frac{\partial \bar{\mathrm{C}}}{\partial \mathrm{x}}\right)+\frac{\partial}{\partial \mathrm{y}}\left(\mathrm{D_H}\frac{\partial \bar{\mathrm{C}}}{\partial \mathrm{y}}\right)+\lambda_{\mathrm{d}}\bar{\mathrm{C}}+\mathrm{S}$$

$\frac{\bar{C}_{eq}-\bar{C}}{T_s}$, $\bar{C}_{eq}=\frac{\vec{S}_{sus,eq}}{|\bar{u}|h}$,

$\vec{S}_{sus,eq}=\left|\int \bar{u}C_{eq}d_z\right|$ --------from transport formula of non-cohesive

Where $\bar{C}$ is the depth-averaged sediment concentration, $\bar{C}_{eq}$is the depth-averaged equilibrium sediment concentration, and $\vec{S}_{sus,eq}$: is the depth-integrated suspended sediment transport vector under equilibrium (steady and uniform) conditions. DH and D_V are the horizontal and vertical diffusion coefficient respectively. S is the source sink term, and λ_d is the decay rate. Ts: An adaptation time-scale.

$D_{3D=}max\left(D_{3D}, 0.2L_{oz}^2\sqrt{-\frac{g\partial\rho}{\rho\partial z}}\right),$

D_{3D}: Computed by 3D turbulence closure model, D_V^{back}: user input

Loz: include turbulence due to wave break in stratified flow

$$\boldsymbol{D_V=\frac{\upsilon_{mol}}{\sigma_{mol}}+max\left(D_{3D},D_V^{back}\right)}$$

$$\boldsymbol{D_H=D_{SGS}+D_V+D_H^{back}}$$

Account for turbulence due to motion, mixing and dispersion. Solved by HLES

Include all other turbulence that has not been captured by other part. (user input)

In 2D, vertical variation of horizontal flow is not captured. However, in 3D it will be computed by the 3D advection-diffusion equation.

Settling velocity (ω_s):

For determining settling velocity, the interaction between the particles is taken into account. According to Richardson and Zaki (1954), the hindered settling velocity can be determined depending on grain concentration and non-hindered settling velocity.

$$\boldsymbol{\omega_s = \left(1 - \frac{C_m^{tot}}{C_{Soil}}\right)^5 \omega_{s,0}} \qquad (3.13)$$

where C_{Soil} is the reference sediment density, C_m^{tot} is the summation of all fraction concentration, and $\omega_{s,0}$ is the settling velocity of each particle, which is computed differently for cohesive and non-cohesive sediment.

Cohesive:

$$\boldsymbol{\omega_{s,0} = \begin{cases} \frac{\omega_{s,max}}{2}\left(1 - \cos\left(\frac{\pi S}{S_{max}}\right)\right) + \frac{\omega_{s,f}}{2}\left(1 + \cos\left(\frac{\pi S}{S_{max}}\right)\right), & S \le S_{max} \\ \omega_{s,max} & S > S_{max} \end{cases}} \qquad (3.14)$$

Non –cohesive:

$$\boldsymbol{\omega_{s,0} = \begin{cases} \frac{(s-1)gD_s^2}{18v} & 65\mu m < D_s \le 1000\mu m \\ \frac{10v}{D_s}\left(\sqrt{1 + \frac{0.01(s-1)gD_s^3}{v^2}} - 1\right) & 100\mu m < D_s \le 1000\mu m \\ 1.1\sqrt{(s-1)gD_s} & 100\mu m < D_s \end{cases}} \qquad (3.15)$$

where $\omega_{s,max}$: Settling velocity of sediment fraction at maximum salinity concentration. $\omega_{s,f}$: Fresh water settling velocity of fraction. S: Salinity. S_{max}: Maximum salinity

Sediment Dispersion:

The vertical diffusion term (ε_s) in the advection-diffusion equation, which represents vertical mixing of sediment, is calculated differently for cohesive and non-cohesive sediment. For cohesive sediment, ε_s is assigned directly from the calculated vertical fluid mixing coefficient (i.e., eddy viscosity at each layer) obtained from the turbulence model, whereas for non-cohesive sediment like sand, the mixing coefficient will be multiplied by the Van Rijn beta factor to account for the distinction between sediment and fluid diffusion.

$$\varepsilon_s = \varepsilon_f \qquad \text{Cohesive}$$

$$\varepsilon_s = \beta_{eff}\varepsilon_f \qquad \text{Non-Cohesive}$$

The parameter $\boldsymbol{\beta_{eff}}$ varies depending on which turbulence model is applied:

$\beta_{eff} = 1 + (\beta - 1)\frac{\tau_c}{\tau_\omega + \tau_c}$ k-ε turbulence model

$\beta_{eff} = \beta$ Other turbulence model

$\beta = 1 + 2\left(\frac{\omega_s}{u_{*,c}}\right)^2,$

$u_{*,c}$: Local shear velocity due to current

3.3.2. Non Cohesive Sediment transport

In this study, only the Van Rijn formulae (1984 &1993) are implemented. Bed load and suspended sediment are calculated separately below and above the Van Rijn reference level respectively.

Van Rijn 1993:

Bed load transport rate: $S_b = f_{BED}\eta 0.5\rho_s d_{50} u_*^{'} D_*^{-0.3} T_a$

Bed load direction $S_{b,u} = \frac{u_{b,u}}{u_b}|S_b|$ $S_{b,v} = \frac{u_{b,v}}{u_b}|S_b|$

Van Rijn 1984:

Bed load $S_b = \begin{cases} 0.053\sqrt{\Delta g D_{50}^3} D_*^{-0.3} T^{2.1} & for\ T < 3.0 \\ 0.1\sqrt{\Delta g D_{50}^3} D_*^{-0.3} T^{1.5} & for\ T \geq 3.0 \end{cases}$ $T = \frac{\mu\tau_{bc} - \tau_{bcr}}{\tau_{bcr}}$

Suspended load $S_{sus} = \rho_{cs} q h C_a$

Ta: Non-dimensional bed shear stress.

	Van Rijn1984	**Van Rijn1993**
Critical bed shear stress	$\tau_{bcr} = \rho_\omega \Delta g D_{50} \theta_{cr}$(1+Pm)^3 $\theta_{cr} =$	$\tau_{bcr} = (\rho_s - \rho_\omega) g D_{50} \theta_{cr} (1 + Pm)^3$ $\theta_{cr} = \frac{0.24}{D_*}$ $for\ D_* \leq 4$
Reference level	User defined	$= min\left(0.2h, max\left(AKSFAC.k_s, \frac{\Delta_r}{2}, 0.01h\right)\right)$
Reference concentration	$\text{Ca} = 0.015\frac{d50\ T^{1.5}}{aD\ *^{0.3}}$	$C_a = 0.015\rho_s^\ell \frac{d_{50}(T_a^\ell)^{1.5}}{a(D_*^\ell)^{0.3}}$

3.3.3 Erosion and Deposition

Non-Cohesive:

To determine the rate of erosion and deposition, the sediment transport computation is divided into multiple layers. The first layer above the bed is the Van Rijn layer with height (a). Above this layer is the reference layer, which is known as the kmx layer. All the computation of non-cohesive suspended sediment transport will takes place in the kmx layer. Depending on the settling velocity, sediment may deposit from the water column to the kmx layer. Sediment may also be eroded from the bed layer depending on upward diffusion. Based on the sediment concentration in both the Van Rijn and kmx layers and the diffusion, the erosion flux is computed as shown in Figure (3.2). Deposition is calculated at bottom of the kmx layer according to settling velocity (ω_s) and concentration ($C_{kmx\,(bot)}$).

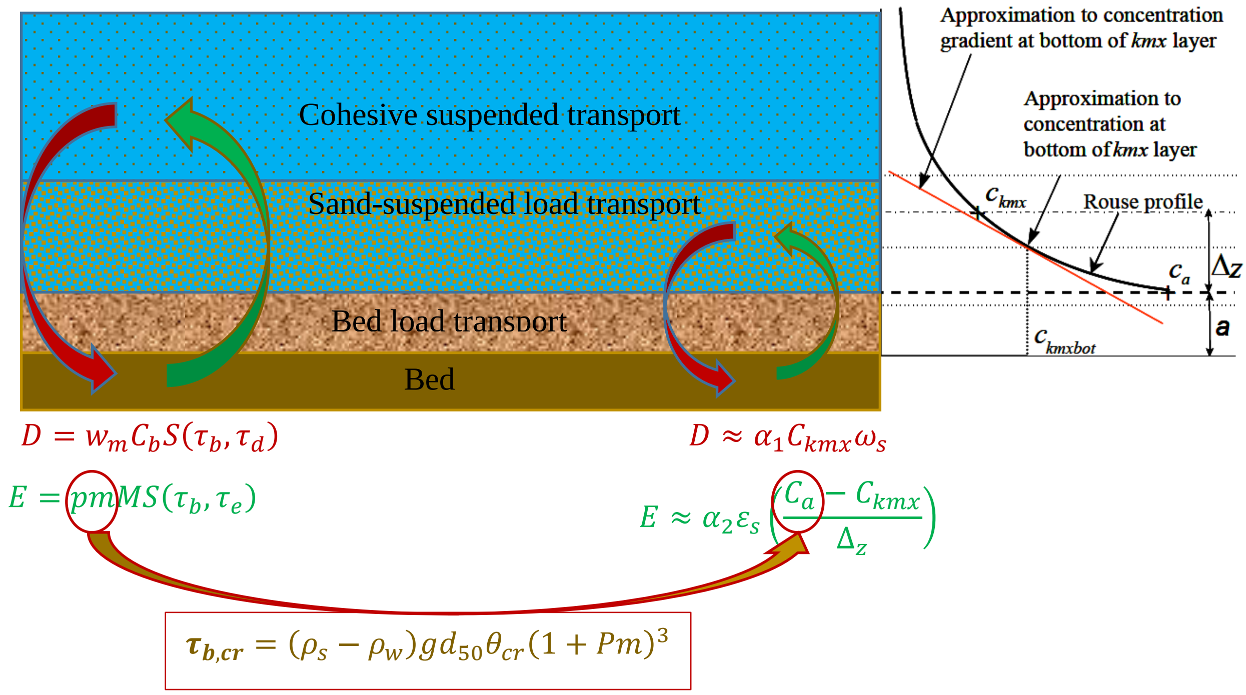

Figure (3.2) Mechanism of sediment transport calculation excluding fluid mud layer (modified from Delft3d manual, 2014)

where α_2: Correction factor for sediment concentration, α_1: correction factor to represent concentration at bottom of the kmx layer, and ε_s: sediment diffusion coefficient computed at bottom of kmx layer. C_a: Reference concentration of sediment fraction. C_{kmx}: Average concentration of the kmx cell of sediment fraction, and Δ_z: Difference in elevation between the centre of the kmx cell and Van Rijn's reference level.

Cohesive Sediment:

For determining and deposition and erosion flux between the bed and the water column when only cohesive sediment is available in the bed, Partheniades-Krone formulations (Partheniades, 1965) are implemented:

$$\boldsymbol{E = MS(\tau_b, \tau_e) = M \begin{cases} \left(\dfrac{\tau_b}{\tau_e} - 1\right) & when\ \tau_b > \tau_e \\ 0 & when\ \tau_b \le \tau_e \end{cases}} \qquad (3.16)$$

$$D = w_s C_b S(\tau_b, \tau_d) = w_s C_b \begin{cases} \left(1 - \frac{\tau_b}{\tau_d}\right) & when\ \tau_b < \tau_d \\ 0 & when\ \tau_b \geq \tau_d \end{cases} \quad (3.17)$$

where τ_b is the bed shear stress, τ_e is the critical shear stress of erosion, M is the user defined erosion parameter, w_s is the hindered settling velocity, and C_b is the average sediment concentration near the bottom layer.

There is still a debate on whether the deposition flux of fine particles is controlled by the critical shear stress of deposition, as stated by Partheniades-Krone, or whether it is dominated only by concentration and settling velocity, as stated by Winterwerp (2007). In this study, the Partheniades-Krone concept is followed.

For both cohesive and non-cohesive sediment, the source and sink terms will be calculated by the erosion and deposition terms, and will be added to the layer above the reference height.

It is crucial to mention that if the bed contains a percentage of mud, depending on its percentage, two regimes are specified. According to Van Ledden (2003), the when mud percentage (pm) is less than the critical mud percentage (Pmcr=30%), the fine particles will erode proportionally with non-cohesive particles. However when the mud percentage is greater than the Pmcr, the sand grains will erode proportionally with cohesive sediment. In Delft3D, all Van Rijn version formulae are updated by applying the term $\{(1+pm)^{\beta}, (\beta=3)\}$ to the critical bed shear stress, as shown in Figure (2.1). Adding this term increases critical bed shear stress; in other words, it slows down the sand movement as was observed in Van Rijn (1993) experiment. This also means that the interaction of mud and sand particles is included in determining sand transport.

When **pm<Pmcr**, mud will be eroded proportionally with sand:

Es_avg = Es_avg + frac(l)*E(l)/ (1-mudfrac)
E (l) = Es_avg

When **pm>Pmcr**, sand will be eroded proportionally with mud fraction:

E(l) = E(l)*(Es_avg/E(l))**((1.0_fp-mudfrac)/(1.0_fp-pmcrit))
Em_avg = [Em_avg + frac (l)*E (l)]/mud frac
E (l) = Em_avg

where Es_avg and Em_avg is the average erosion velocity for sand fractions and mud fraction respectively. E (l) is the sediment erosion velocity for every fraction, and frac (l) is the sediment mass fraction for every defined fraction.

3.3.4 Slope

Bed slope is divided into two main categories. First, there is the longitudinal bed slope, which influences the bed load transport rate. This is taken into account in the equation by ($\boldsymbol{\alpha_s}$). Then, there is the transverse slope change toward downslope. The following influence taken into account differently according to the slope formula that applied as shown in Chart (3.1).

1. No effect of bed slope on bed load transport

(i.e. $\boldsymbol{\alpha_s = 1}$)

$$\boldsymbol{S_b'' = f_{FIXFAC} S_b''}$$

$$\boldsymbol{S_b' = \alpha_s S_b''}\text{---(W.L point)}$$

2. Bagnold (1966) for longitudinal slope and Ikeda (1982, 1988) as presented by Van Rijn (1993):

$$\alpha_s = 1 + \alpha_{bs}\left(\frac{\tan\emptyset}{\cos\left(\tan^{-1}\left(\frac{\partial z}{\partial s}\right)\right)\left(\tan(\emptyset) - \frac{\partial z}{\partial s}\right)} - 1\right)$$

Transverse bed slope:

$$S_{b,x} = S'_{b,y} + S'_{b,y}\,\alpha_{bn}\sqrt{\frac{\tau_{b,cr}}{\tau_b}}\frac{\partial_{zb}}{\partial_n}$$

$$S_{b,y} = S'_{b,x} + S'_{b,x}\,\alpha_{bn}\sqrt{\frac{\tau_{b,cr}}{\tau_b}}\frac{\partial_{zb}}{\partial_n}$$

3. Koch and Flokstra (1980) as extended by Talmon et al. (1995).

$$\alpha_s = 1 + \alpha_{bs}\frac{\partial_z}{\partial_s}$$

Bed load direction is adjusted by:

$$\tan(\varphi s) = \frac{\sin(\varphi\tau) + \frac{1}{f(\theta)}\frac{\partial zb}{\partial y}}{\cos(\varphi\tau) + \frac{1}{f(\theta)}\frac{\partial zb}{\partial x}}$$

$$f(\theta) = A_{sh}\theta_i^{B_{sh}}\left(\frac{D_i}{H}\right)^{C_{sh}}\left(\frac{D_i}{D_m}\right)^{D_{sh}}$$

4. Parker and Andrews (1985).

All other formula are the same as Koch and Flokstra (1980)

$$f(\theta) = \frac{cL}{1 + \mu cL}\sqrt{\frac{\theta}{\max\left(\frac{1}{10}\theta, \xi\theta_{cr}\right)}}$$

Longitudinal bed slope: $\frac{\partial zb}{\partial s} = \frac{\partial z_{(u)}}{\partial x}\frac{S''_{b,x}}{|S''_b|} + \frac{\partial z_{(v)}}{\partial y}\frac{S''_{b,y}}{|S''_b|}$ Transverse bed slope : $\frac{\partial zb}{\partial n} = \frac{\partial z_{(u)}}{\partial x}\frac{S''_{b,y}}{|S''_b|} + \frac{\partial z_{(v)}}{\partial y}\frac{S''_{b,x}}{|S''_b|}$

Chart (3.1) Slope formulas in Delft3D

3.3.5 Bathymetry updating

During morphodynamic calculations, the following equation is used to update the bed elevation based on bed load erosion and deposition calculated at each model grid point. Note that the change in bed elevation due to suspended sediment is also considered in the bathymetry update.

$$\boldsymbol{\Delta_{SED}^{(m,n)}} = \frac{\boldsymbol{\Delta t f_{\mathrm{MORFAC}}}}{\boldsymbol{A^{(m,n)}}} \begin{pmatrix} \boldsymbol{S_{b,uu}^{(m-1,n)} \Delta y^{(m-1,n)} - S_{b,uu}^{(m,n)} \Delta y^{(m,n)} +} \\ \boldsymbol{S_{b,vv}^{(m,n-1)} \Delta x^{(m,n-1)} - S_{b,vv}^{(m,n)} \Delta x^{(m,n)}} \end{pmatrix} \qquad \textbf{(3.18)}$$

Where $\Delta_{SED}^{(m,n)}$= change in quantity of bottom sediment at location (m; n), f_{MORFAC}= user-defined morphological acceleration factor, MORFAC. $A^{(m,n)}$ = area of computational cell at location m, n. $S_{b,uu}^{(m,n)}$= computed bedload sediment transport vector in u direction, held at the u point of the computational cell at location (m; n), $\Delta x^{(m,n)}$ = cell width in the x direction, held at the V point of cell (m; n), and $\Delta y^{(m,n)}$= cell width in the y direction, held at the u point of cell (m; n).

3.4. Hydraulic Structure

Hydraulic structures like gates, barriers, sluices, groynes, weirs, bridge piers, and porous plates represent obstacles to the flow. As a result, there will be a loss in energy or change in flow direction. In Delft3D, in order to model the force produced as the result of the presence of a hydraulic structure, the flow in the computational layer is blocked and a quadratic energy or linear loss term is added to the momentum equation.

In Delft3D, groynes can be represented in a 2D model by a 2D weir, which is a fixed non-movable construction generating energy loss due to constriction of the flow. The HKRU is taken into account in drying and flooding algorithms to determine if the velocity point is wet or dry (Figure3.3). This concept was developed by Wijbenga (1990). Instead of computing the energy loss by a convective term, another term will be added to the momentum equation to account for this loss.

$$\boldsymbol{M_x = -\frac{gH\Delta E_{weir}}{\Delta x}} \qquad \textbf{(3.19)}$$

For subcritical flows, energy loss (ΔE_{weir}) is based on either $\Delta E_{\mathrm{Table}}$ or the Carnot equation (ΔE_{Car}). The flow velocity at the weir crest is determined depending on the discharge upstream and the crest height. Depending on the velocity at the crest of the weir, the energy loss may be determined differently. If the velocity is less than 0.25m/s, the energy loss will be calculated according to the Carnot formula, and the $\Delta E_{\mathrm{Table}}$ will be applied if the velocity is in the range 0.25-0.5m/s. Otherwise, the loss will depend on the average value of those two formulas.

$$U_{weir} = \frac{Q_{weir}}{\Delta y(\zeta_{up} + HKRU} \qquad (3.20) \qquad U_{down} = \frac{Q_{weir}}{\Delta y(\zeta_{down} + HKRU + d_{sill})} \qquad (3.21)$$

$$\Delta E_{Car} = \frac{(U_{weir} - U_{down})^2}{2g} \qquad (3.22)$$ ……………. energy loss by CarnotThe loss will be added to the momentum equation, as follows:

(3.23)

$$\frac{\partial U}{\partial T} + \cdots = \cdots - \frac{g\Delta E^n U^{n+1/2}_{i+1/2,j}}{\Delta x U^n_{i+1/2,j}}$$

(3.24)

$$\Delta E^n = (1 - \theta)\Delta E^n + \theta \Delta E^{n-1/2}$$

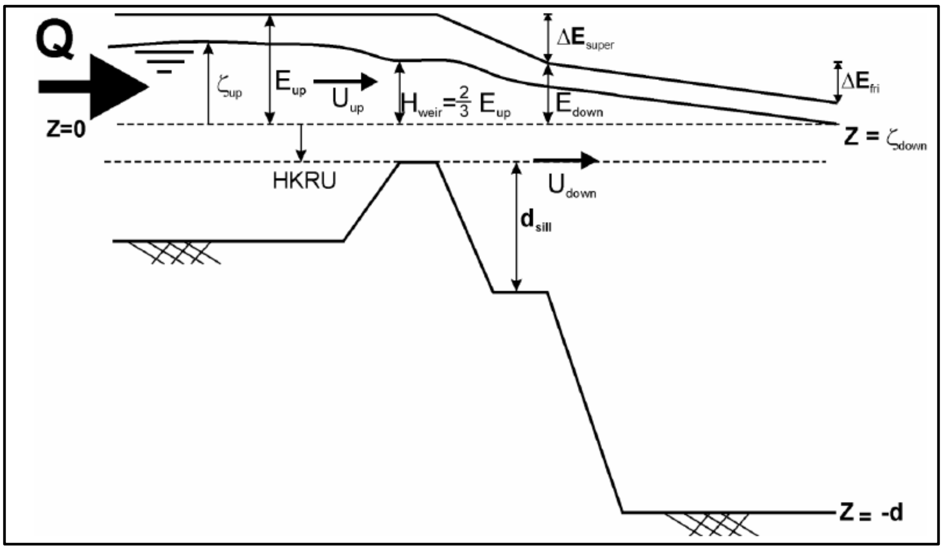

Figure (3.3) The defined term of a 2D weir equation (from Delft3D manual, 2011)

3.5. Delft3D: Numerical Description

Momentum Equation

In Delft3D, finite difference method is applied in solving partial differential equations based on discretizing the equations on a curvilinear grid (structure). The variables in the equations are arranged on the grid by applying a staggered grid; for example, water level is defined at the grid center, and velocity at the corner of the cell. For solving advection terms, three methods can be implemented, which are Waqua, Cyclic, and Flood. In both Cyclic and Waqua, the advection terms are integrated implicitly (Stelling, 1984; Stelling and Leendertse, 1992). In the Flood scheme, the advection terms are integrated explicitly, and unlike the two other methods, it has a time step restriction by Courant number. This is implemented in the case of a rapid varying flow, like a hydraulic jump (Stelling and Duinmeijer, 2003). The time integration is based on ADI (Alternating Direction Implicit). One of the characteristics of this method is that the water levels and velocities are coupled along grid lines, leading to systems of equations with a small bandwidth.

Transport Equation

For discretizing horizontal advection in the transport equation, two schemes are available: Cyclic and Van Leer. Cyclic is based on implicit time step integration for advection and diffusion (Stelling and Leendertse, 1992). Although the Van Leer scheme depends on explicit time step integration, which requires less computation time, it has a time step restriction by Courant number (Van Leer, 1974).

To prevent negative concentration, the sink term is integrated implicitly, whereas the source term is solved explicitly. Furthermore, the Forester filter is included in the model to prevent nonphysical oscillation that leads to negative concentration. This filter is more applicable to those areas with coarse grids and steep gradients (Forester, 1979).

4. Study Area

4.1. Area Description

Drava River is located in south central Europe, with a length of 749 km. Its source is in the Puster Valley of South Tyrol, Italy (Wikipedia). This river passes through Austria, Slovenia, Hungary, and Croatia. The study area is a part of Drava River located in the western part of Austria's Carinthia province.

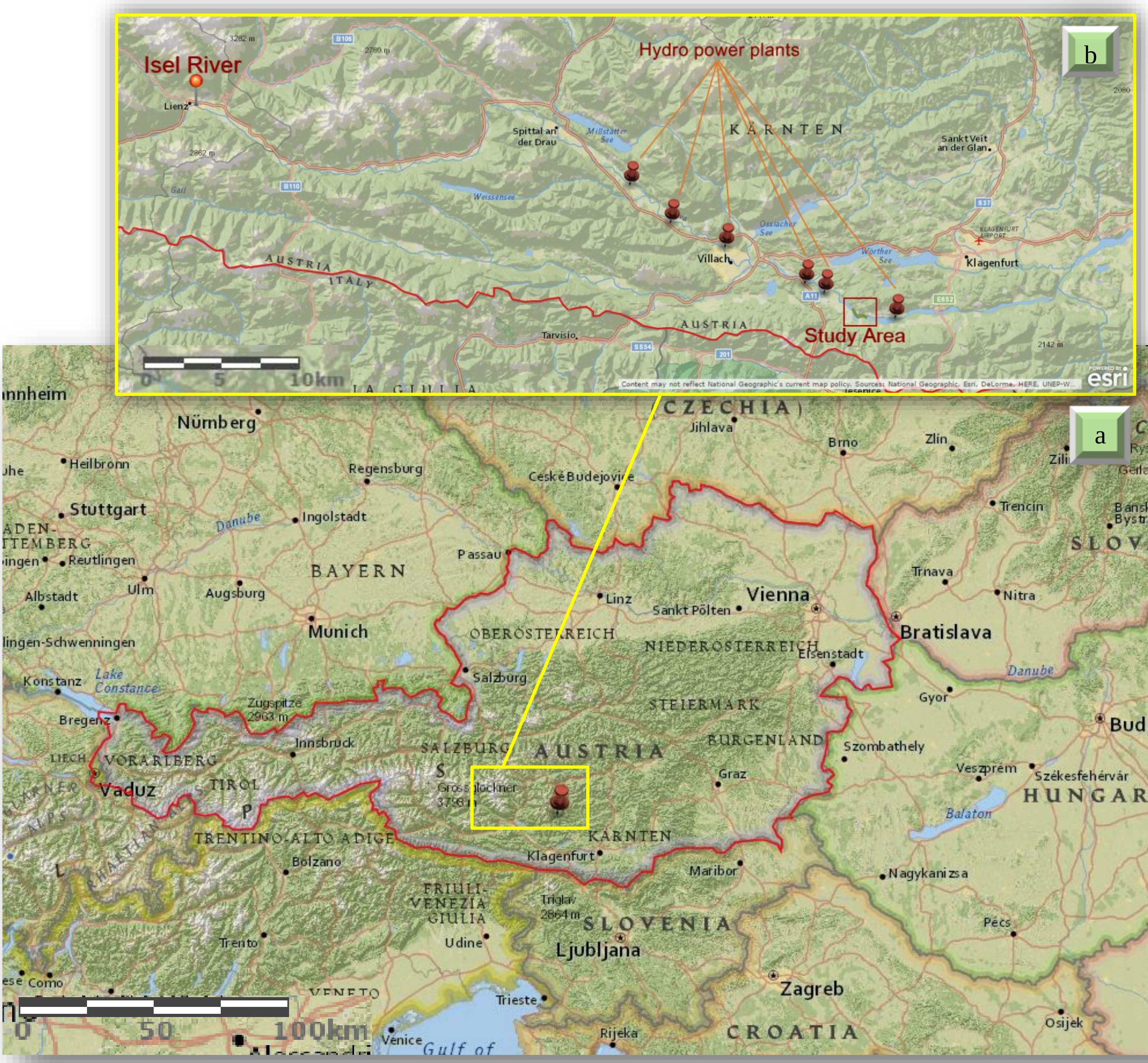

Figure (4.1) a- Austria map; b-Location of hydropower plant on Drava River. Flow is from NW to SE.

The portion of the river located in Austria is about 214km long. Only 27% of this length is free-flowing, because of the hydropower plants constructed along the river. According to Habersack (1996), the only source of bed load sediment is from the Isel River. From the intake of the Isel River to upstream of the study area, there are five hydropower plants, which may have an important influence on the amount of sediment that reaches the study area, as shown in Figure (4.1-b).

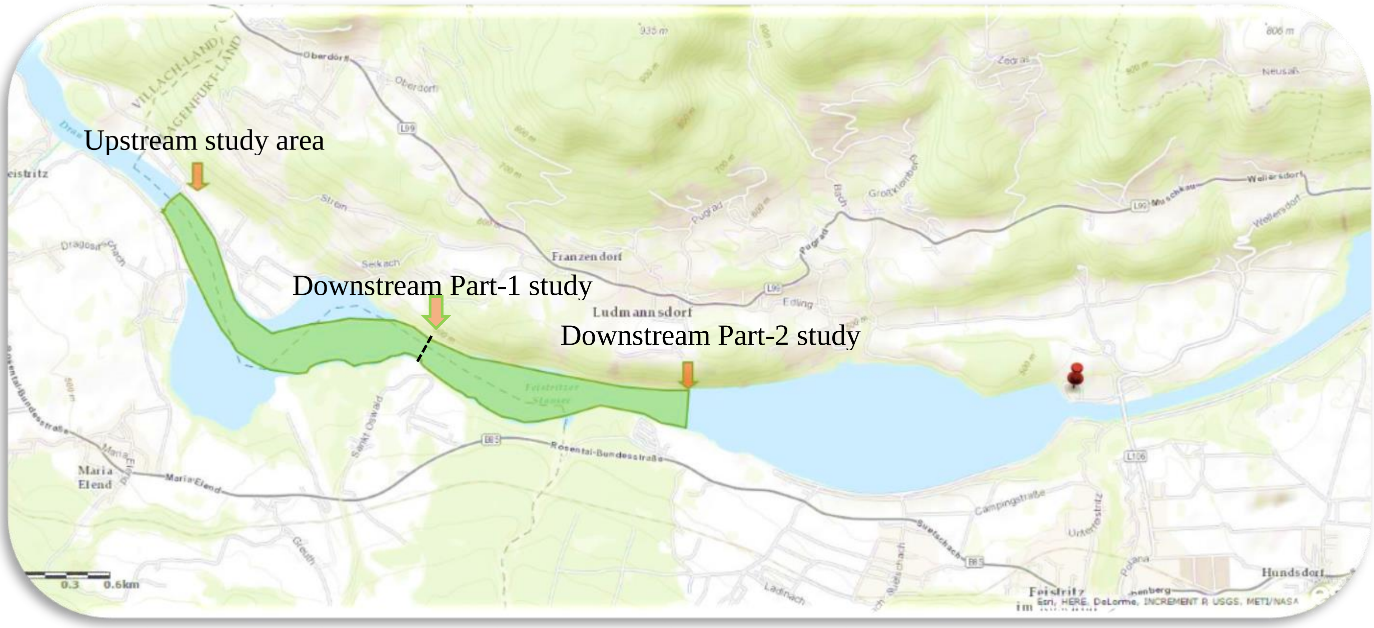

Figure (4.2) Study area (highlighted in green) and hydropower plant (shown by red pin). Flow is from left to right.

The first part of this research focused on the upper portion of the study area, which is a meandering river with a length and average width of 2.6km and 250m respectively (Fig. 4.2). In the second part, the study area extended toward the mouth of the reservoir. As can be seen from Figure (4.2), the area is located before a reservoir. Estimating the rate of sediment transport will have a significant effect on managing the reservoir, because according to Dorfmann and Knoblauch (2008), during 40 years of operation, the power plant turbine has faced severe problems because of suspended sediment. From data collected by Dorfmann at a station upstream of this reach, the average discharge during summer and spring is about 350-400m^3/s, and in winter the discharge is only 200m^3/s. However, high discharge is usually observed during fall, and reaches about 1200m^3/s. Although the rate of flood discharge varies between years, the duration of flooding may take days, and several discharge peaks may occur. In addition to discharge, both the suspended sediment upstream and water level downstream were measured in the same year. A high percentage of cohesive sediment is supplied to the area during high discharge, with concentrations as high as 7kg/m^3. During the rest of the year, the sediment supply is much lower, approximately 0.5kg/m^3. It is believed that change in sediment supply related to the hydropower plant that located to the upstream of this area that release sediment especially during flushing.

4.2. Field Data

4.2.1. Bathymetry

After hydropower plant construction in 1968, several surveys were carried out in the study area. Topographic surveys were taken at several cross-sections in 2012, 2013, and 2014 by Verbund-VHP (unpublished). These data were collected with an Acoustic Doppler Current Profiler. The section locations are shown in Figure (4.3), and will be referred to throughout this thesis. The pre- and post-flood profiles for the 2012 surveys are shown in Figure (4.4-b). In addition, in the meandering part, on the 10thof October, 2014, a side-scan survey was carried out by Verbund-VHP (unpublished). Although the side-scan survey completely covered the area along the river, in some locations full river sections were not recorded, as shown in Figure (4.3). However, the individual cross-section data for the river cover the complete river section.

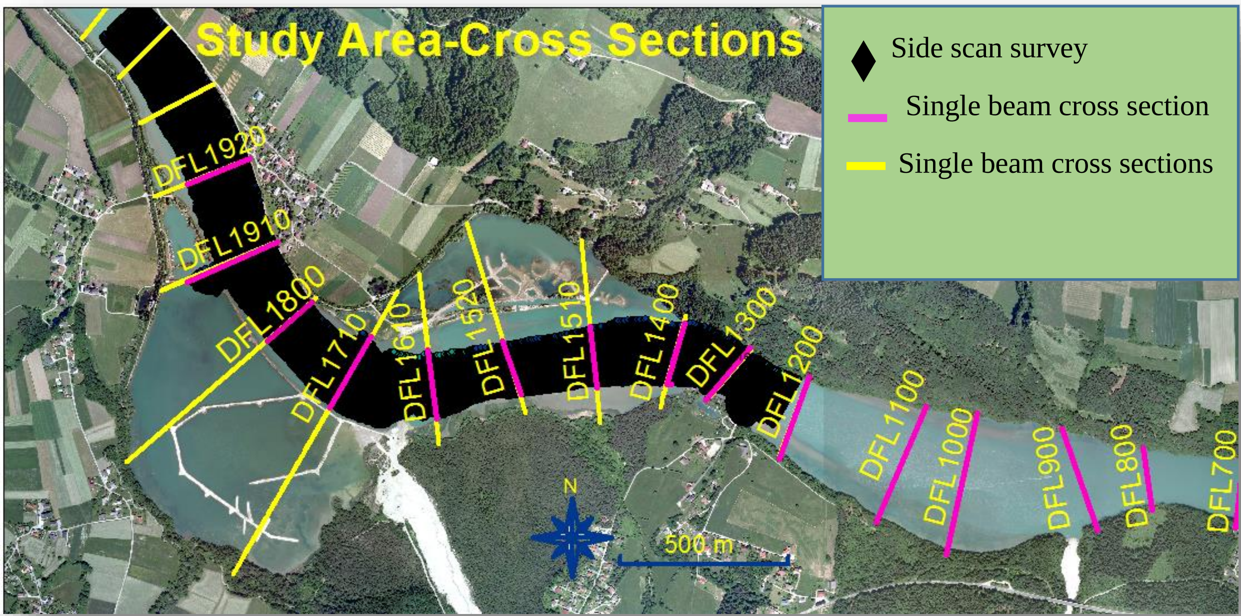

Figure (4.3) Side-scan and single-beam survey (Flow is from left to right)

It is crucial to compare the side-scan and single-beam surveys for multiple reasons: first, to examine the alignment between the surveys, and second, to check if there is a change in morphology between the times of the velocity measurement and the side-scan survey. As shown in Figure (4.4-a), in some sections the two surveys do not have good alignment. For example, in section DFL1910 the channel's left margin from the side-scan data does not align with the individual cross-section data. However, the alignment appears to be suitable for most sections, which allows for the estimation of channel changes between the side-scan survey and the individual section surveys. Furthermore, most of the sections underwent slight scouring between July 2014 and October 2014, with the exception of sections DFL1710 and DFL1610, where filling occurred on the inner bank point bar on the left side of the channel.

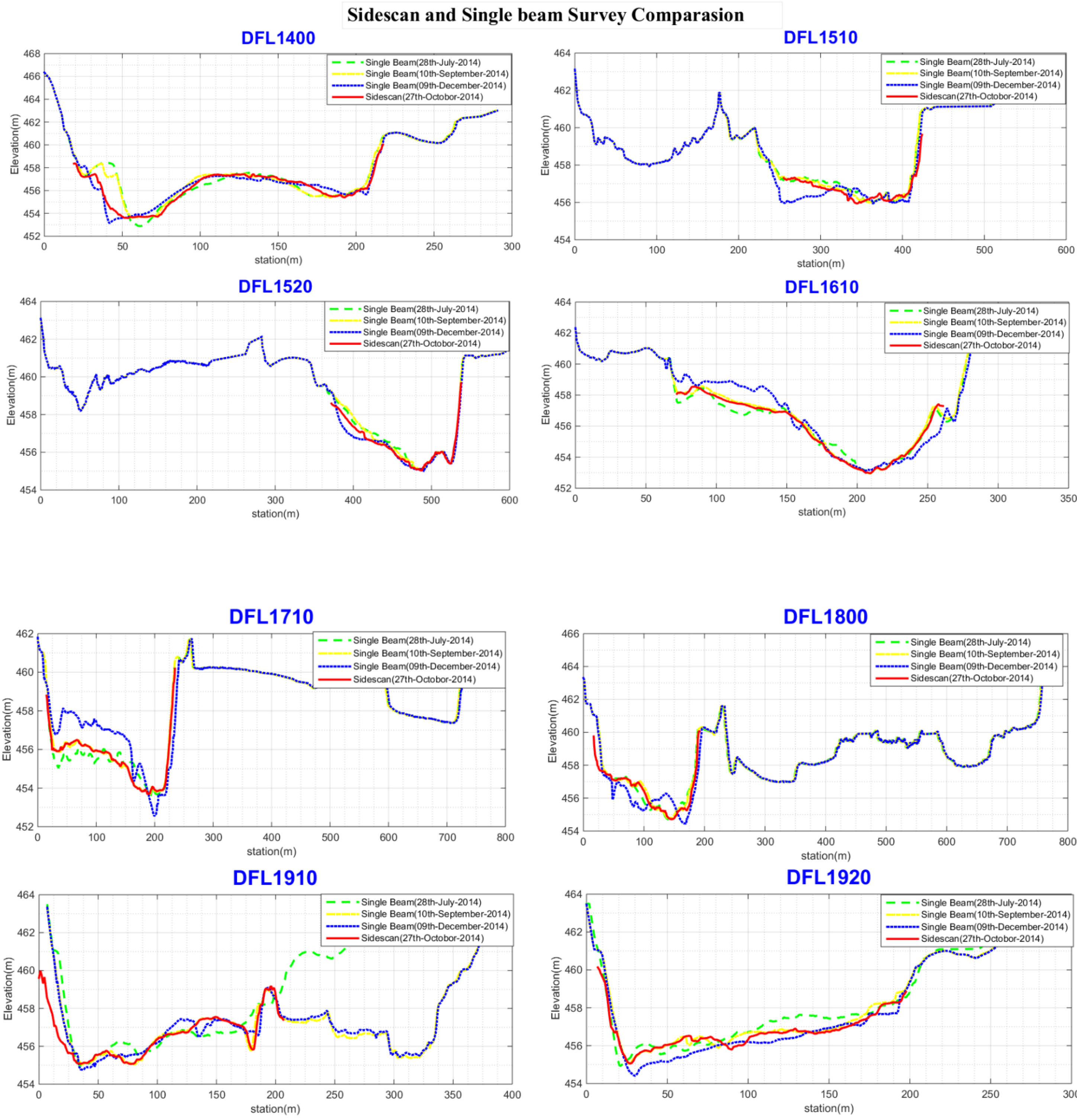

Figure (4.4-a) Bed profile by side scan and single beam; Sections seen from left to right, looking downstream.

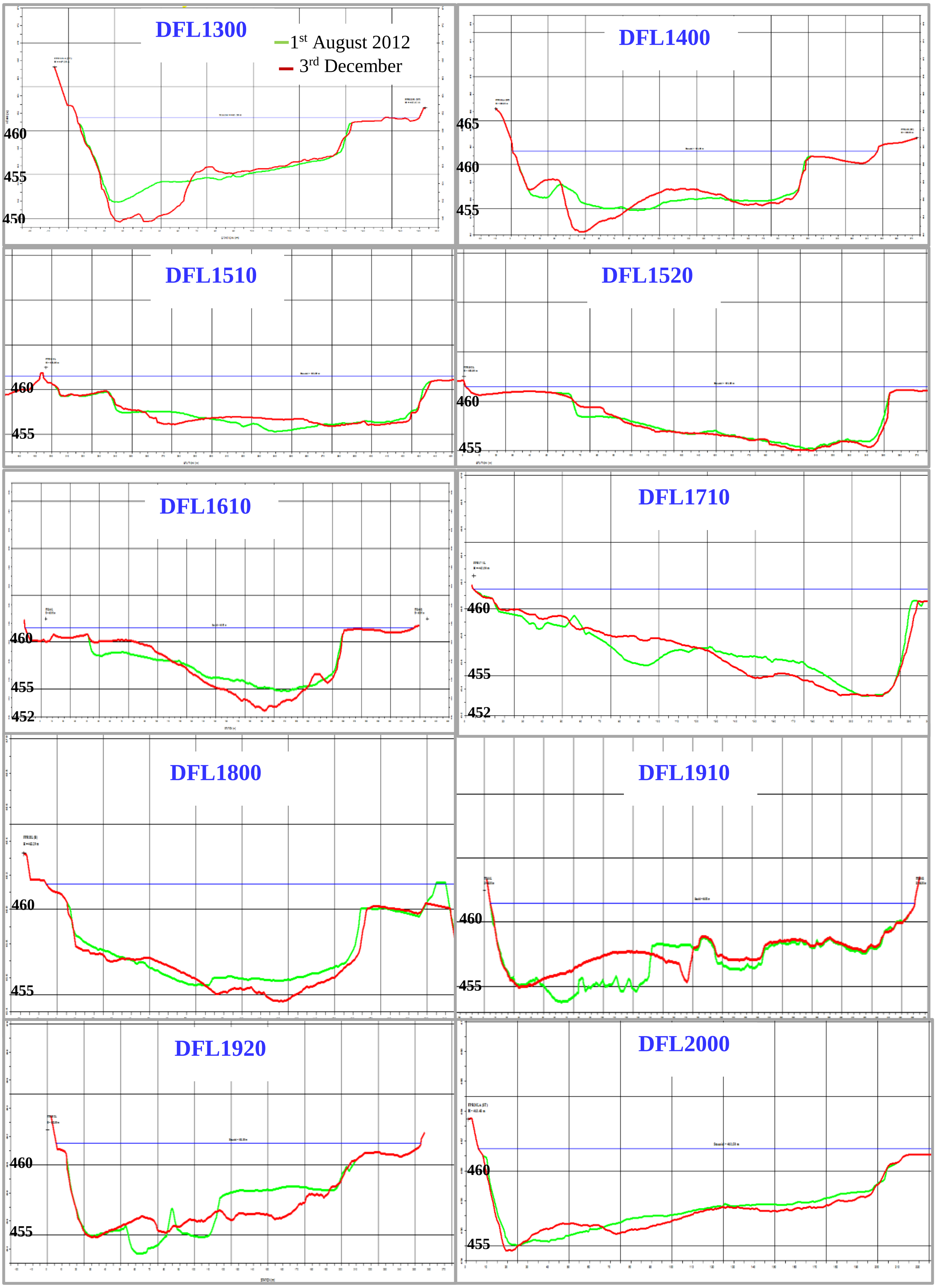

Figure (4.4-b) 2012 pre- and post-flooding morphology measurement at 10 cross-sections; sections seen from left to right, looking downstream

4.2.1. Hydrodynamic

Velocity measurements were carried out on 7th May and 8th May, 2014, by Dorfmann (unpublished). The measurements were obtained for eight cross-sections at meandering with an Acoustic Doppler Current Profiler. In addition, time series data for discharge and water level were collected for one year (June 2012-June 2013). The discharge station was located near the inlet of the study area, at Selkach Bridge, and the water level station was located near a hydropower plant (Fig 4.5). The highest discharge was recorded in the fall season, and at this time, the lowest water level was recorded downstream. This occurs due to opening the gate, which is known as the flushing period.

4.2.1. Sediment

Suspended sediment concentration was also measured by Verbund-VHP (unpublished) for 1 year (June 2012-June 2013) at the station located near the inlet of the study area at Selkach Bridge (Fig. 4.5).

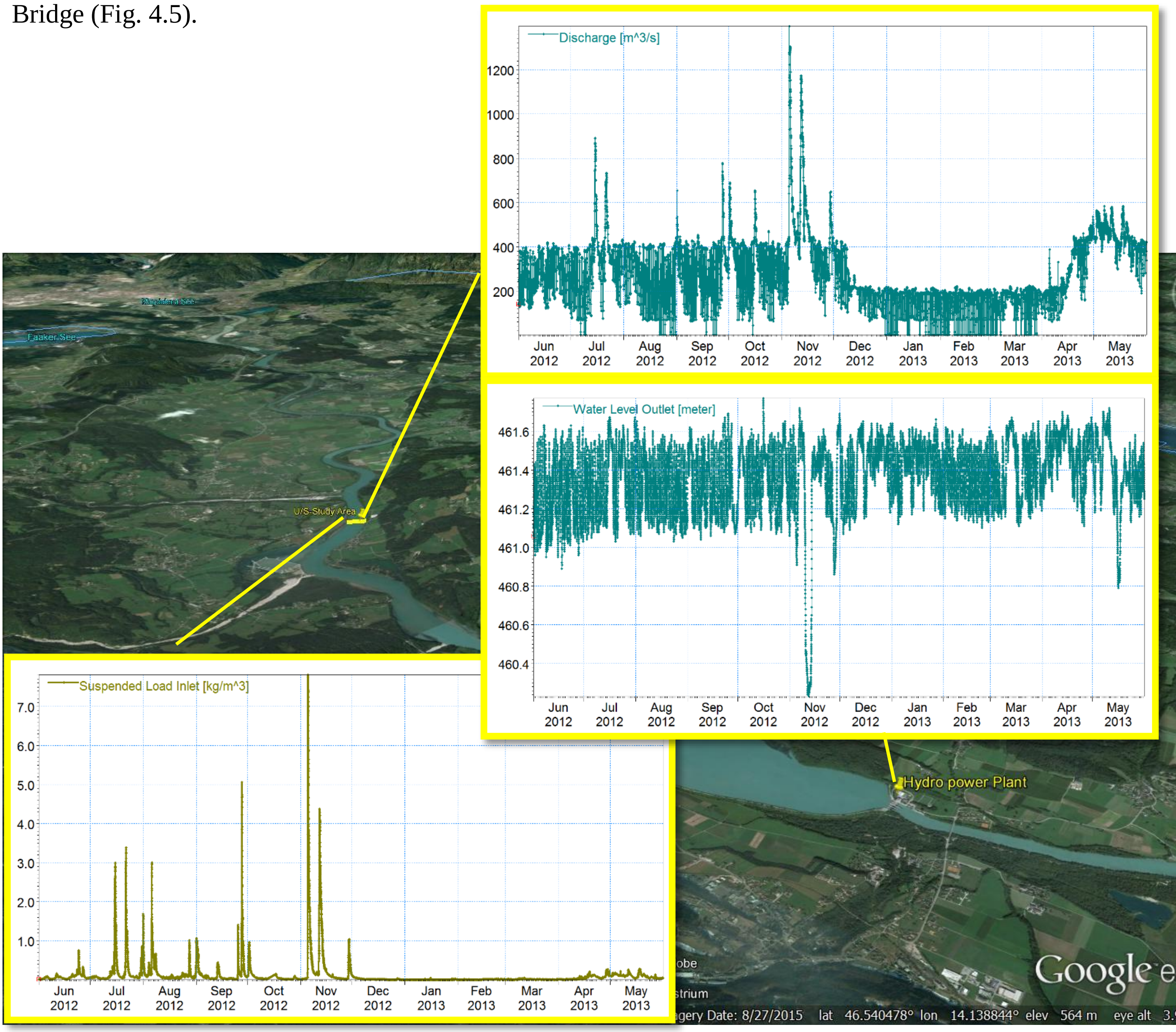

Figure (4.5) Collected data include discharge and suspended sediment at upstream and water level at downstream

Four suspended sediment samples were collected in November 2012 at Selkach Bridge (Chart 4.1, Table 4.1). It can be seen the suspended sediment ranges between 0.15mm fine sand and 0.005mm clay.

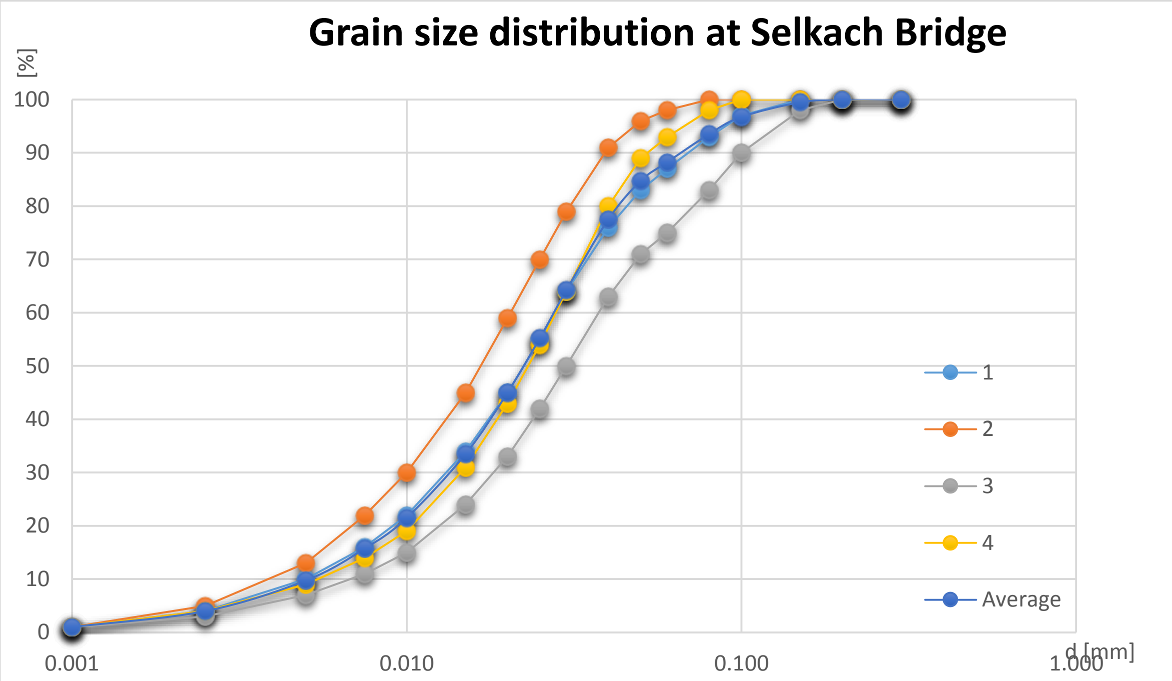

Chart (4.1) Grain size distribution of measured suspended sediment at Selkach Bridge

Table (4.1) Grain size distribution

Grain sizes		13/11/2012	12/11/2012	05/11/2012	05/11/2012	Average
<1µm	%	1	1	1	1	1
1-2,5µm	%	3	4	2	3	3
2,5-5µm	%	6	8	4	5	5.75
5-7,5µm	%	6	9	4	5	6
7,5-10µm	%	6	8	4	5	5.75
10-15µm	%	12	15	9	12	12
15-20µm	%	11	14	9	12	11.5
20-25µm	%	10	11	9	11	10.25
25-30µm	%	9	9	8	10	9
30-40µm	%	12	12	13	16	13.25
40-50µm	%	7	5	8	9	7.25
50-60µm	%	4	2	4	4	3.5
60-80µm	%	6	2	8	5	5.25
80-100µm	%	4	0	7	2	3.25
100-150µm	%	3	0	8	0	2.75
150-200µm	%	0	0	2	0	0.5
200-300µm	%	0	0	0	0	0
		100	100	100	100	100

To save computational time, the above distribution was reduced to five grain size classes by applying inverse distance weighted interpolation. Regarding grain size distribution in the bed, not enough information was available. The bed material in the study reach was estimated from a 1D model of the whole chain of the hydropower plant to consist of three main particles (Table 4.2).

Table (4.2) Estimated bed grain size distribution

Grain size (mm)	Percentage
0.05	33
0.22	33
15	33

The smallest particle overlaps with the suspended particle size and the biggest grain may be nearly immobile. Therefore, only the (0.22mm) size class was included with the other five particle classes in the model. The percentages below were applied in determining the concentration of each grain size. Because the concentration of 0.22mm grains was not available, it was estimated as having the same concentration as 0.158mm grains when the flux is greater than 400m^3/s. If the flux is less, the concentration is considered as equal to the same concentration divided by three (Table 4.3).

Table (4.3) Grain size percentage multiplied to total concentration for model inlet boundary

Grain Size(mm)	**Percentage%**
0.00750	22
0.01974	34
0.03941	29
0.07958	12
0.15769	3
0.22000	1/3(concentration)

5. Model Setup -Meandering (Part 1)

5.1. Domain

5.1.2. Grid

In this study, horizontally, curvilinear grid, and vertically, б grids were implemented. Horizontally, the computational grid was divided into 12,928 cells, as can be observed from Figure (5.1). Vertically, 10 layers were implemented. The input latitude is 46.54 degrees.

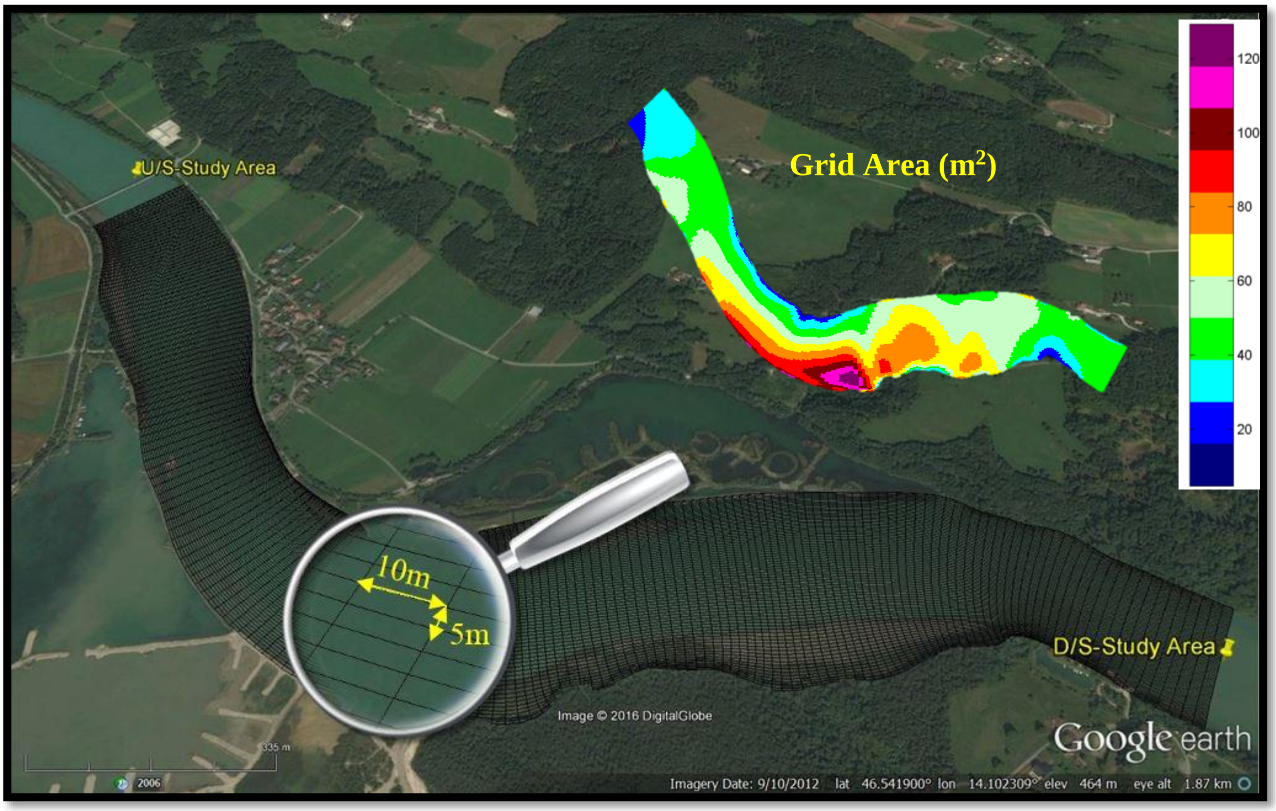

Figure (5.1) Computational grid of the study area (Part-1)

5.1.2 Bathymetry

In hydrodynamic calibration Bathymetry of sided scan survey -2014 is applied. However, since the morphodynamic survey and sediment boundary condition was obtained in 2012, it was essential to depend on bathymetry 2012. Therefore based on bathymetry of 2014 side scan and morphodynamic cross section of 2012 prior flooding, the bathymetry for morphodynamic calibration is prepared by Cokriging interpolation (Figure 5.2). Prior starting interpolation, the Cokriging condition like (checking normality distribution, checking for stationary, checking for trend, and autocorrelation) have been satisfied.

After that at the bend, the river divided to two parts and for each of them interpolation are conducted. The reason for this division was to satisfy the lag of the semivariogram map of the kriging. In the interpolation setup, anisotropy changed to true; number of lags, lag number, direction, and minor range have been modified to have lowest root mean square error.

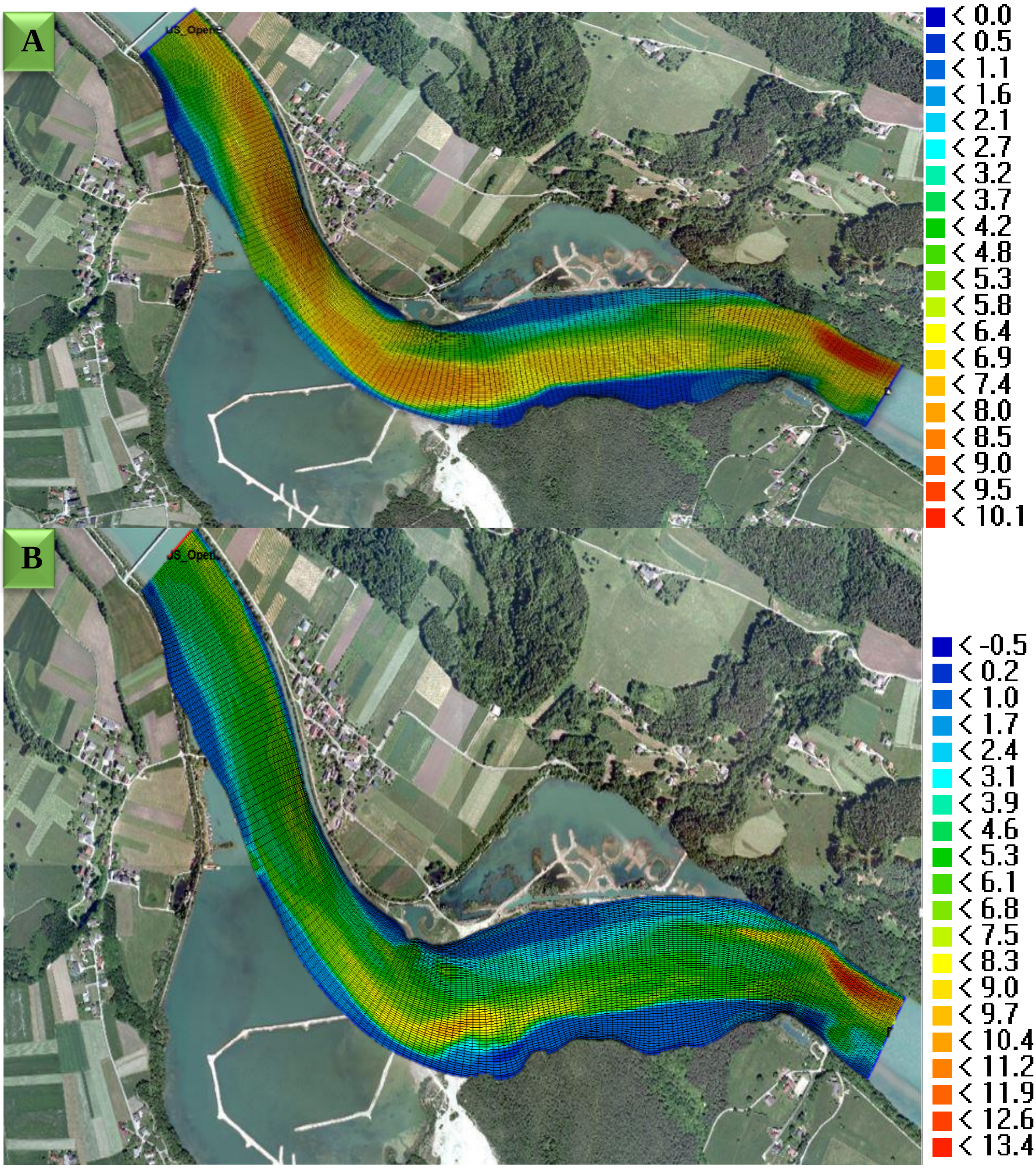

Figure 5.2 a) Bathymetry 2012; b) Bathymetry 2014

5.2 Time Frame

In most cases, the time step plays an important role in model stability. In Delft3D, in the case of a б grid excluding waves, the following formula for the Courant-Friedrichs-Lewy number (CFL) needs to be satisfied:

$$CFL = \frac{\Delta t\sqrt{gH}}{\{\Delta x, \Delta y\}} \qquad < 1$$

In the current model, Δt=0.05min, and with the grid size shown in Figure (5.1), this condition is satisfied. However, some other time step restrictions must be satisfied that change depending on the process in the simulation. In Delft3D, if this condition is not satisfied, a warning will be given in the diagnostic file. For more information, refer to the manual.

5.3 Boundary Condition

Hydrodynamic- Steady State

In the hydrodynamic validation for May 7th and May 8th, 2014, discharges of 390m^3/s and 420m^3/s at the model inlet and water levels of 461.5m and 461m respectively at the outlet boundary were applied. In the 2D simulation, the inflow conditions were assumed to be uniformly distributed, whereas in the 3D simulation, they were presumed to be distributed logarithmically in the vertical direction.

Morphodynamic-Unsteady State

In the morphology model, at upstream both the River flux and sediment concentration and at downstream, water level are prescribed. The concentration of individual grain sizes was determined by multiplying the percentages of grains in the grain size distribution by the total concentration. In Delft3D, for boundary type, total discharge- time series and water level time series are chosen.

5.4 Initial Condition

In the steady state simulation, the initial water level was assumed to be at level (461.5m-Normal period) for both discharge fluxes, 390 and 420 m^3/s. In unsteady state, i.e., the first morphology simulation on bathymetry 2012, an initial water level of 461.5m and a zero suspended sediment concentration were applied. This applied for the period between 1st August 2012 and 1st October 2012. The rest of the simulation of each subsequent season depended on the previous season's results.

5.4 Physical Parameters

In both the hydrodynamic and morphology model setups, the physical parameters were obtained from a model assessment. This was done by comparing the model results (water velocity and bed level change) with the field observation data. Based on the steady state hydrodynamic model assessment in comparison with the ADCP velocity data, both the roughness and horizontal eddy viscosity were obtained by sensitivity analysis, which is presented in Section (6.1). Based on the bed level assessment in comparison with the observed scour and fill, various sediment parameters were chosen, which is discussed in Section (6.2).

The model assessment depends on statistical errors represented by Mean Absolute Error (MAE), Root Mean Square Error (RMSE), and coefficient of determination (R^2).

MAE	RMSE	R^2
$\frac{\sum(\mathbf{Model}-\mathbf{ADCP})}{\mathbf{n}}$	$\sqrt{\frac{1}{n}\sum(\mathrm{Model}-\mathrm{ADCP})^2}$	$\frac{\sum(\mathrm{ADCP}-\mathrm{Model})^2}{\sum\left(\mathrm{ADCP}-\overline{\mathrm{ADCP}}\right)^2}$

6. Model Assessment

6.1. Hydrodynamic Calibration and Validation

6.1.1. Roughness

Three simulations were conducted in order to determine the best value for bed roughness. As can be seen in Table (6.1), Run1 and Run2 were 2D models including secondary flow model corrections. In these runs only the roughness was changed, and the parameters for horizontal eddy viscosity and diffusivity remained the same, with values of 0.1 and 10^{-6} respectively. In Run1, where a constant roughness (Manning-n =0.025sm$^{-1/3}$) was applied, the velocity near the bank was overestimated. This is because the river near the bank has a higher shear stress and lower tangential velocity compared to the main channel. To solve this, in Run2, the roughness near the bank was increased to 0.040 sm$^{-1/3}$ and the roughness in the rest of the river was set at the same as for Run1. This change increased the coefficient of determination for resultant velocity from 53.8% to 63.6%. In Run3, the roughness at the outer bank in the downstream section (DFL1300) was changed to 0.015 sm$^{-1/3}$ and the rest was set at the same as for Run2. This change did not increase the model's accuracy. The reason for this analysis was to see if the extensive scour that occurred in 2012 had a relationship with the roughness.

Table (6.1) Overall error results for 8 cross-sections (Flux=390m^3/s, H. Eddy Viscosity=0.1m^2/s, diffusion=10-^{6}m^2/s, βc=0.5)

	Roughness	**Velocity**	**R^2**	**MAE**	**RMSE**
Run1	Constant(0.025)	U(Vx)	0.629	0.052	0.078
		V(Vy)	0.930	0.038	0.049
		$R=\sqrt{(U^2+V^2)}$	0.538	0.057	0.079
Run2	Spatial Vary(0.025@ main channel& 0.040@bank)	U(Vx)	0.685	0.049	0.075
		V(Vy)	0.939	0.036	0.046
		$R=\sqrt{(U^2+V^2)}$	0.636	0.053	0.076
Run3	Spatial Vary (0.025@ main channel& 0.040@bank, 0.015@Downstream)	U(Vx)	0.685	0.052	0.076
		V(Vy)	0.914	0.042	0.055
		$R=\sqrt{(U^2+V^2)}$	0.598	0.062	0.085

6.1.2 Secondary flow-2D (βc) Analysis

The second essential analysis was on the secondary flow model correction in the 2D model. As mentioned before, the effective horizontal shear stress will be added to the momentum equation to account for secondary flow if the secondary flow model is evoked. Analysis of βc, which is a user-defined parameter in the mentioned equation, shows that including a secondary flow correction in the 2D model decreased the model prediction (Table 6.2). The depth-averaged velocity vectors for the various model runs are shown in Figure 6.1-a. The reverse flow along the outer bank, observed in both the measurements and the model results (see also Figure 6.1-b), may have occurred because of the channel curvature. As can be seen from Figure (6.1-a), although the shape of the secondary flow in the 3D model and (2D_ βc=0.5) are similar, the depth-averaged velocity is overestimated in Run4 compared to the ADCP data, especially near the inner bank (see also Figure (6.1-b)). Furthermore, from comparing the outer bank and inner bank spiral flows in Figure (6.1-b), it can be seen that including the secondary flow model in the simulation decreased the reverse flow estimation at the outer bank but increased the secondary flow estimation at the inner bank. The secondary flow momentum correction algorithm based on channel curvature was not designed specifically to predict a reversing flow along channel banks. Furthermore, according to Kalkwijk and Booij (1986), who developed this secondary flow model, the model has restrictions on the applicable width and curvature of the channel. Overall, it can be seen that the 3D model provided better estimates of the depth-averaged velocity distribution, although it was only marginally better than the 2D model without secondary flow correction.

Table (6.2) Overall error results for 8 cross-sections (Flux=390m^3/s, Viscosity=0.1m^2/s, diffusion=10^{-6}, roughness=spatial roughness, as in Run2)

	Roughness	Velocity	R^2	MAE	RMSE
Run4	2D, secondary flow correction Beta (βc=0.5)	U(Vx)	0.685	0.049	0.075
		V(Vy)	0.939	0.036	0.046
		$R=\sqrt{(U^2+V^2)}$	0.636	0.053	0.076
Run5	2D, secondary flow correction Beta (βc=0.2)	U(Vx)	0.754	0.045	0.066
		V(Vy)	0.943	0.035	0.044
		$R=\sqrt{(U^2+V^2)}$	0.724	0.049	0.067
Run6	2D, secondary flow correction Beta (βc=0.01)	U(Vx)	0.796	0.043	0.060
		V(Vy)	0.946	0.034	0.044
		$R=\sqrt{(U^2+V^2)}$	0.777	0.046	0.061
Run7	2D, without secondary flow correction (βc=0)	U(Vx)	0.798	0.042	0.059
		V(Vy)	0.946	0.034	0.044
		$R=\sqrt{(U^2+V^2)}$	0.780	0.046	0.061
Run8	3D simulation (K-Epsilon)	U(Vx)	0.836	0.038	0.053
		V(Vy)	0.948	0.034	0.043
		$R=\sqrt{(U^2+V^2)}$	0.828	0.042	0.054

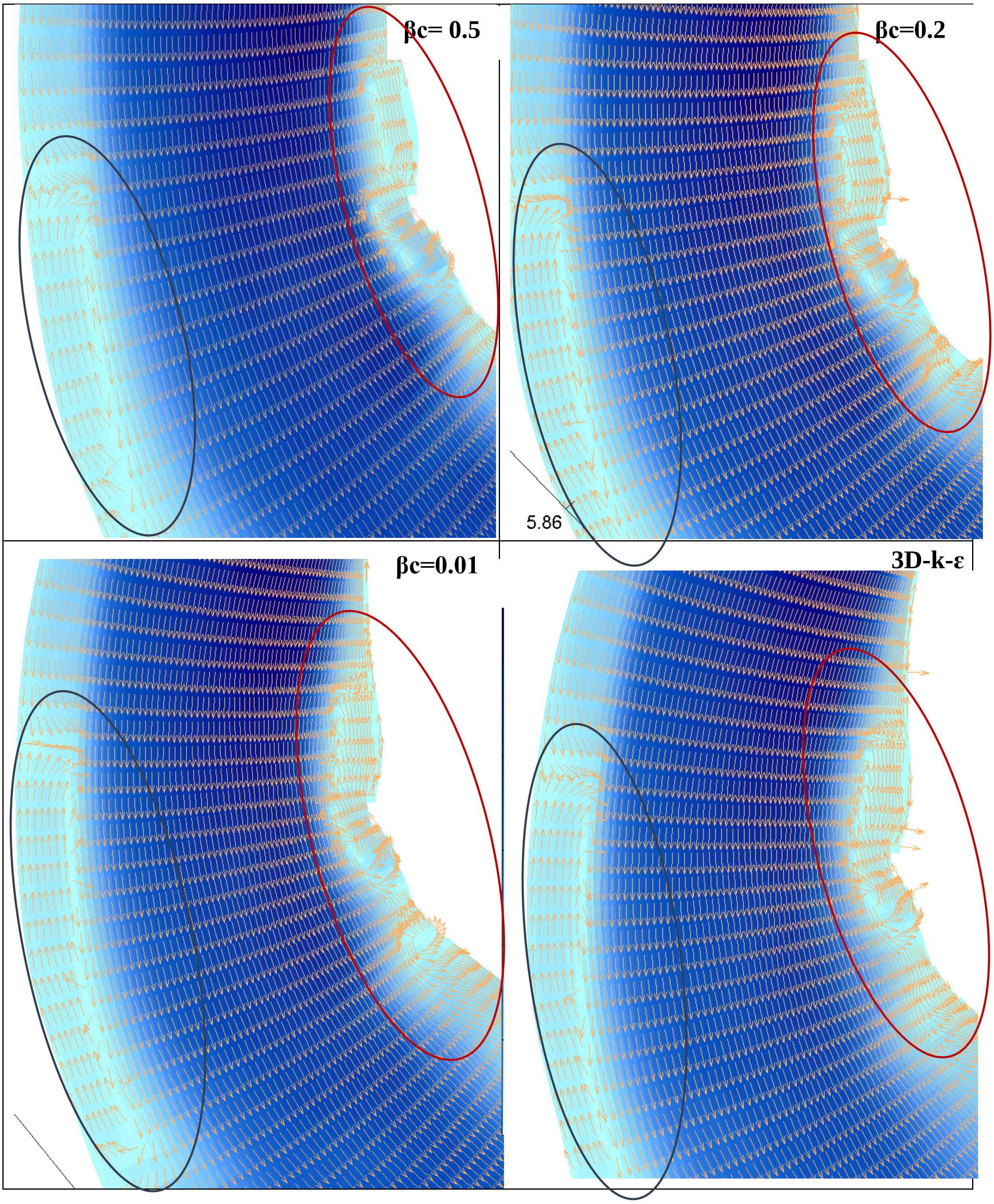

Figure (6.1-a) Spiral motion from depth-averaged velocity results

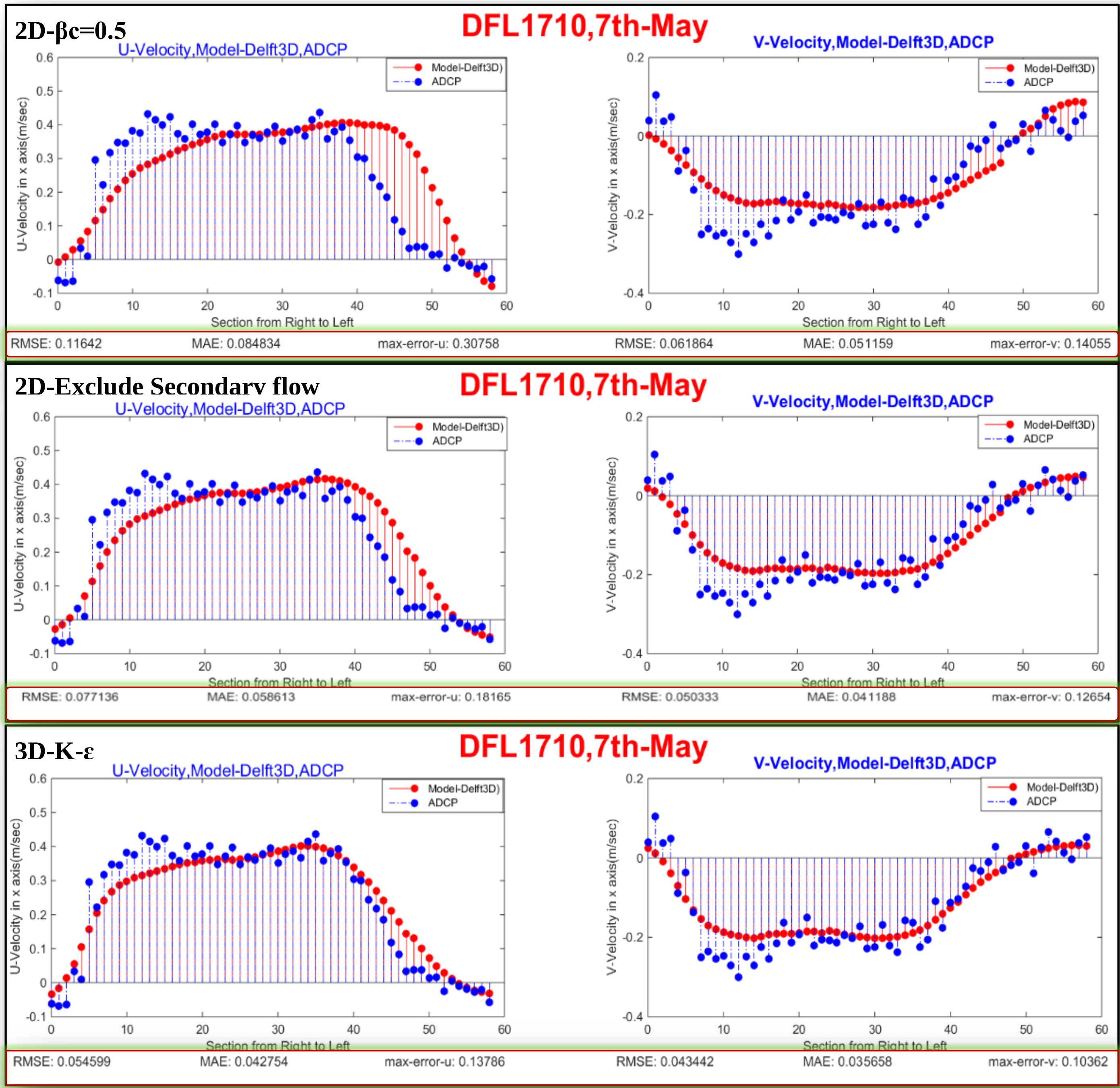

Figure (6.1-b) Depth-averaged velocity results for cross-section at the bend. Looking from upstream, from right to left.

6.1.3 Horizontal Eddy Viscosity

This analysis is conducted to show the influence of horizontal eddy viscosity in a 2D model with and without a secondary flow model. As can be seen from Table (6.3-a, b), when the secondary flow model is included in the simulation, the model has the lowest errors when the horizontal eddy viscosity is equal to $0.3m^2/s$. On the other hand, lower errors are achieved when the secondary flow model is excluded, and the best predictions are obtained with an eddy viscosity equal to ($0.1m^2/s$).

Table (6.3-a), 8 cross-sec., (Flux=$390m^3/s$, 2D simulation, secondary model included, spatial roughness as in Run2),

	Horizontal Eddy Viscosity	Velocity	R^2	MAE	RMSE
Run9	Constant Viscosity $0.5m^2/s$	U(Vx)	0.692	0.050	0.069
		V(Vy)	0.936	0.036	0.047
		$R=\sqrt{(U^2+V^2)}$	0.675	0.050	0.068
Run10	Constant Viscosity $0.3m^2/s$	U(Vx)	0. 711	0.048	0.069
		V(Vy)	0.939	0.035	0.046
		$R=\sqrt{(U^2+V^2)}$	**0.693**	0.050	0.068
Run11	Constant Viscosity $0.1m^2/s$	U(Vx)	0.685	0.049	0.075
		V(Vy)	0.939	0.036	0.046
		$R=\sqrt{(U^2+V^2)}$	0.636	0.053	0.076

Table (6.3-b), 2D simulation, Secondary model excluded, spatial roughness as in Run2,

	Horizontal Eddy Viscosity	Velocity	R^2	MAE	RMSE
Run12	Constant Viscosity $0.5m^2/s$	U(Vx)	0.729	0.047	0.065
		V(Vy)	0.940	0.034	0.045
		$R=\sqrt{(U^2+V^2)}$	0.728	0.048	0.063
Run13	Constant Viscosity $0.3m^2/s$	U(Vx)	0.772	0.044	0.061
		V(Vy)	0.942	0.034	0.044
		$R=\sqrt{(U^2+V^2)}$	0.772	0.045	0.060
Run14	Constant Viscosity $0.1m^2/s$	U(Vx)	0.798	0.042	0.059
		V(Vy)	0.946	0.034	0.044
		$R=\sqrt{(U^2+V^2)}$	**0.780**	0.046	0.061
Run15	Constant Viscosity $0.08m^2/s$	U(Vx)	0.795	0.043	0.061
		V(Vy)	0.945	0.034	0.044
		$R=\sqrt{(U^2+V^2)}$	0.773	0.047	0.062

6.1.4 Horizontal Eddy diffusivity

When the secondary flow model is implemented in a two-dimensional model, a diffusion coefficient will also be activated in the hydrodynamic model. In this analysis, different values for the diffusion coefficient are applied in the simulation. As can be seen in Table 6.4, the model including a secondary flow model yielded better predictions when the horizontal eddy diffusivity was increased. However, errors are still greater compared to the model excluding a secondary flow model.

Table (6.4) 8 cross-sec., 2D simulation, secondary model included, viscosity (0.1m^2/s), spatial roughness as in Run2, Flux=390m^3/s

	Horizontal eddy diffusivity	Velocity	R^2	MAE	RMSE
Run16	Constant 10 m^2/s	U(Vx)	0.702	0.049	0.073
		V(Vy)	0.940	0.036	0.046
		$R=\sqrt{(U^2+V^2)}$	0.657	0.053	0.075
Run17	Constant 10^{-6} m^2/s	U(Vx)	0.685	0.049	0.075
		V(Vy)	0.939	0.036	0.046
		$R=\sqrt{(U^2+V^2)}$	0.636	0.053	0.076

6.1.5. Comparing 2D results for 390 and 420 m^3/s fluxes

In comparing between the 390 and 420 m^3/s fluxes, it will be more accurate to depend on the values of MAE and RMSE instead of R^2. The reason for this is related to the difference in the number of points used in the validation of the model. It can be seen in Table (6.5) that the model based on a discharge flux equal to 420m^3/s had greater error than the model developed for a discharge flux of 390 m^3/s. The velocity results for both fluxes are shown in Figure 6.2-a.

Table (6.5) 8 cross-sec., 2D simulation, viscosity (0.1), spatial roughness as in Run2

		Velocity	R^2	MAE	RMSE
Run7	2D, without secondary flow correction (βc=0)-390 m^3/s	U(Vx)	0.798	0.042	0.059
		V(Vy)	0.946	0.034	0.044
		$R=\sqrt{(U^2+V^2)}$	0.780	0.046	0.061
Run8	2D, without secondary flow correction (βc=0)-420 m^3/s	U(Vx)	0.868	0.044	0.061
		V(Vy)	0.952	0.040	0.053
		$R=\sqrt{(U^2+V^2)}$	0.758	0.054	0.069

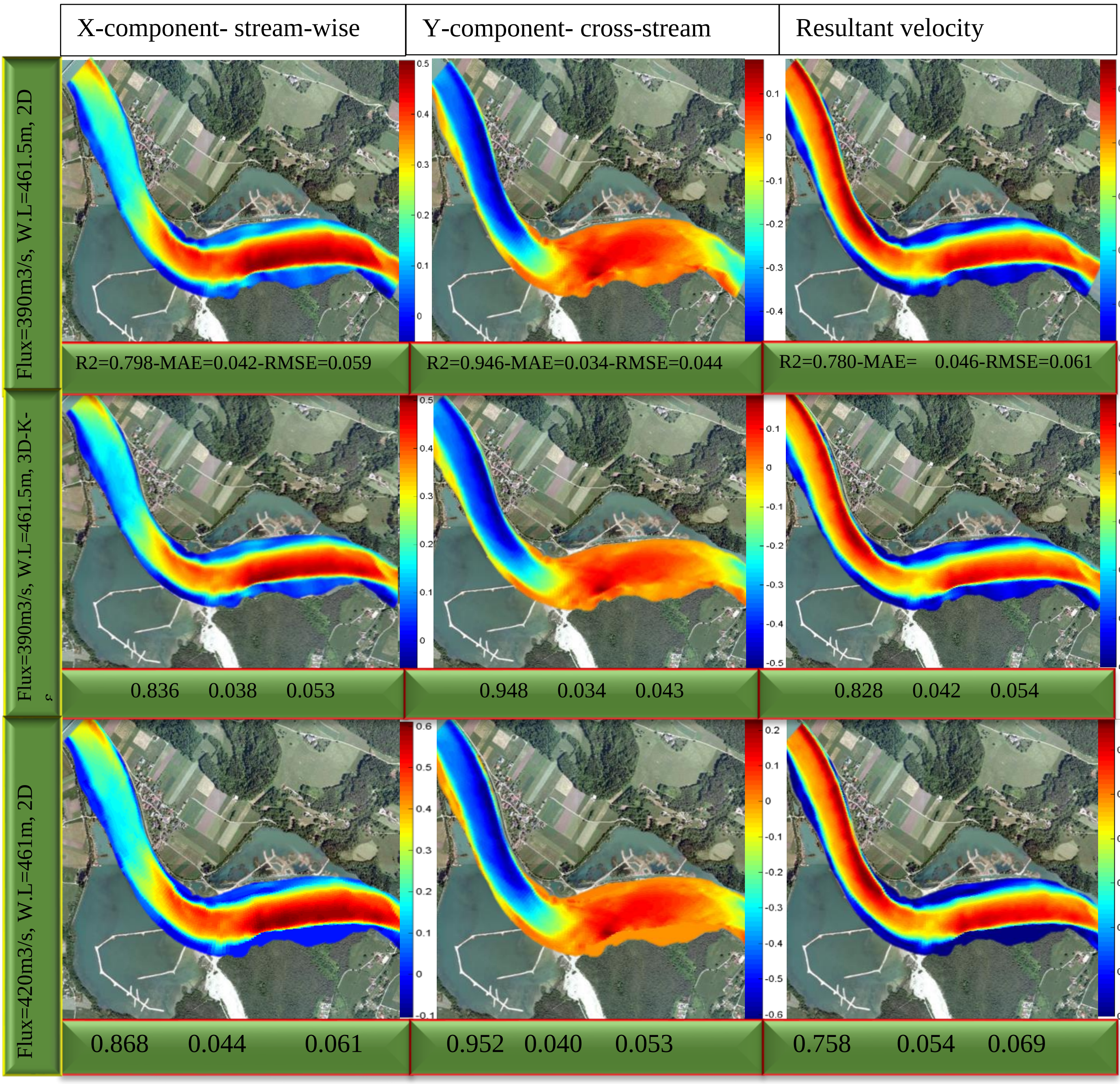

Figure (6.2-a) Depth-averaged velocity (m/s) (x-component- stream wise velocity, y-component- cross-stream velocity and resultant of both component)

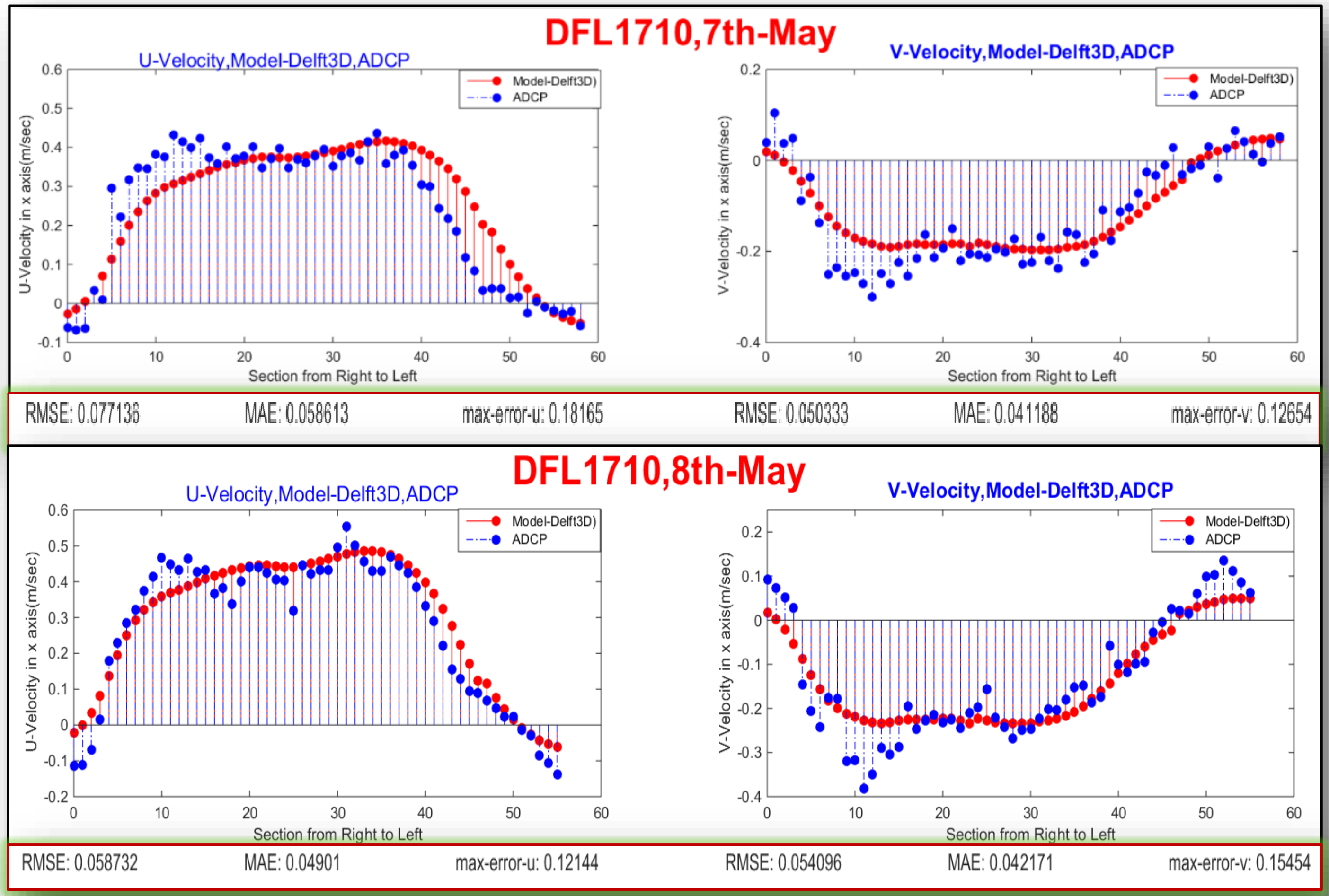

Figure (6.2-b) Depth-averaged velocity (m/s) (x-component- stream wise velocity, y-component- cross-stream velocity at the bend cross-section for both fluxes (390&420) of the 2D model. Section seen from right to left looking from upstream

Figure (6.2-b) compares the measured and modelled stream-wise and transverse velocities at the bend cross-section for both discharge scenarios (390 m^3/s on May 7 2014, and 420 m^3/s on May 8 2014). The stream-wise velocities in the 390 m^3/s model were under-predicted near the left bank and over-predicted near the right bank. The 420 m^3/s model had relatively lower stream-wise velocity error; however, the predicted transverse secondary flow at both the inner and outer banks was lower than observed in the field measurements.

6.2. Morphodynamic Calibration and Validation

6.2.1 Physical parameters

Based on hydrodynamic analysis, the morphodynamic model is started with a horizontal eddy viscosity of $0.1 m^2/s$ and spatial roughness of 0.025 & 0.04 $sm^{-1/3}$ at the main channel and the bank respectively, without the secondary flow model in 2D. The horizontal diffusion parameter was set to $10^{-3} m^2/s$.

6.2.1.1 Sediment parameters

Table (6.6) Non-cohesive sediment parameter input

Sediment Name	SedimentG3	Sediment03	Sediment12
	Fine sand	Fine sand	Fine sand
Percentage-for concentration-inlet	3% or (1/3*Sed03)	3%	12%
Grain size (µm)	220	158	79.5
Dry bed density (kg/m^3)	1600	1600	1600

Table (6.7) Cohesive-sediment parameter input

Sediment Name	Sediment29	Sediment34	Sediment22
Percentage-for concentration-inlet	29%	34%	22%
Particle size (µm)	39	19	7.5
Critical shear stress of erosion (N/m^2)	0.1	0.065	0.03
Critical shear stress of deposition (N/m^2)	0.09	0.050	0.02
Dry bed density (kg/m^3)	500	500	500
Erosion parameter (kg/m^2/s)	0.0001	0.0001	0.0001

The required parameters for the non-cohesive and cohesive grains are shown in Table 6.6 and 6.7 respectively. The initiation of motion for the cohesive sediment depends on the critical shear stress of erosion. In most cases these values will be obtained from field measurements. However, in this study, due to lack of data, these values were obtained from Van Rijn (2016), as shown in Figure (6.3). In this curve, cohesion between the particles is excluded. It is essential to mention that since in Delft3D the sediment calculation is applied on each particle individually, it is more accurate to apply the values from this curve than from literature, in which the critical bed shear stress accounts for the cohesion between the particles. Nevertheless, the interaction between particles will be taken into account in both the non-cohesive and cohesive sediment transport equations, as mentioned in Section (3). Regarding the critical shear stress of deposition, as mentioned before in Section (3), there is still a debate on whether the deposition of fine sediment is controlled by the critical shear stress of deposition or only the settling velocity and concentration. Therefore, in this study both methods will be applied and the difference between them will be shown.

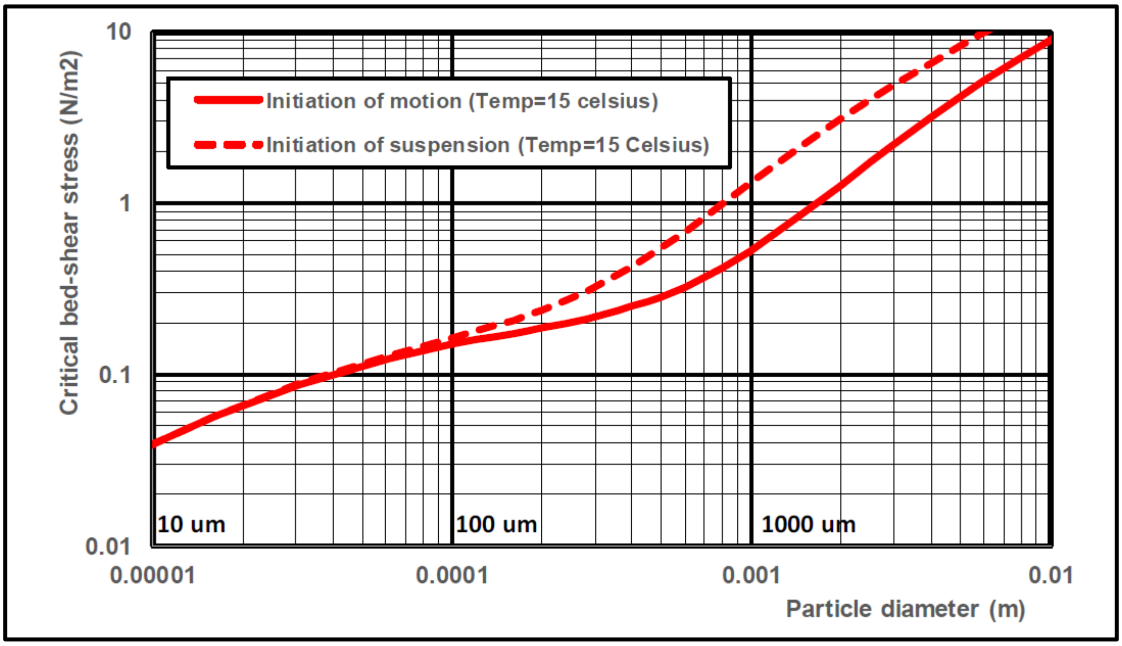

Figure (6.3) Critical bed shear stress estimation by Van Rijn (2016)

6.2.1.2 Morphology parameters

There are many parameters to be defined in a Deflt3D morphological model. Some of these parameters were held constant during all simulations, whereas some of them were specified for each individual simulation, as shown in Table 6.8-a. The parameters that were modified will be mentioned in each analysis. In the first analysis, most of the parameters started with the default setup of Delft3D.

Table (6.8-a) The required parameter input in the morphology file

MorFac	Morphological scale factor	1
MorStt	Spin-up interval from T Start till start of morphological changes	720 min
Thresh	Threshold sediment thickness for transport and erosion reduction	0.05m
MorUpd	Update bathymetry during FLOW simulation	true
EqmBc	Equilibrium sand concentration profile at inflow boundaries	false
DensIn	Include effect of sediment concentration on fluid density	false
AlfaBs	Stream-wise bed gradient factor for bed load transport	1
AlfaBn	Transverse bed gradient factor for bed load transport	1.5
Bed	Multiplication factor for bed-load transport vector magnitude	1
Sus	Multiplication factor for suspended sediment reference concentration	1
SedThr	Minimum water depth for sediment computations	0.6m
ThetSD	Factor for erosion of adjacent dry cells	0
Islope	Bed slope formulation (options 1-4 see manual Table B.6)(2=Default)	2
Upwind Bed load	Use upwind bed load (true, default) or central bed load (false)	true

Under layer

In Delft3D, the bed can be defined either as a well-mixed bed or as a stratigraphic layer. Since in most cases the sediment bed is found sorted from finest at the top to coarsest at the bottom, bed stratigraphy was implemented. In this study, only two layers were defined: the top was the "active" layer, and under this was a base layer. The first simulation started with a constant distribution of the sediment for the whole reach, as shown in Table (6.8-b).

Table (6.8-b) The required parameter input in the morphology file, under-layers

IUnderLyr	**Stratigraphy schematisation model (1 = single layer, 2 = multiple layers)**	**2**
MxNulyr	Maximum number of under-layers (excluding transport and base layers)	0
TTLForm	Transport layer thickness formulation	1
UpdBaseLyr	Update option for composition and thickness of base layer	1

Inicomp: Initial bed composition:

Layer	**Thick (m)**	**Sediment G3**	**Sediment 03**	**Sediment 12**	**Sediment 29**	**Sediment 34**	**Sediment 22**
Active Layer	4	40%	30%	30%	0	0	0
Base layer	5	100%	0	0	0	0	0

*The above setup that shown in sediment and morphology will be referred to it as Setup #1.

Most initial simulations were conducted over 14 days (3rd Nov - 18th Nov, 2012) to evaluate the sensitivity of the model to the various input parameters. In this sensitivity analysis, comparisons were made with the bathymetry observation cross-section data (Figure 4.4b). The last calibration was conducted on simulation of the four-month period between August and December 2012 (see Section 6.2.9).

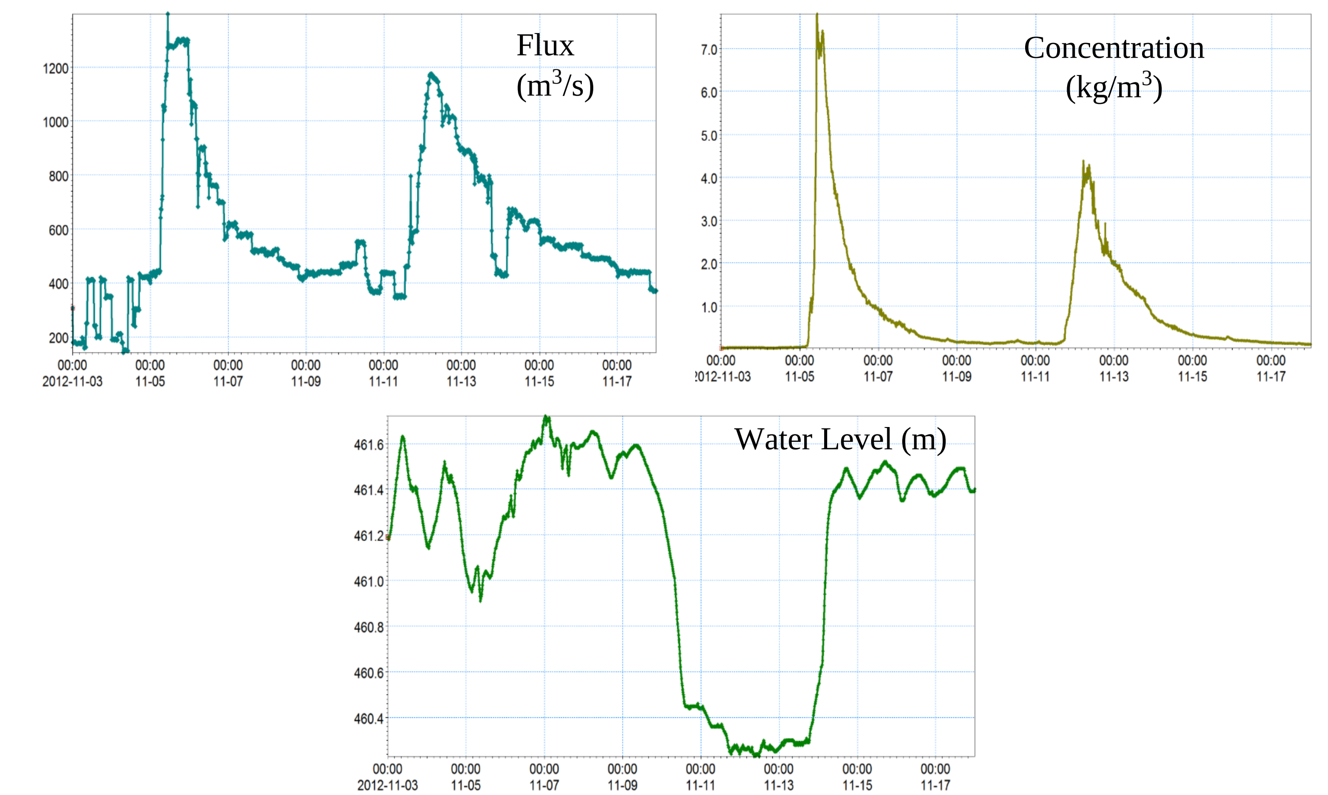

Figure (6.4) Boundary data for 14 days

6.2.2 Sediment Transport rate

An important part of morphology modelling is estimating the correct rate of sediment transport. This value, for both suspended and bed load, is influenced by many parameters such as slope, transport formula, and calibration coefficient (Bed, Sus). Therefore, due to the absence of measured transport rates, the following sensitivity analyses were performed.

6.2.2.1 Bed Load Transport

The two versions of the Van Rijn formula in Delft3D calculate bed load transport differently. For example, in Van Rijn (1984), reference height is a user-defined parameter, whereas in version (1993), it will be determined by the model. Some other differences will be explained depending on model results.

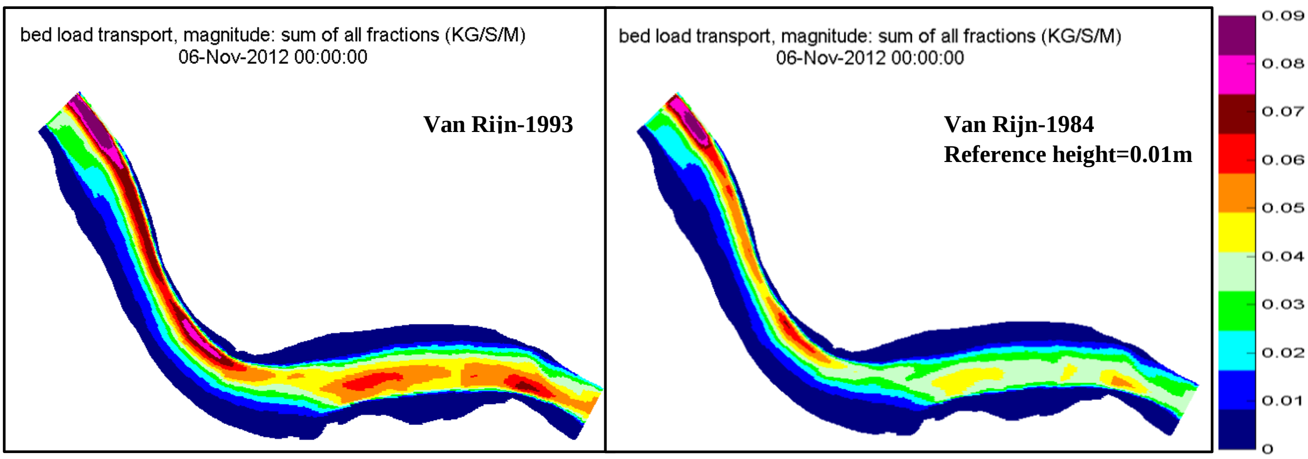

Figure (6.5) Results of Setup #1 for 14 days (3rd Nov 2012 - 18th Nov 2012)

Figure (6.5) shows the results of simulation after the first flood period (6th Nov). The highest rate of bed load transport is estimated by applying Van Rijn (1993). The low transport rate estimated by the (1984) formula may be correlated with the reference height, which has an influence on effective shear stress. The reference height in the (1993) version estimation depends on water depth, whereas for the 1984 model it has to been defined by the user. This figure shows that bed load transport extends all the way through the bend in the (1993) model, whereas in the (1984) model the high transport rate continues only up to the head of the point bar.

6.2.2.2. Suspended Sediment Transport

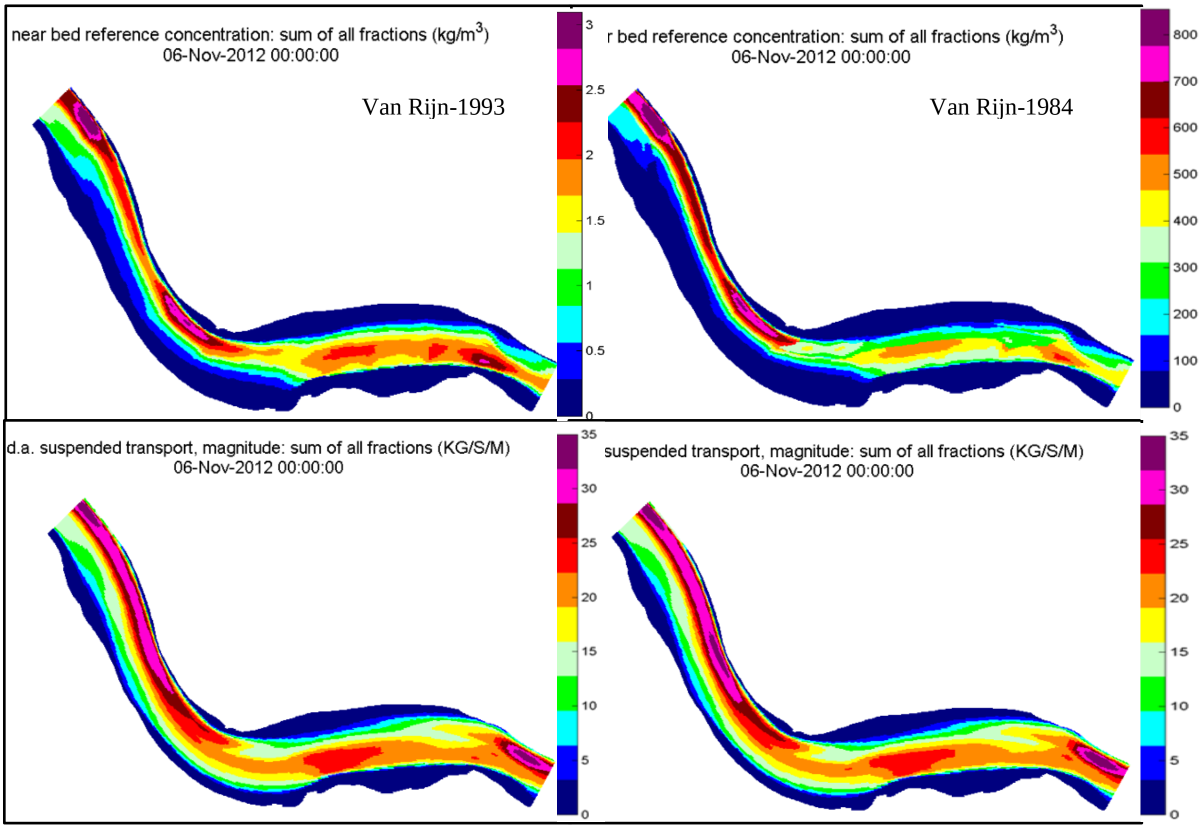

Figure (6.6) Near-bed reference concentration and suspended sediment transport of summation all fraction - Model Setup #1

In Figure (6.6), although the near-bed reference concentration of the Van Rijn (1984) version is much higher compared to the Van Rijn (1993) version, the overall depth average-suspended transport rate of all fractions is almost the same in the two models. In Figure (6.7), the result of only one non-cohesive sediment fraction (sediment12) shows a high value of near-bed reference concentration in the Van Rijn (1984) version. It is known that sediment transported as bed load increases with reference height. In other words, increasing the reference height will decrease the rate of non-cohesive suspended sediment transport, which can be observed clearly in Figure (6.7). However, it is not clear why there is such a large difference between the reference concentrations between the 1984 and 1993 models. One question that is to ask is how the same suspended sediment transport is estimated by the two models despite this huge difference in near bed reference concentration. It may be that the influence of the near-bed reference concentration is corrected by the calibration coefficient in the 1984 version.

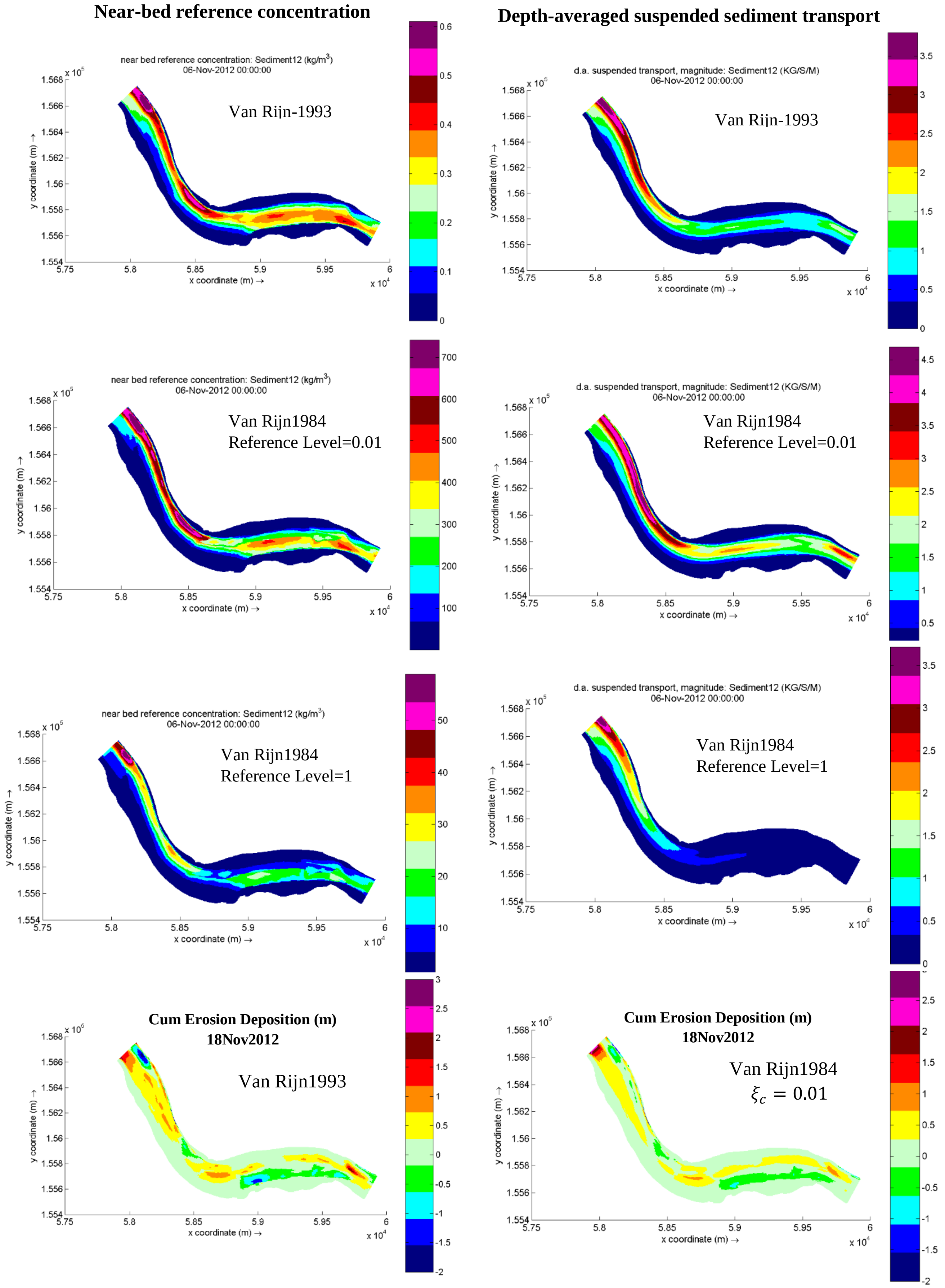

Figure (6.7) Near-bed reference concentration and depth-averaged suspended sediment transport of sediment 12

Figures 6.5 and 6.7 allow the examination of the predicted bed load transport and erosion-deposition pathways. The overall patterns are similar in the 1984 and 1993 versions of the Van Rijn model. Although the bed load transport is calculated as being higher at the upstream left side of the channel compared to downstream of the outer bend, deposition is estimated upstream, whereas erosion is estimated downstream. The sediment deposited in the upstream zone is likely due to bed load that is transported into the model domain from upstream during flood conditions.

6.2.3 Slope Formula Analysis: (Van Rijn, 1993)

The purpose of this analysis was to find out if the observed scour at the downstream pool can be estimated by different slope formulae compared to the observed bed level measured in 2012 in Figure (4.4-b), as shown in Section 4. In addition, the analysis examined the influence of changes in bedload transport rate on those areas that need to be eroded as in the field data. Note that the Parker and Andrews (1985) formula which is defined by (Islope=4) in the model was not implemented because this formula was developed for bed grain transport in the size range 0.45-0.78mm, and one of the parameters in this equation is a hiding and exposure coefficient which is not available when fine sediment is present in the bed.

In Figure (6.8a), the results in the first row were based on Setup #1 but with a different slope formula. The results shown from the second row until the last row were for a run with a different morphological factor (= 2) and bed coefficient (= 20). Figure (6.8a) demonstrates that applying a different slope formula results in different erosion and deposition rates, especially when bed load transport was dominant. With the original Setup #1 (shown in the first row (a_1, a_2, and a_3), the erosion-deposition rates estimated by the three slope formulae were slightly different, whereas as shown in the second row (b_1, b_2, b_3), significant differences can be seen between the slope formulae with the revised morphological factors and bed coefficients. Both Islope=1 and Islope=2 increased bed load transport, which resulted in erosion at the upstream left side (sections DFL1920-DFL1910). However, applying Islope=3 resulted in deposition. In addition, in the second row, at the head of the inner bend, erosion is estimated when slope was excluded (Islope=1), whereas implementing Islope=3 produced deposition in this zone. This difference was less in the first row (a_1, a_2, and a_3). Furthermore, comparing the downstream area, the right side of cross-section (DFL1610-1510) showed almost the same erosion by Islope=3 in row-2 (b_1, b_2, and b_3) compared to row-1(a_1, a_2, and a_3), whereas the other two Islopes produced much higher erosion in row-2 (b_1, b_2, and b_3) compared to row-1 (a_1, a_2, and a_3). Overall, the Islope=3 formula decreased both bed and suspended sediment transport rates compared to the other formulas.

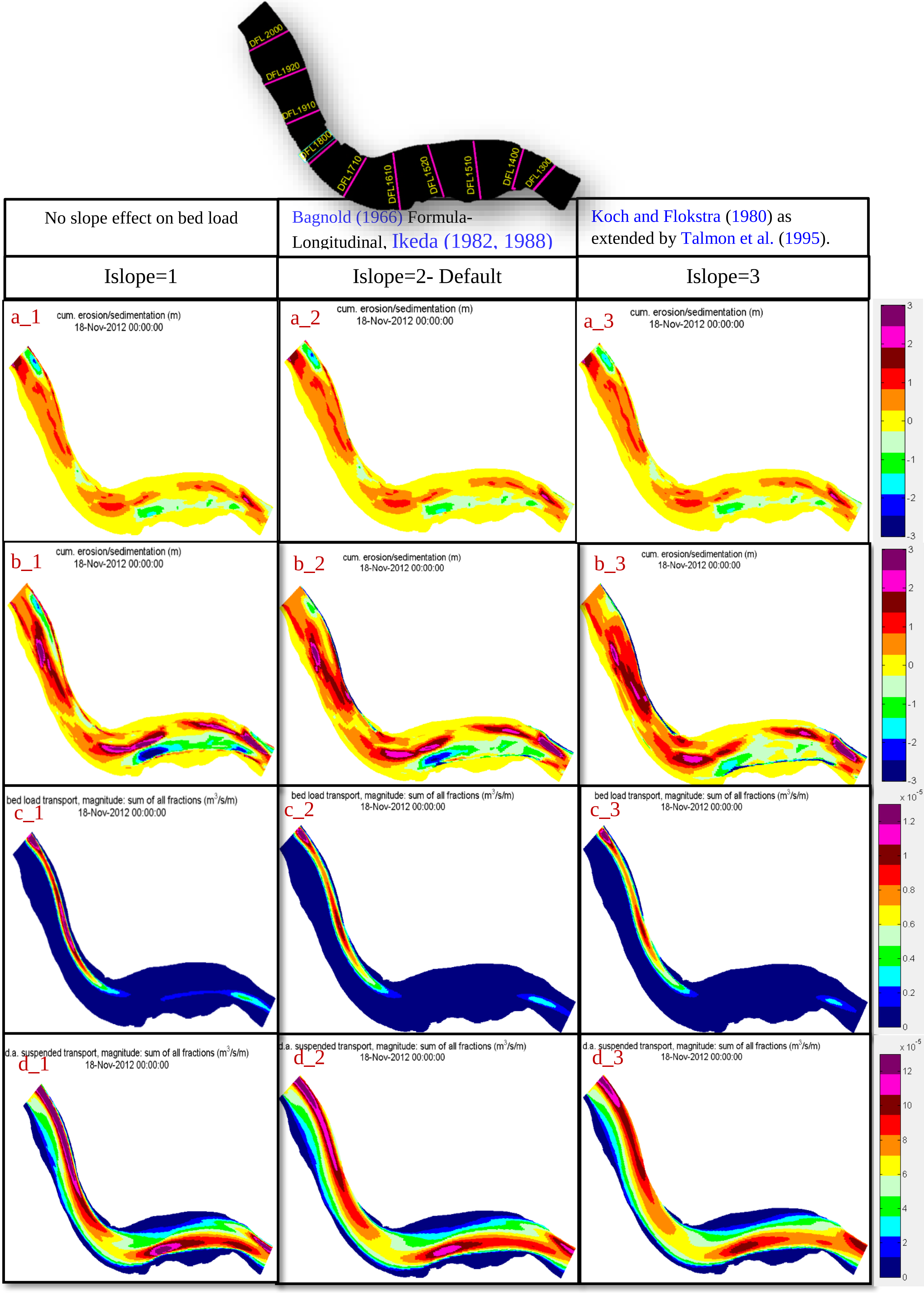

Figure (6.8) Cumulative erosion deposition, bed load transport, and suspended load transport at the end of the 14-day simulation with implementation of different slope formulas.

6.2.4 3D-Morphodynamic

A 3D simulation was conducted on Setup #1 with 10 vertical layers using the sigma model while applying Islope=3 (Figure 6.8b). Similar to the field measurements (Fig. 4.4b), at the bend, the estimated deposition at the inner bank was almost the same as indicated in the field measurements, although the outer bank erosion was not predicted. In contrast with the field measurements (Fig. 4.4b), erosion was not estimated on channel left between sections DFL1400 and DFL1300. In addition, in the upstream end of the model domain, at the left side of section DFL 1910-DFL 1920, erosion was estimated instead of deposition.

Comparing the 2D and 3D results, the rates of bed load and suspended load transport were almost the same (compare Figs. 6.8a and 6.8b). Furthermore, the 3D results for erosion-deposition were similar to the 2D model without the bed slope effect, even though in 3D Islope=3 was applied, as mentioned before. Comparing 2D for Islope=3 and 3D shows dissimilar pattern in erosion and deposition. For example, in the upstream end of the model domain, at the left side of section DFL 1910-DFL 1920, erosion was estimated in the 3D model, whereas the 2D model predicted deposition (in keeping with the field measurements; see Fig. 4.4b). This occurred because in this zone the bed shear stress estimated by 3D was higher compared to 2D.

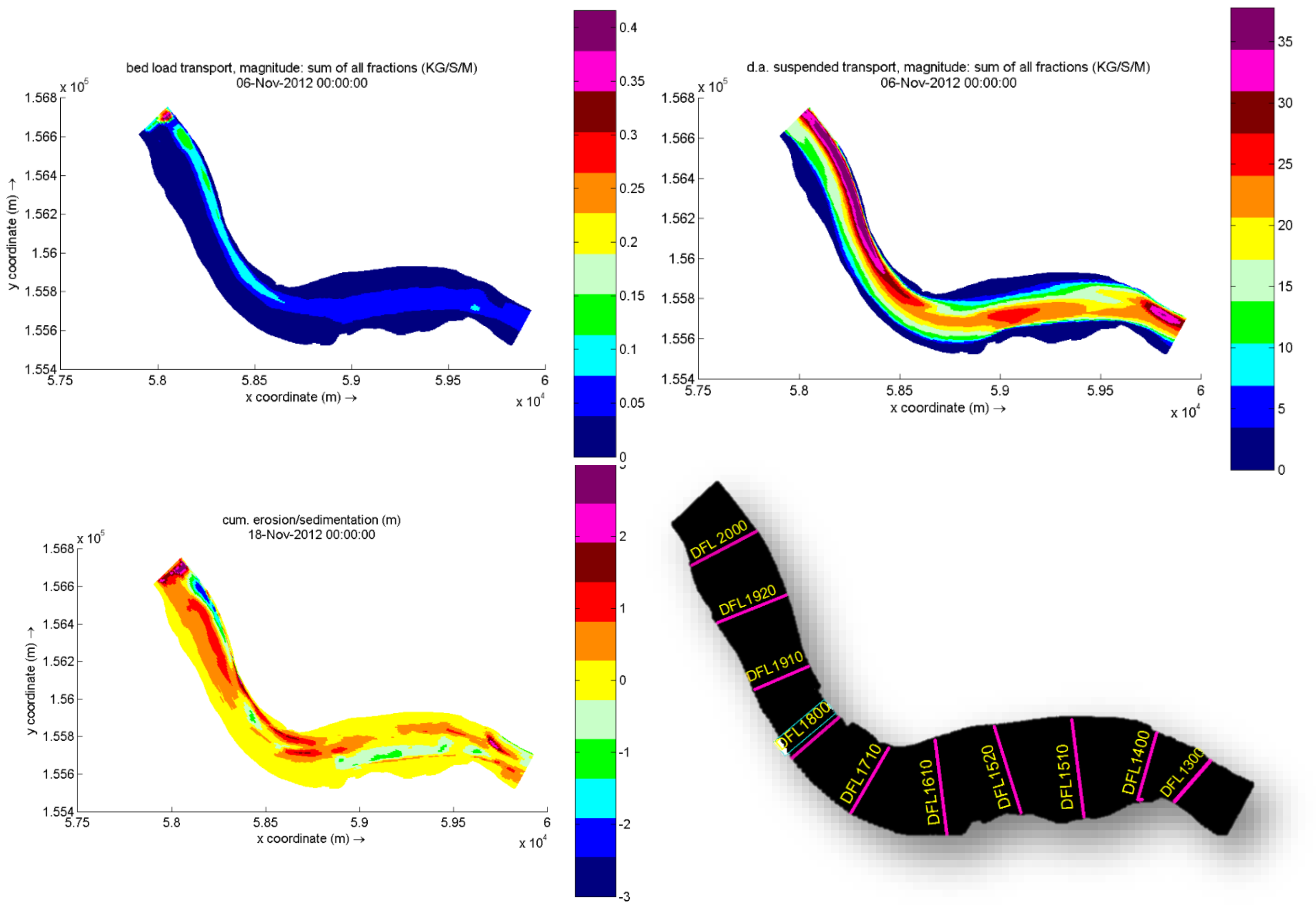

Figure (6.8b) 3D simulation (10 layers and k-ε turbulence model) for 14 days on Setup #1 model

6.2.5. Grain size analysis

Bed composition and grain size distribution are both important parameters that control morphological change. However, due to the absence of this information, a sensitivity analysis was essential to determine which particle size result is compatible with the observation data. All the previous results demonstrate that by having bed-load sand grains the observed erosion at outer bend and left side of downstream section (DFL1300 & DFL1400) are not estimated despite changes in the slope formula and transport formula. This result may be because of shear strength of the fraction that balance source and sink produced deposition instead of erosion. This may suggest that smaller grain sizes are present in those locations. Based on the 2012 cross-section morphology surveys, previous model sensitivity results, and following the pattern of deep locations, a spatial distribution of bed-material grain size was implemented. Comparing the bathymetry survey of 2014 and the post-flood cross-section survey of 2012, not much difference was detected (Figure 4.4-a, 4.4-b). Consequently, it was assumed that the 2014 side-scan bathymetry survey is sufficiently representative of the post-flood 2012 bathymetry. Following the deep water path in the 2014 bathymetry, fine grain sizes (0.039mm) were designated for the right side of cross-section DFL1710 and the left side of DFL 1400 and DFL 1300, as shown in Figure (6.9). In addition, at the right side of DFL1910 and DFL1920, this grain size was also assigned. Although this area is not as deep as the other regions, this improved prediction of the erosion at this location. The rest of the model domain consisted of sand particles following the grain size distribution in Setup #1. Figure (6.9) shows the distribution at the top layer (active layer) with a thickness of 4m. The base layer composition has not changed. With the only change in bed fraction this setup will be referred to as Setup-A.

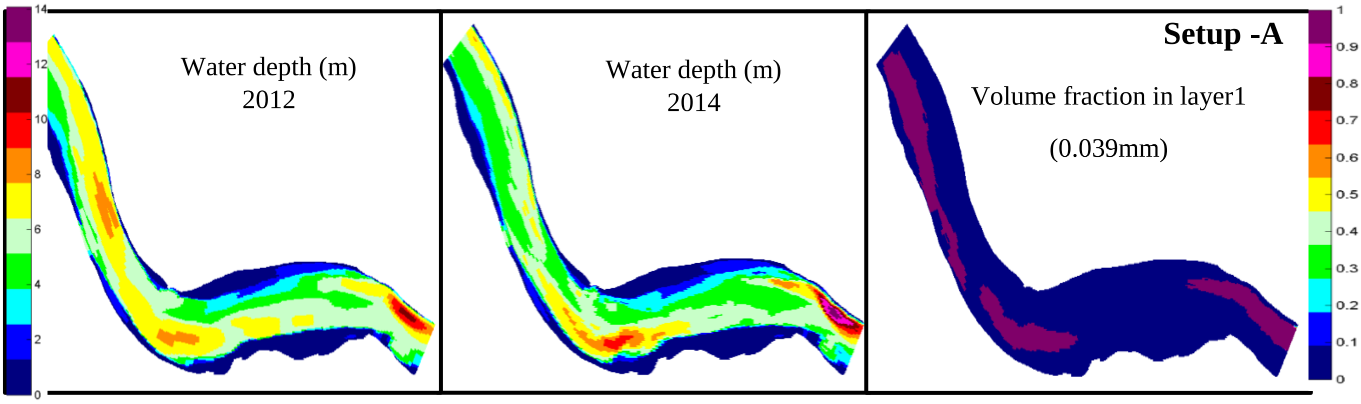

Figure (6.9) Water depth for 2012 (pre-flooding - 1st August) and 2014 surveys and sediment 29-volume fraction in in active layer

Table (6.9) Different setups for simulation analysis

Setup Name	**What changed in Setup#1**
Setup-A	Applying spatial grain size in active layer as shown in (Fig 6.9)
Setup-B	Depend on Setup-A, and Morfac changed to (2)
Setup-C	10% of sediment-29 (0.039mm) added to blue are of Setup-A in figure(6.9)
Setup-D	Depend on Setup-C, and Morfac changed to (2)
Setup-E	Depend on Setup-A, with applying equilibrium condition at boundary for sand fraction (EqmBc=true)
Setup-F	Depend on Setup-A with change in critical shear stress of deposition
Setup-G	Depend on Setup-A with change in critical shear stress of erosion
Setup-H	Depend on Setup-G with change in critical shear stress of deposition
Setup-I1	Depend on Setup-A, with horizontal diffusion coefficient equal to (0.2 m^2/s)
Setup-I2	Depend on Setup-A, with horizontal diffusion coefficient equal to ($1m^2/s$)
Setup-J	Depend on Setup-I1
Setup-K	Depend on Setup-I1, with Bed=10 during 1st November-3rd - December, 2012 simulation
Setup-L	Depend on Setup-I, with applying Morfac time series
Setup-M	Depend on Setup-K with applying Morfac time series

Figure (6.10-a_1) shows the results of the 14-day simulation for (Setup-A). As can be seen, erosion estimated at the location that erosion observed in the field. However, the amounts of deposition and erosion in the reach were still not equivalent to those of the field observations (Figure 4.4b). Therefore, another simulation was conducted for (Setup-B), and in this setup, the Morfac parameter was changed to (2) (Figure 6.10, a_2). The morphological factor has a huge role in changing morphology, and has an influence on transport rate for bed load as well as on the erosion-deposition flux for suspended load.

Overall erosion and deposition increased with the morphological factor equal to two. For instance, looking at the change in cumulative erosion and deposition at the left side of cross-section DFL1300 during the 14 days (Figure 6.10, a_3 and a_4), in the first flood period (5^{th}-6^{th} Nov), erosion was estimated to be 0.2m and 0.4m for morphological factors 1 and 2 respectively. The cumulative erosion and deposition gradually increased until the second flood (flushing period, 12^{th}-13^{th} Nov), in which the bed scoured by 0.5m and 0.75m respectively. Looking at the sedimentation in the middle of the section, it can be seen that deposition only occurred during the two flood periods. Furthermore, it is clear from (Fig. 6.10, a_4) that the morphological factor has a large influence on the direction of sand deposition. This effect can be seen more clearly after the second flushing. The width of the hole on channel left decreased with the morphological factor equal to 2. This probably occurred because of increasing sediment erosion on the right side of the channel and subsequent transport toward the left side of the river.

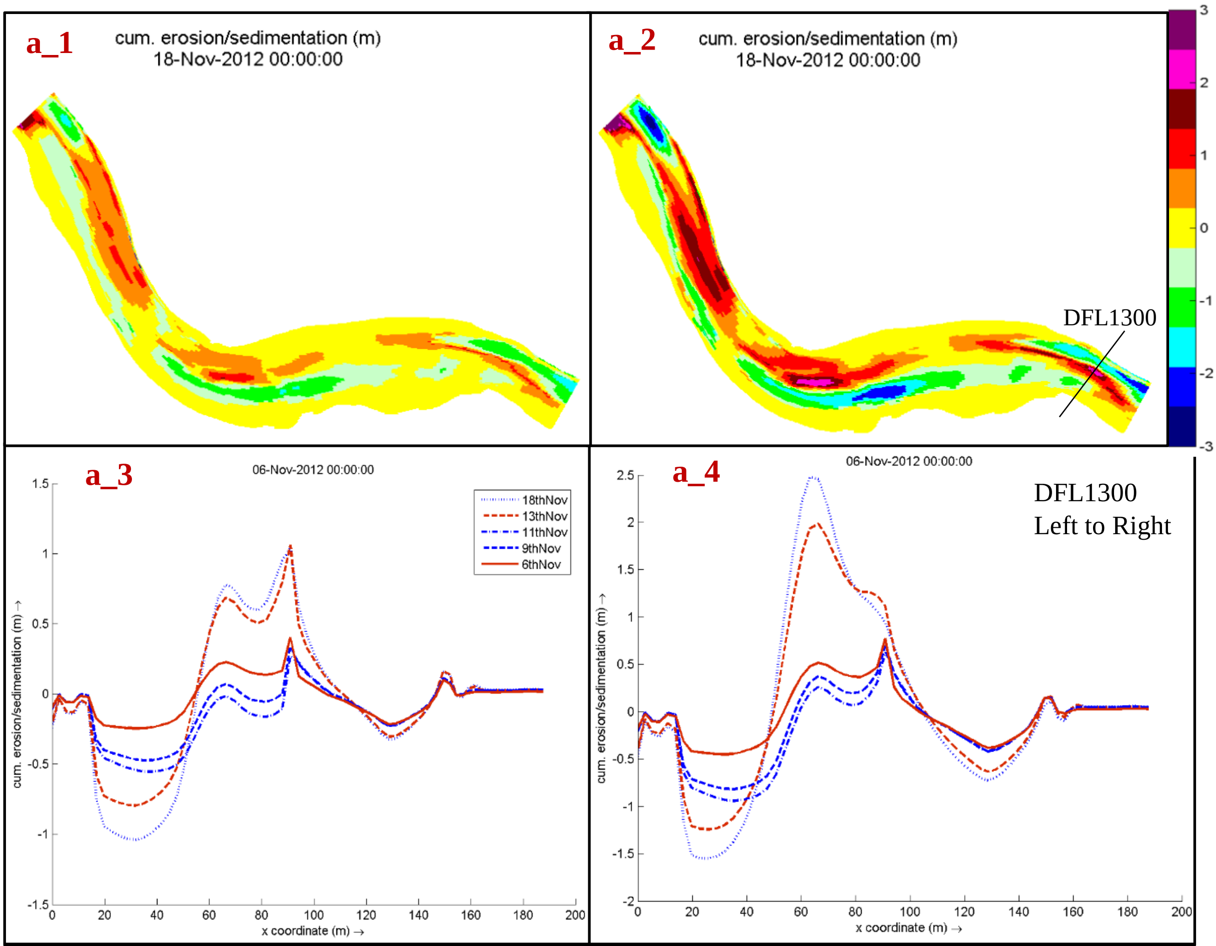

0% mud by mass in blue area of figure (6.9), Morfac=1	0% mud by mass in blue area of figure (6.9), Morfac=2

Figure (6.10) Cumulative erosion and deposition results at the end of flood period (14 days). a_1) simulation of Setup-A, a_2) simulation for Setup-B, a_3) DFL1300 cross-section of Setup-A, a_4) DFL1300 cross-section of Setup-B.

Sensitivity analysis was also performed on the percentage of fine particles in the blue area in Figure (6.9). For this analysis, 10% by mass of (0.039mm) was added to the blue area. All other conditions remained the same as in Setup-A. This setup will be referred to as Setup-C. The results are shown in Fig. 6.11.

First, similar to the previous setup, the rates of erosion and deposition increased with the morphological factor (Figure 6.11, a_2). In addition, comparison of (Fig. 6.11, a_3 and a_4) for bed level changes in the middle of cross-section DFL1300 demonstrates that at first all the silt particles will be eroded. Once only sand remains, sediment begins to deposit. This can be seen clearly when the morphological factor is equal to two.

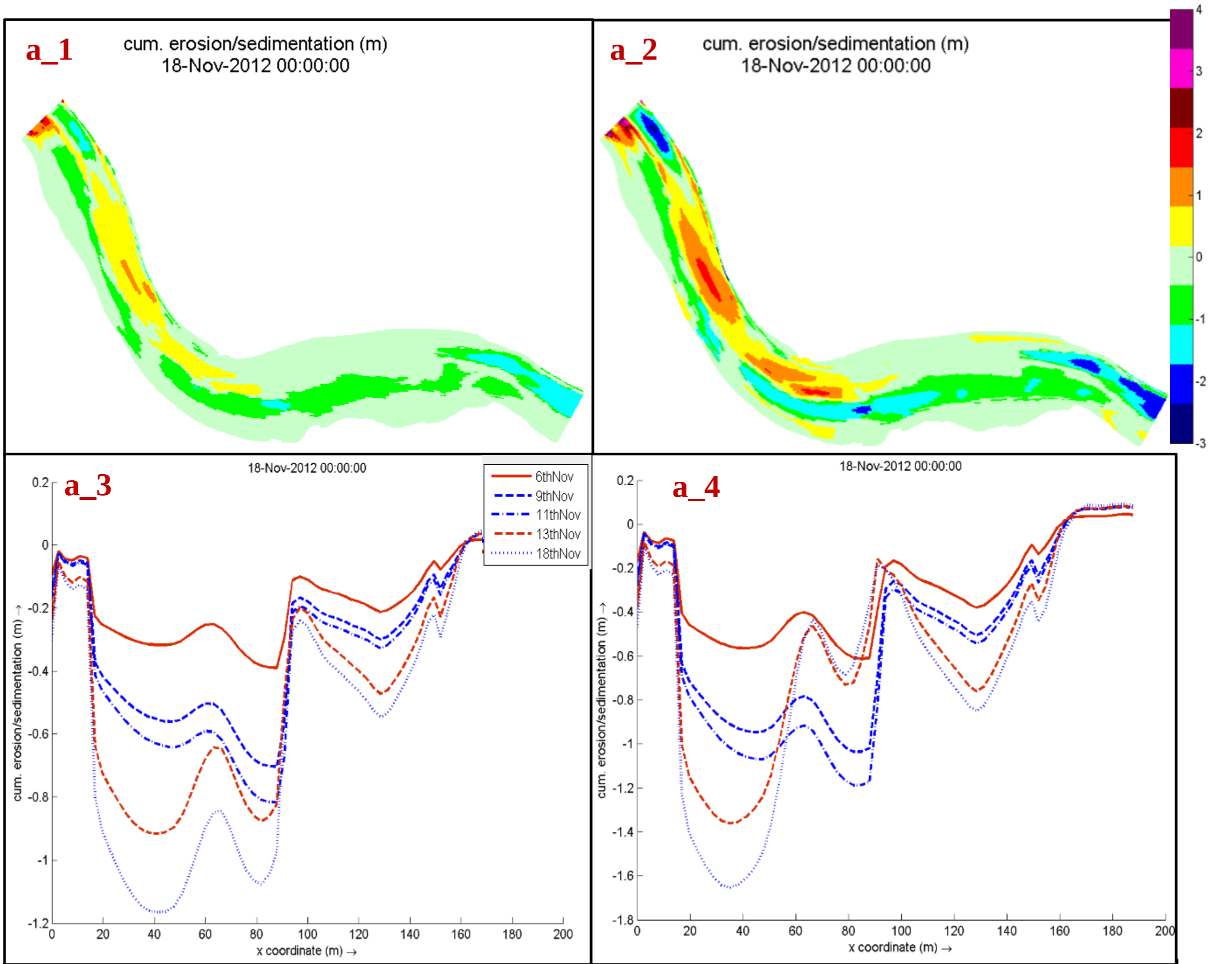

10% mud by mass in blue area of figure (6.9), Morfac=1	10% mud by mass in blue area of figure (6.9), Morfac=2

Figure (6.11) Cumulative erosion and deposition results at the end of flood period (14 days). a_1) simulation of Setup-C, a_2) simulation for Setup-D, a_3) DFL1300 cross-section of Setup-C, a_4) DFL1300 cross-section of Setup-D.

6.2.6. Equilibrium vs Non-equilibrium concentration of non-cohesive sediment at inlet

Prescribing an equilibrium concentration of non-cohesive sediment at the upstream open boundary produced more erosion and less deposition (Figure 6.12, a_2) compared to a non-equilibrium concentration prescription (Figure. 6.12, a_1). For instance, at the bend, deposition extended all the way to the middle of the bend in the non-equilibrium simulation, whereas in the equilibrium simulation there was a gap in deposition between the inner bend and the channel center. Equilibrium sediment concentrations differed between the two simulations, as demonstrated for an observation point at the upstream left side (Figure 6.12, a_3). This dissimilarity is much higher during flood periods, especially in the second flood period. Furthermore, applying the non-equilibrium condition leads to sand accumulation at the inlet of the model, which has a tremendous influence on the model's stability, especially if it is applied with a morphological factor greater than one.

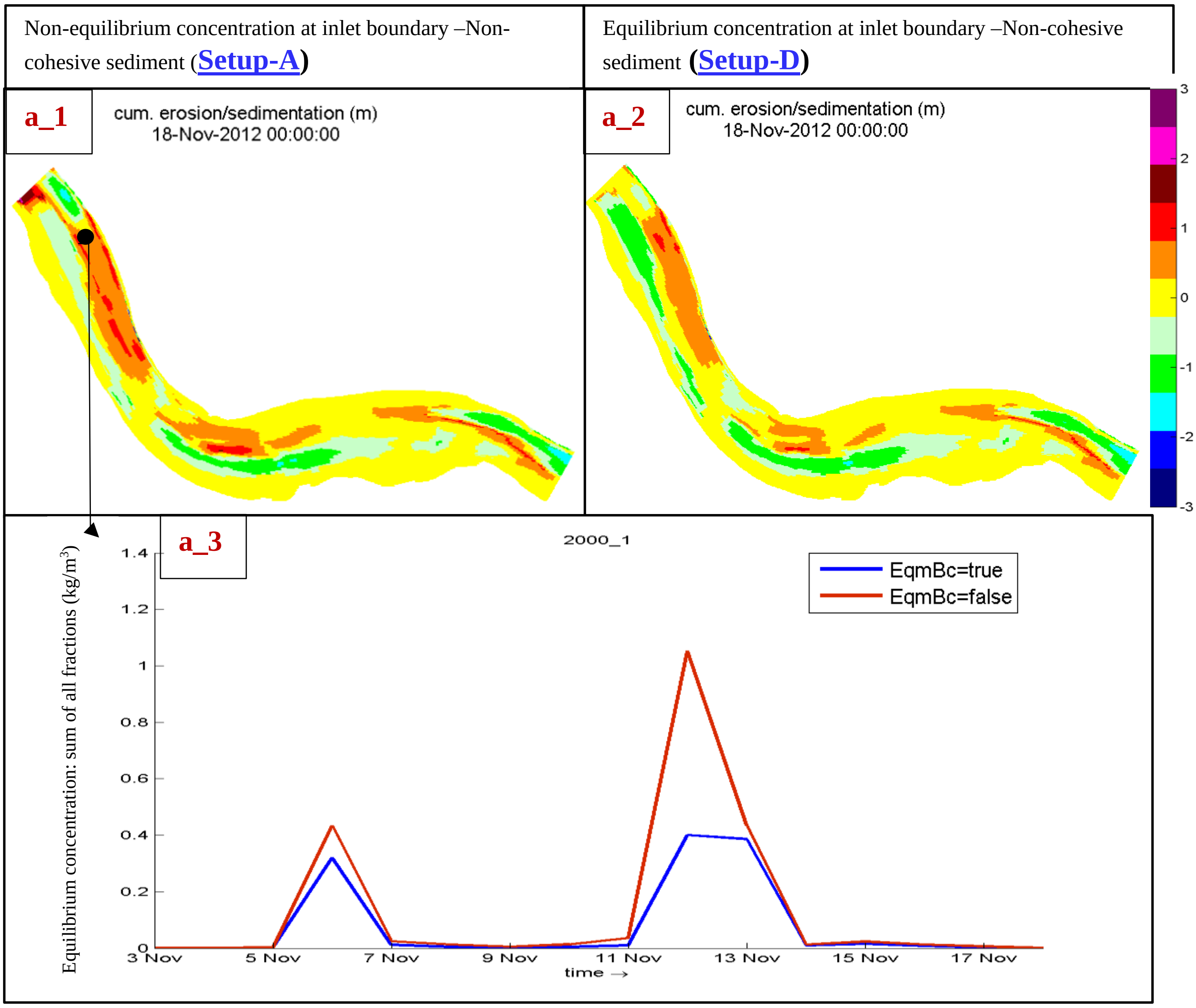

Figure (6.12) Cumulative erosion and deposition results for the 14-day period). a_1) Applying non-equilibrium concentration of sand fraction at boundary inlet, a_2) Applying equilibrium concentration of sand fraction at boundary inlet, a_3) Equilibrium concentration of summation of all fraction at the observation point at the left side of cross-section DFL2000

6.2.7 Critical Shear Stress of Erosion and Deposition

Setup-A

τ_e (N/m^2)

Sediment29	Sediment34	Sediment22
0.1	0.065	0.03

τ_d (N/m^2)

Sediment29	Sediment34	Sediment22
0.09	0.05	0.02

Setup-F

τ_e (N/m^2)

Sediment29	Sediment34	Sediment22
0.1	0.065	0.03

τ_d (N/m^2)

Sediment29	Sediment34	Sediment22
800	600	400

Setup-G

τ_e (N/m^2)

Sediment29	Sediment34	Sediment22
0.5	0.1	0.03

τ_d (N/m^2)

Sediment29	Sediment34	Sediment22
0.4	0.05	0.02

Setup-H

τ_e (N/m^2)

Sediment29	Sediment34	Sediment22
0.5	0.1	0.03

τ_d (N/m^2)

Sediment29	Sediment34	Sediment22
800	600	400

Figure (6.13) Different values for critical shear stress of erosion and deposition

As has been mentioned before, the critical shear stress of erosion was obtained from the Van Rijn curve, and the critical shear stress of deposition was given a value less than the critical shear stress of erosion. However, until now, there has been a debate on whether the deposition of cohesive sediment is governed by the critical shear stress of deposition or if it is controlled only by concentration and settling velocity. Therefore, this analysis has been conducted, and some different setups are shown in (Figure 6.13).

The results show that the critical shear stress of erosion plays a major role in sediment deposition, whereas the critical shear stress of deposition does not have any influence on sediment deposition in the main reach. For example, looking at the first and second columns in (Figure 6.14, Setup-F and Setup-A), it can be seen that when the critical shear stress of erosion is low, nor fraction (0.039mm), (Figure6.14, f_1, a_1), or (0.019mm), (Figure 6.14, f_2, a_2) has deposited in the main channel. However, in column three (Setup-H) and column four (Setup-G), both cohesive sediment have deposited and with almost the same amount, despite the difference in the critical shear stress of deposition (Figure 6.14, h_1, g_1, h_2 and g_2). The only place the critical shear stress of deposition has an influence is in the circulation zone at the downstream right side (DFL1300). This can be seen clearly in (Figure 6.14, f_3 and a_3). This will be discussed further in the Discussion section.

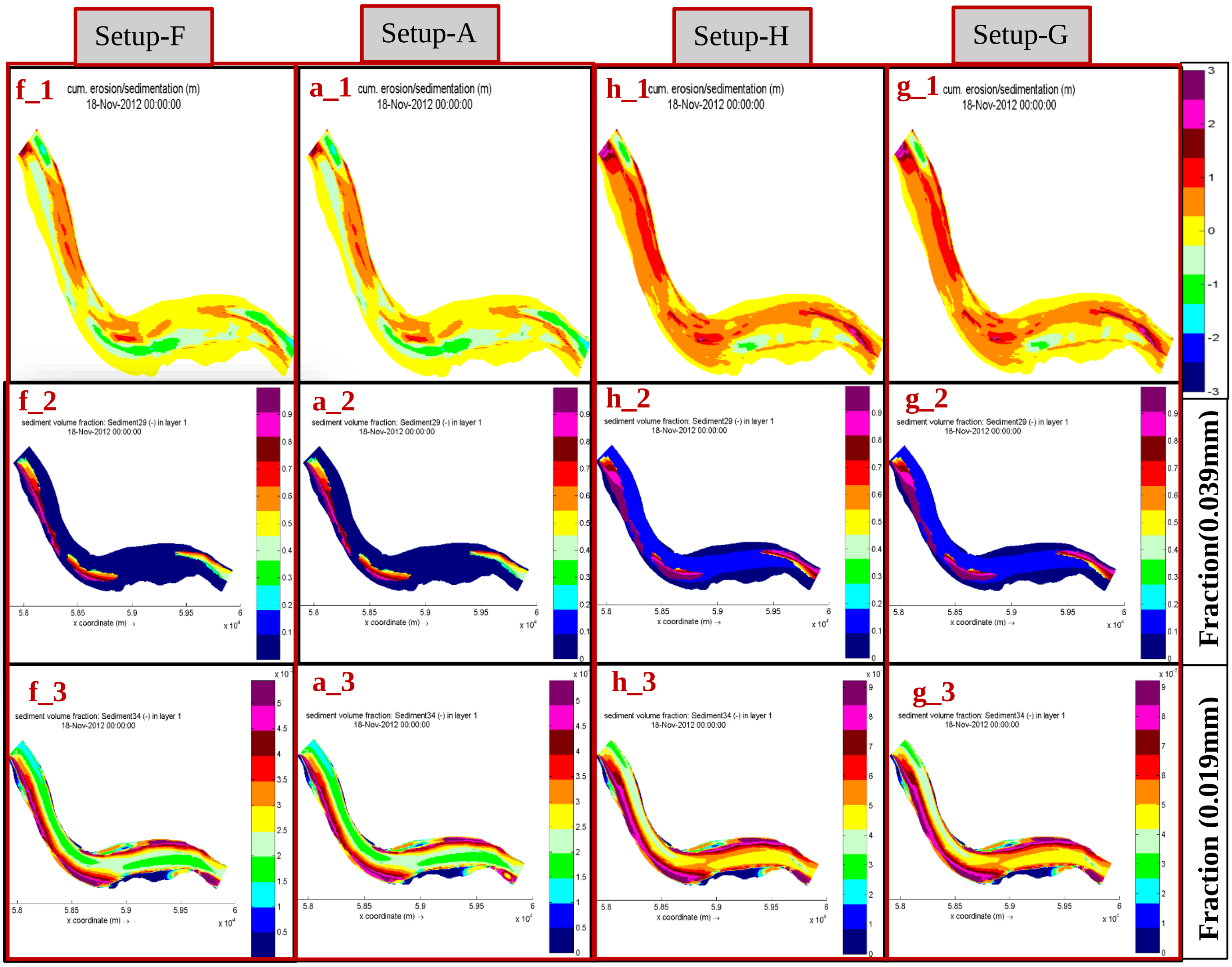

Figure (6.14) Critical shear stress of erosion and deposition analysis results. f_1, a_1, h_1, g_1) cumulative erosion and deposition of the 14-day simulation with different setups, f_2, a_2, h_2, g_2) Sediment volume fraction (0.039mm) in the active layer, f_3, a_3, h_3, g_2) Sediment volume fraction (0.019mm) in the active layer.

6.2.8 Horizontal eddy diffusivity

Because of the high percentage of suspended sediment, it was crucial to evaluate sensitivity to the horizontal eddy diffusion coefficient. As has been mentioned before, when the secondary flow model correction is included in a 2D model, the diffusion coefficient will influence both advection and diffusion. However, if the correction is excluded, the diffusion coefficient will only influence the diffusion. This coefficient is probably more dominant during normal periods compared to flood periods. This means that it may have more influence on the deposition locations of suspended sediment. To examine this different diffusion coefficient inspected (Setup-A, SetupI1, and Setup-I2). This analysis examines the path of suspended sediment fraction (0.019mm), its concentration across the river, and the erosion and deposition results.

As can be seen in Figure (6.15), although not much difference can be observed in the suspended sediment transport rate, the suspended sediment concentration and erosion-deposition in the whole reach changed slightly with the different model runs. Increasing the horizontal-eddy diffusion coefficient leads to the dispersion of sediment equally across the river (Figure 6.15, a_1, b_1, c_1). This result is expected based on the advection-diffusion equation (Eq. 3.12). In addition, if we compare the results when the coefficient is equal to one (Figure 6.15, a_2, b_2, c_2), it can be seen that the rate of suspended sediment is slightly higher, especially at the upstream left side of the river (DFL 1910 and DFL 1920). Furthermore, it can be seen that the pattern of erosion deposition changed depending on this coefficient (Figure 6.15, a_3, b_3, c_3). For instance, when the diffusion coefficient was equal to one, at the upstream left side of the river (DFL 1910 and DFL 1920) there was a gap in deposition and the sediment is mostly deposited at the boundary, whereas in the other cases (Figure 6.15, a_3 and b_3) continuous deposition was predicted. This may have happened due to the dominance of diffusion versus advection, leading to decreasing concentration in that zone. On the other hand, more erosion at a concave bend is estimated by the diffusion coefficients (0.001 and 0.2) compared to (diffusion=1).

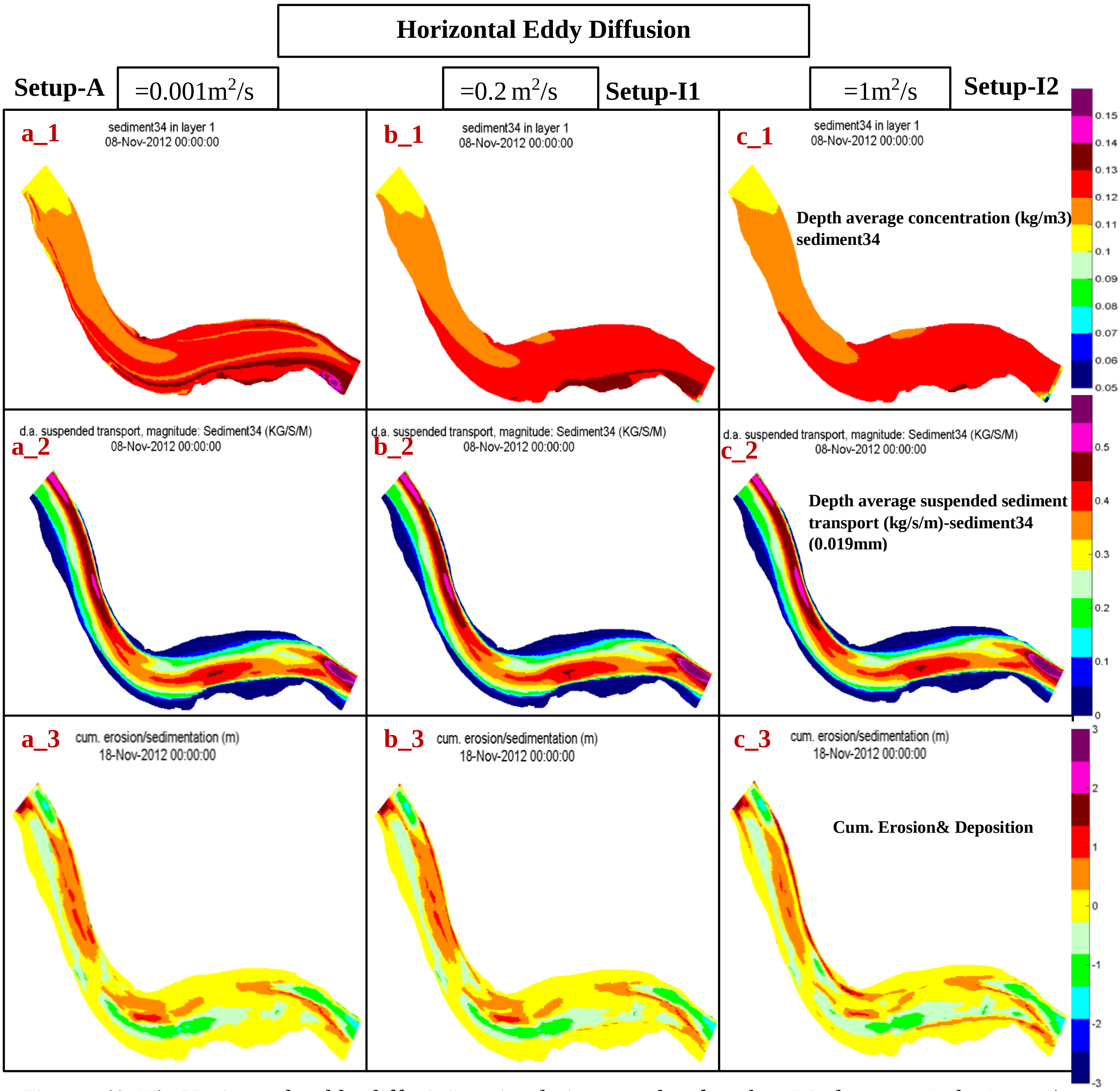

Figure (6.15) Horizontal eddy-diffusivity simulation results for the 14 days. a_1, b_1, c_1) sediment 34 concentration (kg/m3) for eddy diffusion (0.001, 0.2 and 1 m^2/s), a_2, b_2, c_2) Depth-averaged suspended sediment transport for eddy diffusion (0.001, 0.2 and 1 m^2/s), a_3, b_3, c_3) Cumulative erosion deposition (m) for eddy diffusion (0.001, 0.2 and 1 m^2/s)

6.2.9. Long-term simulation

All the previous simulations were conducted for 14 days during the flood season for calibration and analysis; however, the morphology surveys were conducted in August and December 2012. Therefore, it was essential to calibrate the exact bed-level change model for this period, although the bed level does not change much during August to November. The first simulation of this period was conducted using Setup-J (see Table 6.9), as this was deemed to be the best model parameterization for the 14-day period analyzed during the model sensitivity analysis. At the beginning, the cold-start simulation was carried out from 1st August to 1st October 2012. In this period, both morphological factor (Morfac) and (Bed) parameters were equal to one. Based on the results, which included both changes in bed level and bed composition, the second simulation, from October to November, and third simulation from November to December, were carried out. The entire simulation was then repeated using the preferred parameter values for the Morfac and Bed parameters. Sensitivity to the Morfac factor was explained in Section 6.2.5. The Bed parameter works as a calibration factor for the bed load transport equation, with the calculated bed load transport multiplied by the Bed factor. For example, if the bed transport rate is equal to 0.02kg/m/s, it will be changed to 0.2kgm/s. Kasvi et al. (2015) calibrated their model by reducing Bed from 1 to 0.7 to match the bed-load transport rate measured in the field. Figure (6.16) shows the results of four different simulations. In the first column of each cross-section, during the entire four-month simulation the Morfac and Bed factors were equal to one (Table 6.9, Setup-J). The second column shows a simulation with the same model parameterization except that a time series Morfac factor is applied (Table 6.9, Setup-L), as shown in Figure (6.16, K). In the third column model setup, the Bed parameter was changed to 10 for the period November to December, while the other parameters remained as in the first column setup (Table 6.9, Setup-K). In the fourth column (Table 6.9, Setup-M), both Bed=10 and the Morfac time series were applied. In the last column, the observation data are shown. Although the bed-load transport rate was not measured, the predicted versus observed bed morphology at the end of the simulation period can be used to evaluate the reliability of the morphodynamic model. It is clear from the results that a change in morphology is not estimated without changing the Bed parameter. In addition, the morphological factor plays an important role in estimating the change that occurs in the bed during the flood period. Both parameters together increase the deposition rate in the whole reach. In other words, the model results in the fourth column show that most of the deposition was estimated because of transporting the bed load from upstream. For instance, in the third simulation (Setup-K), deposition can be seen at the left side of both cross-sections (DFL1920, Figure 6.16, (I_3) and DFL2000, Figure 6.16, (J_3)); however, in the fourth simulation (Setup-M), the deposition in DFL2000, (Figure 6.16 (J_4)) decreased in and passed to downstream of section DFL1920 (Figure 6.16, (I_4)). To some extent, it can be said that this interpretation is correct because during this season the flushing period occurred, which means that the water level downstream decreased. It has been seen that all the deposition occurred during the second flood period when the water level downstream dropped by 1.5m.

Due to the absence of cross-section morphology data, the comparison between the model and observation data can be done only by visualization without finding any error percentage.
It can be seen that for some parts of the sections, the model results are not compatible with the field observations. For instance, in the middle of cross-section DFL1300 (Figure 6.16, a_4), deposition was observed in the field, and this deposition by the model result of fourth column is slightly lower. This underestimation in deposition occurred also at the left side of DFL1610 (Figure 6.16, e_4) and at the middle of DFL1510 (Figure 6.16, c_4). However, the deposition estimation at the left side of DFL 1910 (Figure 6.16, h_4) and DFL1920 (Figure 6.16, I_4) is almost compatible with the field observations. Furthermore, in general the erosion zones identified in all cross-sections are quite well matched with the observation data.

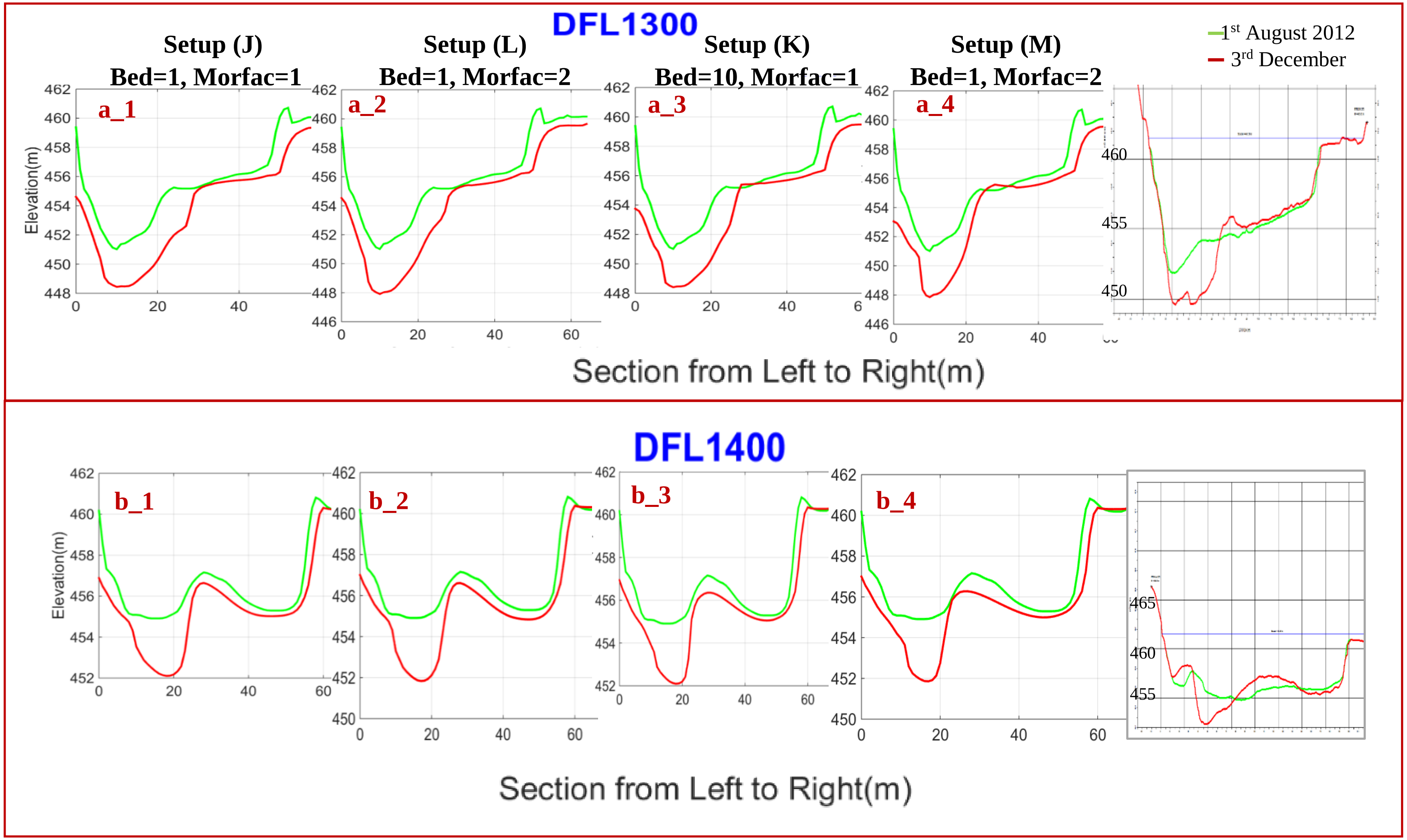
DFL1300
Setup (J)
Bed=1, Morfac=1
Setup (L)
Bed=1, Morfac=2
Setup (K)
Bed=10, Morfac=1
Setup (M)
Bed=1, Morfac=2
1st August 2012
3rd December
a_1
a_2
a_3
a_4
Elevation(m)
Section from Left to Right(m)
DFL1400
b_1
b_2
b_3
b_4
Elevation(m)
Section from Left to Right(m)

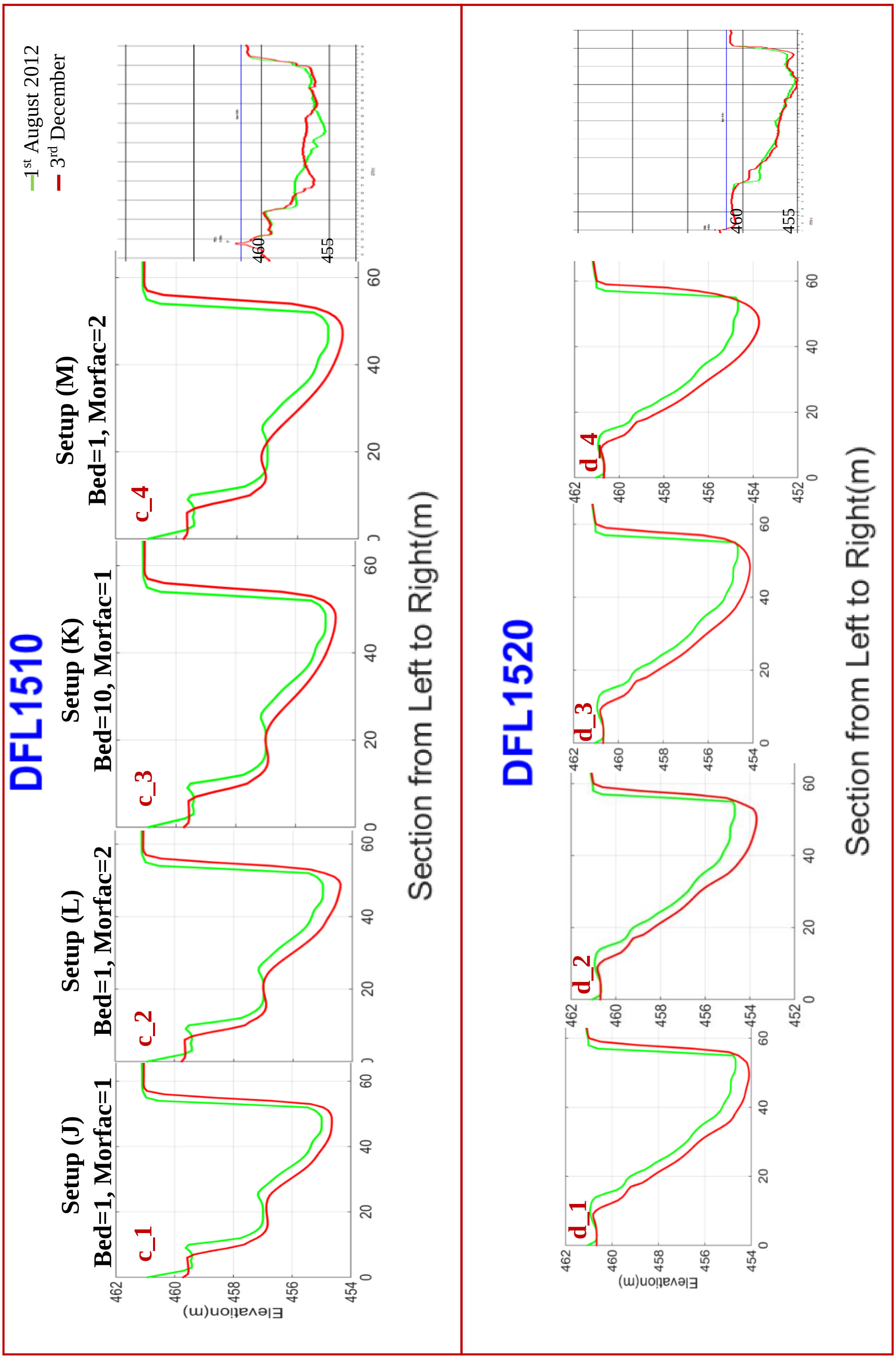
DFL1510
Setup (J)
Bed=1, Morfac=1
Setup (L)
Bed=1, Morfac=2
Setup (K)
Bed=10, Morfac=1
Setup (M)
Bed=1, Morfac=2
c_1
c_2
c_3
c_4
1st August 2012
3rd December
Elevation(m)
Section from Left to Right(m)
DFL1520
d_1
d_2
d_3
d_4
Elevation(m)
Section from Left to Right(m)

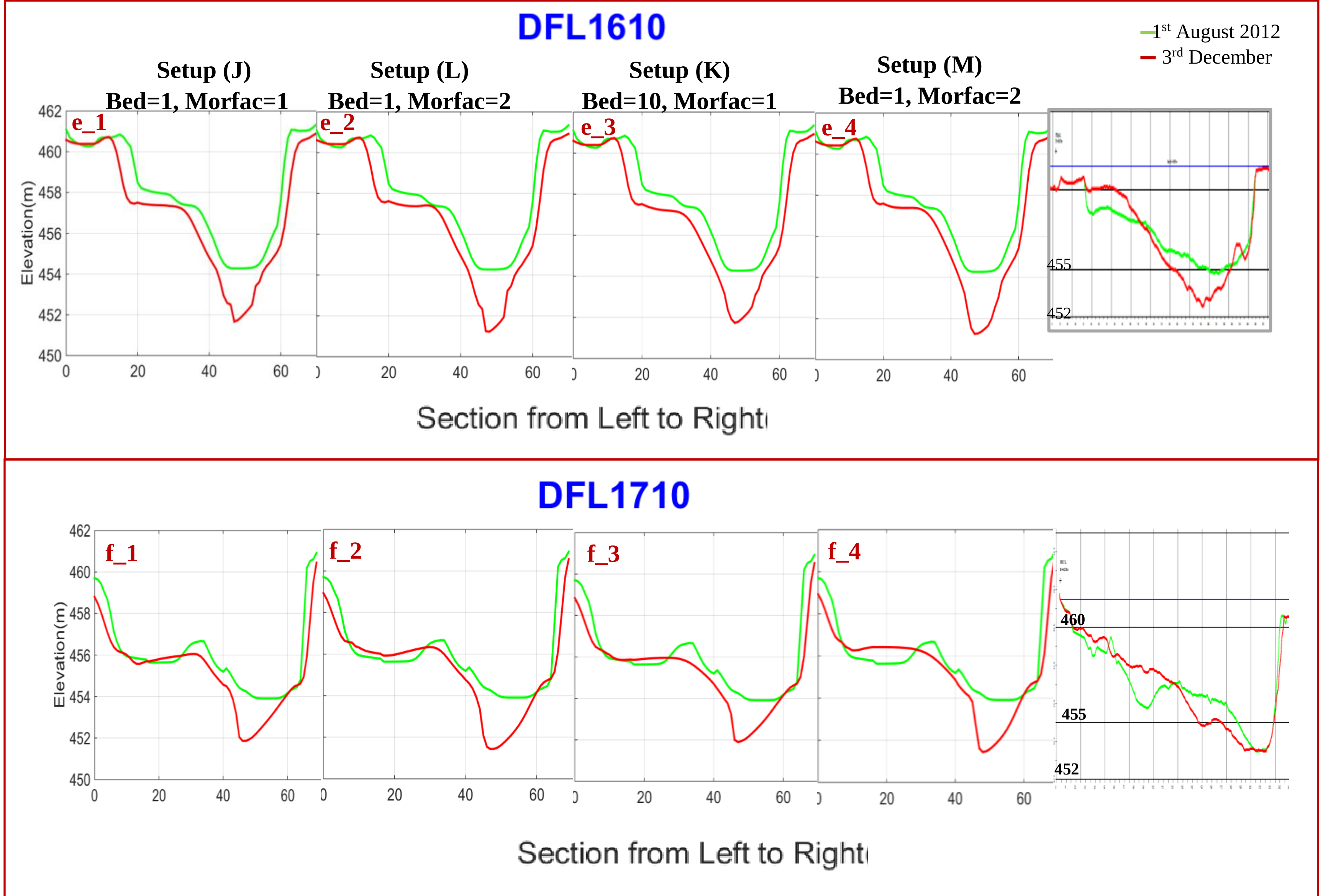
DFL1610
1st August 2012
3rd December
Setup (J)
Bed=1, Morfac=1
Setup (L)
Bed=1, Morfac=2
Setup (K)
Bed=10, Morfac=1
Setup (M)
Bed=1, Morfac=2
e_1
e_2
e_3
e_4
Elevation(m)
462
460
458
456
454
452
450
0
20
40
60
455
452
Section from Left to Right
DFL1710
f_1
f_2
f_3
f_4
460
455
452
Section from Left to Right

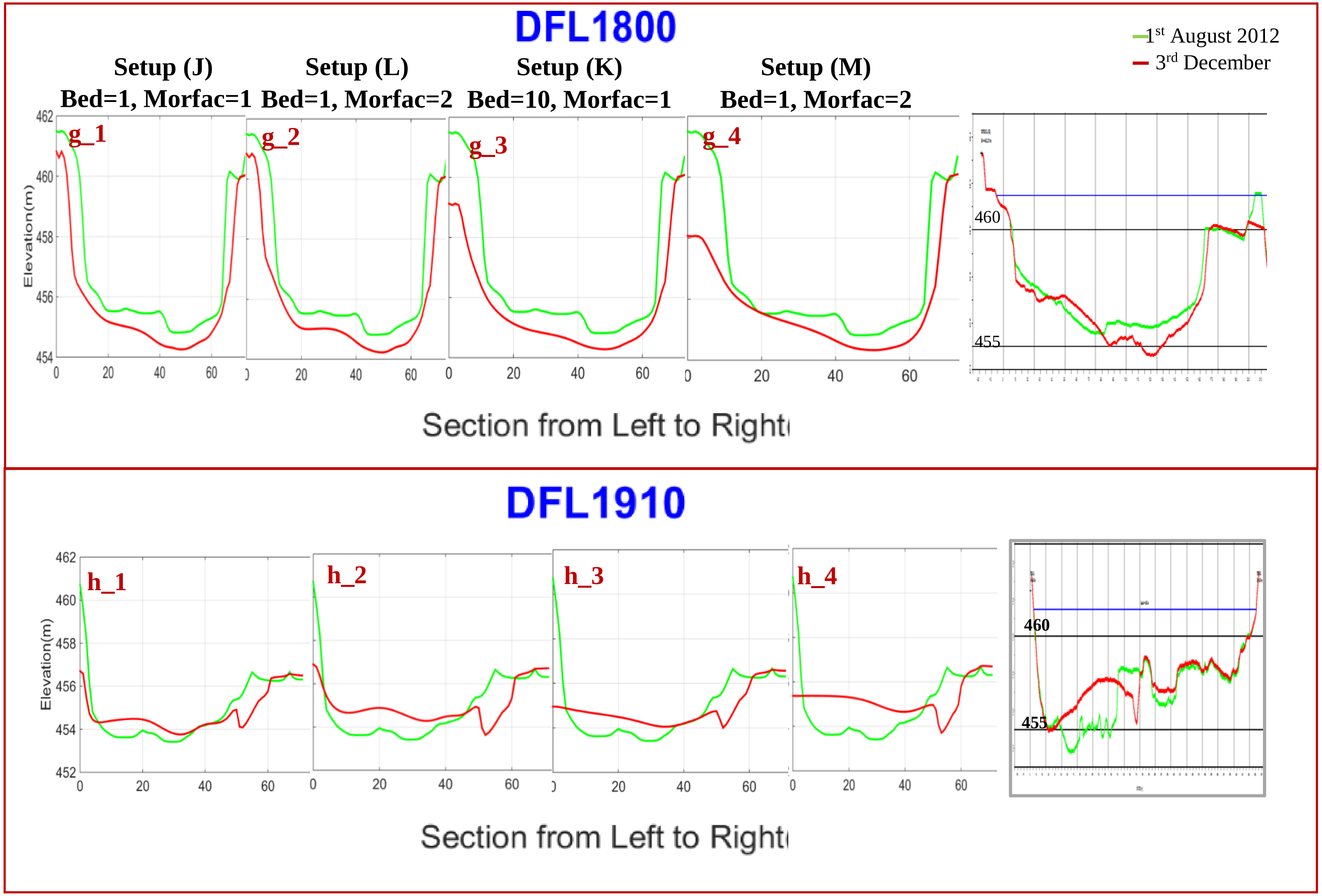

DFL1800
1st August 2012
3rd December
Setup (J)
Bed=1, Morfac=1
Setup (L)
Bed=1, Morfac=2
Setup (K)
Bed=10, Morfac=1
Setup (M)
Bed=1, Morfac=2
g_1
g_2
g_3
g_4
Elevation(m)
462
460
458
456
454
0
20
40
60
460
455
Section from Left to Right
DFL1910
h_1
h_2
h_3
h_4
Elevation(m)
462
460
458
456
454
452
0
20
40
60
460
455
Section from Left to Right

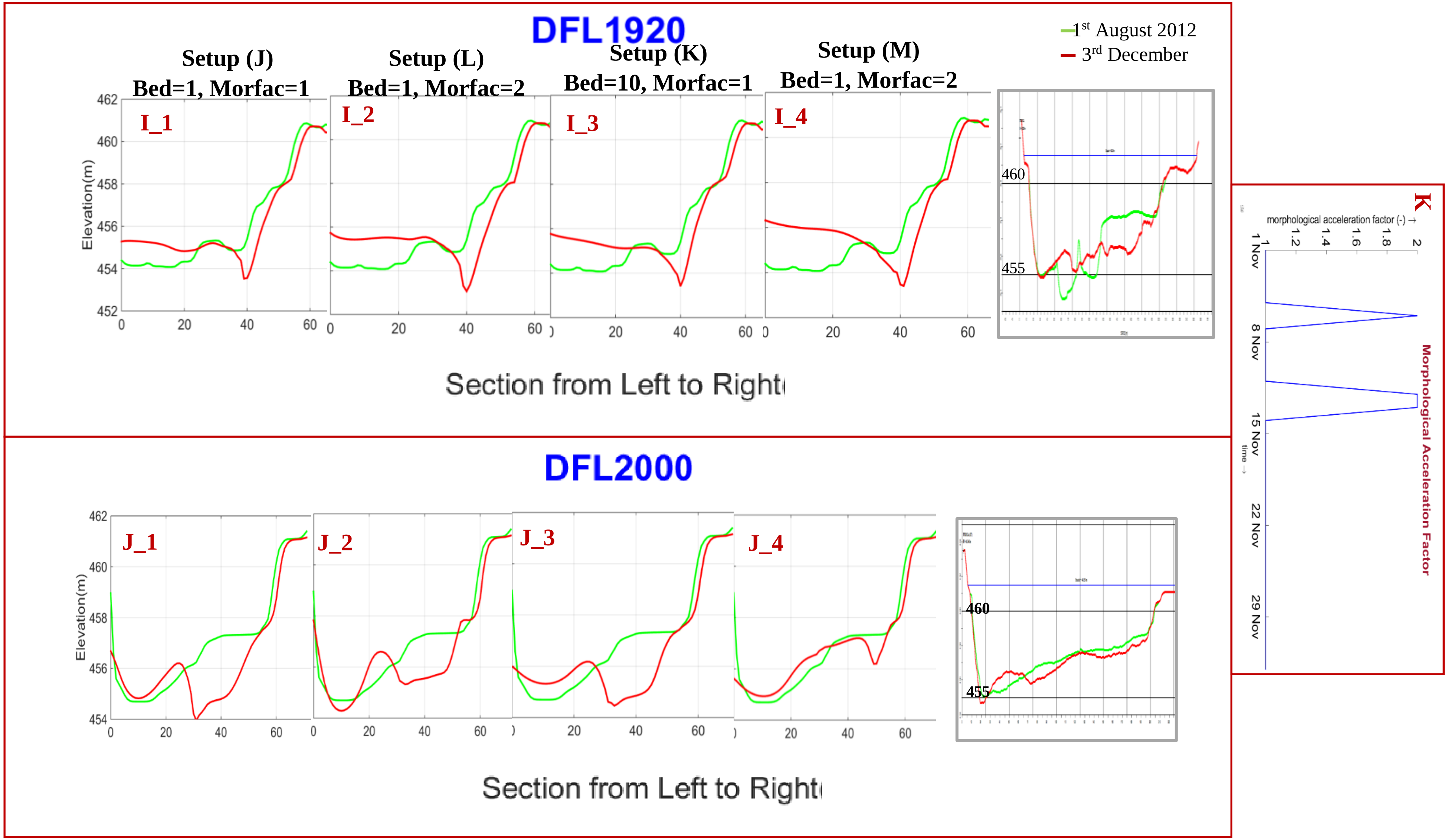

Figure (6.16) Cross section model result and field observation data (far right subplot) sorted from out let of the model to the upstream inlet of the river (a-j), as well as time series morphological factor (K)

6.3 Discussion

In contrast to Kasvi et. al. (2015-b) and in agreement with Nicholas (2003), inclusion of the secondary model flow in the 2D model decreased model estimation. This may have occurred due to the radius of curvature, which has an influence on the velocity profile across a river bend.

The prediction of bed load and suspended load by both Van Rijn models (1984 and 1993) were almost the same when the reference height of the 1984 model was 0.01m. Despite a large difference in the near-bed reference concentrations, the predicted suspended sediment transport rates were almost the same in both equations. According to Van Rijn (2007) study on multiple rivers and flumes, the near-bed concentration is estimated to be in the range 0.5-50kg/m^3 for depth-averaged velocity, reference height, and particle size of 2.5m/s, 0.1, and 8-200µm respectively. This range of values is more compatible with Van Rijn's (1993) results.

The two slope formulae that were applied in this model sensitivity analysis were developed based on different concepts. The Bagnold formula accounts only for bed load transport. In this approach, the bed load transport is dominated by gravity, and it gives only a minor role to turbulence on bed load trajectory (Van Rijn, 1987). In contrast, the Koch formula was developed for meandering rivers with the presence of suspended sediment. This formula places emphasis on the influence of spiral flow and bed slope in determining the direction of bed load transport (Talmon et al., 1995). The sensitivity analysis demonstrated that although only a slight change could be detected between the slope formulae results when the bed load transport is low, the results of the Koch formula are more representative of what happens in reality when the bed load increases. We can compare this with other Delft3D morphodynamic meandering river models. Kasvi et al. (2015-a) applied only the default formula (Bagnold formula), and suspended load was not dominant in his model. However, he decreased the transverse slope coefficient (AlfaBn) to zero to reduce pool filling at the bend. To some extent, we obtained similar results at the left side of the downstream hole; some scour was estimated, but no erosion was produced at the outer bend. In addition, it produced erosion upstream, which is not representative of the field observations.

Similar to Kasvi et al. (2015-a; 2015-b), in this study the Delft3D model required a spatially distributed bed material grain size to predict morphological changes along the river. The morphology prediction became higher when small grain size are applied in the outer bend and on downstream areas with higher depth. Kasvi et al. (2015-b) conducted a study on multiple meandering rivers, and made extensive measurements of the sediment size distribution in the bend zone. They found that in most meandering rivers, larger grain sizes are located at the point bars. They explained that only during flooding does most deposition occur in the inner bed, which was due to high bed load transport compared to suspended load transport. The predicted bed load transport, suspended transport, and deposition time series at the point bar in this study are compatible with the observations of (Kasvi et al., 2015) in meandering rivers. To some point, this may prove our hypothesis that finer sediment is located at the outer bank.

This study shows that the critical shear stress of deposition only has an influence when the velocity is low or negative. This result is obtained from (Equation 3.17). This result is compatible with Maa's (2008) study in which the critical shear stress of deposition was only dominant in the circulation zone with low bed shear stress. This means that Winterwerp's (2007) study, which suggested that deposition of sediment is only controlled by concentration and settling velocity, is only valid when the flow rate is high. In addition, Yuanita's (2008) study on modeling sediment transport in an estuary showed that an increase in critical shear stress of erosion resulted in increasing deposition. Similar results are found in the present study (Section 6.2.7).

7. Estimating Sediment Transport for 1 Year

The morphodynamic of the study reach was evaluated over a one-year simulation, between August 2012 and August 2013. The model setup and results for the period between August and December 2012 were presented in Section 6.2.9. Based on these results, two hot-start simulations were conducted in series. First, a simulation was done between December2012 and April 2013, with a second simulation between April 2013 and August 2013. For each simulation, only the boundary condition changed depending on the collected data shown in Section 4.2.1.

7.1 Bed load transport

In the model, to obtain the bed load transport that enters and leaves, two cross-sections were put laterally across the river, one after the inlet and one before the outlet. In these cross-sections, the accumulated bed load transport was recorded during the simulation.

In Figure (7.1), which shows the bed load transport for three non-cohesive fractions at the inlet and outlet, monthly results represent the accumulated sediment transport for each month. For example, (1-September-12) represents the accumulated sediment transport from 1st August to 1st September. At the inlet, the maximum rate of bed load transport was predicted for the November flood period. In addition, in a few other months like September, May, and July, some bed load transport was estimated at the inlet. By comparing this with the hydrograph at the inlet, it can be seen that bed load was dominant when the discharge flux was higher than 400m^3/s. Bed load transport at the outlet showed that only during the flooding season was bed load transported toward the reservoir. In the other months, the bed load in the model remained in this reach, as shown in the difference between the inlet and outlet in Figure (7.2). Furthermore, this figure also shows that, by comparing all non-cohesive fractions, the fraction with the greatest mass remaining in this reach was the 0.22mm size class.

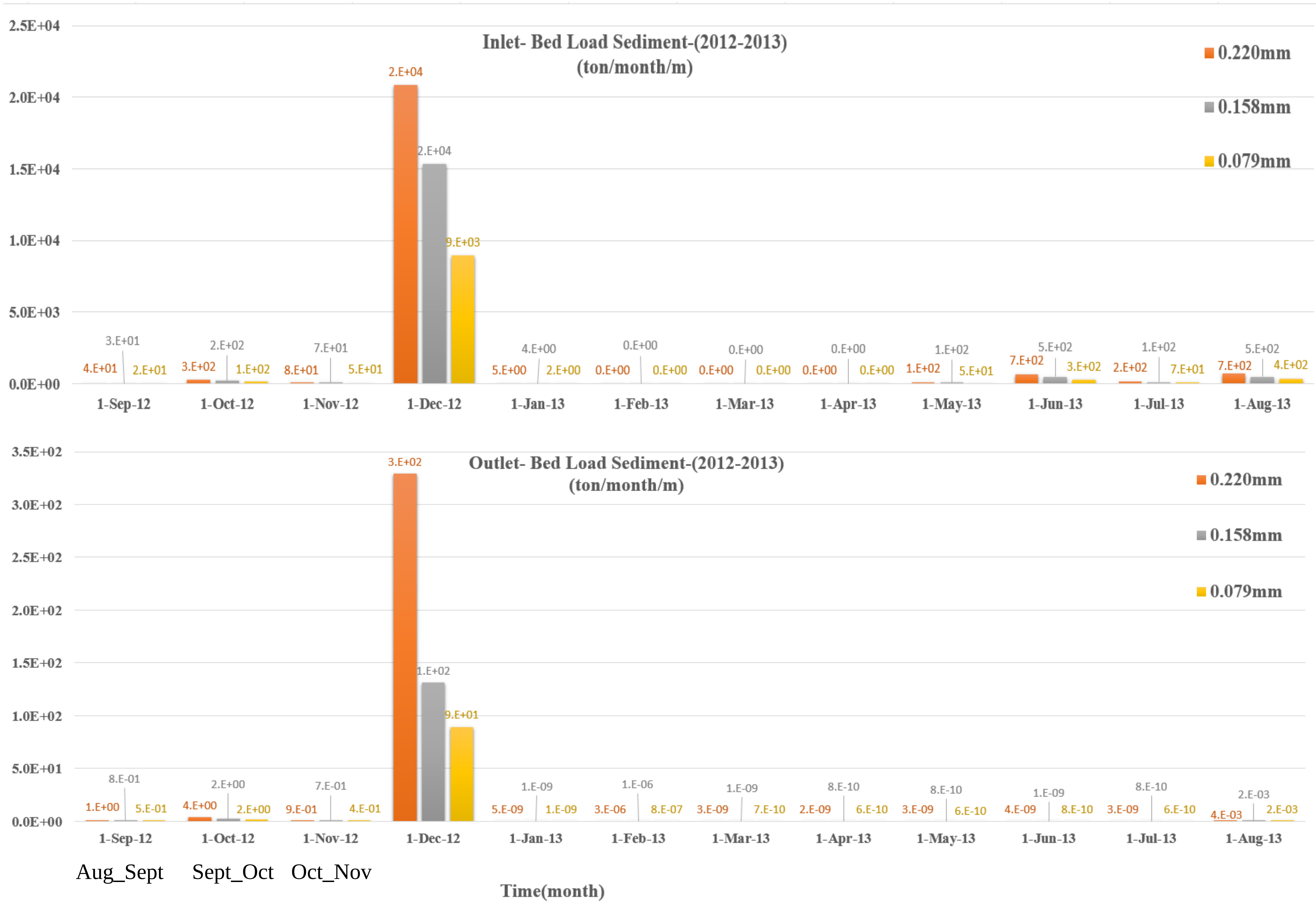

Figure (7.1) Bed load transport at inlet and outlet of three fractions for 12 months (2012-2013)

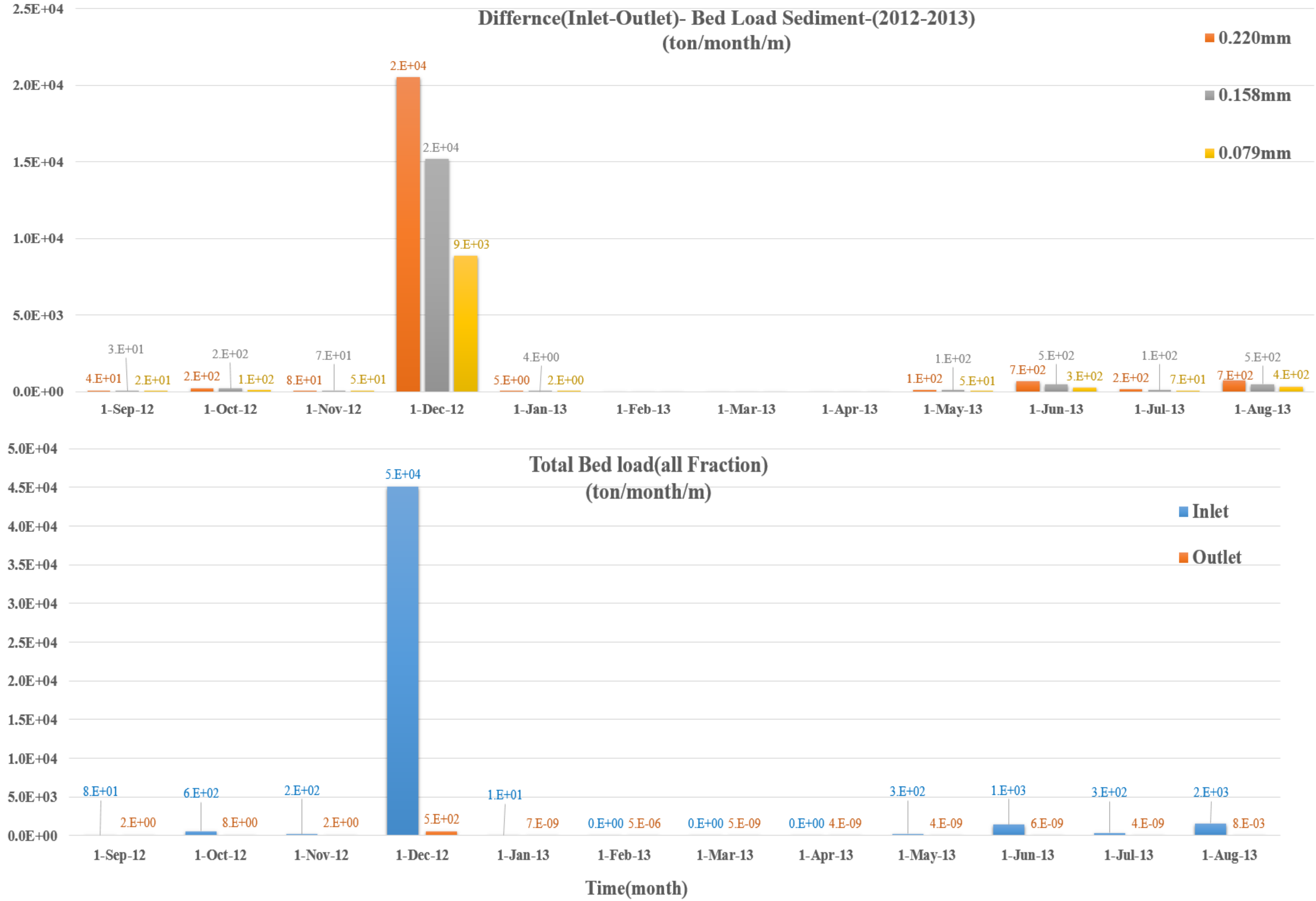

Figure (7.2) Difference between Bed load inlet and outlet of three fractions, summation of all bed load fraction at inlet and outlet for12 months (2012-2013)

7.2 Suspended load transport

In Figures 7.3 and 7.4-a, b, depending on the grain size distribution measurement at the inlet, non-cohesive suspended sediment entered the model domain in all months except the winter season, whereas cohesive sediment was high in all months. At the outlet, non-cohesive suspended transport was dominant only in November, which means that most of the non-cohesive sediment remained in this reach during the other months. On the other hand, the rate of cohesive transport toward the reservoir was higher than for non-cohesive transport. Furthermore, in Figure (7.5), which shows the difference between the inlet and outlet, it can be seen that only sediment 29 (0.039mm) had large negative values; i.e., this size fraction was entrained from the bed and transported out of the reach. However, in the winter season even this grain size was not transported.

Figure (7.6) shows that the outlet suspended sediment in most months was cohesive sediment. In another words, all the non-cohesive suspended sediment fractions that came into this reach mostly remained in this reach and were not transported downstream.

In Figure (7.7), it can be seen that in all months except September 2012 and July 2013, the sediment transport at the outlet was slightly higher compared to the sediment transport at the inlet. This suggests a net erosion over the model domain during the one-year simulation. In addition, the overall sediment results for the one-year simulation (Figure 7.8) show that the sediments that remained in the reach are from the bed load, which would be non-cohesive sediments. Furthermore, the suspended load at the outlet was slightly higher compared to the inlet due to the cohesive sediment available in the bed.

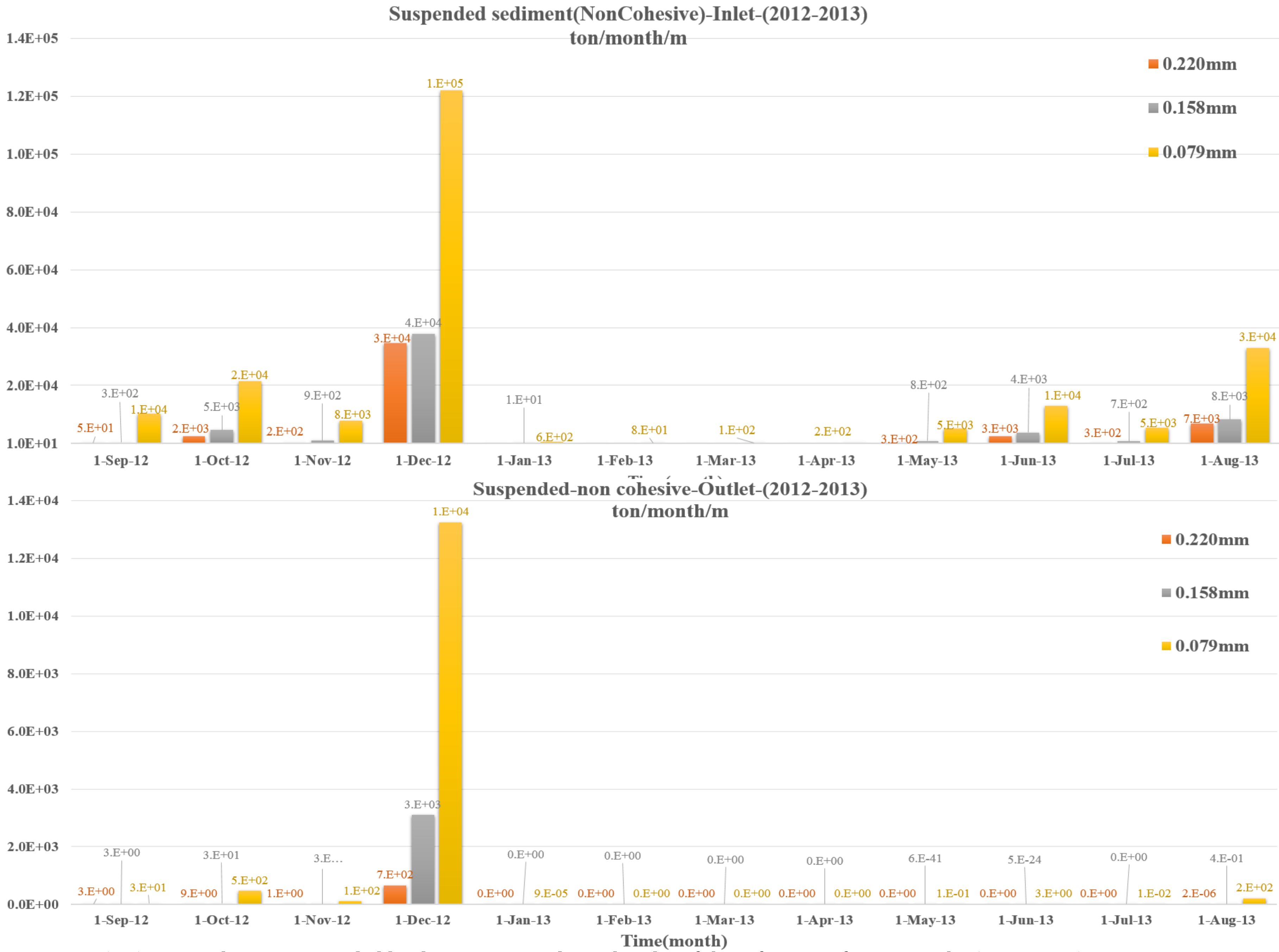

Figure (7.3) Non Cohesive Suspended load transport at inlet and outlet of three fractions for 12 months (2012-2013)

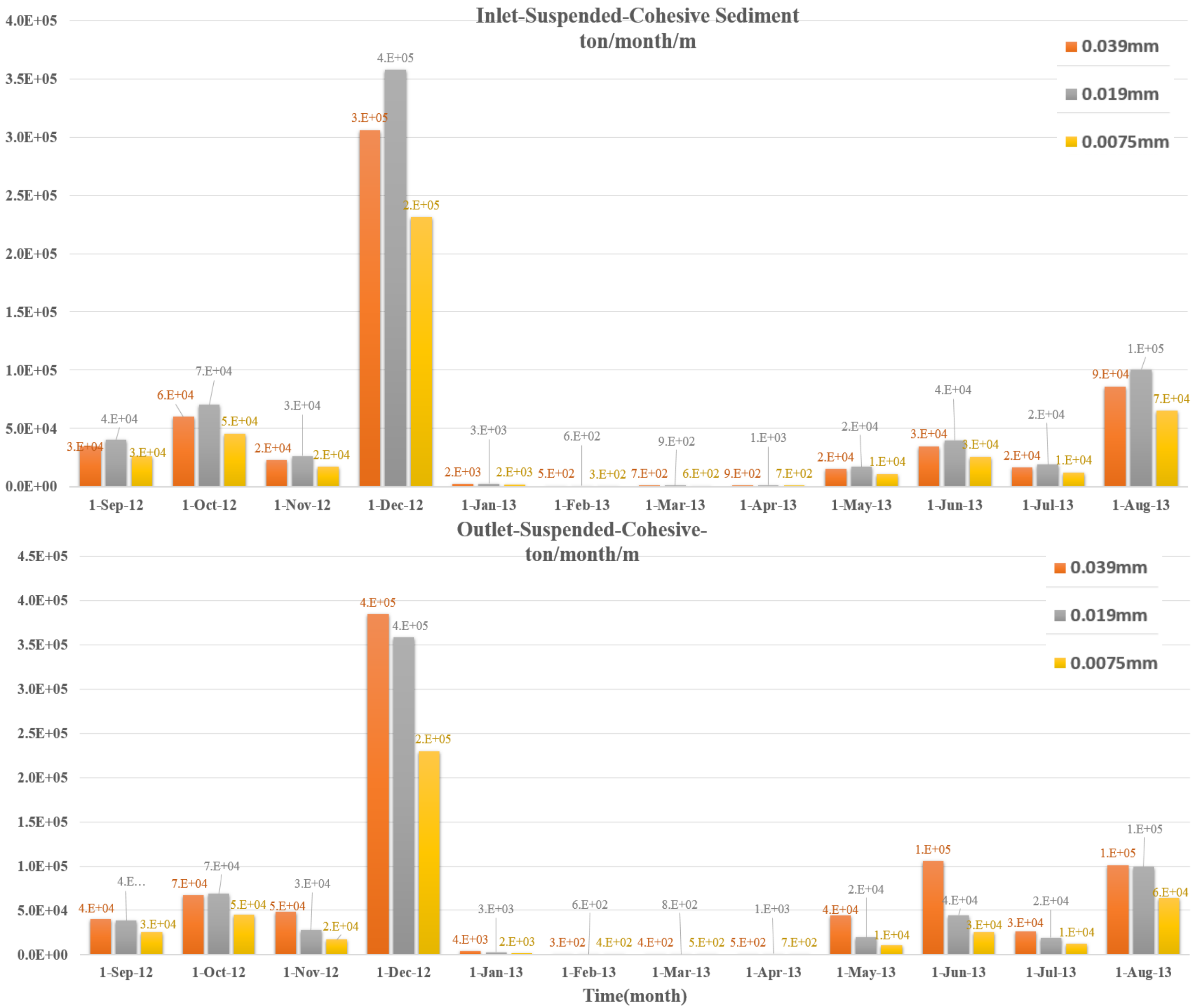

Figure (7.4-a) Cohesive Suspended load transport at inlet and outlet of three fractions for 12 months (2012-2013)

Figure (7.4-b) Cohesive Suspended load transport at inlet and outlet of three fractions for 12 months (2012-2013)

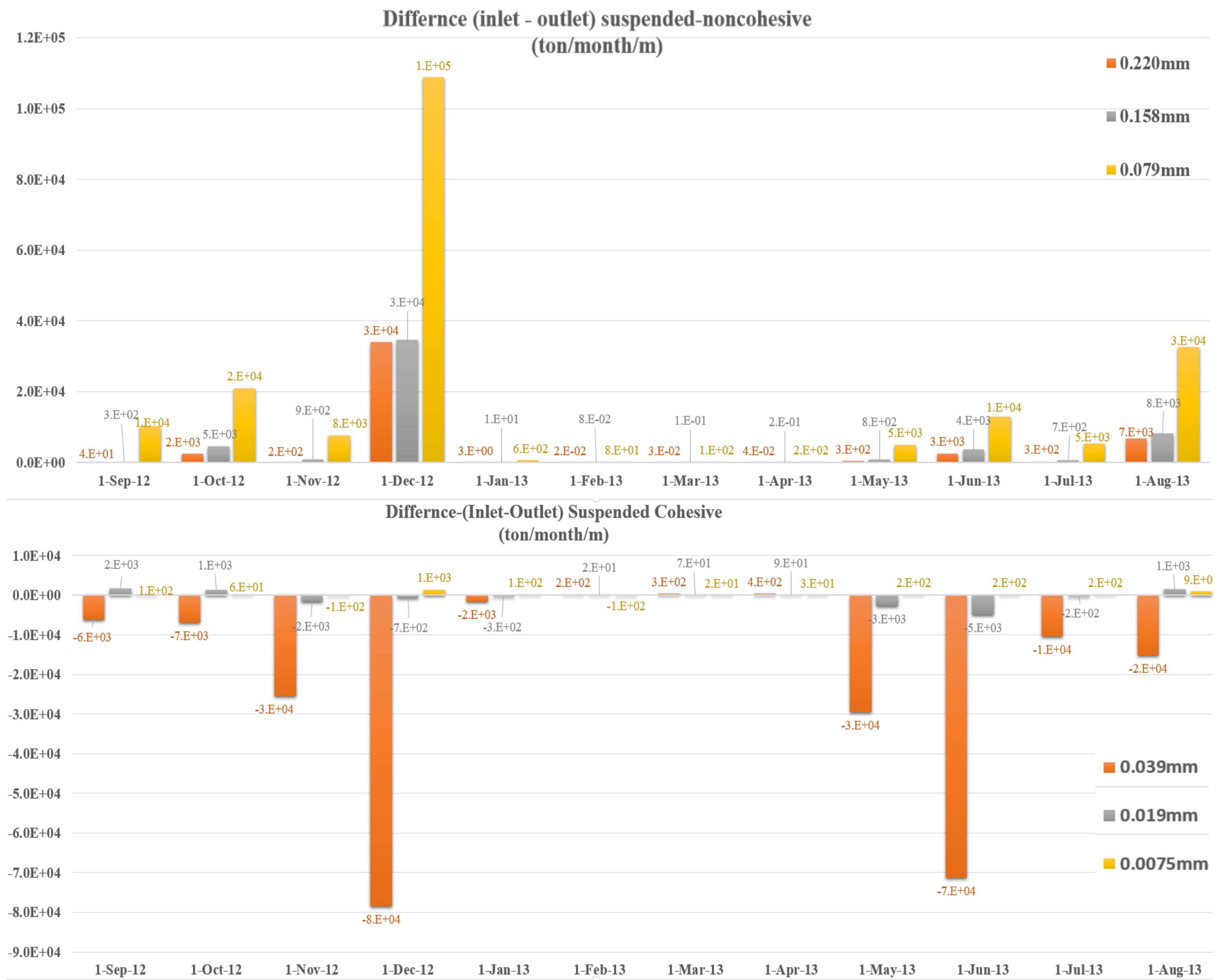

Figure (7.5) Difference between Suspended load (cohesive+non-cohesive) inlet and outlet of three fractions for 12 months

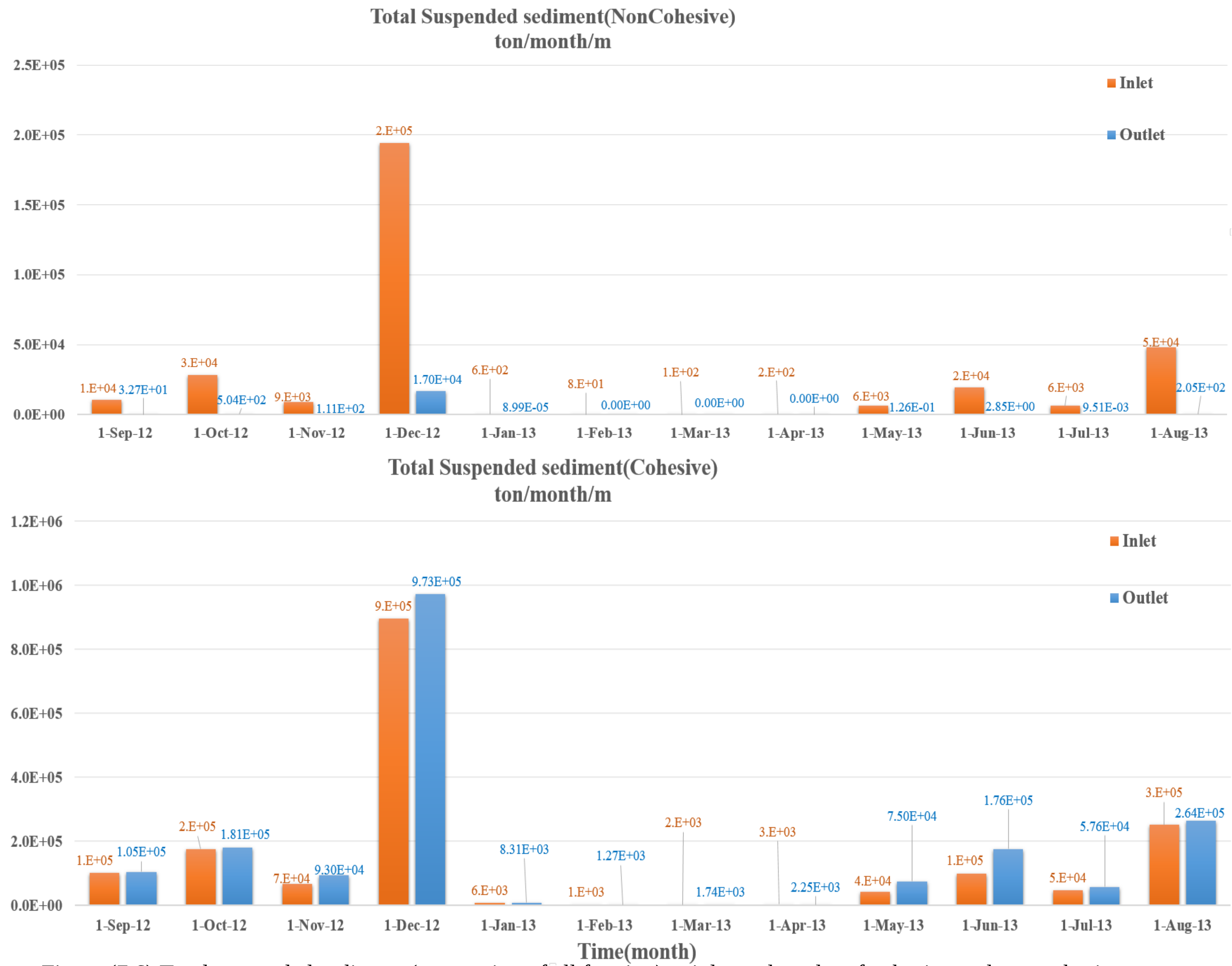

Figure (7.6) Total suspended sediment (summation of all fraction) at inlet and out let of cohesive and non-cohesive

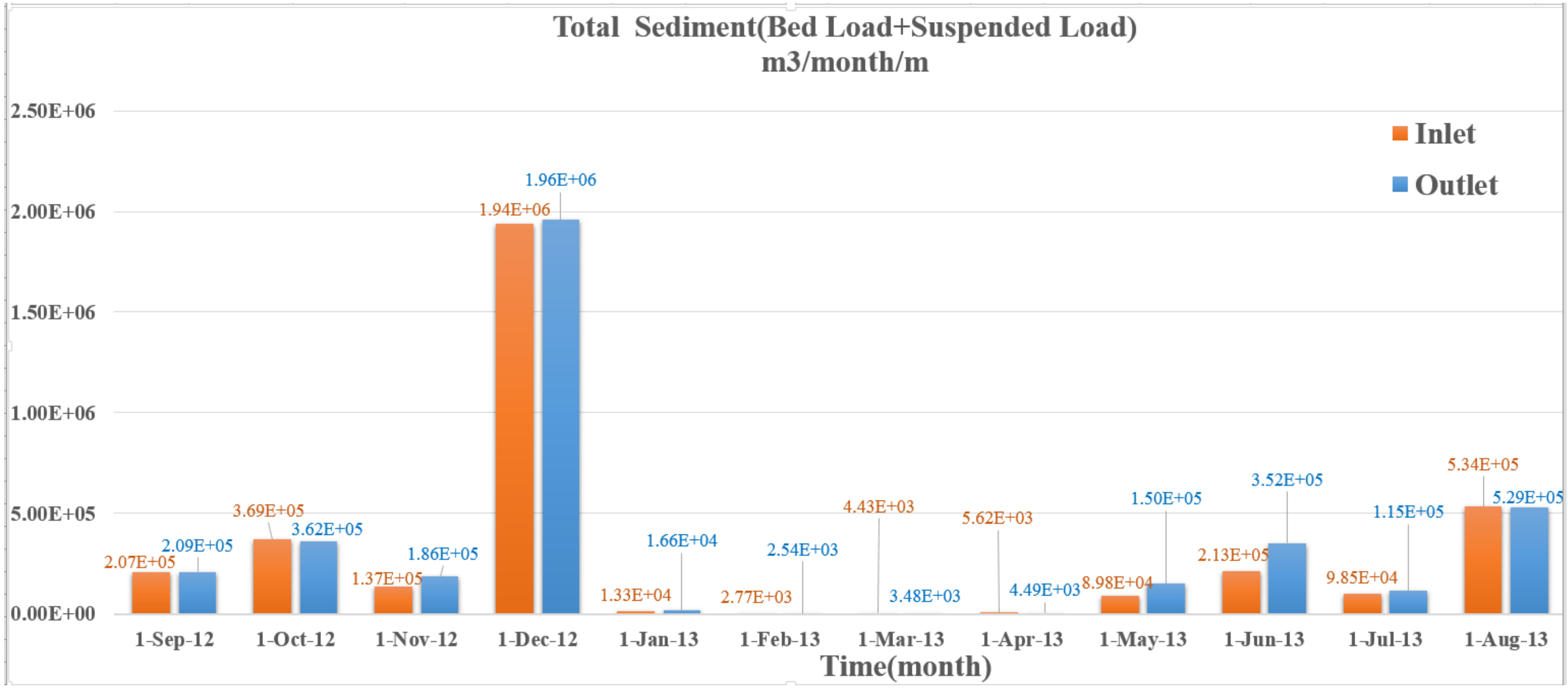

Figure (7.7) Total Sediment transport (Bed load+ Suspended Load) at inlet and outlet

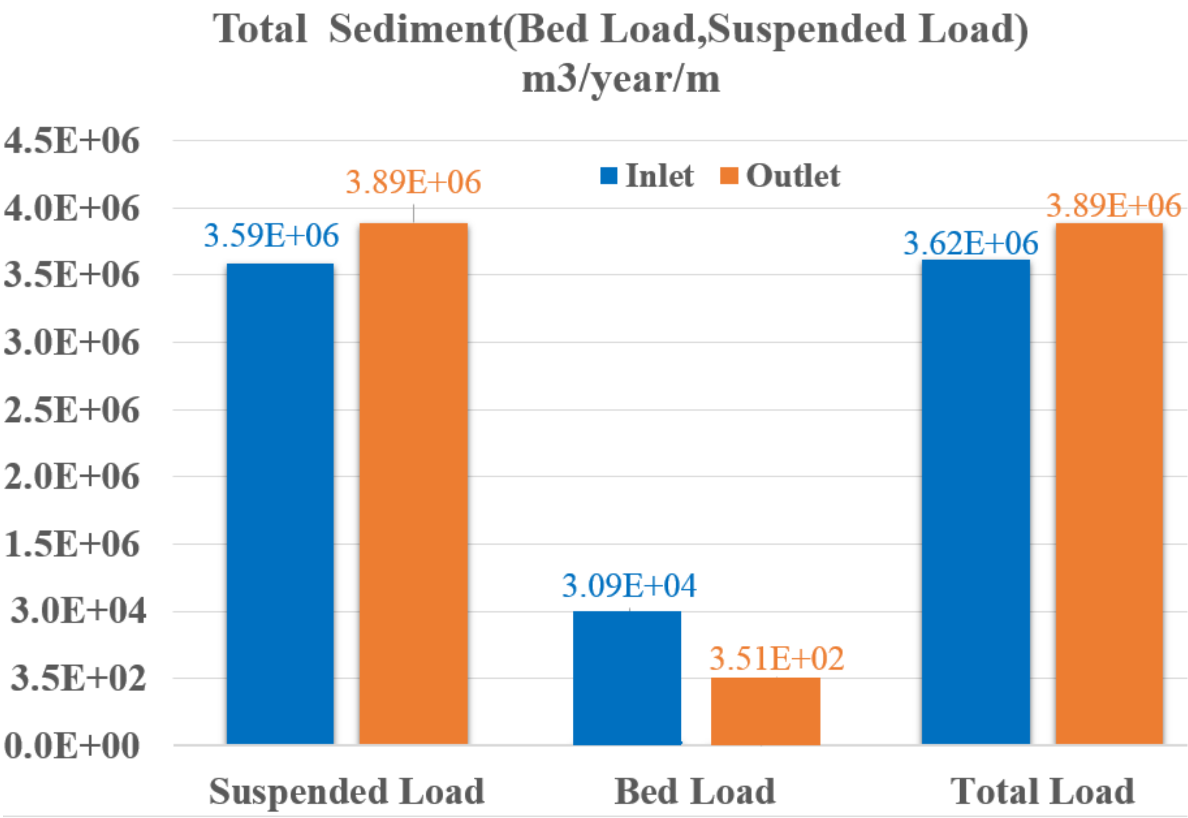

Figure (7.8) Total load, suspended load, and bed load totals for one year (2012-2013)

8. Flushing Analysis

Water level management, or in other words gate opening management, plays a major role in gaining back the capacity of the reservoir and the river during flood periods. As is shown in Figure (8.1), in 2012 the river passed through two peak floods, on 5th - 6th November and 12th - 13th November. In the first peak, the rate of concentration was high in the reach (7-8kg/m^3), whereas in the second peak the concentration was almost half of the first. Looking at water level, it can be seen that only one effective flushing during the second peak occurred. This type of flushing can be categorized as “flood flushing”, as defined in Section 2.3. The period of flushing is divided into three sub-periods: 1) period of lowering the water level before starting flooding (emptying the reservoir); 2) period of flushing sediment, which starts from peak flood until the time the water level curve goes up; and 3) period of filling up the reservoir. These sub-periods are shown clearly in Figure (8.1).

In this analysis, in the first flood peak, the water level downstream was changed in order to find its influence on the amount of sediment transport toward the reservoir and to determine its influence on bed level change in this reach. The water level was modified in four ways, as shown in Figure (8.1). For each modified water level, the accumulated erosion and deposition from 1st Nov to the end of the first peak (8th November) and second peak (18th November) are shown in Figure (8.2). It has to be mentioned that this simulation was conducted on bed composition from the simulation results for 1st August to1st November 2012 and model setup in Section 6.2.9. Furthermore, the change in water level may produce some changes in the upstream boundary discharge flux in reality, but in this simulation this change was ignored, which means the same flux was used for all the simulations (Figure 8.2).

Looking at the cumulative erosion-deposition on 8th Nov, when applying Trial-1, overall the rate of erosion slightly increased (compare Figure 8.2, a_1 and b_1). For example, the amount of sediment deposited near the inlet decreased because it was transported downstream. This increased the amount of deposited sediment at the middle of both the bend cross-section (DFL1710) and downstream (DFL1300, DFL1400).

From comparing the results of Trial-1 and Trial-2, it can be seen the same amount of erosion and deposition estimated in 8th Nov (Figure 8.2, b_1 and c_1). This occurred because when the flux reached the peak, the water levels of both trials were the same. The difference between these two trials was the starting time for lowering the water level, and the level of water before starting the flood. In other words, the duration of emptying the reservoir was equal to 1 day and 2 days for Trial-1 and Trial-2 respectively (Figure 8.1). Also, the lower the water level in the reservoir before the flood peak, the more effective flushing will be (Fan and Morris, 1992). In addition, comparing the accumulated sediment transport in Figure (8.3, c) shows that the rates of sediment transported as bed load in the model for Trial-1 and Trial-2 were the same. This shows that the amount of sediment eroded from the reach and transported toward the reservoir would not be affected by lowering the water level in the reservoir before the start of the flooding.

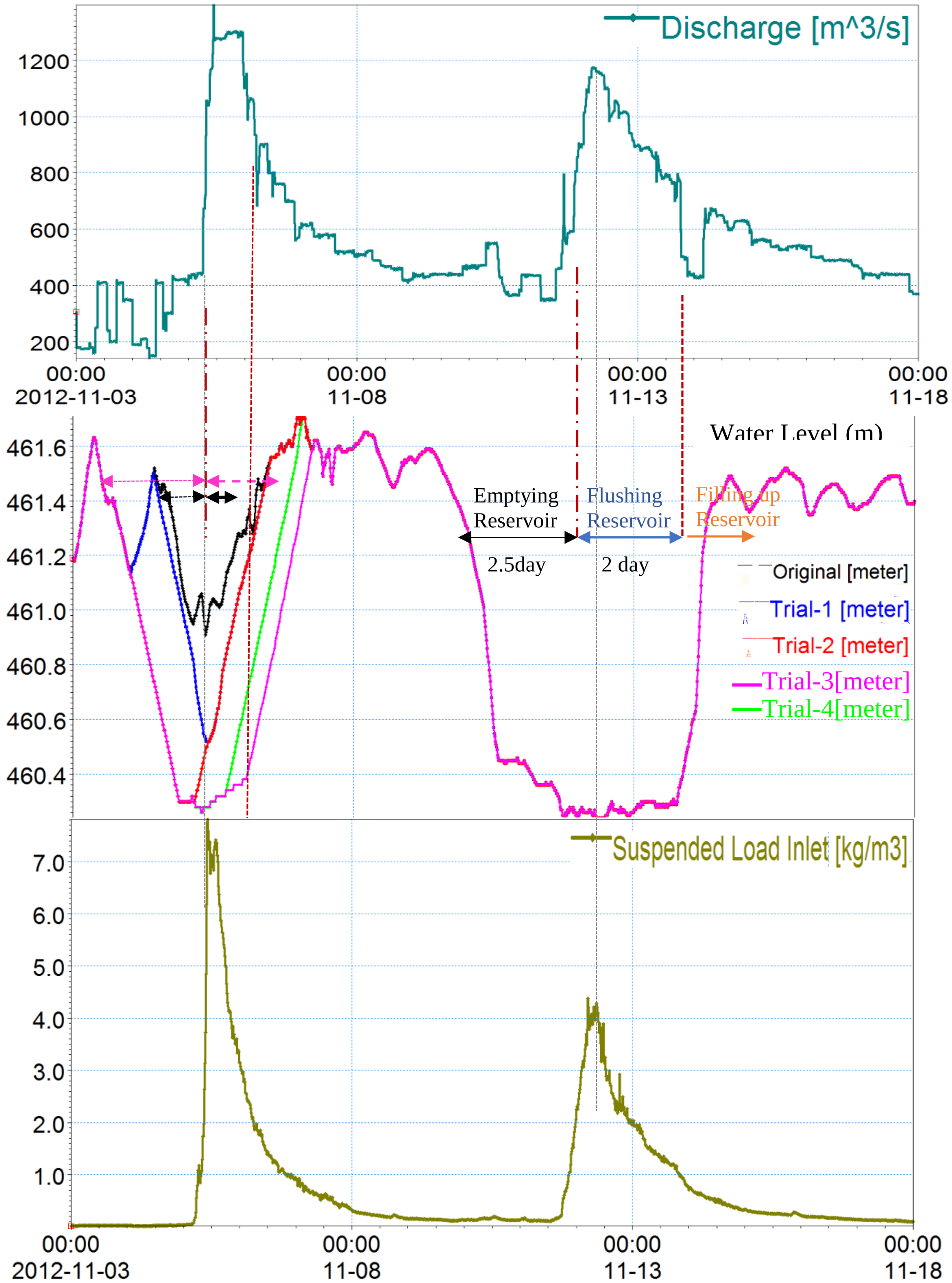

Figure (8.1) From top to bottom: discharge (m^3/s), water level change for all the trials (m), and suspended sediment (Kg/m^3) during flood period

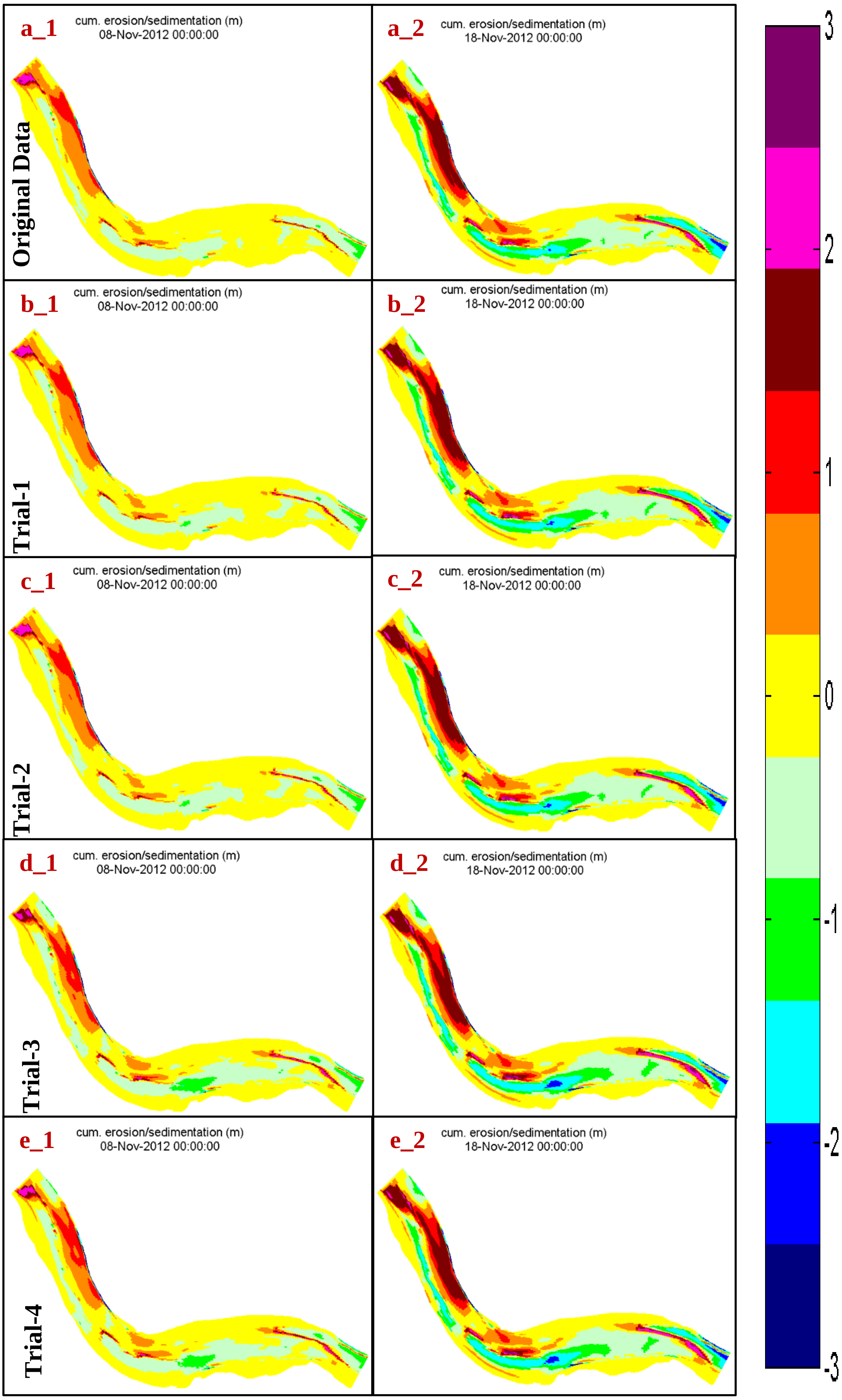

Figure (8.2). a-e_1) accumulated erosion and deposition (m) estimation of simulation between 1st Nov and 8th Dec 2012) for various water levels, a-e_2) accumulated erosion and deposition (m) between 1st Nov-18th and Dec. 2012.

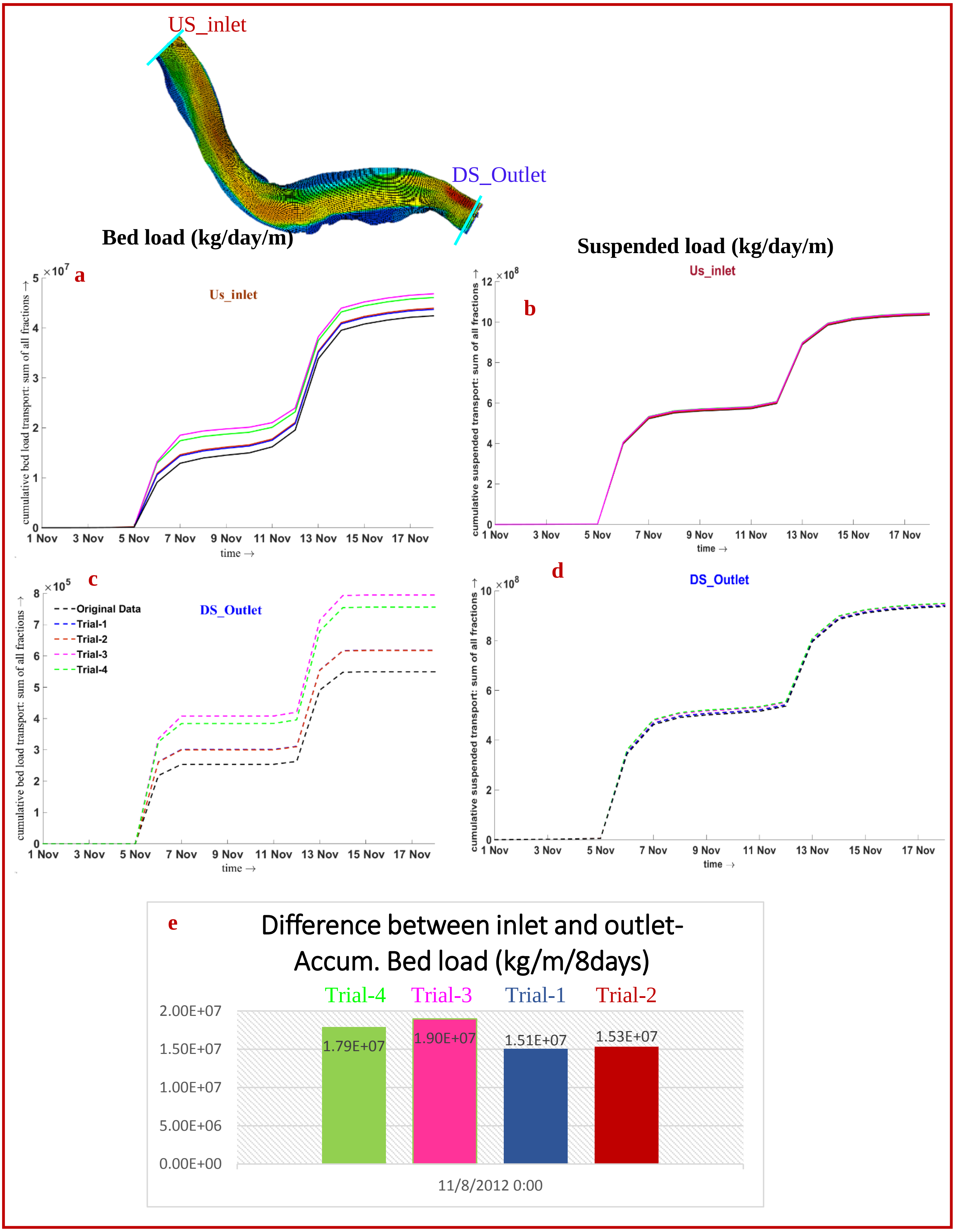

Figure (8.3). a, b) Accumulated bed load and suspended load transport at inlet respectively; c, d) Accumulated bed load and suspended load transport at outlet of the model for 1st Nov-18th Nov 2012. e) Difference between inlet and outlet for accumulated bed load for 1stNov-8th Nov2012

The second essential analysis was on the influence of the duration the water level remained low after starting the flood. For this purpose, the water level was modified in Trials-3 and -4, as shown in Figure (8.1). The water level remained low for one day and for half a day for Trials- 3 and -4 respectively after starting the peak flood. The accumulated erosion-deposition in Trial-3 was slightly higher. For instance, the deposition was higher in downstream at the middle for DFL 1300 and DFL1400 and at the inner bend zone compared to Trial-4 (Figure 8.2, d_1 and e_1). The accumulated bed load transport at the outlet for Trial-3 was higher compared to Trial-4, and the difference between inlet and outlet of Trial-3 is higher (Figure 8.3, c and e). This means that Trial-3 produced more sediment accumulation in this reach. This result shows the longer the gate is open after the peak, the more the change in bed level in the reach, and bed load transport toward the reservoir is expected. However, the rate of discharge at the inlet may have an influence.

In conclusion, the above analysis shows that the duration of lowering the water level at the hydropower plant before flooding might not produce significant changes in sediment flushing in the river reach upstream of the reservoir, at least for the limited duration examined herein. However, it should be recognized that it might make a difference in the reservoir itself because decreasing the volume of water in the reservoir may produce more effective flushing from the reservoir during flooding. On the other hand, the duration of lowering the water level after the flood peak made more difference in bed level in the reach and probably in the reservoir, depending on the water level in the reservoir.

9. Part-2, Extended Reach

9.1 Introduction

The historical bathymetry measurements in Figure (9.1) show that after constructing the hydropower plant in 1968, the river morphology changed significantly. The depth reduction reached about 10m in most sections, especially in those sections near the reservoir. In many rivers, when navigation is desired, groynes are constructed. However, navigation in this river is rare due to the hydropower plants. Nevertheless, decreasing the water depth will have a significant impact on the water supply to the reservoir and on the river's morphology. Therefore, in this section, the impact of groyne structures on river morphology and sediment transport toward the reservoir were studied. Although groyne construction goes back many centuries, hydrodynamic and sediment exchange prediction in the groyne zone is still under development. Many studies have been conducted in both field and laboratory scales to understand the physical characteristics and to develop new criteria in groyne design. Most of these standards have been summarised in Section (2.4). In this study, some of these design criteria were modelled at both flume and river scales. However, each design has different physical characteristics that need to be predicted accurately. Therefore, to validate the model's predictions (hydrodynamic), two previous flume experiments were modelled. The first flume experiment was conducted for a single groyne with various heads, and the second experiment was carried out for a group of groynes. In both experiments, the groynes were impermeable and angled at 90 degrees to the bank. At the river scale, both hydrodynamics and sediment transport between groynes were studied. This included the difference between emerged and submerged groynes, the influence of groyne head shape and aspect ratio on sediment supply to the groyne zone, and entrainment around the groynes and in the main stream.

It is important to mention that there have been only limited previous studies of Delft3D application in modeling groynes in a river reach. In Yossef (2005) thesis, Delft3D (two-dimensional) was applied to model both the hydrodynamics and sediment exchange of a groyne zone in a river for an emerged case and one non-cohesive fraction. His thesis conclusions stated that Delft3D is only capable of predicting part of the hydrodynamic characteristics. For example, turbulence in the mixing layer was not estimated correctly. The results showed sediment accumulation only near the head of the groynes, and morphology change inside the groyne zone was not estimated. According to his interpretation, this shortcoming went back to both the sediment transport formula and underestimation of turbulence in the mixing zone. In Stive (2010) study, Delft3D was applied to model groynes in a coastal area. In his model, a thin dam represented the groynes. This thin dam does not have thickness and in its appearance looks the same as a weir but it does not account for the loss of energy like in applying weirs. He concluded that both the hydrodynamics and sediment dynamics were modelled successfully.

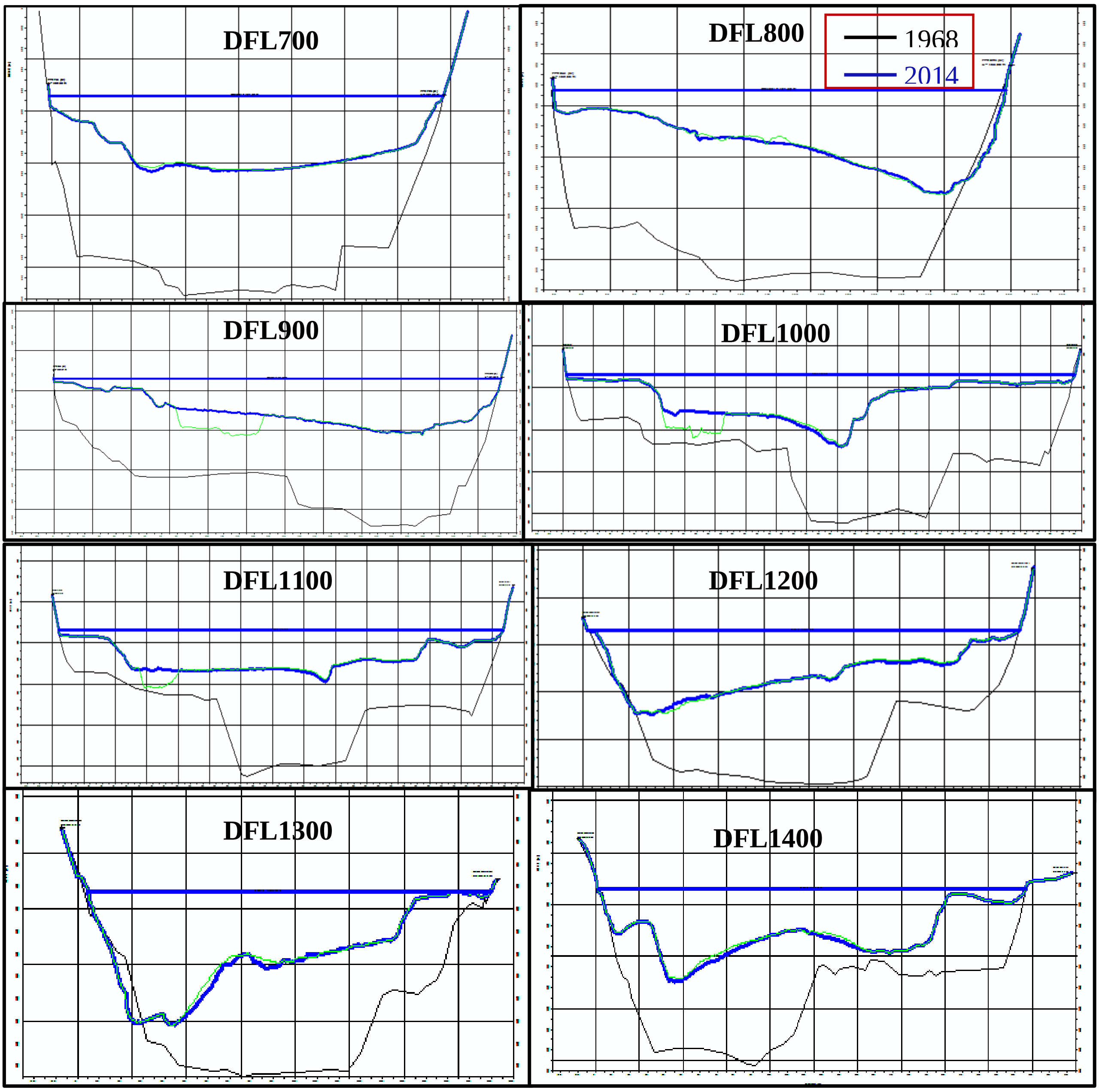

Figure 9.1 Bathymetry profile of the study area in 1968 and 2014, section seen from left to right looking downstream.

9.2. Model Setup

9.2.1. Domain

The previous grid's (Part_1) reach was extended toward the entrance of the reservoir, as mentioned before. Horizontally, the grid was divided into 13240 cells. The reason for implementing the coarser grid was to save computation time (Figure 9.2).

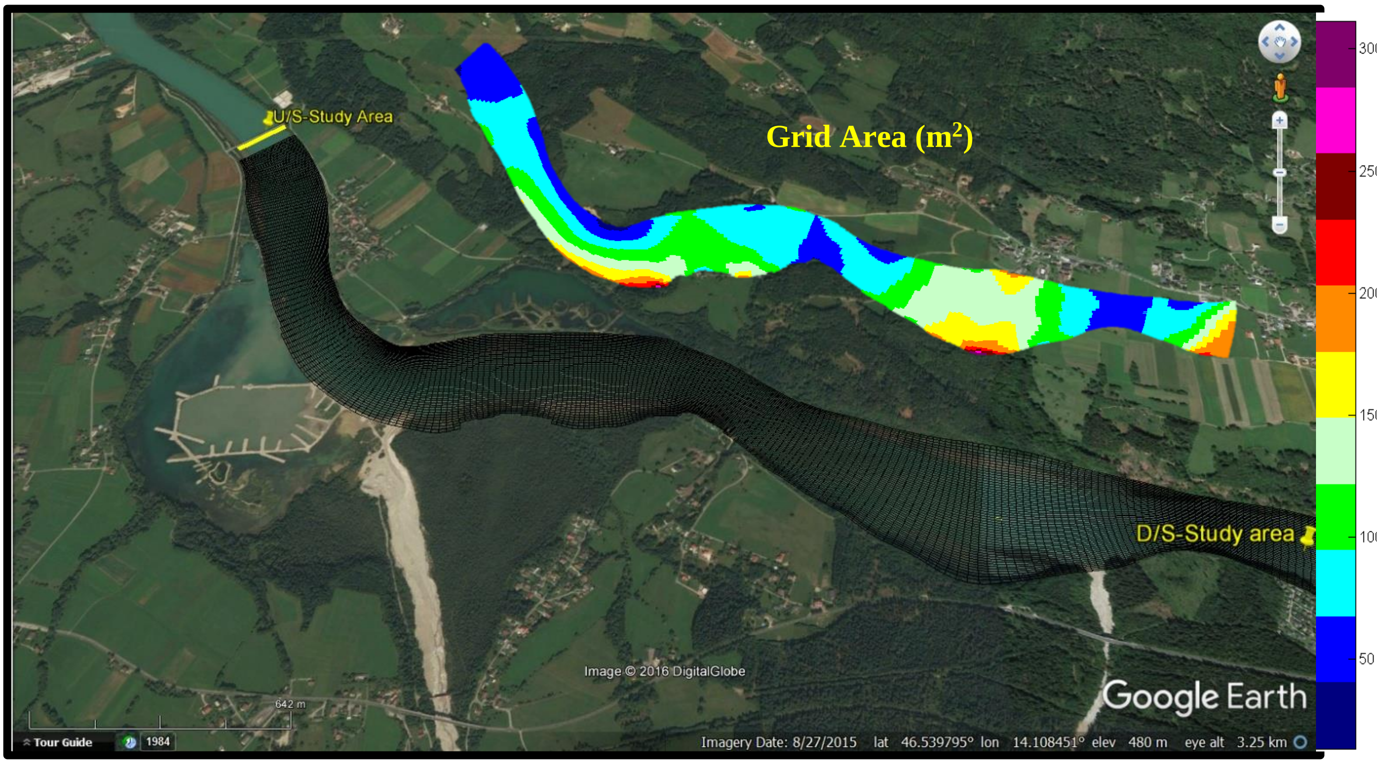

Figure (9.2) Grid of the study area (Part 2)

9.2.2 Bathymetry

The bathymetry was prepared using both the meandering side-scan survey and the single beam cross-section (DFL 1200-DFL700) from 2014 survey, as shown in Figure (9.3).

The initial conditions and time step were set as in the previous model setup, described in Section 6. At the boundary, for hydrodynamic validation, the steady state data from (Section 5.2) were implemented. For morphodynamic simulation, the unsteady state data of 14 days (3rd Novmber-18th November 2012) were implemented.

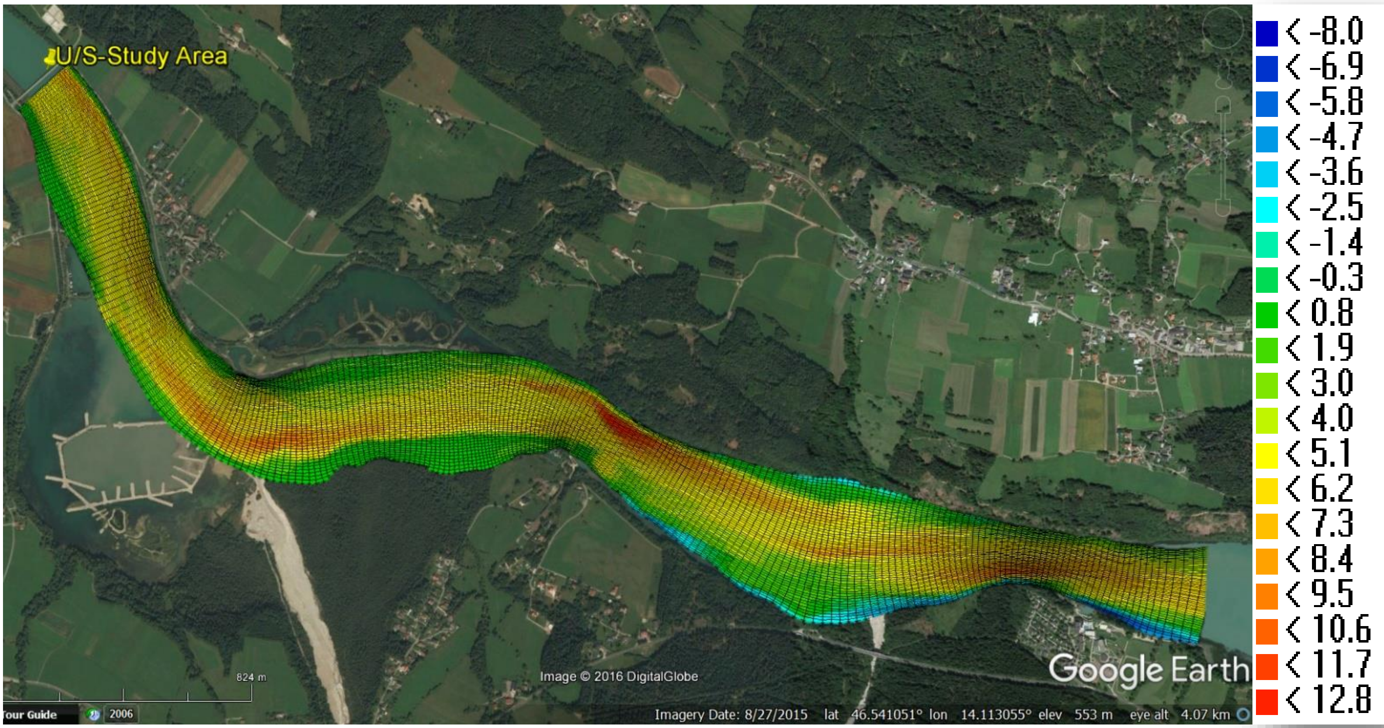

Figure (9.3) Bathymetry setup for extended reach, flow from left to right. Flow depth colour scale in m.

9.2 Model Assessment without Groynes

9.2.1. Hydrodynamic Validation

From the previous hydrodynamic sensitivity analysis results in Section 6.1, horizontal eddy viscosity (0.1m^2/s) and spatial roughness (0.025 and 0.04) $^{sm-1/3}$ at the main channel and near the bank respectively were implemented in this reach. Because of the absence of velocity measurements in the downstream reach, only the meandering part was validated (DFL1920-DFL1400). Table 9.2 shows the error percentage at eight cross- sections of the steady state simulation for two different discharges. The results of hydrodynamic simulation are shown in Figure 9.4.

Table (9.2) 8 cross- sections, 2D simulation, secondary model excluded, viscosity (0.1m^2/s), spatial roughness as in Run2

	Roughness	Velocity	R^2	MAE	RMSE
Run1L	Flux 390m^3/s- secondary flow model excluded	U(Vx)	0.813	0.040	0.057
		V(Vy)	0.950	0.0329	0.043
		R=√(U²+V²)	0.7813	0.043	0.058
Run3L	Flux 420 m^3/s- secondary flow model excluded	U(Vx)	0.863	0.045	0.061
		V(Vy)	0.949	0.040	0.053
		R=√(U²+V²)	0.809	0.053	0.067

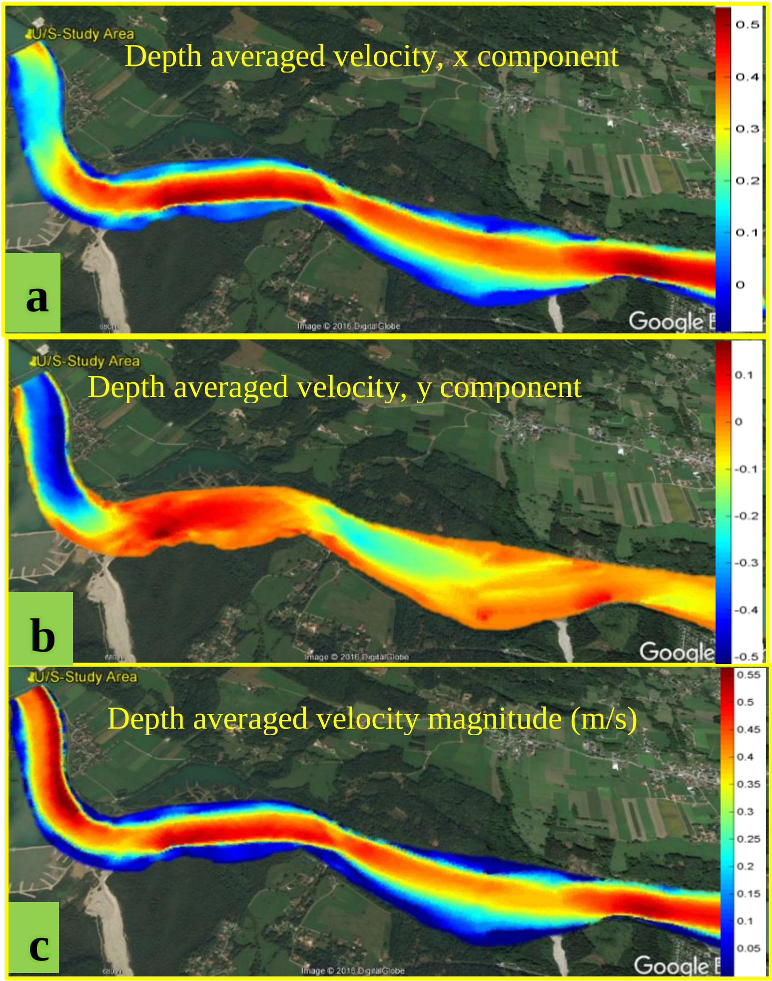

Figure (9.4) Depth-averaged velocity model results (2D): for flux= 390m^3/s, a) stream-wise velocity, b) transverse velocity, c) resultant velocity

Figure (9.5) shows the model estimation at the bend cross-section (DFL1710). Unlike the results for the previous reach in Section 6, the reversed flow at the outer bank was not estimated by either flux (390m^3/s or 420m^3/s). This underestimation may be related to the coarseness of the grid compared to the previous grid, particularly at the outer bank zone.

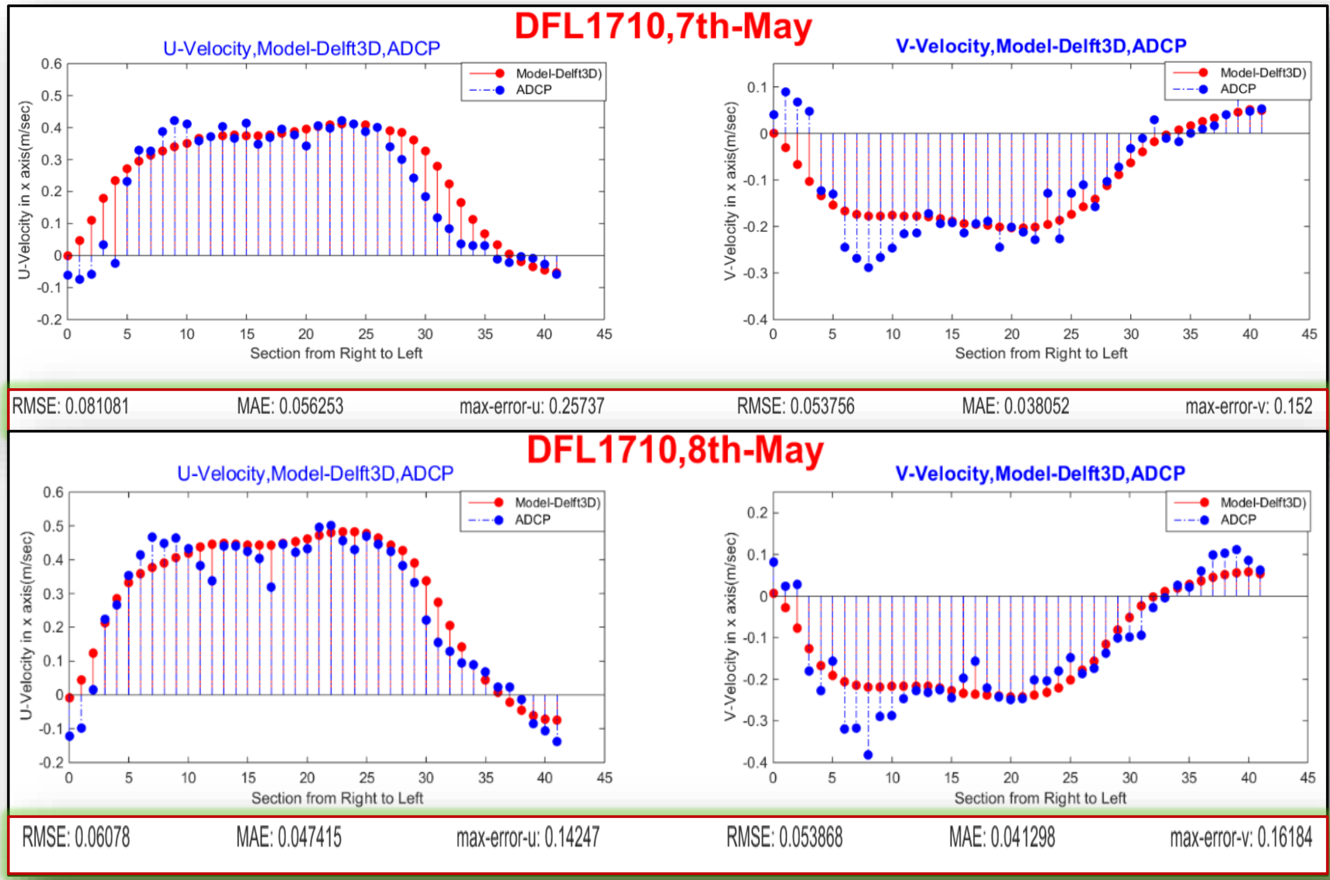

Figure (9.5) Depth-averaged velocity (m/s) (x-component- stream wise velocity, y-component- cross-stream velocity at the bend cross section for both fluxes (top-390m^3/s & bottom420m^3/s). Section seen from right to left looking from upstream

9.2.3. Morphodynamic

Bed Composition

The bed composition in the meandering part depended on the bed composition obtained from the last model simulation results of the one-year (2012-2013) simulation in Section7. For downstream of the meandering reach to the entrance of the reservoir, the bed composition is shown in Table 9.1.

Table (9.1) Bed composition downstream of the meandering reach

Layer	Thick (m)	Sediment G3	Sediment 03	Sediment 12	Sediment 29	Sediment 34	Sediment 22
Active Layer	4	40%	30%	30%	0	0	0
Base layer	5	100%	0	0	0	0	0

Before proceeding with the application of groynes to the river reach, it was essential to conduct several validations. Two flume experiments validated the 2D weir structure that represents the groynes in this model.

9.3. 2D-weir Validation

In most groyne applications in numerical models, groynes are included in the bathymetry setup. However, in this study, groynes were represented as a 2D-weir, which is one of the hydraulic structures in Delft3D that were described in Section 2.4. It was essential to validate this structure before proceeding with its application to the river reach. Two previous flume experiments had contributions in this validation. The first flume test was conducted by Safarzadeh et al. (2016) to look at flow patterns around single groynes with various heads. The second experiment was carried out by Uijttewaal, et al. (2001), who studied the flow pattern around a group of emerged groynes.

9.3.1. First Flume test

9.3.1.1 Experiment Description

The experiment was conducted in a glass flume (L=11m, w=1m) with a bed slope of 0.00033. The water depth and flow rate at the inlet of the model were equal to 0.148m and 60 l/s respectively. In this experiment, three kinds of groyne were tested individually: straight (SD), short T-head (TH) and long T-head (TF), as shown in Figure (9.6). ADV (Nortek AS 2006) -10 MHz down looking with an accuracy of 0.5% and measuring frequency of 200Hz was used for the velocity measurements. The measurement points are shown in Figure (9.7), and for the SD groynes experiment included 7 sections upstream, one at the groynes, and 12 sections downstream of the groynes, with 15 points in the transverse direction for each section. Safarzadeh et al. (2016) looked at the following:

1. Flow characteristics around straight and T-head groynes at different cross-sections vertically
2. The influence of T-head groynes on HSL (horseshoe vortex system) and SDL (dynamic detached shear layer)
3. The impact of the head length on flow characteristics around the groyne zone

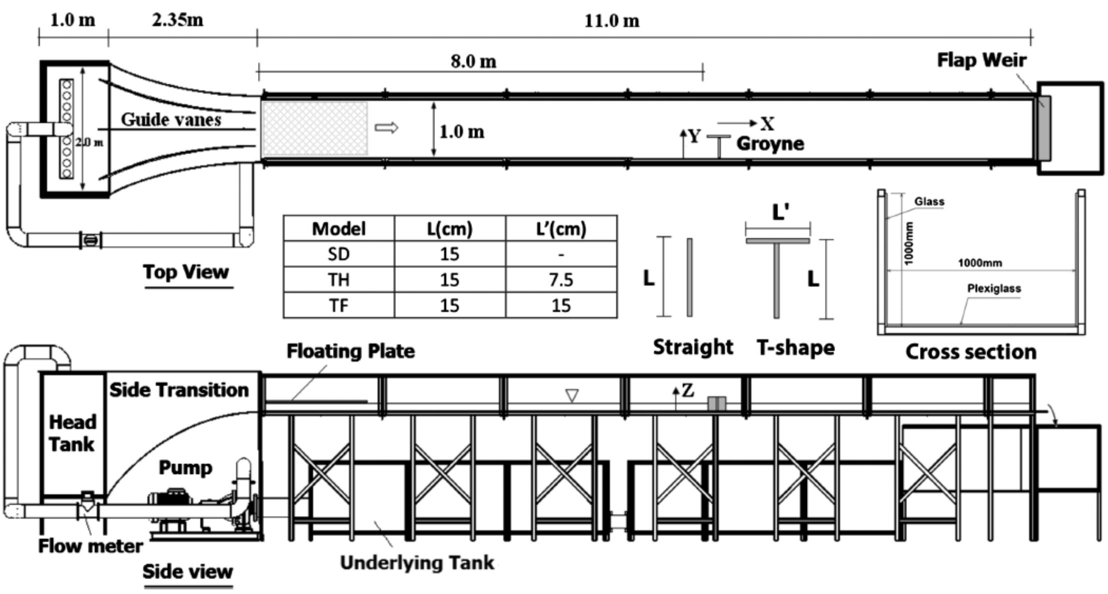

Figure (9.6) Experiment setup of flume experiment-1(Safarzadeh et al., 2016)

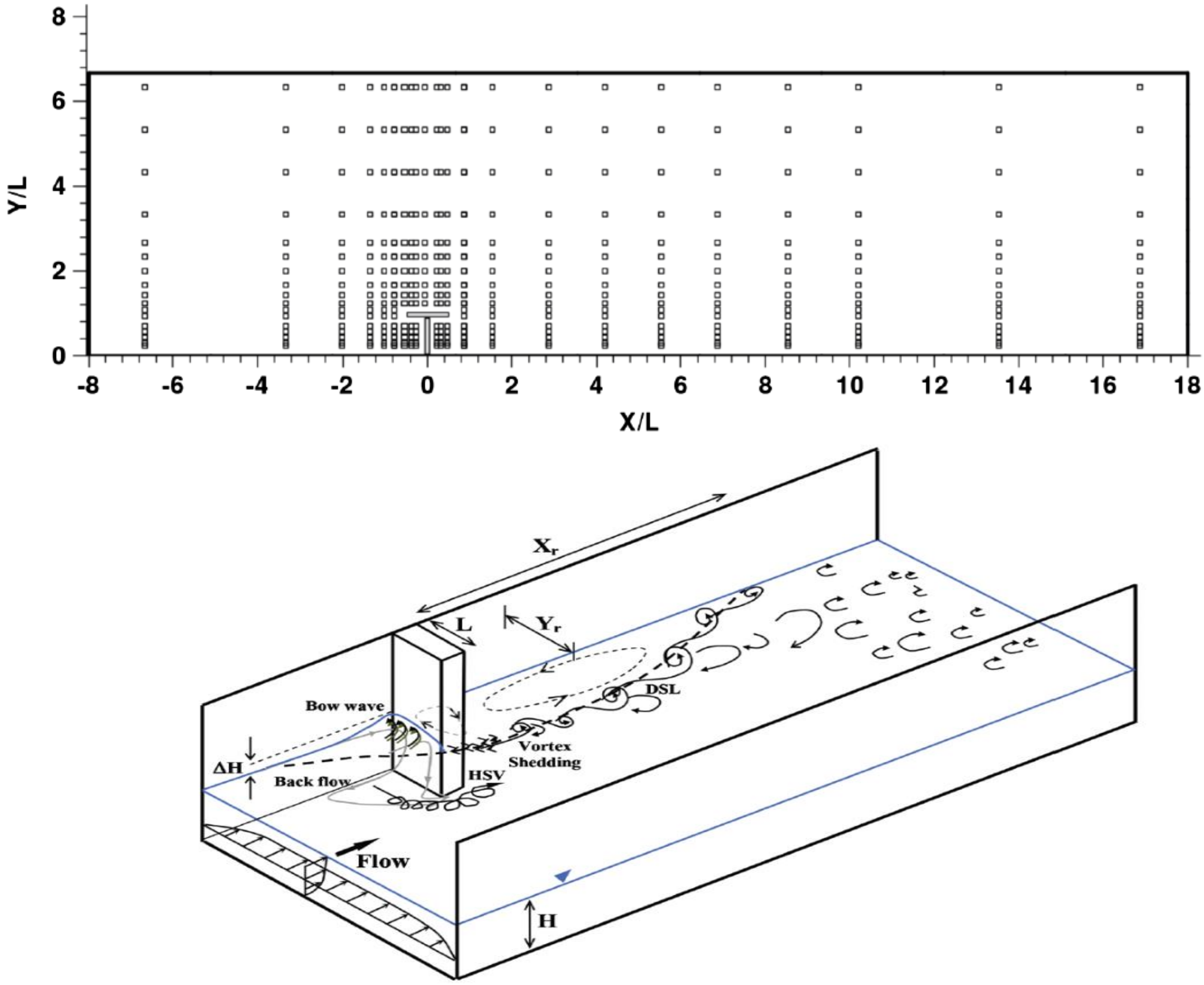

Figure (9.7) Top -measurement points in the flume in the stream-wise and transverse directions; and bottom -some parameters of flow characteristic around groyne (from Safarzadeh et al., 2016)

In this experiment, velocity was measured at a distance (Z/H=0.57 and Z/H=0.03) above the bed. The unit less distance from the groynes to the location that stream-wise velocity is equal to zero was addressed as (Xr/L). L: represent groynes length, Velocity magnitude ($U=\sqrt{u^2+v^2+w^2}$), U_{in}: inlet velocity (m/s), U/U_{in}: unit less velocity

9.3.1.2 Model Setup for the Experiment

The same size of flume was made with a grid cell size of 0.05x0.02m. Figure (9.8) shows the water depth in the flume without groynes.

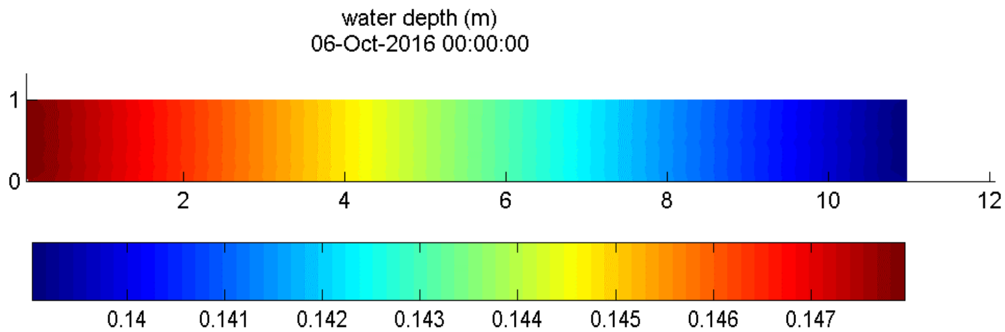

Figure (9.8) Modeled water depth of the first experiment

A 2D-weir, which represents the groynes, was placed at a distance of 8m in the stream-wise direction (x) from the inlet of the flume, as conducted in the experiment. The head width of the TH was 0.075m, but in the model this was changed to 0.1m because of the grid size. In addition, in the experiment, the TF head (0.15 m) was divided equally on both sides, but in the model the right-side length was 0.1m and the left side was 0.05m, as shown in (Figure 9.9).

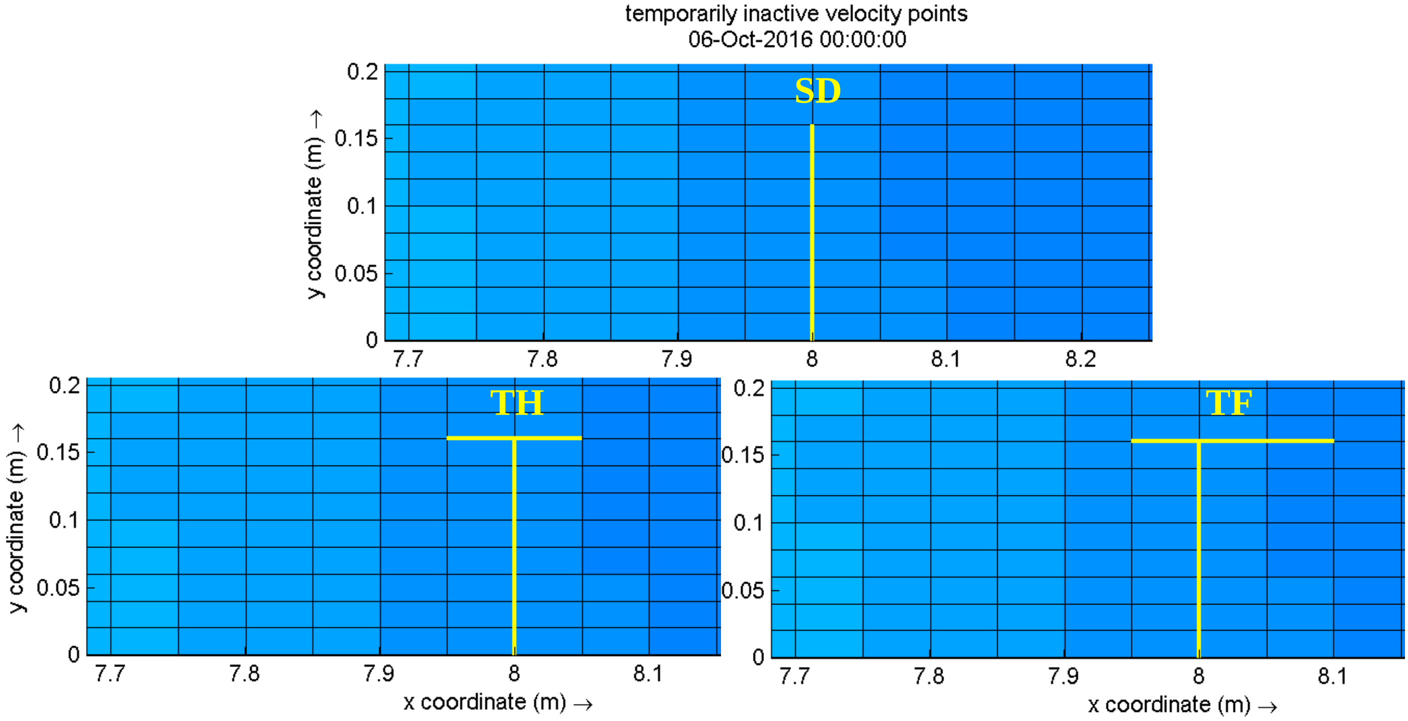

Figure (9.9) Model straight groynes (SD), short T-head groynes (TH), and long T-head groynes (TF).

To satisfy the Courant number condition, a time step of 0.001min was applied. Depending on the experiment, at the inlet and outlet of the flume, a flux of 0.06m^3/s and water level of -0.009m were implemented respectively. These boundary conditions produced a water depth of 0.148m at the inlet of the model. Regarding the physical parameters, after trying several horizontal eddy viscosity values it was concluded that 0.003m^2/s could satisfy the experiment condition to obtain a depth-averaged velocity of 0.41m/s and Froude number of 0.35 at the inlet of the flume. In addition, a Manning-roughness of 0.01$sm^{-1/3}$ was implemented. Furthermore, numerically, in solving the advection of momentum equation, the cyclic scheme was utilized.

Two simulations were carried out; in the first case, (Setup#1) HLES, Horizontal Large Eddy Viscosity was excluded, but in the second case, (Setup#2) HLES was included in the simulation.

8.3.1.3. Model –Experiment Results

According to the experiment results at depth Z/H=0.57, the value of Xr/L for SD groynes was higher than for the TH and TF groynes by ranges of 1.9L=0.285m and 4.4L=0.66m respectively. The modeled experiment shows that the Xr/L of SD was longer than for TH and TF by ranges of 0.65m and 0.7m respectively. Figure (9.10) shows that the velocity vectors were almost the same as in the physical test.

In the experiment, values of U/U_{in} less than 0.32 represented the circulation zone, with a blue color in Figure (9.11). Comparison with the model results for the SD groyne showed that the model prediction of this circulation zone length was almost the same. The difference between the model and the experiment was 0.5L. However, in the case of TH and TF, this difference was increased to 2.6L and 1.25L respectively. Furthermore, the experiment results showed that changing the groyne head produced the same unit less velocity (1.7). The only difference between the groynes was the shape of velocity propagation from the head of the groynes (Figure 9.11). On the other hand, in Figure (9.12-A), although the model results showed almost the same shape of penetrated velocity, the magnitude of the unit less velocity depended on the groyne head.

For example, for SD, the highest value of U/U_{in} was 1.6, which occurred downstream of the groynes and at the tip of the groynes. For TH and TF, the highest unit less velocities were 1.72, and 1.75 respectively at the tip of the groynes, but the penetrated downstream velocity was less.

Including HLES in the simulation resulted in a slightly higher velocity of the penetrated velocity at the head of the groynes. In addition, the length of (Xr) was longer (Figure 9.12-B).

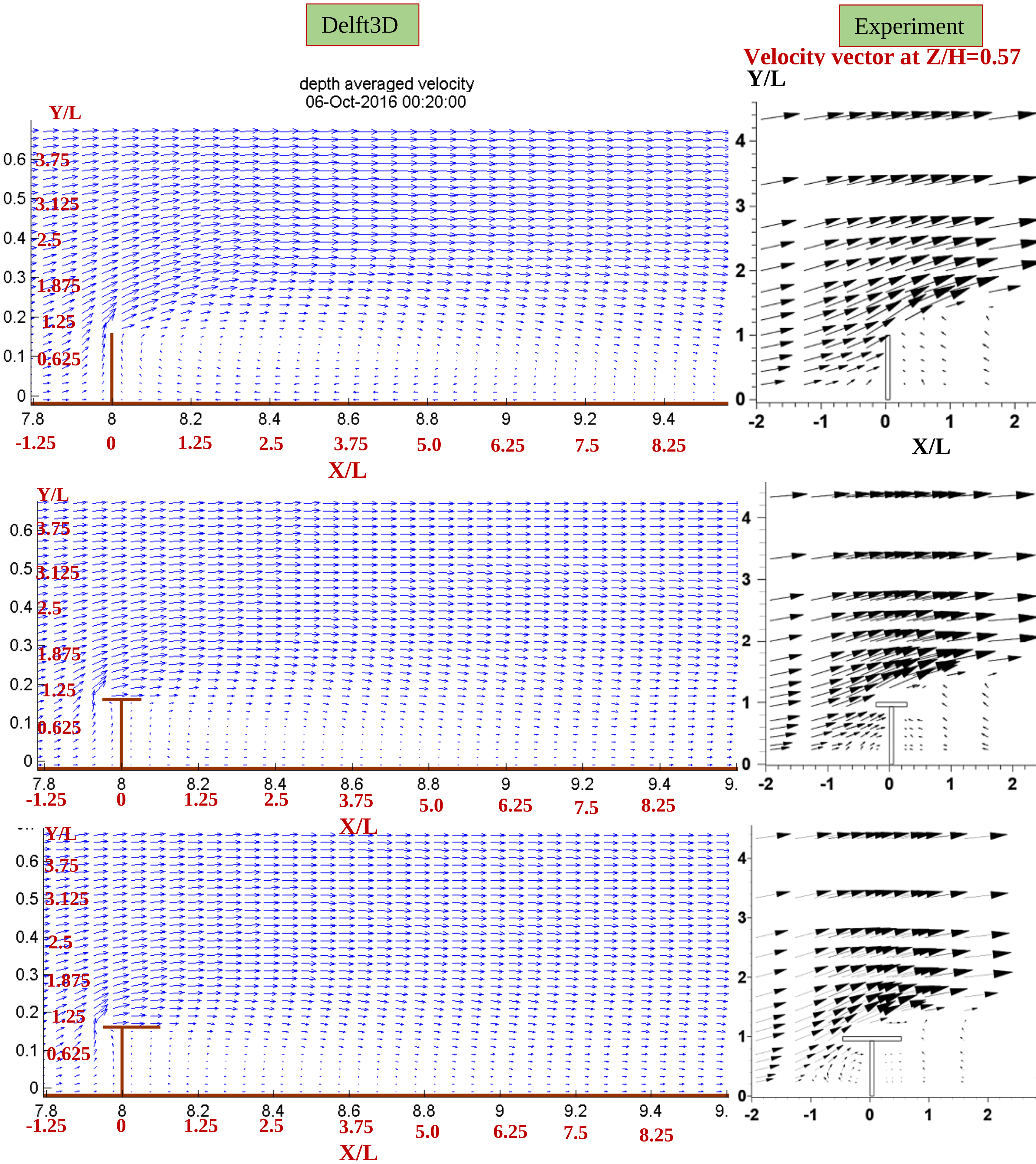

Figure (9.10) Depth-averaged velocity vector for Setup#1 (HLES excluded)

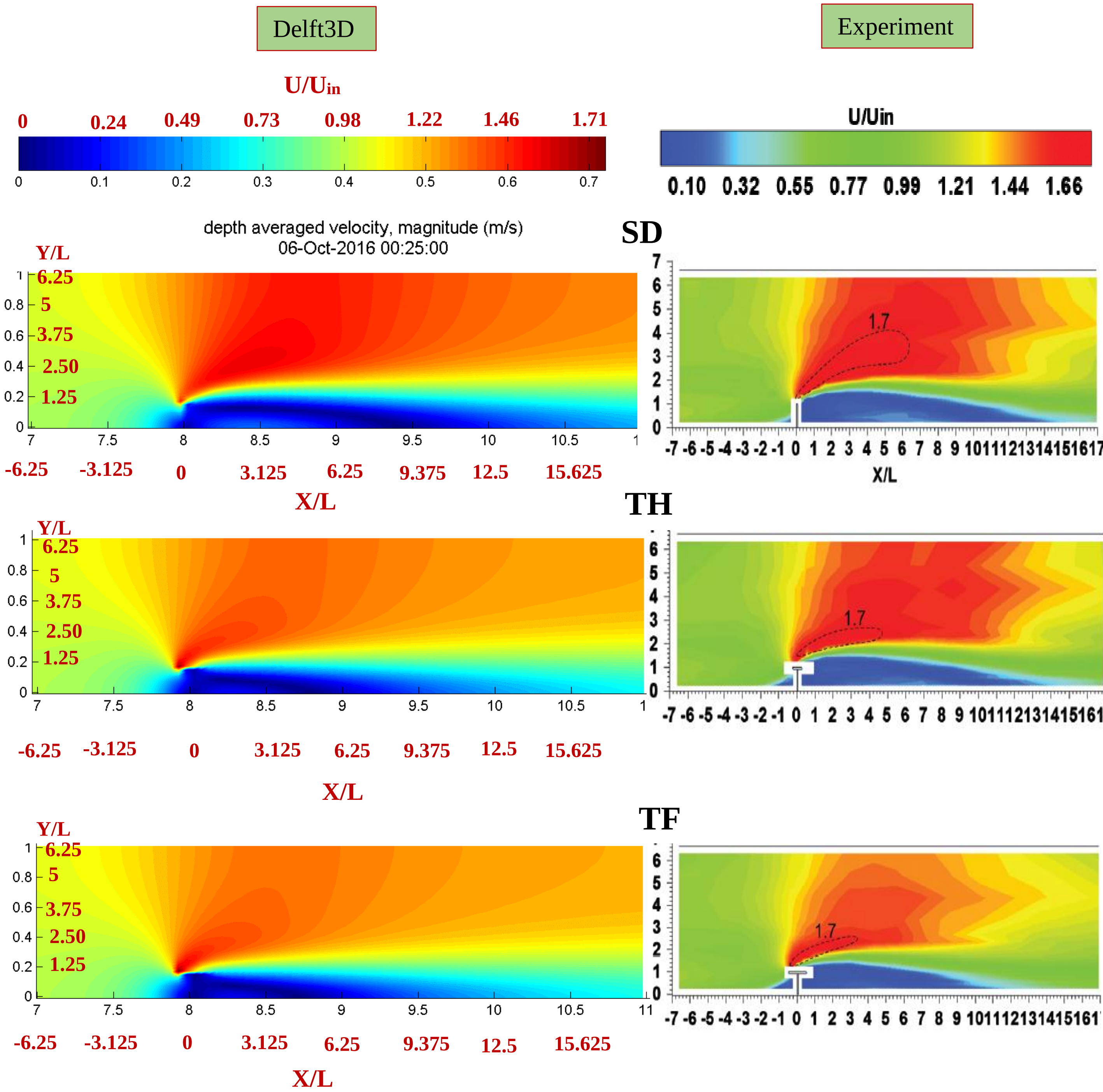

Figure (9.11) Depth-averaged velocity magnitude for Setup#1 (HLES excluded) and experiment velocity magnitude at depth Z/H=0.57

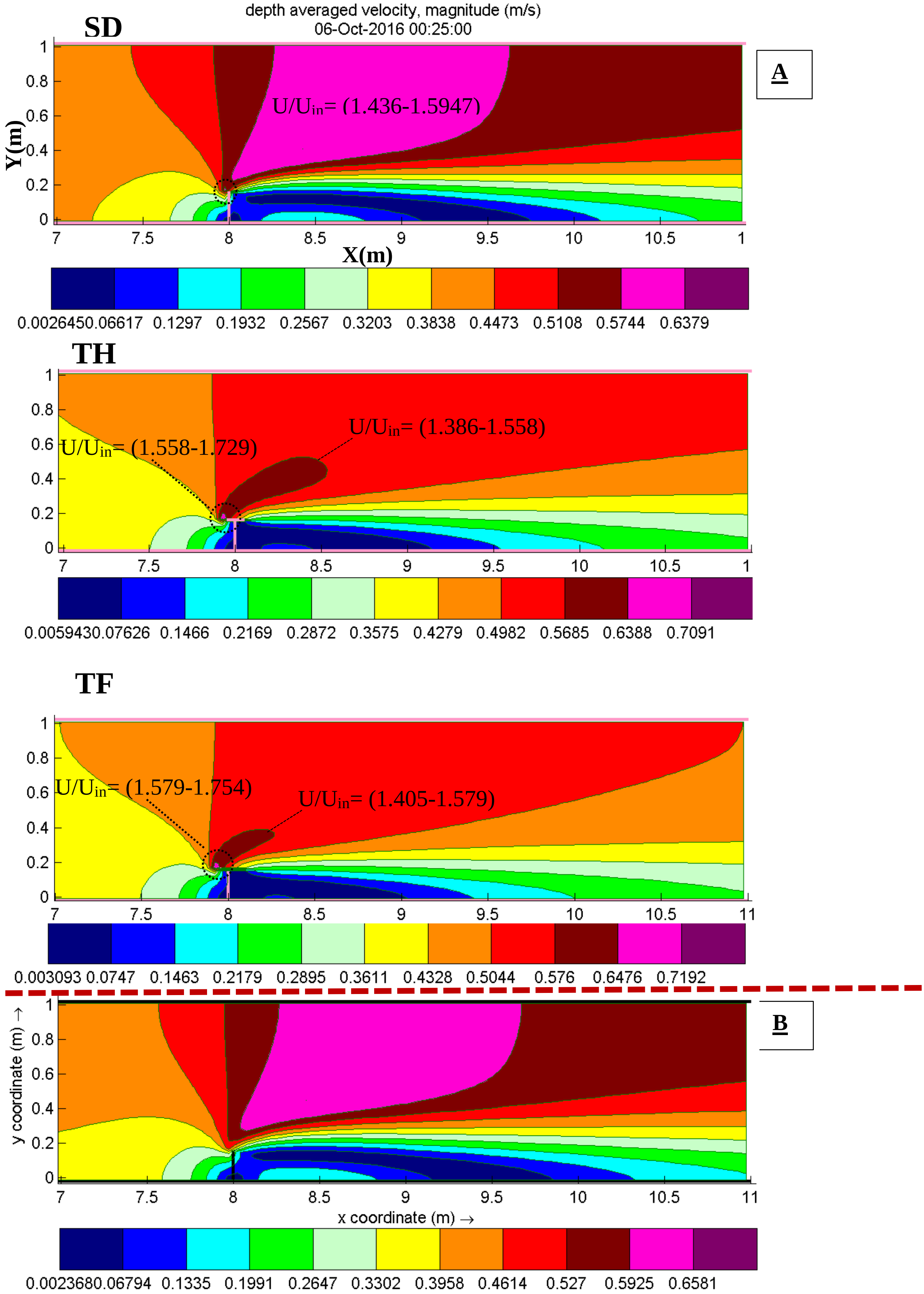

Figure (9.12) Average velocity magnitude for Setup#1 (A-HLES excluded for (SD, TH and TF) groynes, B- Setup#2, HLES included for SD groyne

9.3.2. Second Flume Test

This study was conducted with a flume size of w=3m and L=20m, as shown in Figure (9.13). On one side of the flume, the depth was shallower compared to the rest of the flume. The entrance and outlet width of the flow were 2.25m. The remaining width (0.75m) was dry for a distance of 5m from the inlet and 5m at the end of the flume in the stream-wise direction. A series of groynes was assigned in the intervening length (10m), and two different groyne embayment aspect ratios were examined. In the first setup, the aspect ratio between all the groynes was L_g/L_f=0.7, and in the second setup the aspect ratio was changed to 0.3.

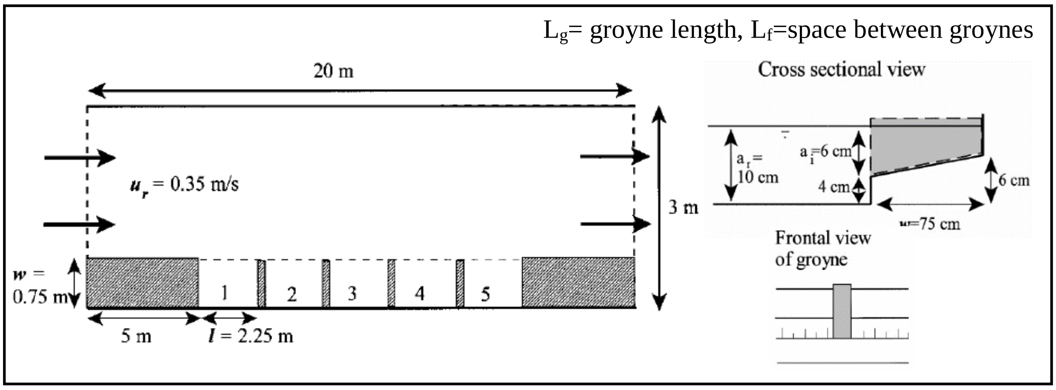

Figure (9.13) Second flume setup from Uijttewaal et al. (2001)

The aim of this study was to show the difference in the flow pattern between the groynes depending on the aspect ratio. This study was expanded in 2002 by comparing the flow patterns in the flume with the flow patterns in Elbe River, as shown in Figure (9.22). In addition, in this river the sediment deposition and scour were measured at the groyne zone, as shown in Figure (9.25). This study played an important role in validating the morphology changes between emerged groynes in the current study.

9.3.2.2 Model Setup for the Second Experiment

The flume experiment was set up with a cell size of 0.25x0.05m. The first groyne was set at a distance of 7.25m from the inlet of the flume for both aspect ratio simulations, as shown in Figure (9.14).

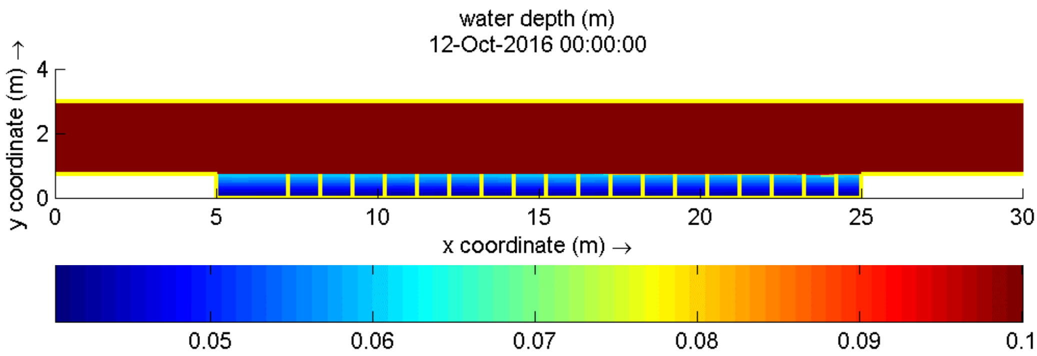

Figure (9.14) Water depth and groynes in the second flume before starting simulation

Like the previous flume model, a time step (0.001min) was applied to satisfy the Courant number condition. In the experiment, the water depth was 0.1m. To obtain this at the inlet and outlet of the flume, a discharge of 0.079m^3/s and water level of -0.009m were implemented respectively. Regarding the physical parameters, a horizontal eddy viscosity of 0.003m^2/s was applied to obtain a depth-averaged velocity of 0.34m/s and Froude number of 0.34 at the inlet of the flume. The other parameters in the model were the same as for the previous flume model (Setup#1-HLES excluded).

9.3.2.3. Model –Experiment Results

The depth-averaged velocity vector and magnitude of the model results were compared with the experiment for both aspect ratios. As shown in Figures 9.15 and 9.16, in both the first and eighth groyne zones for aspect ratio 0.7, the model predictions were almost the same as the observations. The stream-wise velocity magnitude outside the groyne zone was almost the same, but the velocities inside the groyne zone were slightly lower compared to the physical experiment.

However, for aspect ratio 0.3, the model only predicted primary circulation; secondary circulation was not predicted inside the groyne zone, as shown in Figure (9.17). According to the laboratory results, the main circulation took 2/3 of the groyne zone, and the smaller circulation cell appeared at the left side of the groyne zone. The lack of prediction of this secondary cell may be related to the velocity in the main channel near the groynes. Uijttewaal et al. (2001) only referred to the velocity at the flume inlet and did not indicate how much the velocity increased with the presence of groynes in the channel. The model results (Figure 9.18) showed that the velocity in the main channel near the groyne zone was higher than the velocity at the flume inlet.

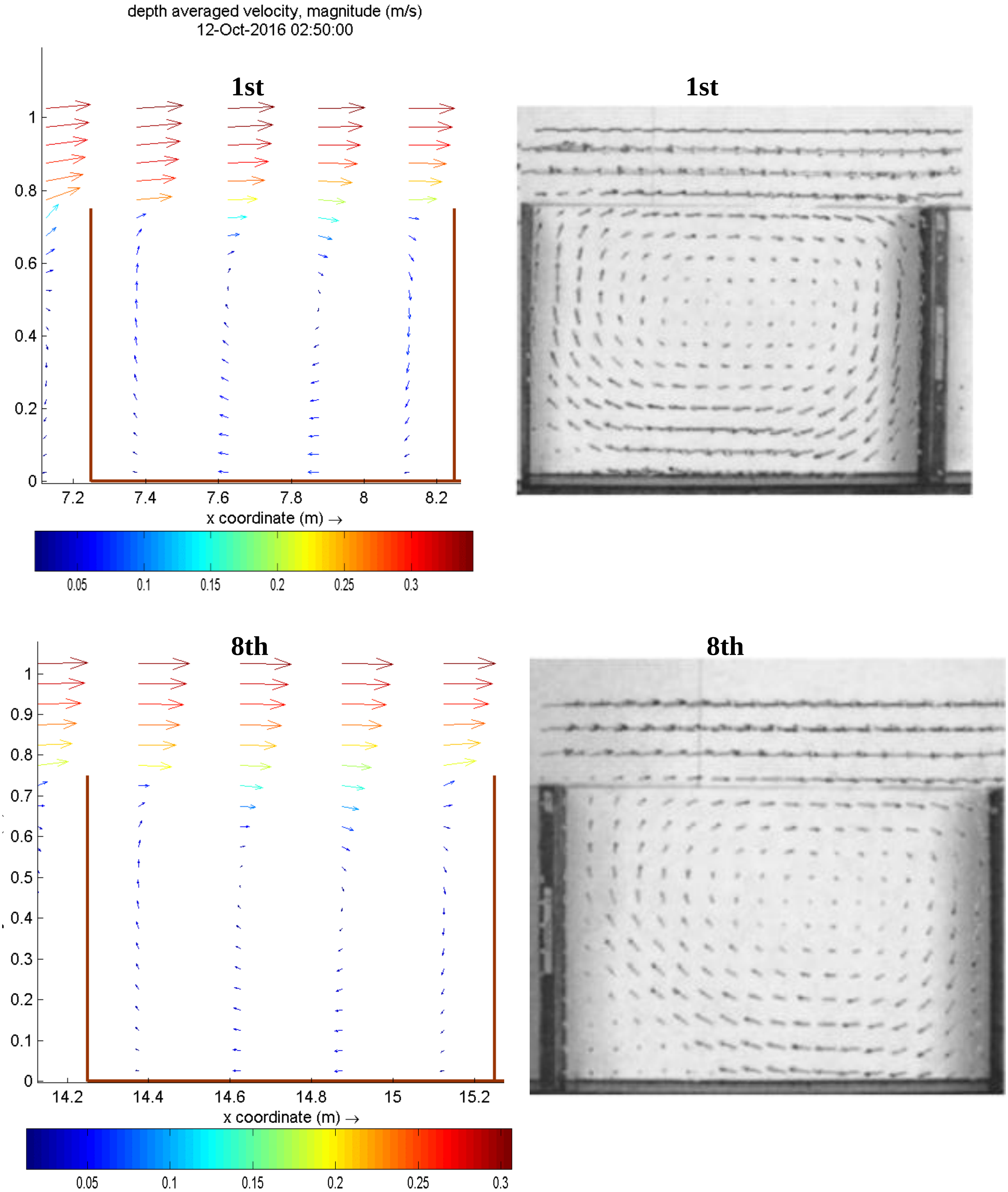

Figure (9.15) Depth-averaged velocity vector of the model results at left and the experiment results at right (from Uijttewaal et al., 2001) for aspect ratio 0.7 at the 1st and 8th groyne zones

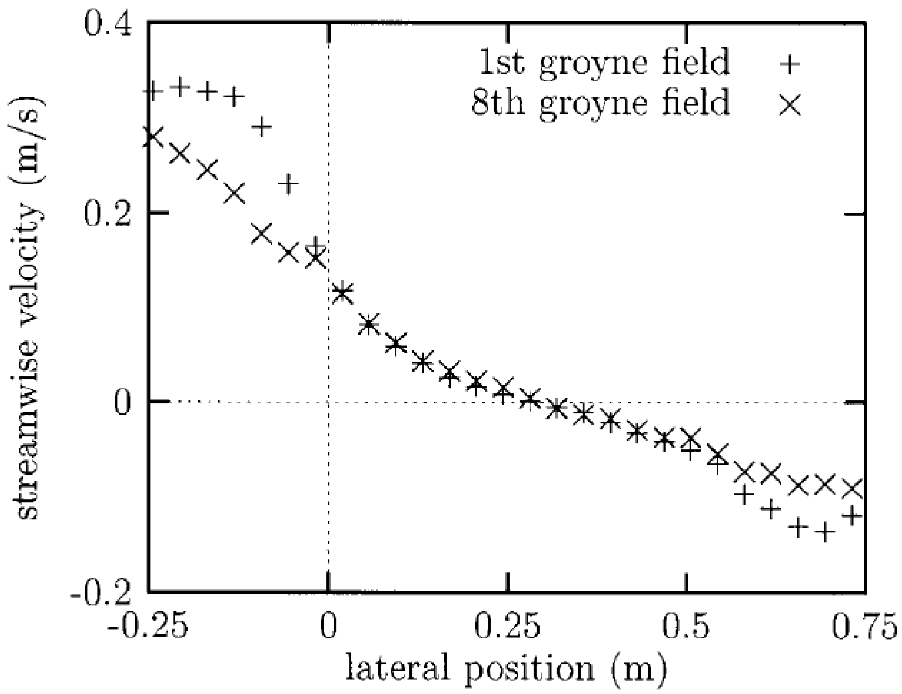

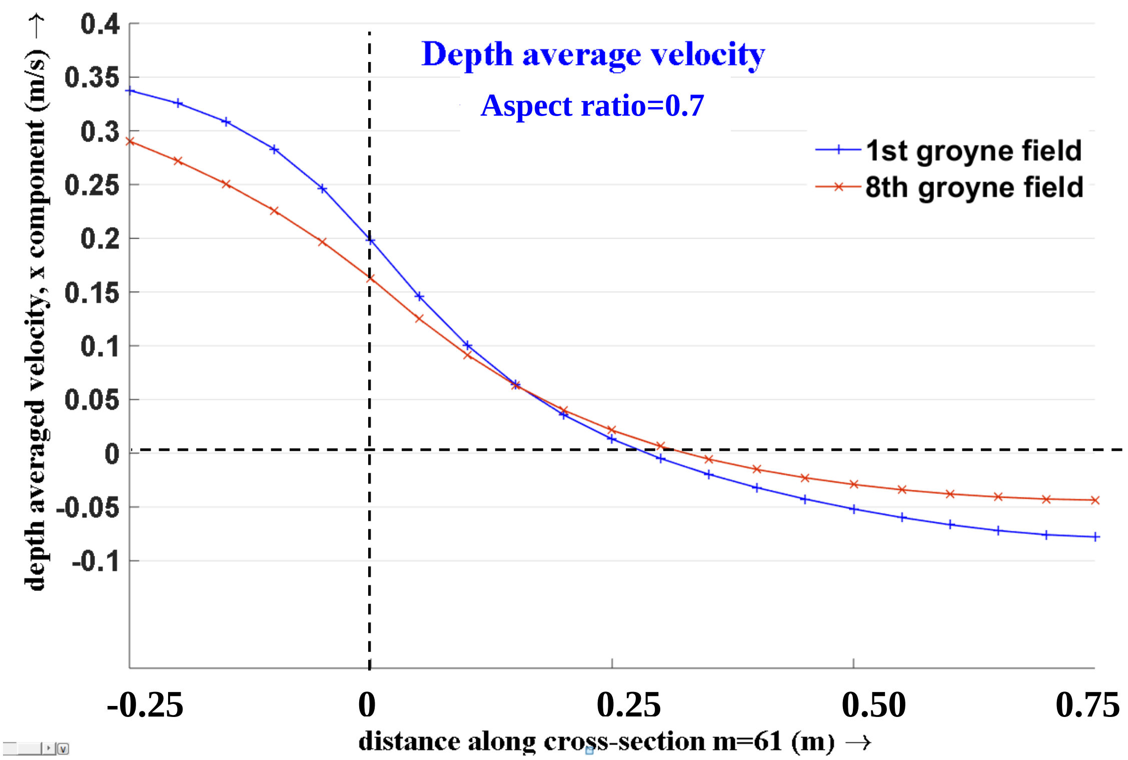

Figure (9.16) Depth-averaged stream-wise velocity at the first and 8th groyne zones for aspect ratio 0.7 (top-experiment, from Uijttewaal et al., 2001), bottom -Delft3d results)

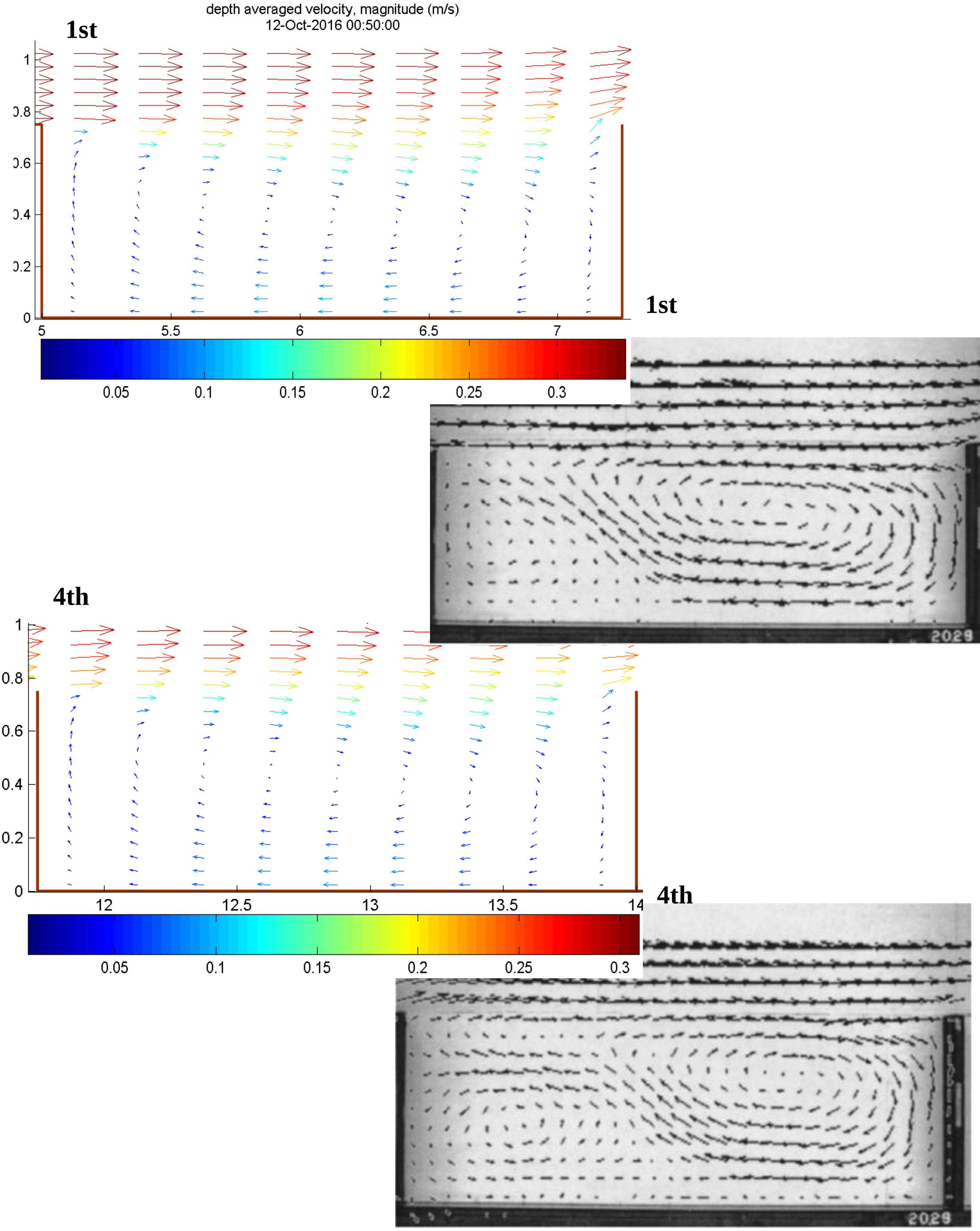

Figure (9.17) Depth-averaged velocity vector of the model results at left and the experiment results at right (from Uijttewaal et al., 2001) for aspect ratio 0.3 at the 1st and 4th groyne zones

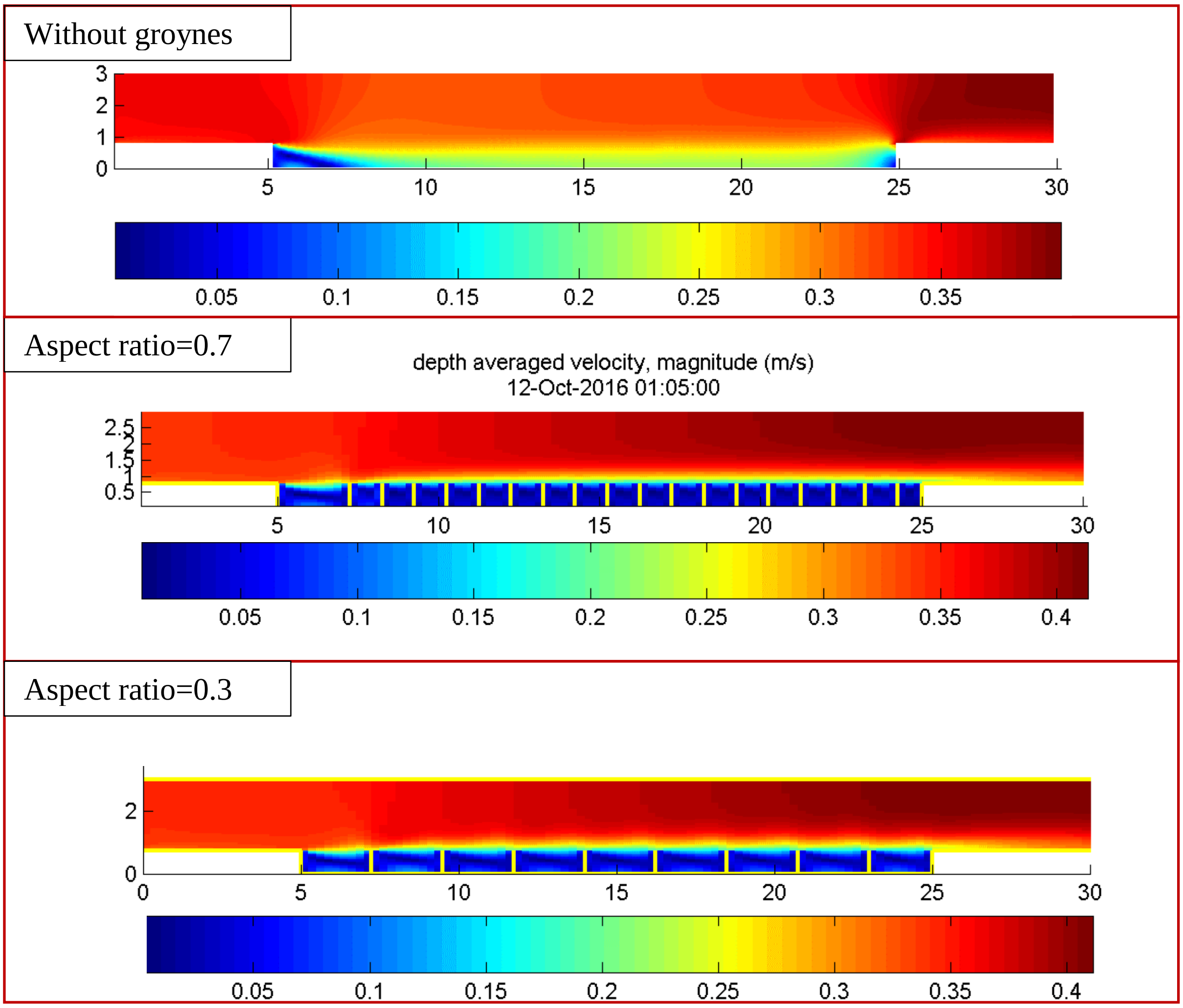

Figure (9.18) Depth-averaged velocity in the flume for aspect ratios 0.7 and 0.3

9.4. Applying groynes to the River (Study Area)

9.4.1. Model Setup

Groyne Structure

In this section, multiple setups are presented. First, multiple setups, differing only in the groyne elevations, are presented to assess the model for both emerged and submerged groynes. This is followed by presenting the impact of modifying groyne length and head shape on the river's hydro-morphodynamic. Whenever possible, these model results were compared to previous field and laboratory experiments. It is important to mention that in this study, only groynes with an angle of 90 degrees to the bank were considered.

Groynes_Setup#1

In this setup, the aspect ratio (L_g/L_f) of all the groynes were in range the 0.5-2, except those that were defined in Zone-1, as shown in Figure (9.19-B). The dimensions of the groynes are given in Table (9.3). When the groynes were included in the model setup (Section 9.2.3), their crest elevations (HKRU) had to be defined. In this setup, the crest elevation of all the groynes was defined at 461.5m, which represents the water level in the normal period. Depending on the groyne classification (in Section 2.4), this setup could be referred to as emerged and impermeable groynes in the normal period. It is crucial to mention that the thickness of the groynes cannot be defined for this structure in Delft3D. Furthermore, it is essential to mention that in the following model setups the other parameters (Section 9.2.3) were not modified, and only the groyne setups were changed.

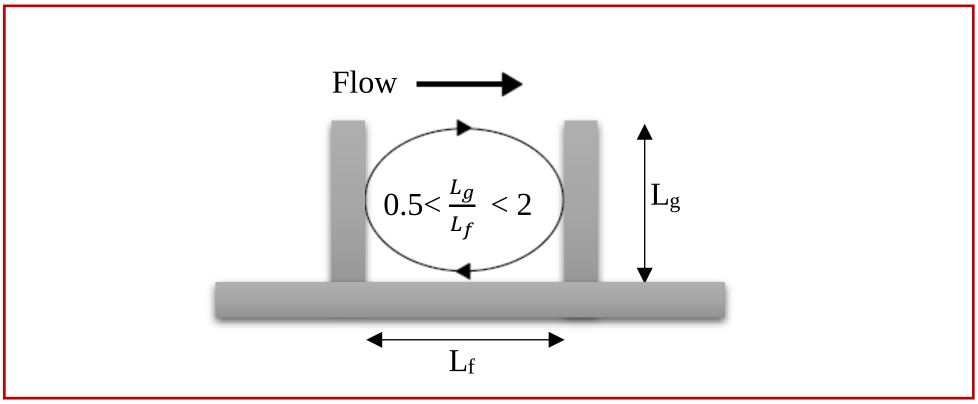

Figure (9.19-A) The flow pattern example in between groynes of aspect ratio between 0.5-2

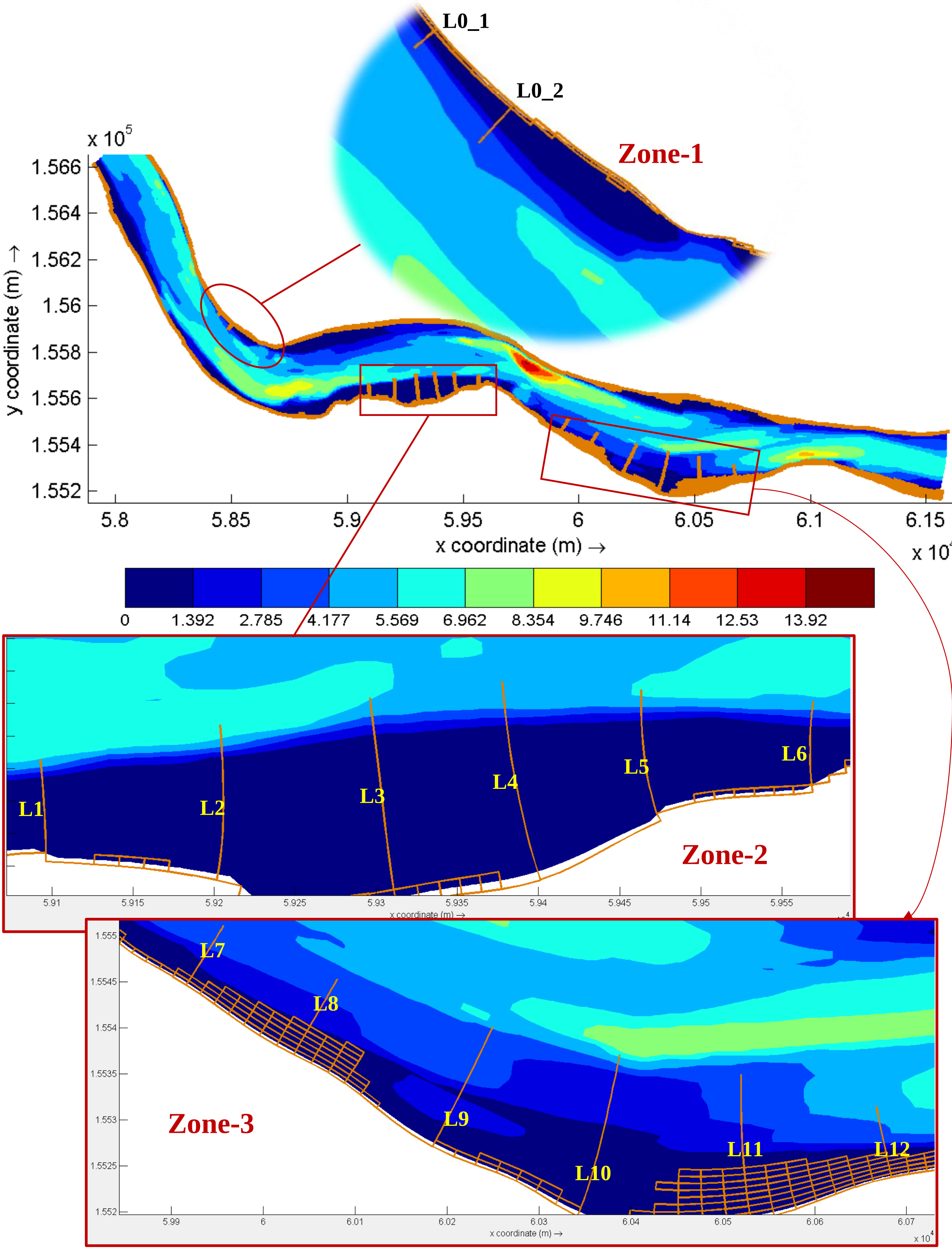

Figure (9.19-B) Water depth and groyne locations before starting the simulation

Table (9.3) Dimensions of impermeable non-submerged groynes

	Setup#1			Setup#2		
Name	Lg(m)	Lf(m)	Lg/Lf	Lg(m)	Lf(m)	Lg/Lf
L0_1	19	70.78	0.268	19	70.78	0.268
L0-2	33.38			33.38		
L1	65	92	0.707	65	92	0.707
L2	95.6	107.57	0.889	87.76	107.57	0.816
L3	129.66	88.67	1.462	121.66	88.67	1.372
L4	124.3	81.07	1.533	116.3	81.07	1.435
L5	82	98	0.837	75.5	98	0.770
L6	56.56			47.26		
L7	77.3	142.72	0.542	72.3	142.72	0.507
L8	93.5	159.1	0.588	87.5	159.1	0.550
L9	145.8	173	0.843	131.8	173	0.762
L10	181.7	152.7	1.190	159.7	152.7	1.046
L11	159	156.6	1.015	137	156.6	0.875
L12	78.2			78.2		

In Setup#1_2 and Setup#1_3, the same setup (#1) was used, with only changes in elevation of the weir crest. In other words, the groynes were submerged in these setups by lowering the groyne crests by half a meter and one meter, respectively. In Setup#2, the length of the groynes was decreased, but the aspect ratio was kept in the range 0.5-2, as shown in Table (9.3). In setup #3_1, the groyne crest height elevation was changed, as shown in Figure (9.20), but the aspect ratio remained the same as in Setup#2. Setup#3_2 was the same as Setup#3_1 except that the elevation of the last segment of groynes was submerged by 0.5m. In the final setup, the heads of the groynes were modified to L-head, but the elevation remained the same as in Setup# 3_1.

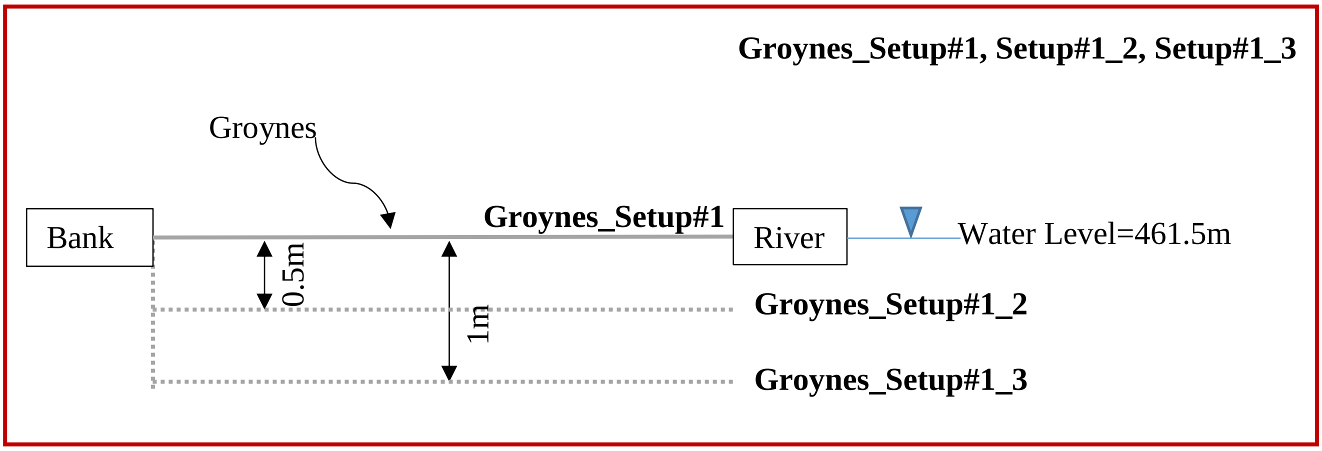

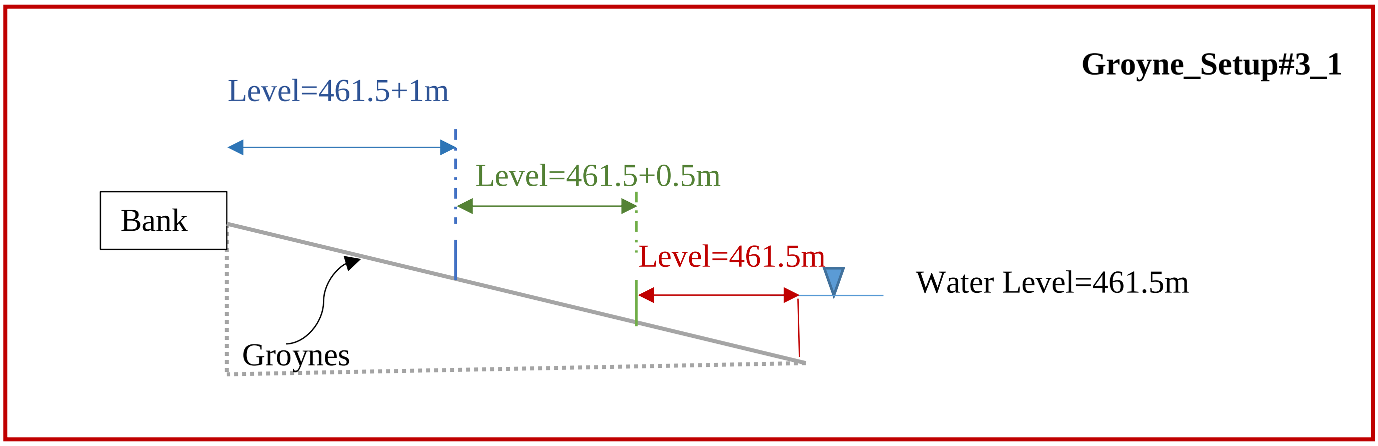

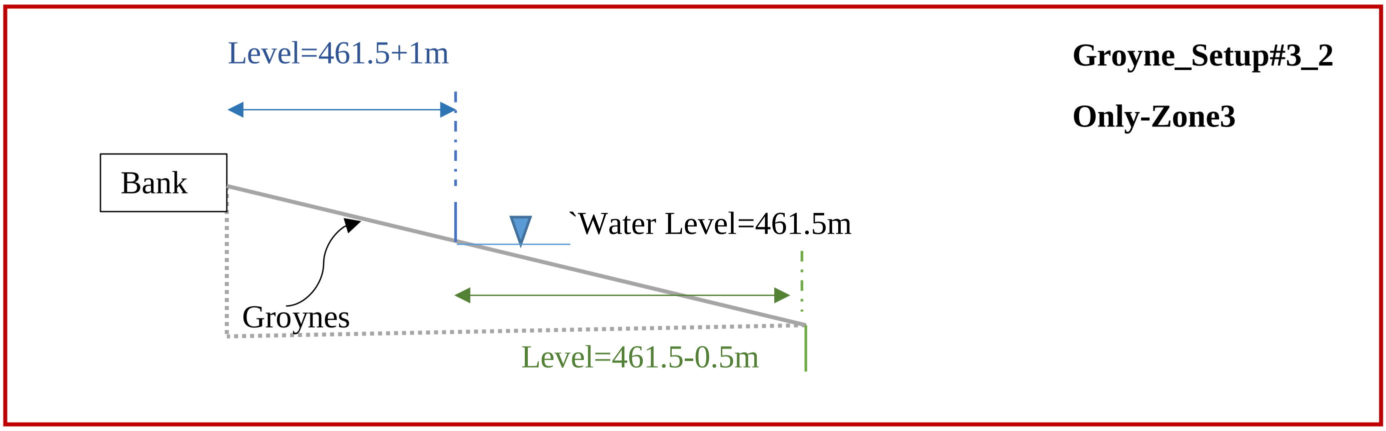

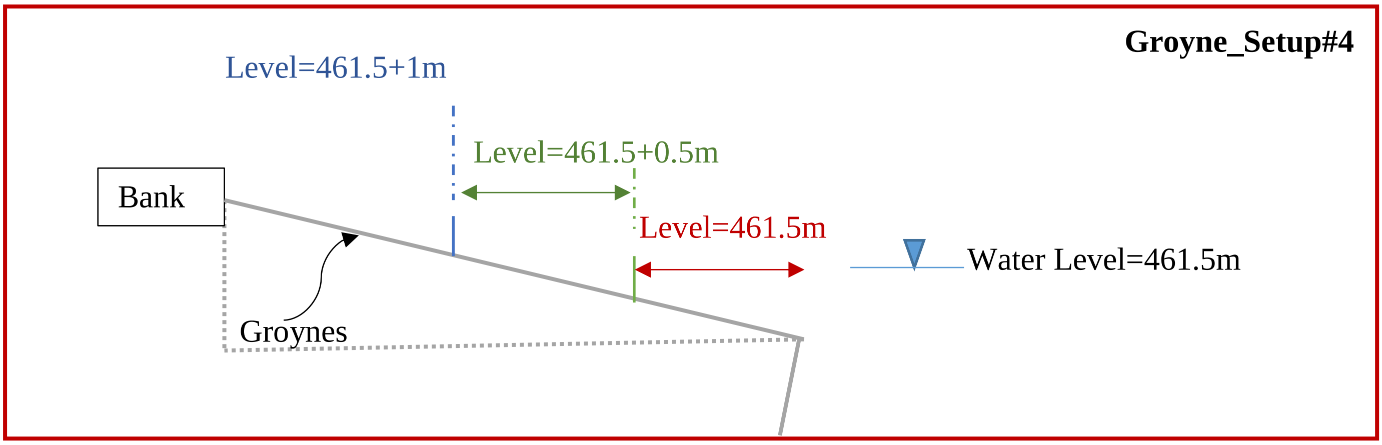

Figure (9.20) Different setups of the groynes in the river model sorted from top to bottom: Setup#1, Setup#1_2, Setup#1_3, Setup#3_1, Setup#3_2, and Setup #4. The groynes are divided into three segments with different elevations represented by the colors blue, green and red.

9.4.2. Model Assessment

Hydrodynamic-Emerged (Setup#1)

Checking the model's predictions was essential in this large scale. Therefore, the model results were compared qualitatively with field measurements collected in Elbe River by Sukhodolov et al., (2002). According to their investigation, when the aspect ratio of the emerged groynes is in the range 0.5-2, one single eddy is formed. Comparing the depth-averaged velocity vector of the model results (Figure 9.21) with the Elbe River measurements (Figure 9.22-a), a similar pattern of circulation was predicted in most of the groyne embayment.

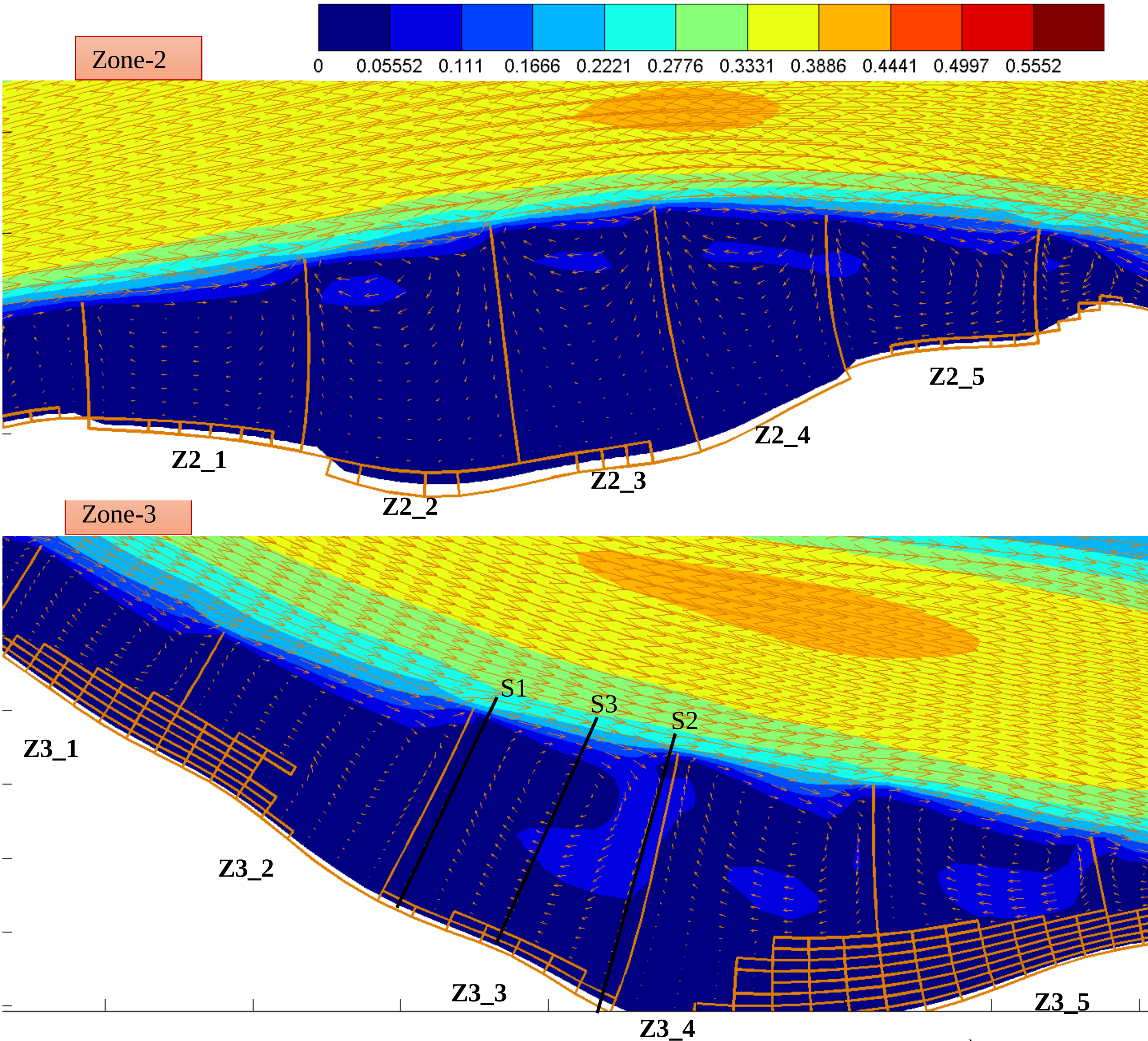

Figure (9.21) Depth-averaged velocity magnitude (m/s) (background color) and vector on 18th Nov 2012 at the end of the 14-day simulation, Setup#1 (emerged groynes shown in orange)

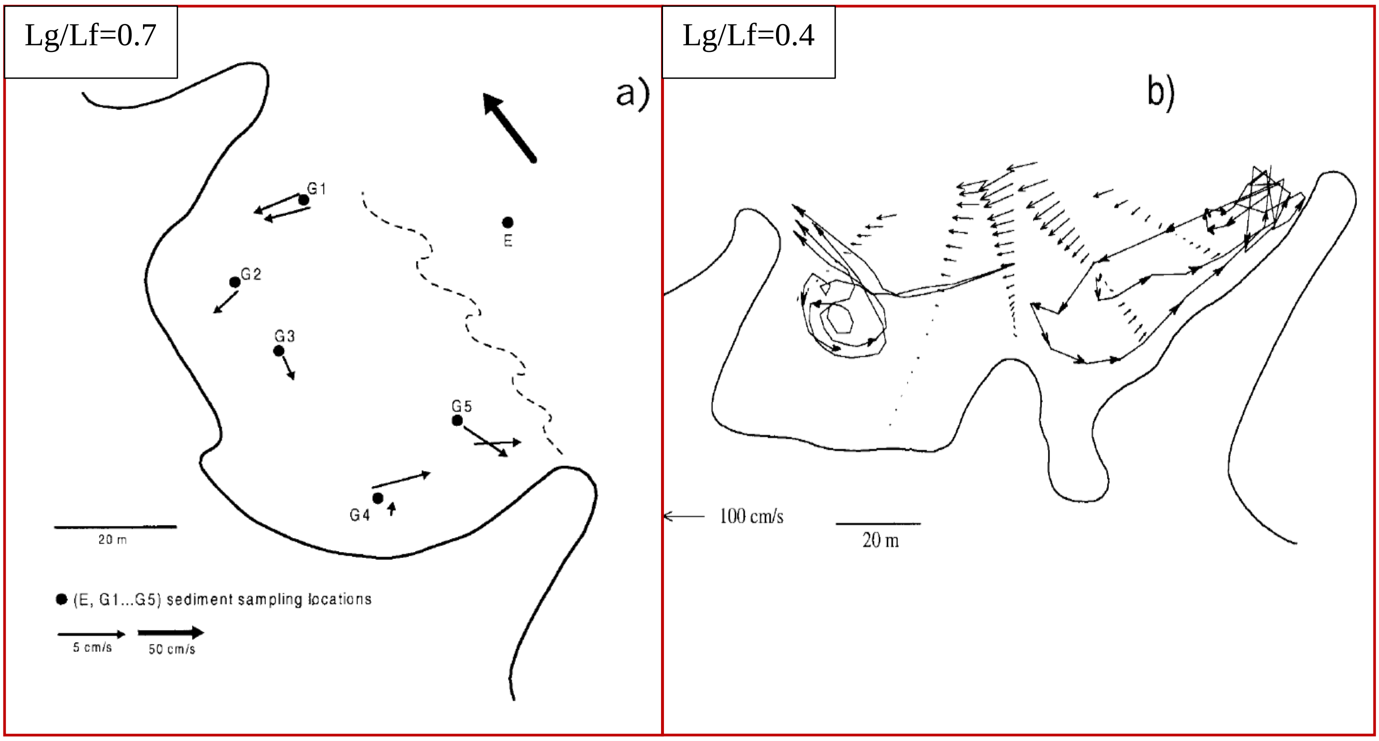

Figure (9. 22) Mean time velocity vector distribution in the Elbe River: a- Depth-averaged velocity in one section of the river (known as river-km317), b- velocity in the middle of the water column, and example of drifter trajectories in section river-km420 (from Sukhodolov et al., 2002)

Quantitatively, for the Elbe River, the velocity in the main channel was 0.5m/s and decreased to about 0.05m/s in the groyne embayment. In the model results, depending on groyne order and location in the river, the circulation quantity varied. For example, in Zone-2, the highest velocity in the main channel was about 0.45m/s, and in the embayment, the velocity was in the range 0.05-0.1m/s, depending on its order in the groynes zone.

Hydrodynamic -Emerged and Submerged

The second validation was conducted for Setup#1, Setup#1_2 and Setup#1_3, which represented emerged, submerged (0.5m), and submerged (1m) groynes respectively. The model results were compared with a flume experiment (Yossef & de Vriend, 2010). Prior to proceeding to the comparison, a brief description of this study is provided.

The experimental test was conducted on a rectangular flume, as shown in Figure (9.23). The bed sediment consisted of sand (D_{50}=0.164mm). The aspect ratio of the groynes was 0.31. The thickness of the bed sediment layer varied from 0.125-0.175m in order to maintain the different levels of submergence of the groynes, as shown in Table (9.4). The exchange of sediment between the main channel and the groyne zone, suspended sediment concentration, bed level change, sediment transport, and flow velocity in the embayment were investigated. Depth-averaged velocity was measured by electromagnetic flowmeters _EMFS at (S1 and S2) Figure (9.23).

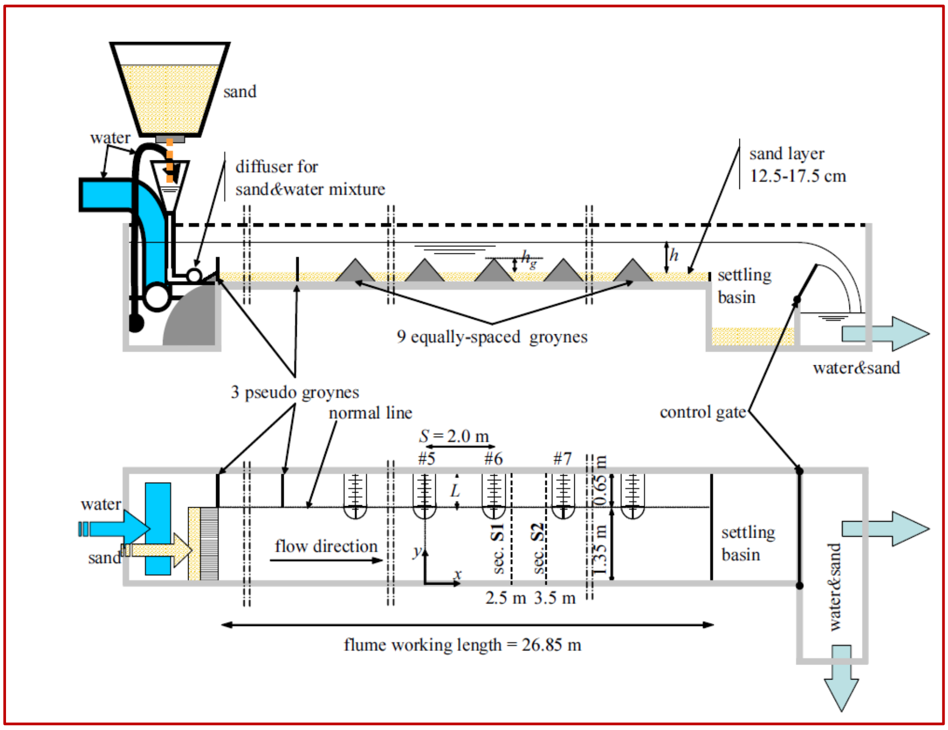

Figure (9.23) Flume setup (from Yossef & de Vriend, 2010)

Table (9.4) Experimental setup (from Yossef & de Vriend, 2010)

Test name	h_g (m)	h/h_g	h (m)	$\bar{u}_{mc}$ (m/s)	Q_w (m^3/s)	Q_s (kg/h)	R	F
G1i	0.125	1[a]	0.125	0.277	0.058	29.03	11,250	0.27
G1a		1.4	0.175	0.298	0.088	33.54	15,626	0.23
G1b		1.7	0.213	0.310	0.111	36.29	19,737	0.21
G1c		2.0	0.250	0.320	0.134	38.67	23,970	0.20
G2i	0.100	1[a]	0.100	0.263	0.044	26.22	7,895	0.27
G2a		1.4	0.140	0.284	0.067	30.51	11,924	0.24
G2b		1.7	0.170	0.296	0.085	33.14	15,089	0.23
G2c		2.0	0.200	0.306	0.103	35.42	18,352	0.22
G3i	0.075	1[a]	0.750	0.245	0.031	22.81	5,523	0.29
G3a		1.4	0.105	0.266	0.047	26.82	8,385	0.26
G3b		1.7	0.128	0.278	0.060	29.29	10,639	0.25
G3c		2.0	0.150	0.288	0.073	31.43	12,967	0.24

[a]Emerged groynes.

After comparison of the current river groyne setup with that of the flume, only the cases of G1i and G1a in Table (9.4) were slightly similar to the river groyne setups (emerged and submerged). In the flume, of the relative groyne submergence (h/hg) had the same value along the length of each groyne. However, in the river model, this value varies due to complexity in the river bathymetry. For comparison with the flume, three sections (S1, S2 and S3) were taken at (Z3-3) groyne zone as shown in Figure (9.21).

In Figure (9.24-a, b), comparing the model's results for the depth-averaged velocity of the emerged and submerged cases with those of the flume showed nearly similar patterns. At both the S1 and S2 sections of the flume, increasing the submergence of the groynes increased the velocity in the groyne embayment and decreased the velocity near the head of the groynes. However, at section S1, for the emerged case, the model's velocity estimation was not less than zero, as was observed in the flume. This may be due to the dissimilarity of the aspect ratios of the flume and the model.

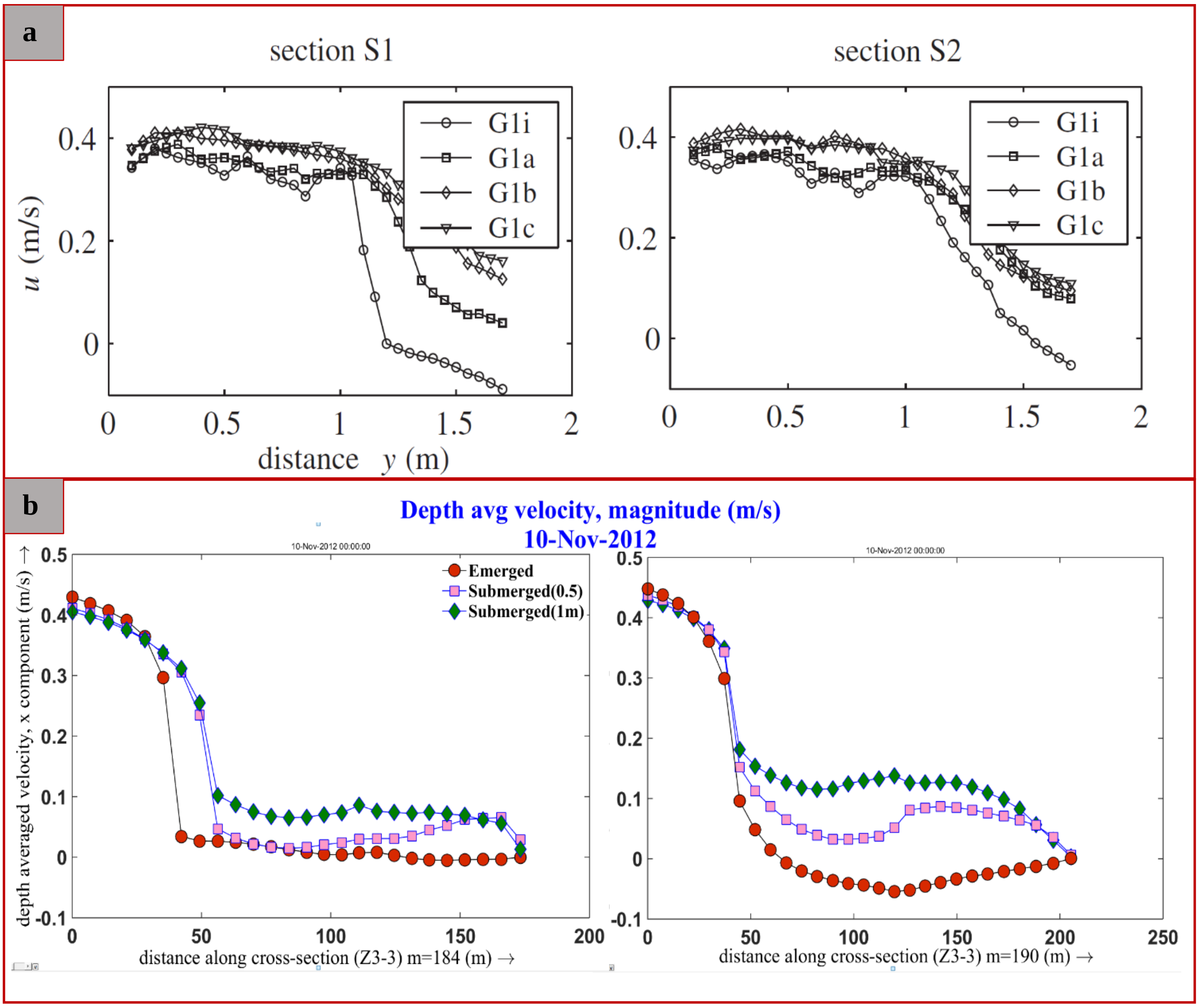

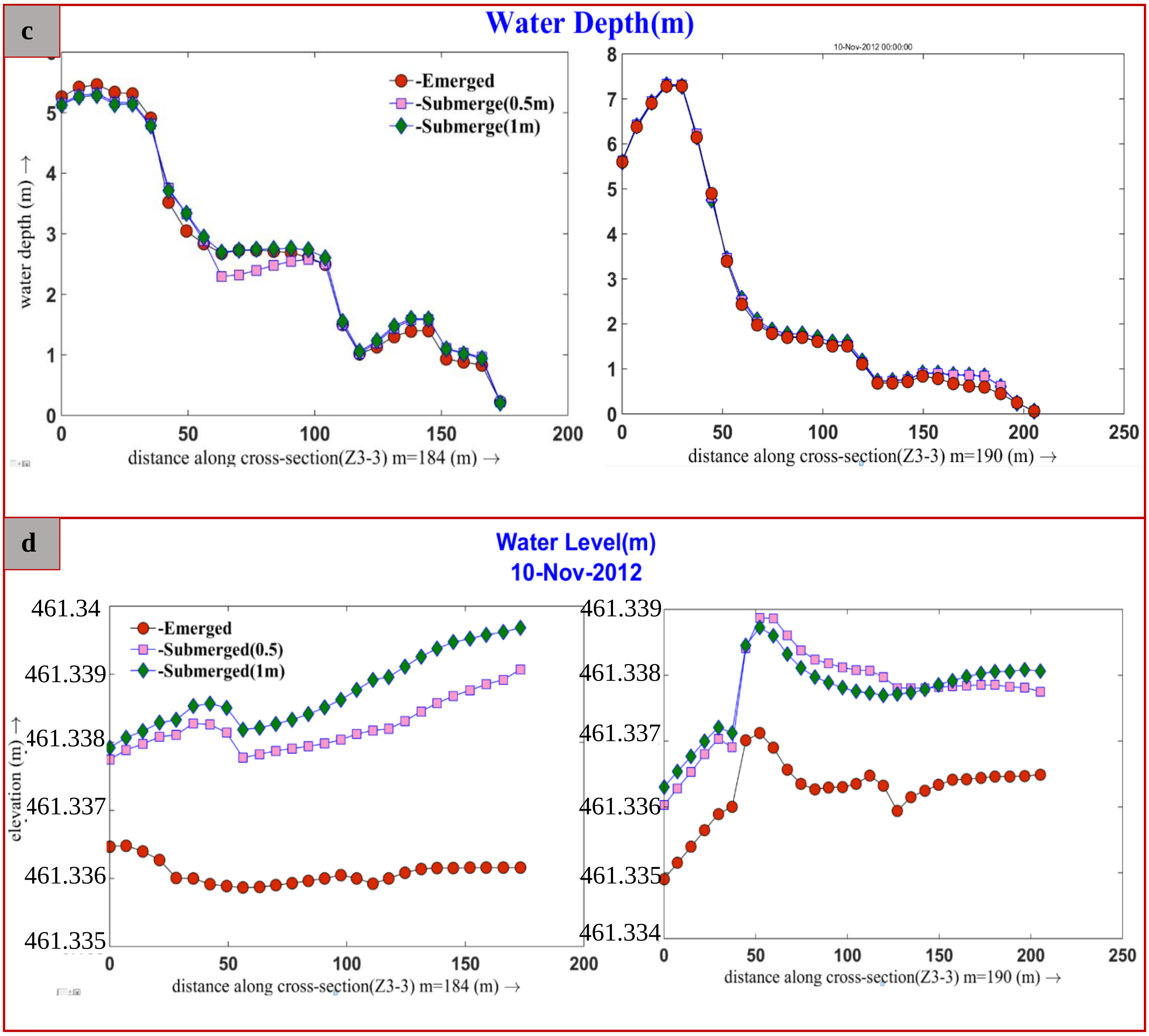

Figure (9.24) a) Depth-averaged velocity at cross-section S1 and S2 of the flume (Yossef & de Vriend, 2010). b) Model depth-averaged velocity at section S1 and S2. c) Model water depth. d) Model water level results for Setup#1 (Emerged), Setup#1_2, and Setup#1_

The emerged and submerged groynes produced different water levels in the groyne embayment Figure (9.24, d). For instance, at section S1 for the emerged case, the water level was slightly lower in the groyne zone compared to the main channel, whereas in the submerged case, the water level in the groyne zone was higher compared to the main channel. In addition, at section S2, for both the emerged and submerged cases, the water level in the embayment was higher compared to the main channel. Furthermore, a contrast in water level patterns near the head of the groynes between S1 and S2 was observed.

Morphodynamic -Emerged, Submerged

To assess the morphodynamic estimation of the embayment, the model results were compared with previous results at both field and laboratory scales.

In the emerged groyne embayment in the Elbe River (Sukhodolov et al., 2002), sediment deposition and entrainment were measured by a Sonar Lite portable echo-sounder system (OHMEX Instruments). The bed consisted mostly of gravel and sand, and the thickness of the deposited fine sediment was measured. It was observed that when the aspect ratio was 0.7, sediment accumulated at the center top between the groynes. This location coincided with the center of the velocity circulation. In addition, it was observed that scour occurred within the groyne embayment downstream of the tip of the groynes, as shown in Figure (9.25, a).

The result of the 14-day simulation (Setup#1) is compared with the Elbe River results in Figure (9.25-a, b). The model produced a similar pattern of deposition in the embayment. However, the scour position was slightly different. In the model, erosion was mostly estimated at the head of the groynes, whereas in Elbe River, entrainment was observed immediately downstream of the head, and penetrated toward the groyne embayment.

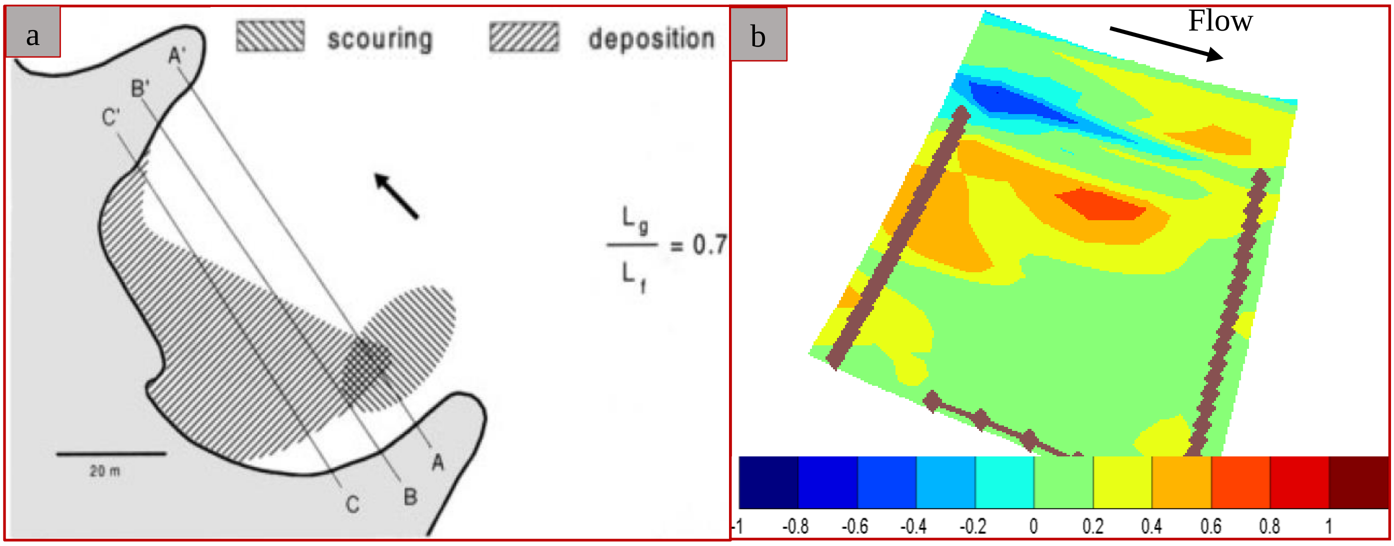

Figure (9.25) a-Area of scouring holes and deposited fine sediment for the groyne field with (Lg/Lf=0.7) of the Elbe River embayment obtained from field measurements (Sukhodolov et al., 2002). b- Cumulative erosion and deposition after 14 days at the Z3-3 groyne zone of Setup#1.

It was not possible to validate the accumulated erosion-deposition quantitatively due to dissimilarity in the river conditions, including flow rate, sediment concentration, grain size, etc. Nevertheless, the lateral concentration profile compared favourably with the flume experiment (Yossef & de Vriend, 2010). According to their flume results, with increasing submergence, sediment concentration in the embayment increased (Figure 9.26-a). The lateral profile of the cohesive sediment concentration showed a similar pattern to the flume results for both the emerged and submerged cases (Figure 9.26-b, c, d); however, the non-cohesive sediment concentration was underestimated Figure (9.26-e). According to Yossef and de Vriend (2010), the underestimation of non-cohesive concentration is related to the non-cohesive transport formula. Illustrating that sediment concentration near the groynes is not in equilibrium.

In addition, comparing the concentrations of all sediment fractions at Section S1 in the groyne zone shows that the sediment concentration decreases with increasing sediment grain size. For instance, looking at the concentration profile of both fractions (0.0075mm and 0.039mm) at Section S1, the difference between the mainstream and groyne zone concentrations of fraction 0.0075mm was lower compared to fraction 0.039mm (Figure 9.26-b,d).

At Section (S2), the cohesive sediment concentration of fractions 0.0075 and 0.019mm for the emerged and submerged (0.5m) cases were similar to those of the flume. However, for fraction 0.039mm, the emerged and submerged (1m) cases were more similar to the experiment. This may due to the difference in the grain size that was utilized in the flume.

For more illustration, the concentrations of cohesive fractions in the groyne zone and the distributed mass fractions in the bed are shown in Figures 9.27 and 9.28 respectively. This figure represents the results of the 14day unsteady simulation. At the end of simulation, the water level is at 461.5m. These figures show that the mass fraction distribution does not totally follow the path of the concentration. It can be said that the fractions will deposit only in places with low velocity.

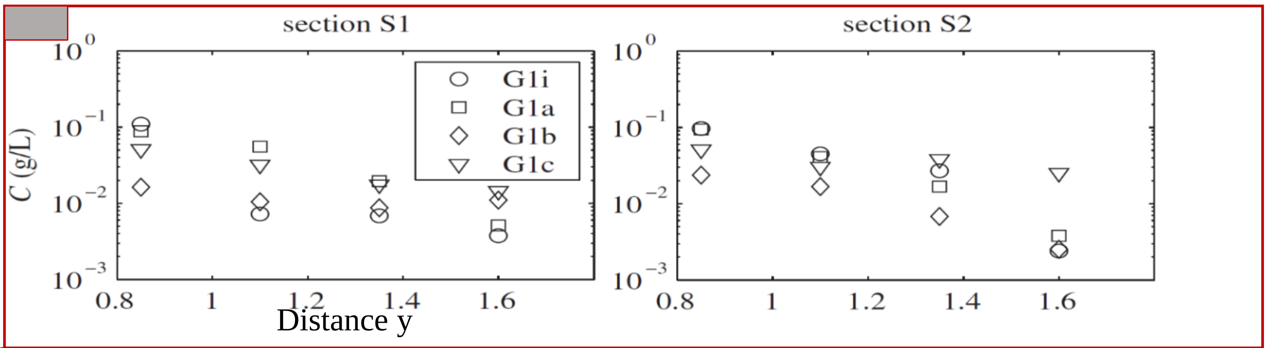

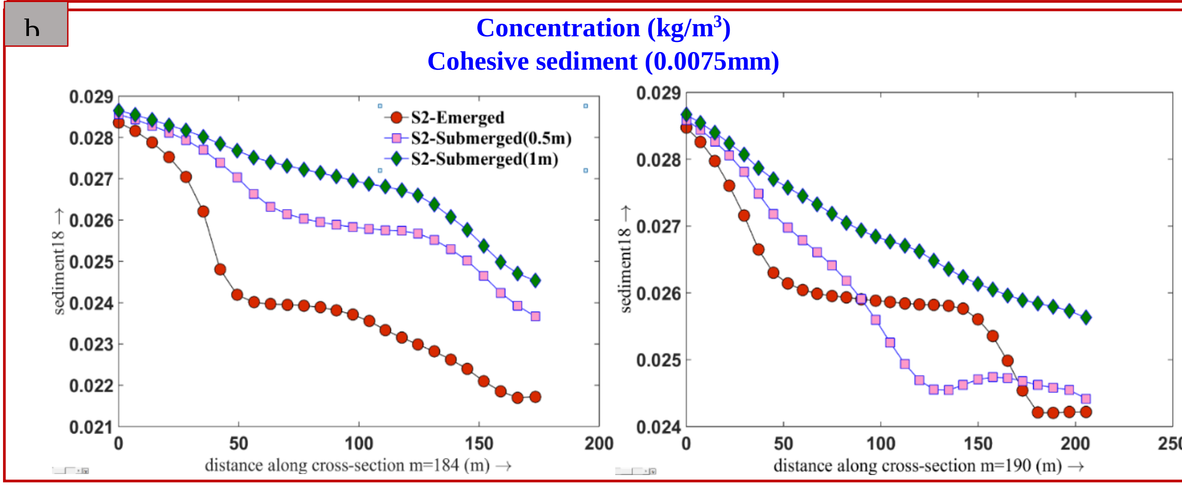

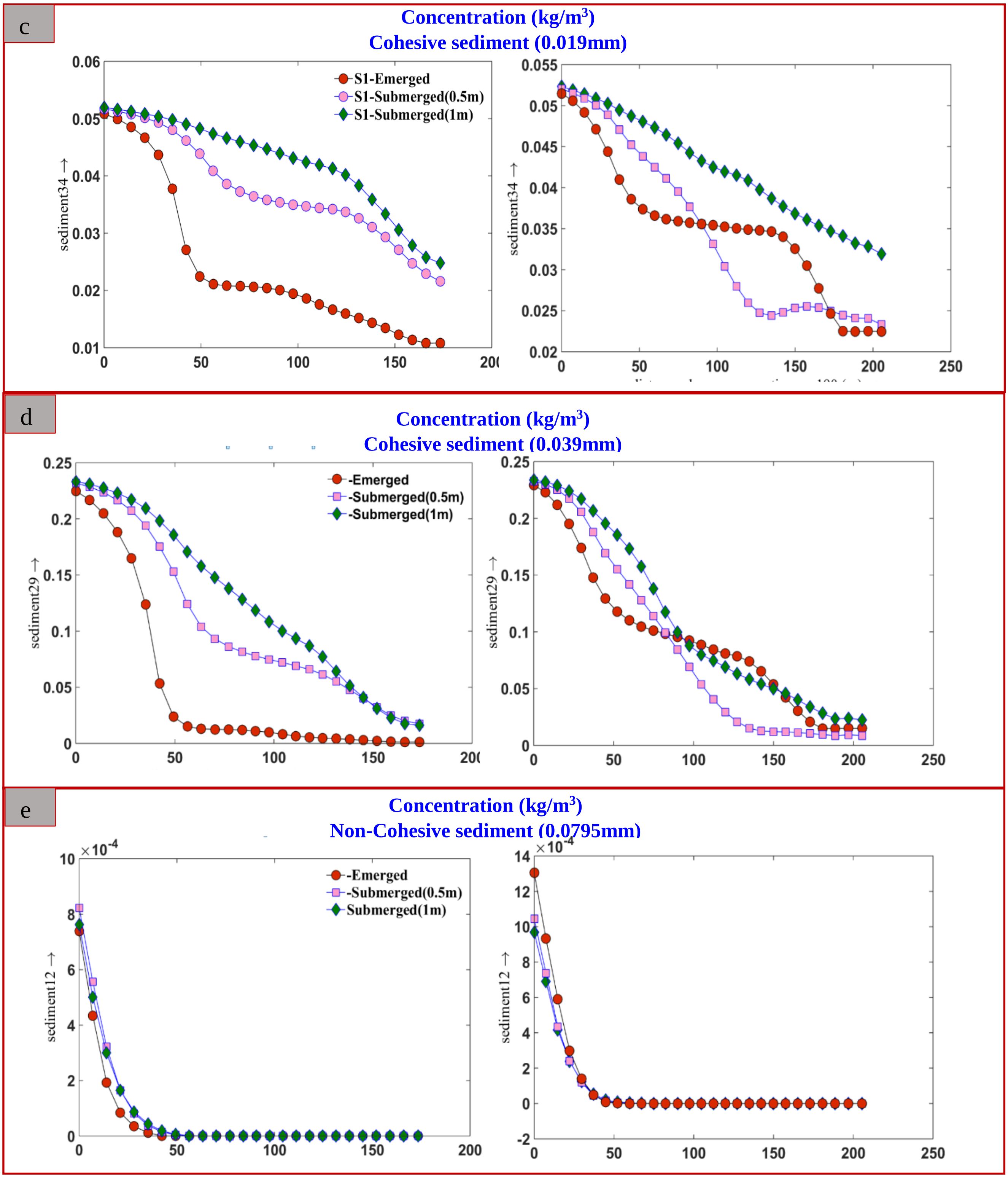

Figure (9.26) a) Sediment concentrations of the flume at the S1 and S2 sections for G1i case (emerged) and G1a, G1b and G1c (different submerged cases) (Yossef & de Vriend, 2010). b, c, d, e) sediment concentration profile at the S1 and S2 sections of the simulation results of the 14-day simulation for Setup#1, Setup#1_2 and Setup#1_3. a) Fraction 0.0075mm, b) fraction 0.019mm, d) fraction 0.039mm, and f) fraction 0.0795

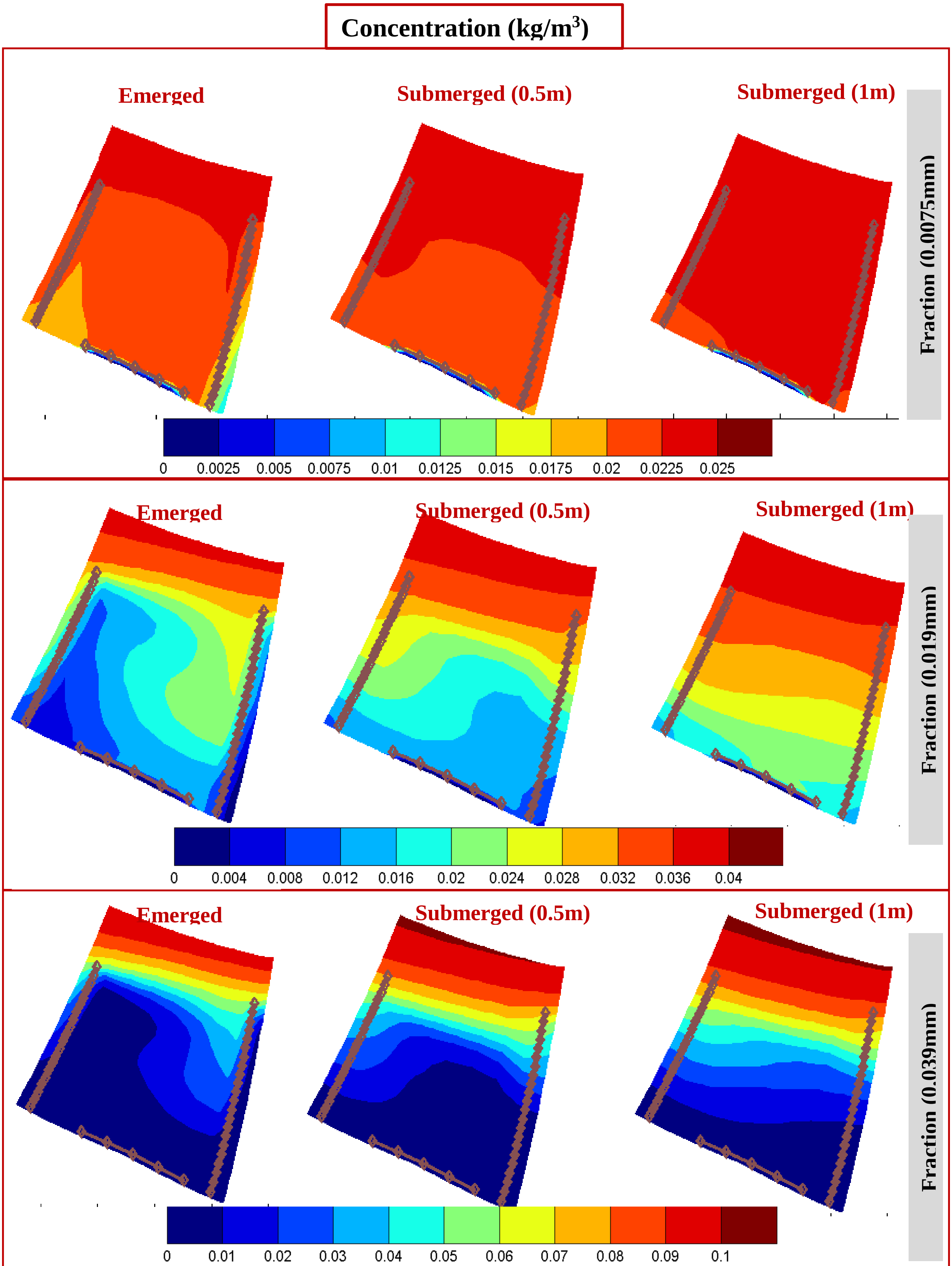

Figure (9.27) Sediment concentration distribution inside groyne zone Z3-3, sorted vertically from finest to coarsest cohesive fraction, and from left to right sorted by submergence level

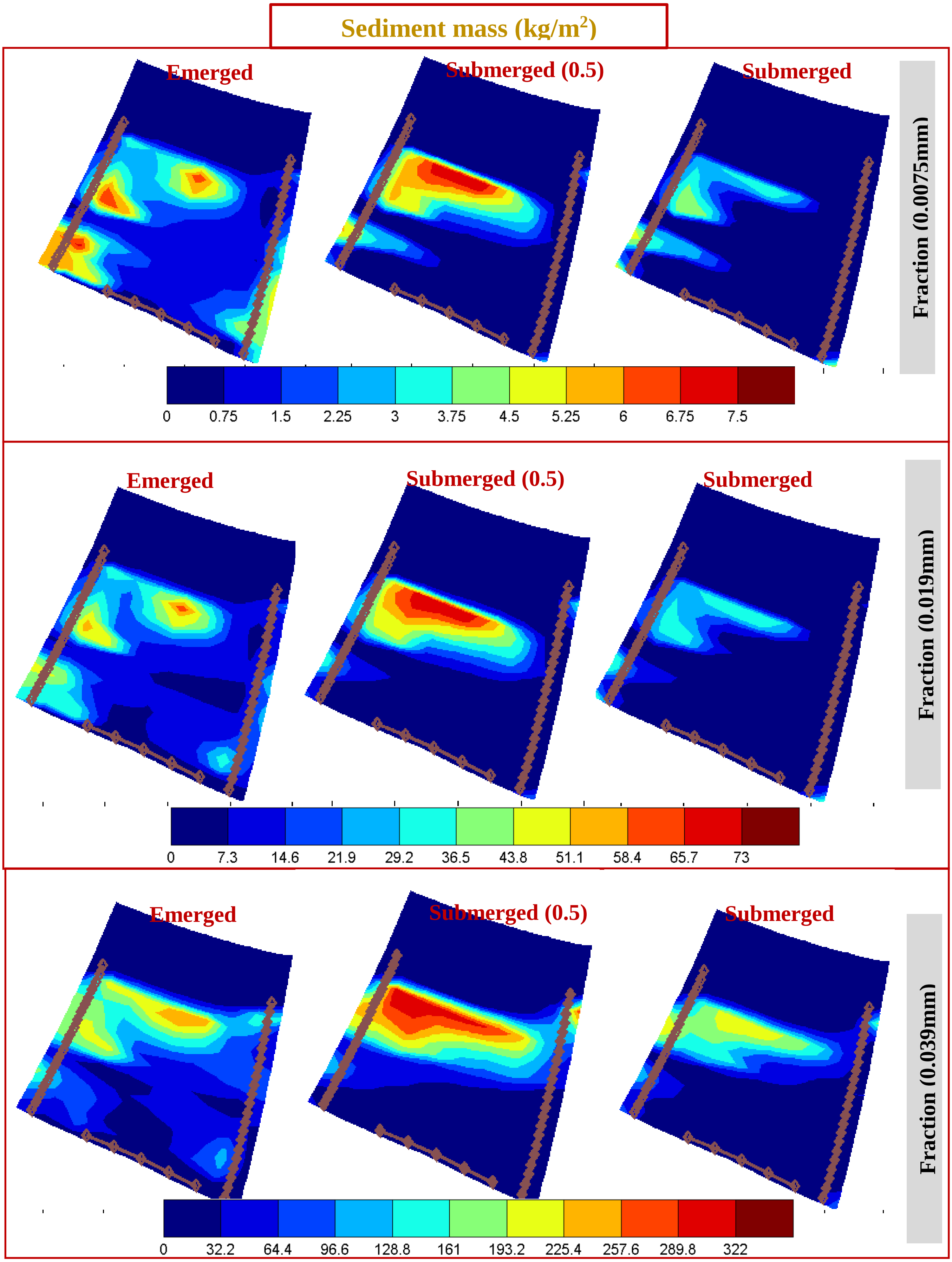

Figure (9.28) Sediment mass (kg/m^2) distribution in the bed (first layer) inside groyne zone Z3-3, sorted vertically from finest to coarsest cohesive fraction, and from left to right sorted by submergence level

In the flume results for the emerged case, most of the deposition was located near the normal line, and the smallest amount was found near the bank (Figure 9.29-a), whereas in the submerged case, deposition along the normal line was wider compared to the emerged case. In addition, the deposition rate of the submerged case (h/h_g=1.4) was less than that of the emerged case. Prior to making the comparison, it is essential to mention that the positions of erosion and deposition of the flume and the model are opposite due to the difference in aspect ratio of the groynes.

Similar to the flume result, the deposition rate of the modelled submerged (1m) case was less than that of the emerged case. However, the sedimentation rate of the emerged case was less than the deposition of the submerged (0.5m) case (Figure 9.29-c). This result may be due to the following:

- Although with groyne submergence, the depth-averaged velocity circulation vanished and the vector became parallel to the main channel, similar to Uijttewaal et al. (2005) and Constantinescu (2009), the zone of low velocity became wider in the submerged (0.5m) case compared to the emerged case (Figure 9.29-b). This resulted in a larger area of low bed shear stress between the groynes. According to Peng et al. (1997, as cited in Yossef & de Vriend, 2010), this low bed shear stress has an association with the ratio of groyne spacing to groyne height (hg). When the groynes become submerged, the flow inside the groyne zone increases, and if the space is not big enough, the flow cannot reattach to the bed, which leads to low bed shear stress.
- According to Constantinescu (2009), the ejection of contaminants from submerged groynes is much faster compared to emerged groynes because of the exchange mass in the top of the flow. This means that the sediment supply to the groyne zone is higher in the case of submergence.

Since the flume experiment was only run for 40 hours, it was essential to compare the model after two days with the flume results. Figure (9.29-d) shows the cumulative erosion and deposition on 6th Nov. 2012 at Section S3. Similar to the flume results, deposition near the groyne heads decreased with submergence of the groynes. However, at S1 and S2, the sedimentation of the emerged groynes was higher near the bank, although near the head the submergence (0.5m) case had the highest deposition.

It can be said that the pattern of (1m) submergence is more similar to the flume. Furthermore, the profile at the three sections in Figure (9.29-e) shows that that the peak deposition of the submerged case was located slightly behind compared to the emerged case.

Regarding entrainment estimation near the head of the groynes for the 14-day simulation, similar to the flume, the model estimated lower erosion for both submergence cases compared to the emerged case (Figure 9.29-c). The erosion estimation for the 0.5m and 1m submerged cases were almost the same. According to the flume results, it was seen that the scour at the head of the groynes fully developed after 10 hours, whereas deposition continued until the end of the 40 hours. In this model, the time series of the cumulative erosion-deposition showed that the change in erosion in the normal period was not high compared to the deposition rate inside the groynes (Figure 9.30 a, b, c). Stopping erosion in the flume at the early hours of operation may be related to thickness of the sediment available in the flume, whereas in the current river model, this low erosion may be due to underestimation of the model turbulence. This result may show that the development of erosion is much faster than deposition.

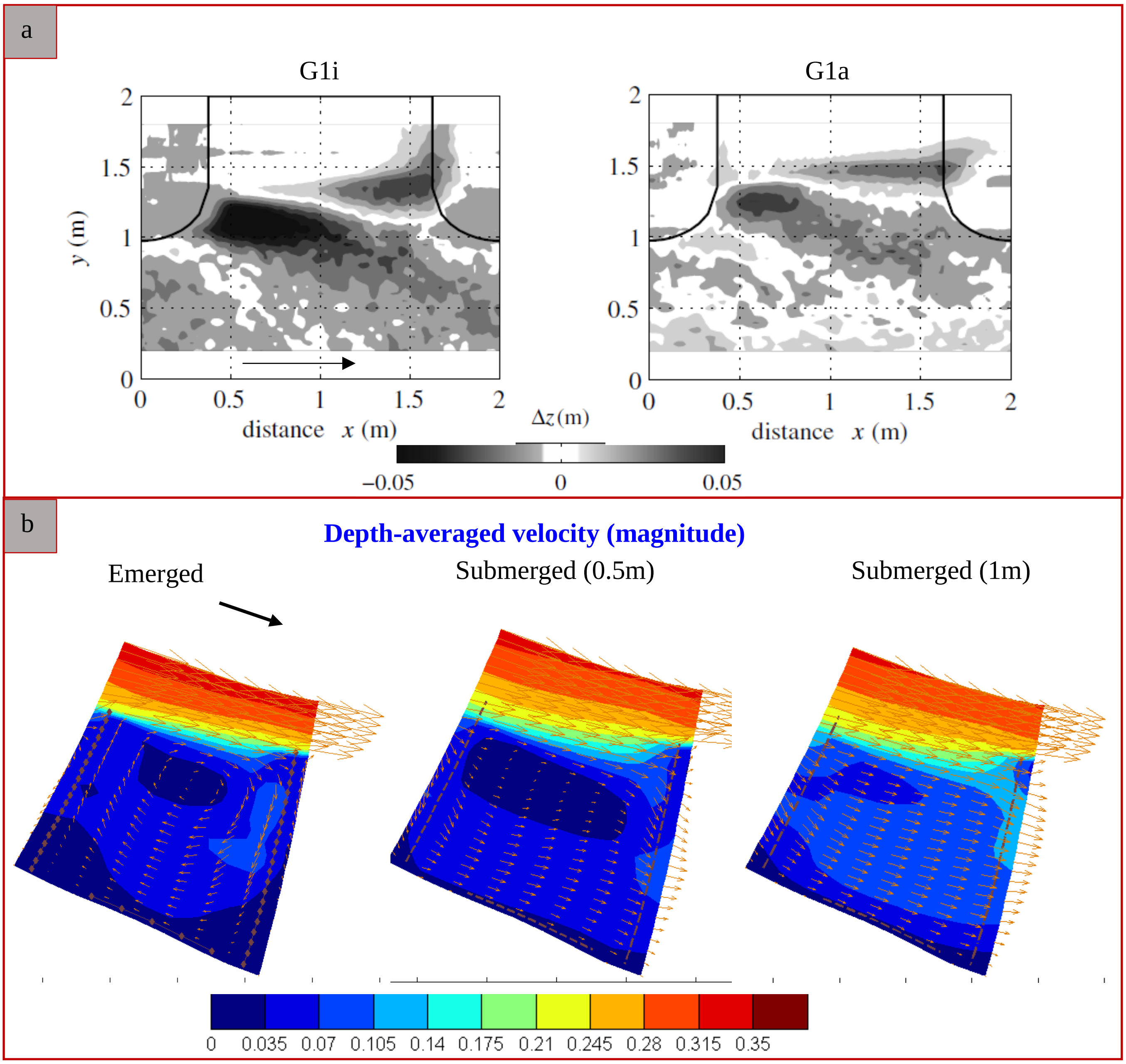

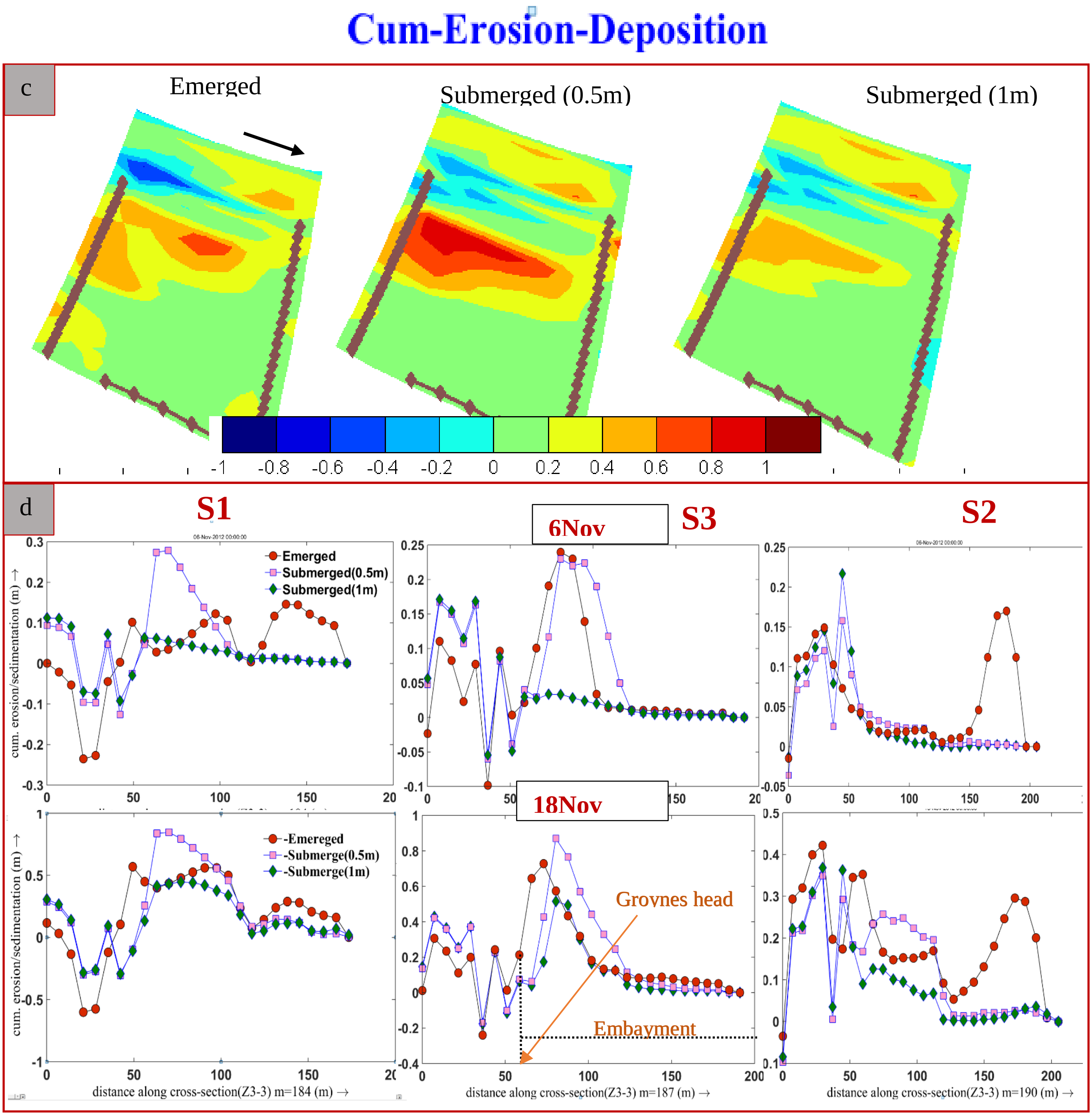

Figure (9.29) a) Accumulated erosion deposition (m) in the flume after 40 hours for emerged (G1i) and submerged (G1a) cases. Model results at the Z3-3 zone (Figure 9.21) b) depth-averaged velocity at the end of 14 days, c) accumulated erosion deposition in the model after 14 days, d) accumulated erosion deposition at three cross-sections (S1, S2, and S3 –Figure 9.21) on 6th Nov and 18th Nov 2012.

The above simulations were conducted without including (HLES). Since the flume simulation in Section (9.3.1) showed slightly better results when HLES was included in the model, it was essential to show the results with HLES included. In addition, it was important to look at the morphology changes at all the groynes.

Figure (9.31) shows the erosion and deposition without groynes at Zone-2 and Zone-3 after 14 days. It can be seen that after applying groynes, in most of the groyne zone erosion changed to deposition.

Comparing the accumulated erosion and deposition of the 14-day simulation of Setup#1 (emerged) in Figures 9.32 and 9.33, the inclusion of HLES produced slightly higher erosion. Therefore, HLES was excluded from all subsequent simulations.

Comparison of Figures 9.31 and 9.32 shows that applying groynes to the river increased erosion near the head of the groynes, presumably due to turbulent flow generated near the groyne tips. This influence of the groynes extended into the middle of the channel. To decrease this entrainment in the main channel, several groyne designs are examined in the next section.

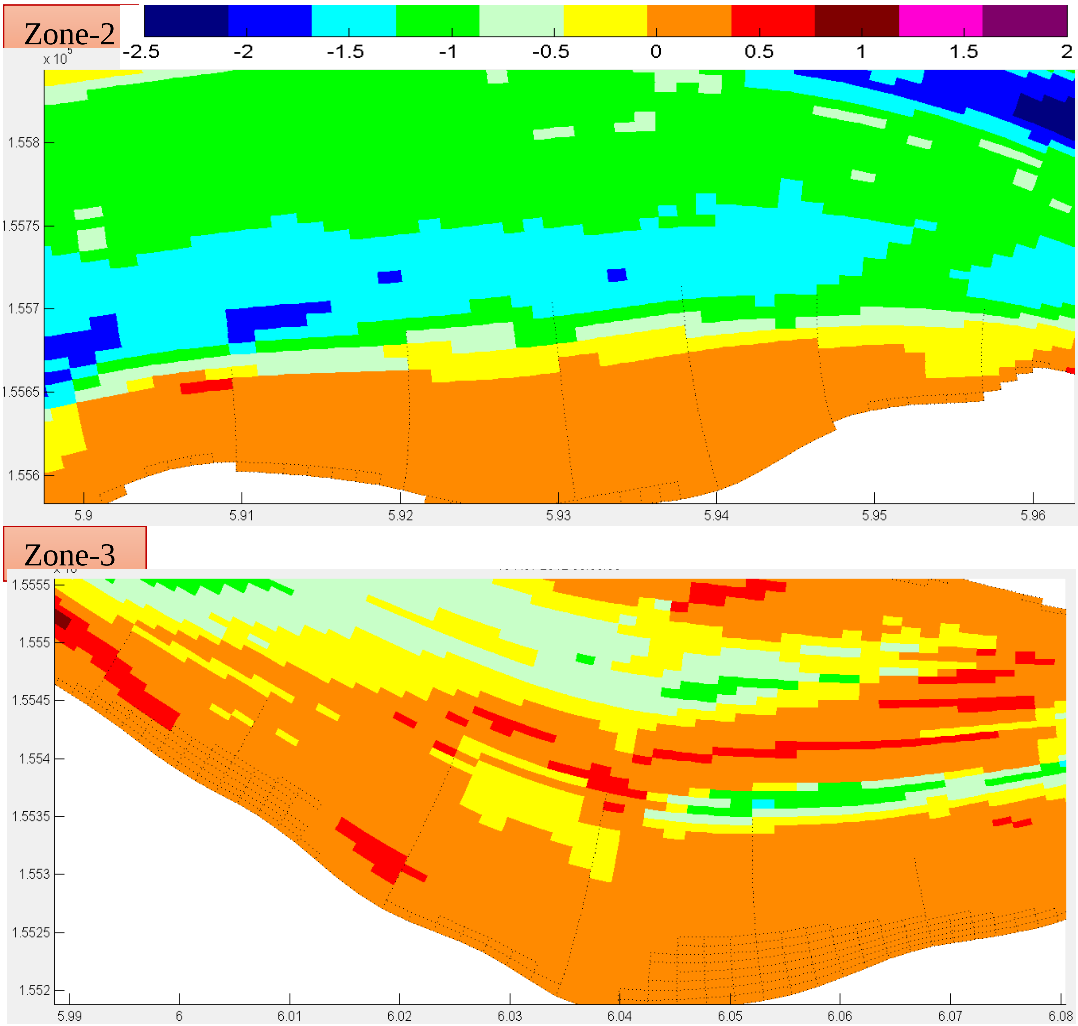

Figure (9.31) Cumulative erosion and deposition of the 14-day simulation without groynes

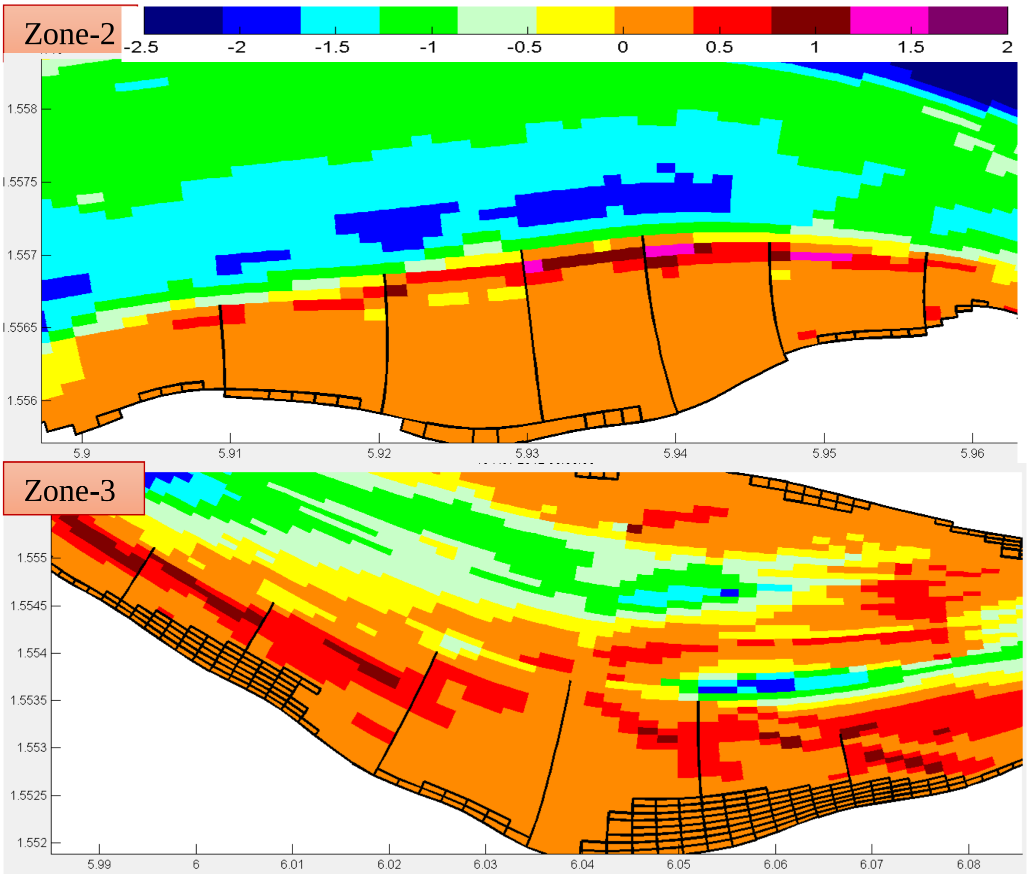

Figure (9.32) Cumulative erosion and deposition of the 14-day simulation of Setup#1 excluding HLES

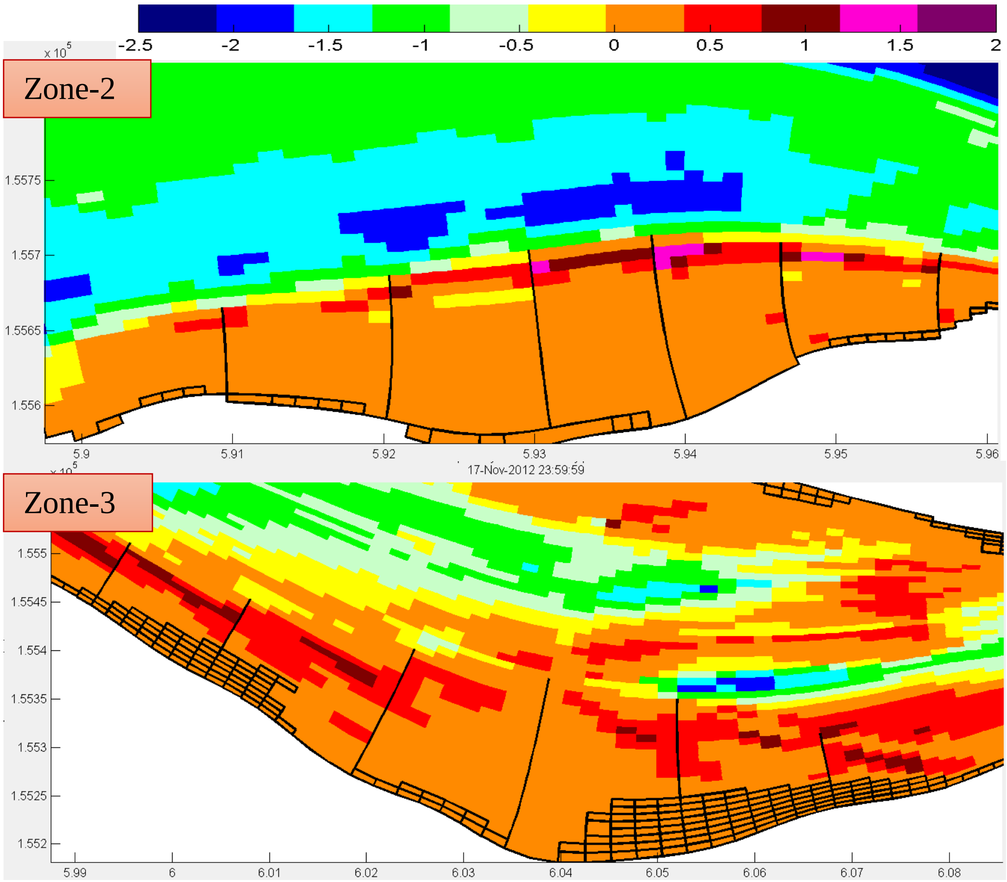

Figure (9.33) Cumulative erosion and deposition of the 14-day simulation of Setup#1 at Zone-2 and Zone-3, including HLES

9.4.3. Comparing different Design Criteria

As has been mentioned previously, the first model runs considered emergent, long groynes with an aspect ratio of 0.5-2 applied in Zone-2 and Zone-3 (Setup#1). This produced high erosion (Figure 9.34). Consequently, both bed and suspended load transport toward the reservoir increased (Figure 9.36). Therefore, in Setup#2, groyne length was decreased, while maintaining the same level from the bank toward the main stream and the aspect ratio in the range 2-0.5 (see Table 9.3 and Figure 9.20). This setup decreased erosion in the main stream and the sediment transport toward the reservoir. Total sediment transport and suspended sediment transport decreased, but bedload transport increased (Figure 9.36). In Setup#3_1, the elevation of the groynes near the bank was changed while maintaining groyne length as in the previous Setup#2 (Figure 9.20). The groynes in these runs were still emergent at normal flows. Depending on design criteria of the groynes, the elevation of the groynes near the bank should be higher in order to prevent any ice cover (Przedwojski et al., 1995). This setup only increased the suspended load transport compared to previous setup (Figure 9.36). In Setup#3_2, the groynes were divided into two segments: one part near the bank where the elevation remained higher than the normal water level, and a second part submerged by 0.5m (Figure 9.20). This setup was only applicable for Zone-3. The results of this setup showed an increase in suspended sediment supply toward the groyne zone (Figure 9.35-e). In the last setup (Setup#4), the groynes were changed to an L-head shape (Figure 9.34-e, 9.35-f). According to Przedwojski et al. (1995), L-head groynes meet the needs of bank protection and less erosion in the main channel. The results showed there was an increase in suspended load transport toward the reservoir compared to Setup#3_1, but a slightly lower bed load transport was estimated. This resulted in a lower total load transport toward the reservoir (Figure 9.36). Overall, the lowest bed load transport toward the reservoir was predicted using L-head groynes (Setup#4), the lowest suspended transport was predicted by a submergence of 0.5m (Setup#3_2), and the lowest total load transport was estimated to be the same for L-head groynes (Setup#4) and submergence (0.5m) (Setup#3_2).

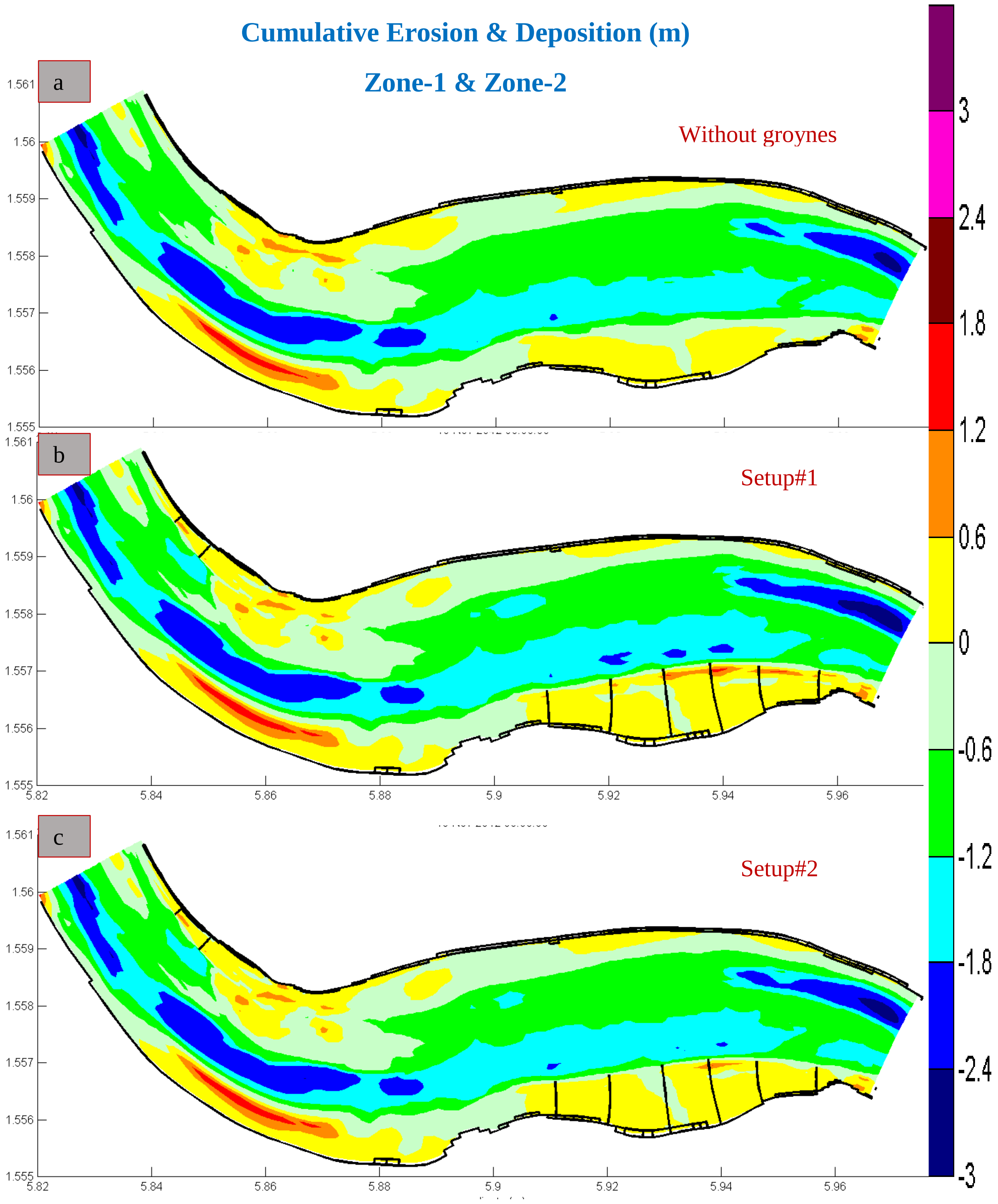

Cumulative Erosion & Deposition (m)
Zone-1 & Zone-2
a
Without groynes
b
Setup#1
c
Setup#2
1.561
1.56
1.559
1.558
1.557
1.556
1.555
5.82
5.84
5.86
5.88
5.9
5.92
5.94
5.96
3
2.4
1.8
1.2
0.6
0
-0.6
-1.2
-1.8
-2.4
-3

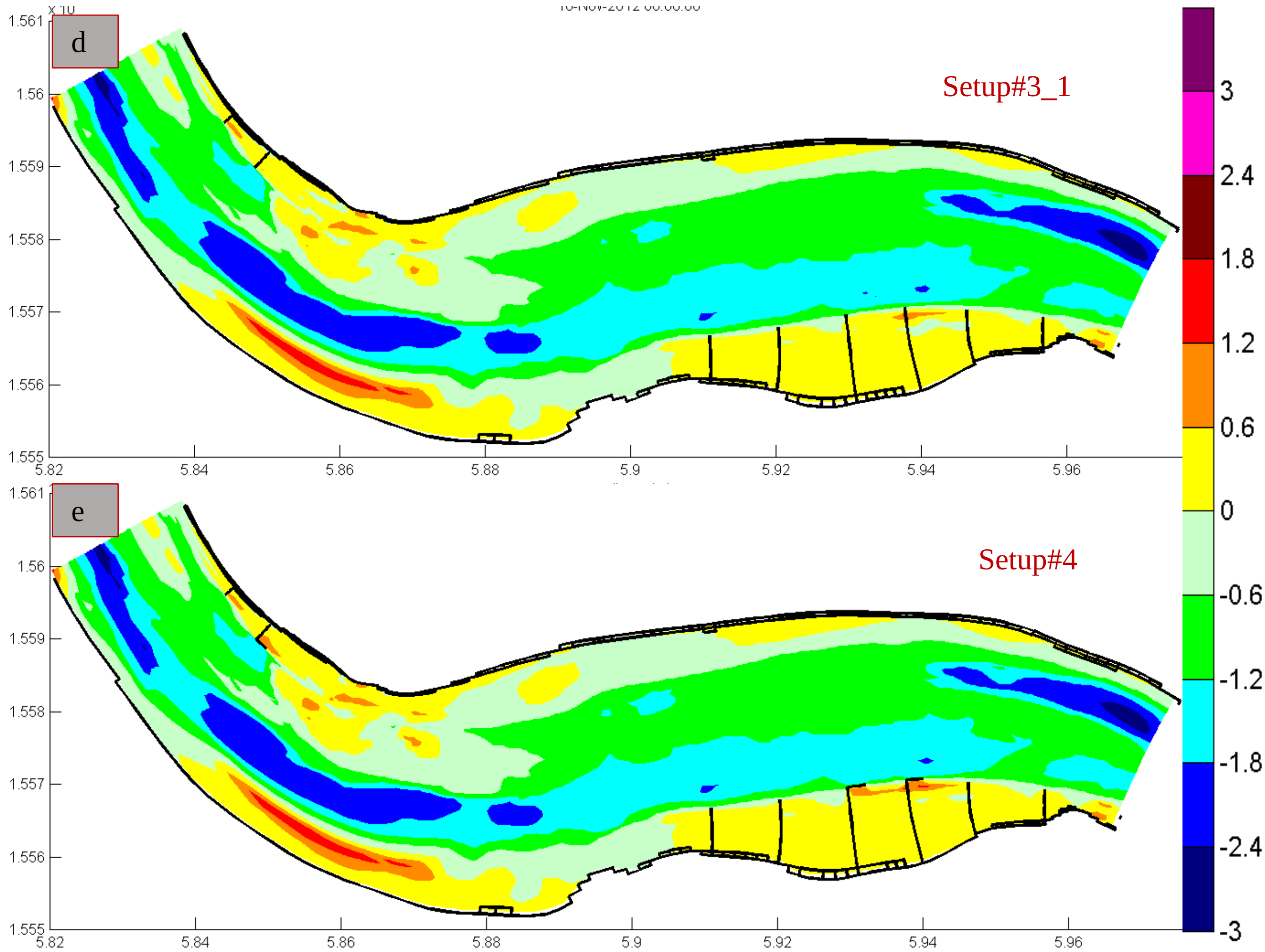

Figure (9.34) Cumulative erosion deposition for 14 days (3rd Nov-18th Nov-2012) for Zones 1 and 2, sorting from top to bottom of different groyne setups: a) without groynes, b) Setup#1, c) Setup#2, d) Setup#3_1, e) Setup#4

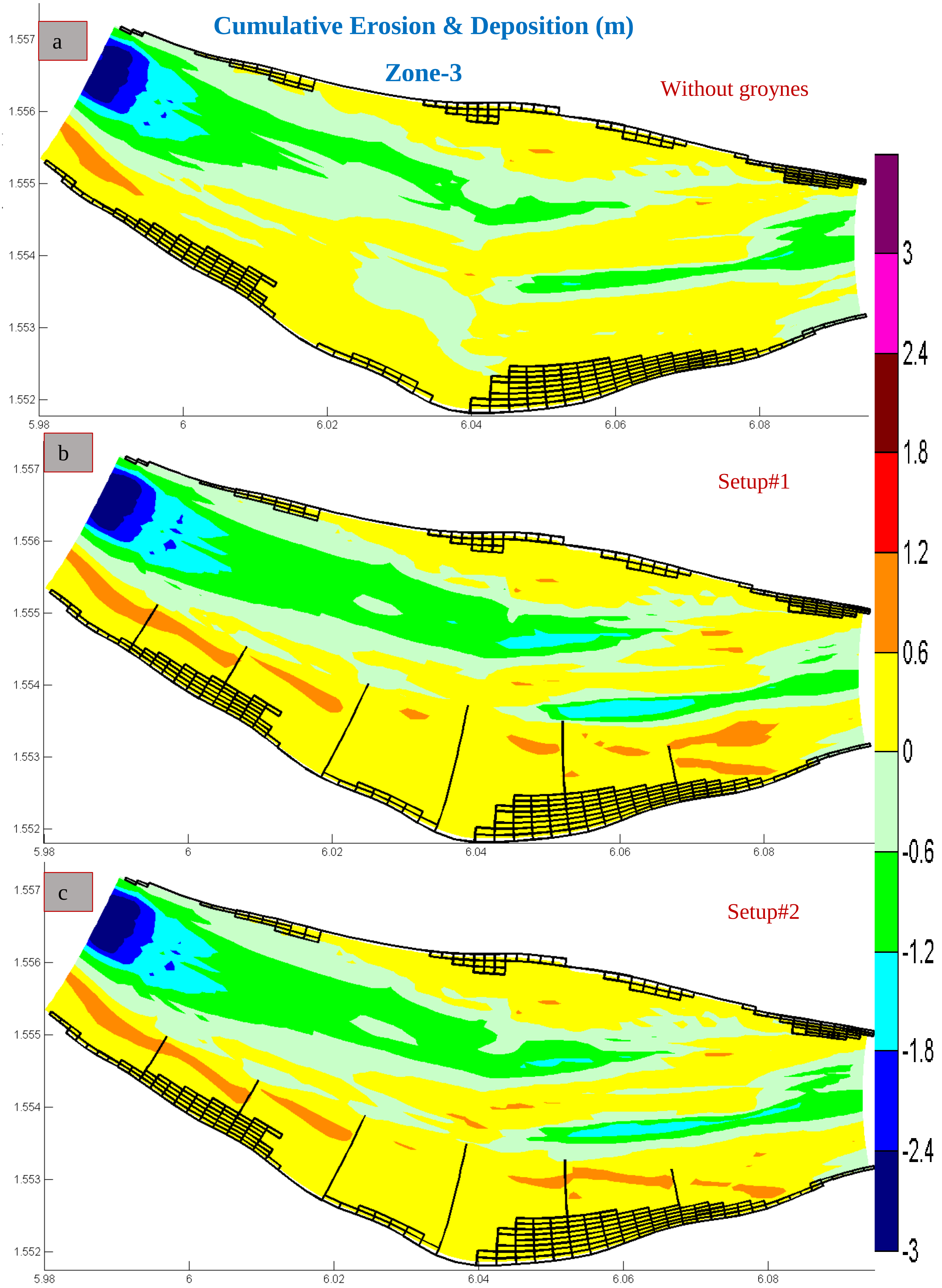
Cumulative Erosion & Deposition (m)
Zone-3
a
Without groynes
b
Setup#1
c
Setup#2
1.557
1.556
1.555
1.554
1.553
1.552
5.98
6
6.02
6.04
6.06
6.08
3
2.4
1.8
1.2
0.6
0
-0.6
-1.2
-1.8
-2.4
-3

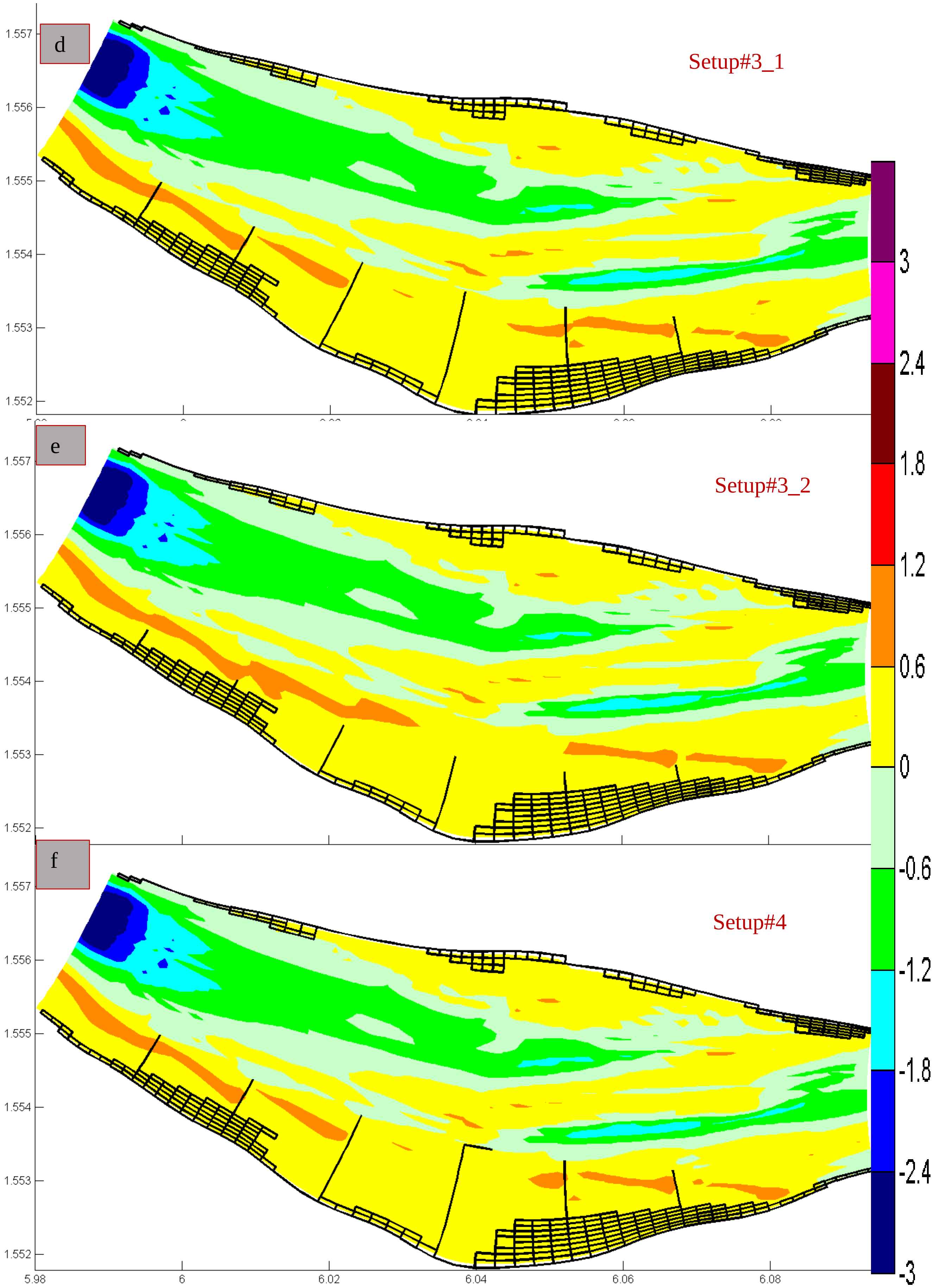

Figure (9.35) Cumulative erosion deposition for 14 days (3Nov-18Nov) of zone 3, sorting from top to bottom of different groyne setups: a) without groynes, b) Setup#1, c) Setup#2, d) Setup#3_1, e) Setup#3_2, f) Setup#4

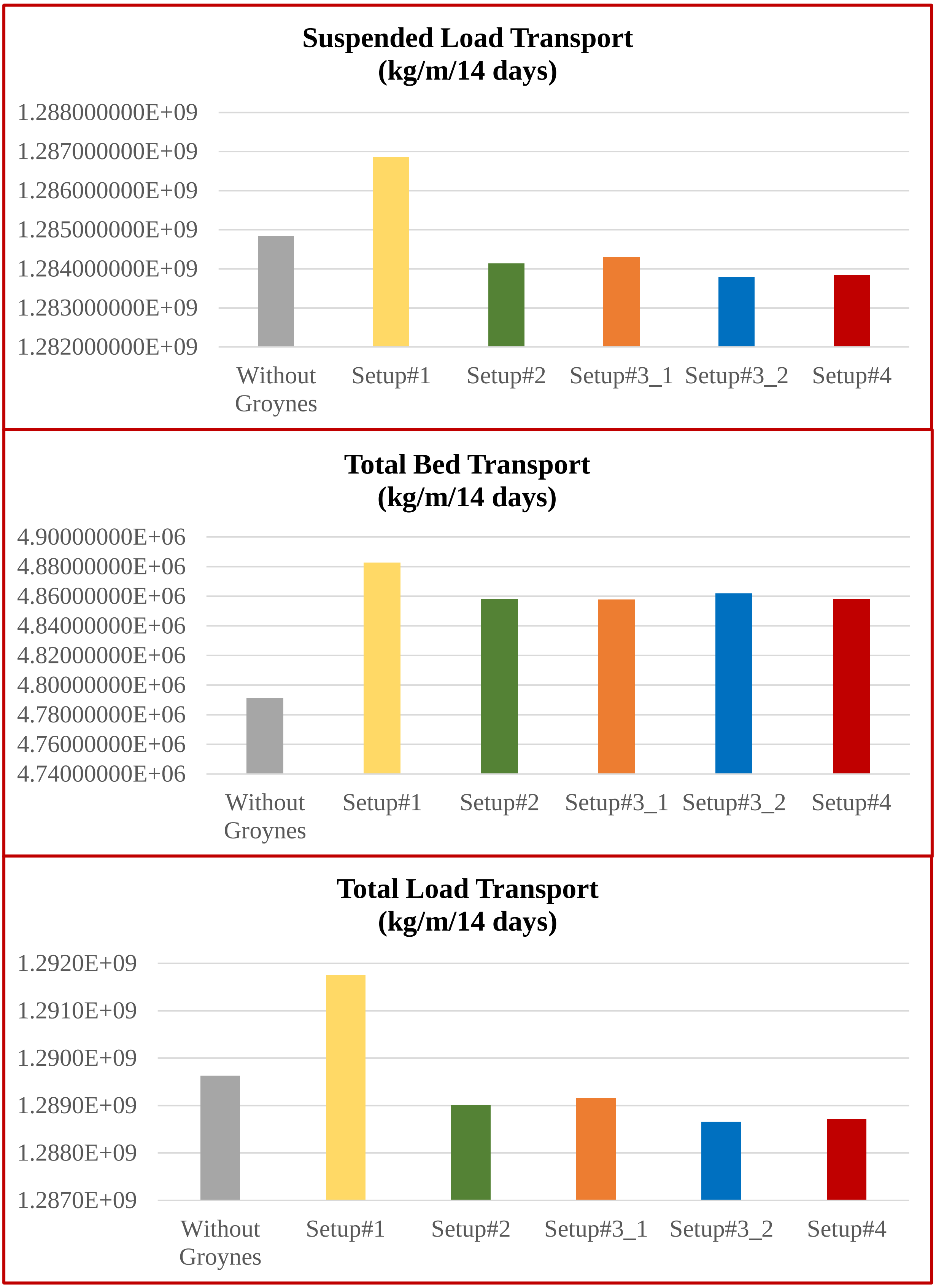

Figure (9.36) Cumulative sediment transport for 14 days at a section at downstream of the model

10. Conclusions and Recommendations

10.1 Conclusions

This study involved the development of a Delft3D morphodynamic model to evaluate sediment transport in a meandering river reach upstream of a reservoir on the Drava River, Austria. The primary conclusion of this study is that the implementation of a series of groynes in the meandering reach may beneficially reduce rates of reservoir sedimentation. This is largely due to capture of transported sediment load within the groyne embayment.

Specific findings of the study are summarized as follows:

- Meandering hydrodynamic validation revealed that the 2D model prediction was better when the secondary flow model correction was excluded. This was because the secondary flow model decreased the estimation of reverse flow at the outer bank that was observed in the measurements.
- Morphodynamic validation showed the underestimation of non-cohesive sediment transport when using the Van Rijn formula, especially during flood season. Consequently, this formula was calibrated using the Bed parameter.
- Different slope formulas did not only produce alterations in bed load transport but also had impacts on suspended load transport. This result may have an association with both the non-cohesive transport formula and bed composition.
- Bed resistance played a major role in validating the meandering morphodynamic model, especially at the concave zone and the deep area of the river.
- The results of 1-year sediment transport modelling in the meandering reach showed that the sediment entering and passing through this reach was not in equilibrium.

While considering that only 2D modelling was applied in this study, and that the modelled groynes were not built into the bathymetry, the following points can be concluded:

- The simulation showed that the eddy viscosity needed for a thin dam was greater than the eddy viscosity required for modelling a 2D weir. This may due to the fact that the equation applied for a 2D weir is not implemented over a thin dam.
- Including HLES) in the simulation led to better estimation of depth-averaged velocity in both the groyne detachment zone and at the head of the groynes in the flume scale.
- Depth-averaged velocity in the groyne embayment zone with an aspect ratio between 0.5-2 was compared for emerged and submerged cases. The results showed that although when the groynes were submerged the circulation pattern disappeared between the groynes, the low velocity zone was large in the submerged (0.5m) groyne case compared to the emergent case. This resulted in a wider zone of low bed shear stress between the groynes compared to the emergent case. However, in the case of submergence (1m), the area of low velocity was smaller compared to the other two cases.

- The above results led to producing highest deposition in the 0.5m submerged case, and lowest deposition in the 1m submerged case. Nevertheless, the sediment supply to the groyne zone is not only a function of the level of submergence, according to previous studies. Many other parameters, like the sediment concentration in the main channel, bed composition, groyne location, and bathymetry may play a role.

- The distribution of cohesive sediment concentration inside the emerged impermeable groyne zone showed that with an increasing grain size of cohesive sediment, the flow has less strength to transport the sediment near the bank. On the other hand, the model results verified previous studies of underestimation of the Rouse profile in determining non-cohesive sediment concentration for both the emerged and submerged cases.

- Although both submerged (0.5m) and L-head groynes were not applied to all the groynes, they produced approximately the same suspended sediment transport toward the reservoir. Nevertheless, applying L-head groynes produced less bed load transport toward the reservoir compared to the submerged case.

- In submerged cases, erosion estimation over the groynes is crucial, but it is not estimated in this model due to not including groynes in the bathymetry.

10.2 Recommendations

- Although the change in water level at the outlet boundary (flushing analysis) showed impacts on both sediment transport toward the reservoir and morphology changes in this reach, it is crucial to look at changes in both the river and the reservoir reaches.

- Further studies need to be conducted to find the relationship between the sediment supply to the groyne zone and the flow patterns between submerged groynes.

This study found that implementation of groynes in the meandering river reach will have clear benefits. These include:

1) Decline in suspended sediment transport toward the reservoir, which is advantageous for the operation of both the reservoir and the turbine.
2) Bed load increase due to the constriction of flow to the main channel, which is useful for regaining flow capacity of the river.

Despite these benefits, further study is required prior to the implementation of groynes, specifically:

1) Comparison of the construction and maintenance costs for these structures to the costs of dredging in this reach and in the reservoir.
2) Modeling long-term impact of such groyne implementation by modeling both the river and reservoir together.
3) Consideration of groyne implementation on dredging operations. It may be that dredging operations will simply be relocated from the reservoir to the groyne embayment. The relative costs of these dredging operations should be considered.

References

Ahmad, M. F., Dong, P., Mamat, M., Wan Nik, W. B., & Mohd, M. H. (2011). The critical shear stresses for sand and mud mixture. Applied Mathematical Sciences, 5(2), 53-71.

Alfrink, B. J., & Van Rijn, L. C. (1983). Two-equation turbulence model for flow in trenches. Journal of Hydraulic Engineering, 109(7), 941-958.

Bagnold, R. A. (1966). An approach to the sediment transport problem. General Physics Geological Survey, Prof. Paper.

Batuca, D. G., & Jordaan Jr, J. M. (2000). Silting and desilting of reservoirs. CRC Press.

Claude, N., Rodrigues, S., Bustillo, V., Bréhéret, J. G., Macaire, J. J., & Jugé, P. (2012). Estimating bedload transport in a large sand–gravel bed river from direct sampling, dune tracking and empirical formulas. Geomorphology, 179, 40-57.

Constantinescu, G., Sukhodolov, A., & McCoy, A. (2009). Mass exchange in a shallow channel flow with a series of groynes: LES study and comparison with laboratory and field experiments. *Environmental fluid mechanics*, *9*(6), 587-615.

Constantinescu, G., Kashyap, S., Tokyay, T., Rennie, C. D., & Townsend, R. D. (2013). Hydrodynamic processes and sediment erosion mechanisms in an open channel bend of strong curvature with deformed bathymetry. Journal of Geophysical Research: Earth Surface, 118(2), 480-496.

Delft3D-FLOW. 2011. Simulation of multi-dimensional hydrodynamic flows and transport phenomena, including sediments. User Manual. Hydro-Morphodynamic, Version: 3.15, Revision: 18392, 7 September2011.

Dey, S. (2014). Fluvial Hydrodynamics. Springer Berlin Heidelberg.

Dorfmann, C., & Knoblauch, H. (2008). ADCP measurements in a reservoir of a run-of-river Hydro Power Plant. In 6th International Symposium on Ultrasonic Doppler Method for Fluid Mechanics and Fluid Engineering, Prague, Tchech Republic (pp. 45-48).

Einstein, H. A. (1950). The bed-load function for sediment transportation in open channel flows (No. 1026). US Department of Agriculture.

Elhadi, N., Harrington, A., Hill, I., Lau, Y. L., & Krishnappan, B. G. (1984). River mixing-A state-of-the-art report. Canadian Journal of Civil Engineering, 11(3), 585-609.

Fan, J., & Morris, G. L. (1992). Reservoir sedimentation. II: Reservoir de siltation and long-term storage capacity. Journal of Hydraulic Engineering, 118(3), 370-384.

Groenenboom, J. (2015). Modelling sand-mud-bed interaction in the Scheldt estuary (Doctoral dissertation, TU Delft, Delft University of Technology).

Habersack, H. M. (1996). Lack and surplus of sediments being transported by river systems. IAHS Publications-Series of Proceedings and Reports-Intern Assoc Hydrological Sciences, 236, 565-574.

Hassanzadeh, H., Faiznia, S., Bajestan, M. S., & Motamed, A. (2011). Estimate of Sediment Transport Rate at Karkheh River in Iran Using Selected Transport Formulas. World Applied Sciences Journal, 13(2), 376-384

Hey, R. D., & Thorne, C. R. (1975). Secondary flows in river channels. Area, 191-195.

Jamieson, E. C., Rennie, C. D., & Townsend, R. D. (2013). 3D flow and sediment dynamics in a laboratory channel bend with and without stream barbs. Journal of Hydraulic Engineering, 139(2), 154-166.

Kalkwijk, J. P. T., & Booij, R. (1986). Adaptation of secondary flow in nearly horizontal flow. Journal of Hydraulic Research, 24(1), 19-37.

Kashyap, S. (2010). Numerical modeling of flow around submerged groynes in a sharp bend using large eddy simulation (Doctoral dissertation, University of Ottawa).

Kasvi, E., Vaaja, M., Kaartinen, H., Kukko, A., Jaakkola, A., Flener, C., & Alho, P. (2015). Sub-bend scale flow–sediment interaction of meander bends—a combined approach of field observations, close-range remote sensing and computational modelling. Geomorphology, 238, 119-134.

Kasvi, E., Alho, P., Lotsari, E., Wang, Y., Kukko, A., Hyyppä, H., & Hyyppä, J. (2015). Two-dimensional and three-dimensional computational models in hydrodynamic and morphodynamic reconstructions of a river bend sensitivity and functionality. Hydrological Processes, 29(6), 1604-1629.

Lane, S. N., Bradbrook, K. F., Richards, K. S., Biron, P. A., & Roy, A. G. (1999). The application of computational fluid dynamics to natural river channels: three-dimensional versus two-dimensional approaches. Geomorphology, 29(1), 1-20.

Lesser, G. R., Roelvink, J. A., Van Kester, J. A. T. M., & Stelling, G. S. (2004). Development and validation of a three-dimensional morphological model. Coastal engineering, 51(8), 883-915.

Maa, J. P. Y., Kwon, J. I., Hwang, K. N., & Ha, H. K. (2008). Critical bed-shear stress for cohesive sediment deposition under steady flows. Journal of Hydraulic Engineering, 134(12), 1767-1771.

Nicholas, A. P. (2003). Investigation of spatially distributed braided river flows using a two-dimensional hydraulic model. Earth Surface Processes and Landforms, 28(6), 655-674.

Przedwojski, B., Błazejewski, R., & Pilarczyk, K. W. (1995). River training techniques: fundamentals, design and applications. AA Balkema.

Rijn, L. C. V. (1984b). Sediment transport, part II: suspended load transport. Journal of hydraulic engineering, 110(11), 1613-1641.

Rüther, N., & Olsen, N. R. B. (2006). 3D modeling of transient bed deformation in a sine-generated laboratory channel with two different width-to-depth ratios.

Safarzadeh, A., Salehi Neyshabouri, S. A. A., & Zarrati, A. R. (2016). Experimental Investigation on 3D Turbulent Flow around Straight and T-Shaped Groynes in a Flat Bed Channel. Journal of Hydraulic Engineering, 04016021.

Song, C. G., Seo, I. W., & Do Kim, Y. (2012). Analysis of secondary current effect in the modeling of shallow flow in open channels. Advances in water resources, 41, 29-48.

Struiksma, N., Olesen, K. W., Flokstra, C., & De Vriend, H. J. (1985). Bed deformation in curved alluvial channels. Journal of Hydraulic Research, 23(1), 57-79.

Stive, M. J. F. A Numerical Study on Design of Normal & T-Head Groins (Doctoral dissertation, Delft University of Technology).

Sukhodolov, A., Uijttewaal, W. S., & Engelhardt, C. (2002). On the correspondence between morphological and hydrodynamical patterns of groyne fields. Earth Surface Processes and Landforms, 27(3), 289-305.

Talmon, A. M., Struiksma, N., & Van Mierlo, M. C. L. M. (1995). Laboratory measurements of the direction of sediment transport on transverse alluvial-bed slopes. Journal of Hydraulic Research, 33(4), 495-517.

Uijttewaal, W. S. J., Lehmann, D. V., & Mazijk, A. V. (2001). Exchange processes between a river and its groyne fields: Model experiments. Journal of Hydraulic Engineering, 127(11), 928-936.

Uijttewaal, W. S. (2005). Effects of groyne layout on the flow in groyne fields: Laboratory experiments. Journal of Hydraulic Engineering, 131(9), 782-791.

USDA. (2005). Engineering Technical Note No. 23: Design of Stream Barbs (Version 2.0), Natural Resources Conservation Service, Portland, OR.

Van Rijn, L. C. (1984). Sediment transport, part I: bed load transport. Journal of hydraulic engineering, 110(10), 1431-1456.

Van Rijn, L. C. (1987). Mathematical modelling of morphological processes in the case of suspended sediment transport (pp. Communication-No). Delft: Waterloopkundig Laboratorium.

Van Rijn, L. C. (1993). Principles of sediment transport in rivers, estuaries and coastal seas (Vol. 1006). Amsterdam: Aqua publications.

Van Rijn, L. C., Nieuwjaar, M. W., Van Der Kaay, T., Nap, E., & van Kampen, A. (1993). Transport of fine sands by currents and waves. Journal of waterway, port, coastal, and ocean engineering, 119(2), 123-143.

Van Ledden, M. (2003). Sand-mud segregation in estuaries and tidal basins (p. 221). University of Technology.

Van Rijn, L. C. (2007). Unified view of sediment transport by currents and waves. II: Suspended transport. Journal of Hydraulic Engineering, 133(6), 668-689.

Van Rijn, L. C. (2013). Simple general formulae for sand transport in rivers, estuaries and coastal waters. Retrieved from www. Leovanrijn-sediment. Com.

Van Rijn, L. C. (2016). Initiation of Motion and Suspension; Critical Bed-Shear Stress for Sand-Mud Mixtures.

Wagner, C. R., & Mueller, D. S. (2001). Calibration and validation of a two-dimensional hydrodynamic model of the Ohio River, Jefferson County, Kentucky. US Department of the Interior, US Geological Survey.

Winterwerp, J. C. (2007). On the sedimentation rate of cohesive sediment. Proceedings in Marine Science, 8, 209-226.

Winterwerp, J. C., Kesteren, W. G. M., Prooijen, B., & Jacobs, W. (2012). A conceptual framework for shear flow–induced erosion of soft cohesive sediment beds. Journal of Geophysical Research: Oceans, 117(C10).

Yossef, M. F. M. (2005). Morphodynamic of rivers with groynes. TU Delft, Delft University of Technology.

Yossef, M. F., & de Vriend, H. J. (2010). Flow details near river groynes: experimental investigation. Journal of Hydraulic Engineering, 137(5), 504-516.

Yuanita, N., & Tingsanchali, T. (2008). Development of a river delta: a case study of Cimanuk river mouth, Indonesia. Hydrological processes, 22(18), 3785-3801